INFORMATION TO USERS

This manuscript has been reproduced from the microfilm master. UMI films the text directly from the original or copy submitted. Thus, some thesis and dissertation copies are in typewriter face, while others may be from any type of computer printer.

The quality of this reproduction is dependent upon the quality of the copy submitted. Broken or indistinct print, colored or poor quality illustrations and photographs, print bleedthrough, substandard margins, and improper alignment can adversely affect reproduction.

In the unlikely event that the author did not send UMI a complete manuscript and there are missing pages, these will be noted. Also, if unauthorized copyright material had to be removed, a note will indicate the deletion.

Oversize materials (e.g., maps, drawings, charts) are reproduced by sectioning the original, beginning at the upper left-hand corner and continuing from left to right in equal sections with small overlaps.

Photographs included in the original manuscript have been reproduced xerographically in this copy. Higher quality 6" x 9" black and white photographic prints are available for any photographs or illustrations appearing in this copy for an additional charge. Contact UMI directly to order.

Bell & Howell Information and Learning
300 North Zeeb Road, Ann Arbor, MI 48106-1346 USA
800-521-0600

NUMERICAL SIMULATION OF LANGMUIR CIRCULATIONS IN A WAVY DOMAIN AND ITS COMPARISON WITH THE CRAIK-LEIBOVICH THEORY

A DISSERTATION
SUBMITTED TO THE DEPARTMENT OF MECHANICAL ENGINEERING
AND THE COMMITTEE ON GRADUATE STUDIES
OF STANFORD UNIVERSITY
IN PARTIAL FULFILLMENT OF THE REQUIREMENTS
FOR THE DEGREE OF
DOCTOR OF PHILOSOPHY

Hong Zhou
December 1999

UMI Number: 9961994

Bell & Howell Information and Learning Company
300 North Zeeb Road
P.O. Box 1346
Ann Arbor, MI 48106-1346

I certify that I have read this dissertation and that in my opinion it is fully adequate, in scope and in quality, as a dissertation for the degree of Doctor of Philosophy.

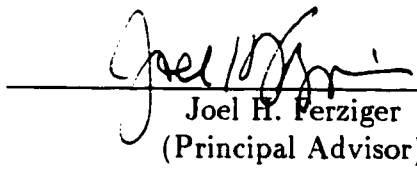

Joel H. Ferziger
(Principal Advisor)

I certify that I have read this dissertation and that in my opinion it is fully adequate, in scope and in quality, as a dissertation for the degree of Doctor of Philosophy.

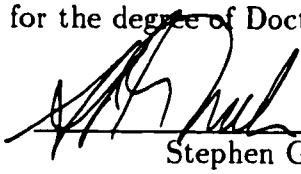

Stephen G. Monismith
(Co-Principal Advisor)

I certify that I have read this dissertation and that in my opinion it is fully adequate, in scope and in quality, as a dissertation for the degree of Doctor of Philosophy.

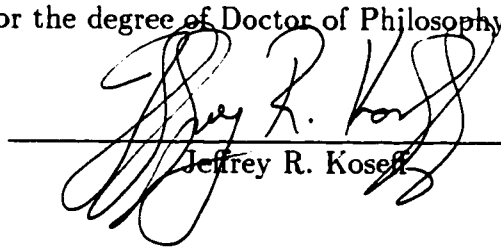

Jeffrey R. Koseff

Approved for the University Committee on Graduate Studies:

Abstract

Langmuir circulations are pairs of counter rotating vortices aligned with the wind in lakes, estuaries, and oceans. They enhance the vertical transport of heat, mass and momentum. Knowledge of the mechanism involved and its influences are essential for the parameterizations used in mixed layer models and for better understanding the dynamics of the upper ocean.

In this study, numerical simulations of laminar and turbulent open channel flows with a moving wavy surface that has the form of a second order Stokes wave are performed. A constant tangential stress is imposed at the top. It drives a mean current that interacts with the surface wave to generate Langmuir circulations. In our model, the Navier-Stokes equations are solved in a curvilinear coordinate system, with kinematic and dynamic boundary conditions applied on the wavy surface. An orthogonal transformation is used to map the wavy physical domain into a rectangular computational domain. The numerical method is a modified version of the fractional step method of Zang *et al.* (1994) for a generalized curvilinear coordinate. For turbulent cases, we used a large eddy simulation approach that models the sub-grid stresses with a dynamically determined Smagorinsky constant.

First, two dimensional free surface flows under a second order Stokes wave are examined. Analytical solutions for the inviscid flow and numerical solutions for the viscous flow are obtained. Two components of the velocity field important to Langmuir circulations are identified: the Stokes drift caused by the irrotational wave motion, and the Eulerian mean flow induced by the top wavy boundary layer.

In the three dimensional wavy flow, the initial perturbations grow exponentially in time. Higher modes with short wavelengths develop first. They later combine and there are large counter rotating Langmuir cells in the final equilibrium state. As observed in the field, the Langmuir cells are asymmetric, the downwind velocity being greater at the convergence zone than at the divergence zone. They coexist with the wave field and are modulated by the surface wave.

The numerical results are compared with those from the simulations based on the

Craik-Leibovich (CL) theory in a rectangular domain. It is suggested that, in addition to the Stokes drift included in the CL theory, the Eulerian mean flow induced by the surface wavy boundary layer is also important. Including its effects in the simulation based on the CL theory is essential in predicting the correct quantitative properties of Langmuir circulations, especially the pitch, which is the ratio of the maximum downwind jet velocity to the maximum downwelling velocity. For laminar flows, a two dimensional simulation based on the Craik-Leibovich theory shows that the cell merging process resembles the inverse energy cascade in two dimensional turbulence. Furthermore, when the wave-induced stress is included, excellent agreement is achieved between the computed streamwise-averaged wavy flow and that predicted by the CL theory.

For the turbulent case, the Langmuir circulations are embedded in a much stronger, chaotic instantaneous field; nonetheless, they can be clearly identified by time averaging. Relative to non-wavy stress-driven open channel flow, the streamwise turbulent fluctuations are weaker but the spanwise and vertical perturbations are stronger. Unlike the open channel flow turbulence, in which the streamwise momentum is transported mainly by the turbulent motion, in Langmuir turbulence, the mixing due to the turbulence and the mean Langmuir circulations are approximately of equal importance. The mean flow is also modified. Close to the bottom wall, the logarithmic region is destroyed by the penetration of the Langmuir circulation. Near the top surface, Langmuir circulations destroy most of the logarithmic profile in turbulent Couette flows, leading to a more uniform mean current. The turbulent kinetic energy budget shows that in the top surface layer, the production rate is enhanced in Langmuir turbulence. The pressure transport term is also significant in this region; this is not the case for turbulent Couette flow. Although the Langmuir circulation structure is similar in turbulent wavy flow and the flow obtained using CL theory, significant quantitative differences are observed. For $La_t = (u_*/2S)^{1/2} = 0.3$, where u_* is the shear velocity at the wavy surface, and S the characteristic Stokes drift velocity, CL theory produces stronger Langmuir cells but weaker turbulence.

Acknowledgements

I am blessed to have Professor Joel Ferziger and Professor Stephen Monismith as my advisors. I am indebted to my principal advisor, Professor Joel Ferziger, for his support and encouragement throughout my Ph.D. study. I have greatly enjoyed working with him. And I admire his optimistic attitude, quick thinking and ability to explain complex things in a simple way. I thank Professor Stephen Monismith, my co-principal advisor, for his valuable contribution to this work. His enthusiasm to research and insight to the physical problems have constantly inspired me.

I thank professor Jeffrey Koseff for serving on my reading committee and for providing helpful assistance to my research. I am grateful to Professor Robert Street for his insightful comments on this work. I also thank Professor George Homsy for willing to chair my university oral examination.

I thank Dr. Yan Zang for sharing his version of computer code for an orthogonal curvilinear system, which have provided a good starting point for my work. Many thanks are due to Dr. Rajat Garg for giving me his unpublished work on Langmuir circulation, which has greatly benefited my early attacks on this complex problem. I especially thank Charles Pierce for the indepth discussions on turbulence and numerical methods.

Thanks to the Zang gang people (the people who have used Dr. Yan Zang's code) in the Environmental Fluid Mechanics Laboratory (EFML), Dr. Ben Hodges, Dr. Ron Calhoun, Dr. Ann Cui, Oliver Fringer, Emily Zedler and Li Ding, for their useful inputs during group meetings.

I am so lucky to spend my Ph. D. years in EFML. Its friendly atmosphere and exciting research environment have made my stay at Stanford unique and pleasant. I thank all of the volunteer system administrators, especially Oliver Fringer, Li Ding, Emily Zedler and Tina Katopodes for patiently accommodating my numerous requests. I am grateful to Lisa Lucas for giving me her thesis template that have saved me so much time. I thank Rajat Garg, Lucinda Shih, and Amy Stewart for being wonderful officemates.

I also want to thank my friends Kathy Liu, Li Ye, Steven Li, Jeff Xu, Xingang

Liang, Yue Yang, Shishun Chang, Steve Bryson and Martin Lauchli for their friendship and the good times together.

Most importantly, I thank my parents back in China for their love and support.

Financial support for this work was provided by the Office of Naval Research under Grant No. N00014-92-J-1611, with Dr. Lou Goodman as the technical monitor.

Abbreviations

Roman Symbols

a	Wave amplitude.
A, B	Metric coefficients for the 2D wavy analytical solution.
C	Model coefficient in the dynamic subgrid scale model.
C_w	Phase speed of the surface wave.
C_{ij}	Mean velocity transport for $< u_i'' u_j'' >$.
D_{ij}	Viscous diffusion rate for $< u_i'' u_j'' >$.
$\overline{F_i^m}$	Flux tensor of the filtered momentum equation in the curvilinear system.
Fr	Froude number. $Fr = \frac{U}{\sqrt{gh}}$.
G^{mn}	Metric skewness tensor.
J	Jacobian.
L_x, L_y	Domain length in the streamwise and spanwise directions, respectively.
$\mathcal{L}_{ij}$	Leonard tensor.
p	Modified pressure, with the hydrostatic part subtracted.
P	Pressure that includes the hydrostatic part.
Pt	Pitch of Langmuir circulation.
P_{ij}	Production rate for $< u_i'' u_j'' >$.
q_{ij}	Anisotropic part of the subgrid scale stress tensor, τ_{ij}.
Q_{ij}	Anisotropic part of the subgrid scale stress tensor, $\mathcal{T}_{ij}$.
R	Rayleigh number: $R = \sqrt{Re_s Re_*^2}$

Re_τ	Reynolds number: $Re_\tau = u_\tau h/\nu$.
Re_*	Reynolds number: $Re_* = u_*^d h/\nu$.
Re_{*eff}	Generalized Re_* that can include the Eulerian mean flow effects.
Re_s	Reynolds number: $Re_s = Sh/\nu$.
S	Characteristic Stokes drift velocity. $S = \epsilon^2 C_w^d/2$
$\overline{S}_i$	Source term of the filtered momentum equation in curvilinear system.
$\overline{S}_{ij}$	Resolved strain rate tensor.
t	Time.
T_{ij}	Turbulent transport rate for $< u_i'' u_j'' >$.
T_{ij}^{sgs}	SGS transport rate for $< u_i'' u_j'' >$.
$\mathcal{T}_{ij}$	Subgrid scale stress tensor under test-scale filter.
$u(i)$	Physical components of the velocity in ξ^i direction of the curvilinear system.
u_e	Eulerian velocity
u_e^{LH}	Eulerian mean flow velocity predicted by Longuet-Higgins
u_l	Lagrangian velocity
u_i	Cartesian velocity components: $u_1 = u, u_2 = v, u_3 = w$.
u_i^*	Intermediate Cartesian velocity components.
u_τ	Bottom boundary friction velocity.
u_*	Upper boundary friction velocity.
u, v, w	Cartesian velocity components in the streamwise, spanwise and vertical directions, respectively.

U Generalized velocity scale.

U_i Ensemble averaged, resolved velocity components. $U_i =< \overline{u}_i >$.

U_e Eulerian velocity in the fixed coordinate system for wavy cases.

U_l Lagrangian velocity in the fixed coordinate system for wavy cases.

U_w Wind speed.

U^m Volume flux in curvilinear system.

U^{*m} Intermediate flux velocity in curvilinear system.

V^m Contravariant velocity in curvilinear system. $V^m = JU^m$.

X_i Fixed Cartesian coordinates for wavy cases.

x_i Cartesian coordinates. $x_1 = x, x_2 = y, x_3 = z$. For wavy cases, this system moves at the phase speed of the surface wave.

x, y, z Cartesian coordinates in streamwise, spanwise and vertical directions, respectively. For wavy cases, this system moves at the phase speed of the surface wave.

Greek Symbols

α Stretch parameter for vertical coordinate.

β Ratio of the wind-driven current shear to the Eulerian mean flow shear.

γ Ratio of the wind-driven stress to the Eulerian mean flow stress.

$\overline{\Delta}$ Filter size.

ϵ Wave slope.

ε_{ij} Viscous dissipation rate for $< u_i'' u_j'' >$.

ε_{ij}^{sgs} SGS dissipation rate for $< u_i'' u_j'' >$.

η_s	Surface wave height, with zero mean.
η^m	Intermediate curvilinear coordinates.
κ_x	Wave number of the surface wave (streamwise).
κ_y	Wave number of the Langmuir circulations (spanwise).
μ	Parameter of the second order component of Stokes wave.
ν	Molecular viscosity.
ν_t	Eddy viscosity.
ξ^m	Curvilinear coordinates in computational domain.
Π_{ij}	Pressure transport rate for $< u_i'' u_j'' >$.
ϖ	A complex number in the normal modes solution in 2DCL stability analysis. The magnitude of its imaginary part is the growth rate of the flow.
τ_*	Tangential stress at the top surface.
τ_{ij}	Subgrid-scale stress tensor.
τ_{ij}^m	Ensemble averaged stress tensor due to molecular viscosity.
τ_{ij}^{sgs}	Ensemble averaged subgrid-scale stress tensor (anisotropic part).
τ_{ij}^r	Resolved Reynolds stress.
τ_{ij}^{total}	Total stress. $\tau_{ij}^{total} = \tau_{ij}^m + \tau_{ij}^{sgs} + \tau_{ij}^r$.
ϕ	Pseudo-pressure.
ϕ_{ij}	Pressure-strain redistribution for $< u_i'' u_j'' >$.
ω_i	Vorticity components in x_i direction.

Other Symbols

$\mathcal{O}()$	Order of magnitude.
$\overline{(\cdot)}$	Grid filter operator.
$\widetilde{\overline{(\cdot)}}$	Test-scale grid filter operator.
$(\cdot)^n$	Index of the time step.
$(\cdot)^d$	Dimensional variable.
$<(\cdot)>$	Ensemble average. It implies a time averaging for turbulence that reaches statistical steady state and averaging over homogeneous directions of the flow, if any exists.
$(\cdot)''$	Fluctuation components. It is equal to the resolved instantaneous value minus the ensemble average of the resolved value.

Abbreviations

2Dwavy	Two dimensional flow under a wavy surface.
2DCL	Two dimensional flow in a rectangular domain with Craik-Leibovich equations.
3Dwavy	Three dimensional flow under a wavy surface.
3DCL	Three dimensional flow in a rectangular domain with Craik-Leibovich equations.
3DOChan	Three dimensional open channel flow in a rectangular domain with zero pressure gradient and stress on the top.
ADI	Alternate Direction Implicit.
CFL	Courant-Friedrichs-Lewy.
DNS	Direct numerical simulation.
LES	Large eddy simulation.
SGS	Subgrid scale.

Table of Contents

List of Tables

List of Figures

Chapter 1

Introduction

1.1 Background

Mixing processes in the upper ocean are of great importance in environmental predictions. For example, they greatly affect the global climate. The prediction of the heat, momentum and gas exchange at the air-sea surface is a significant element in weather prediction. The mixing also determines the distribution of chemical pollutants, which is a major concern in industrial waste disposal. Furthermore, the transport of oxygen and carbon dioxide from the air above and nutrients from the bottom water influences biological productivity as well as offshore fisheries.

The mechanisms of mixing, however, are poorly understood. The complexities arise from the simultaneous existence of several processes, including wave breaking (both on the surface and from internal waves), shear instability due to the wind stress, convective motions due to nighttime cooling as well as salinity gradients, and the circulations generated by the interactions of surface waves and the wind-driven currents. Therefore, successful parameterization must take into account of all these components with quantitative accuracy.

A logical first step in constructing such a model is to isolate each of the key processes and to fully understand its mechanisms and dynamics. In this dissertation, we focus on the interactions of the surface waves and wind-driven currents, especially the phenomenon known as Langmuir circulations.

Langmuir circulations are pairs of counter rotating vortices aligned roughly with the wind in lakes, estuaries and oceans. They were first reported by Langmuir (1938) and bear his name. During a trip on the Atlantic Ocean in 1927, Langmuir noticed a large number of "streaks", or windrows formed by floating seaweed parallel to the wind direction with spacings ranging from 100 to 200 meters and lengths up to 500 meters. Langmuir hypothesized that these streaks are formed by a series of longitudinal helical

vortices of alternating sense below the water surface. This conjecture was later proved by Langmuir with remarkable flow visualization experiments in Lake George.

The following basic properties of Langmuir circulations were observed. Associated with the longitudinal vortices are downwelling zones, above which the windrows are formed, and upwelling zones, above which the flow diverges in the spanwise direction. The convergence lines are roughly aligned with the wind. Langmuir cells are asymmetric. Furthermore, the downwind current at the convergence zone is greater than that at the divergence zone, and is known as the "current anomaly".

Since Langmuir's pioneering work, the potential significance of Langmuir circulations has created great interest in them. First of all, the vigorous mixing caused by their convective motions calls into question the validity of the widely used one dimensional "slab" model of the mixed layer. The one dimensional model in Phillips (1977), for example, assumes the mixed layer responds to atmospheric forcing with rapid mixing of heat and momentum (Pollard 1977a). Models with parameters obtained by fitting laboratory experiments predict changes in the mixed layer depth and averaged buoyancy and velocity as functions of the surface buoyancy fluxes and wind stress. However, as argued by Turner (1973), the laboratory experiments may not include the mixing due to the Langmuir circulations and thus may underestimate the mixing. Therefore, the mixed layer model should be improved to include not only the effects of surface wind stress and buoyancy flux, but also the sea state that is important to the formation of the Langmuir circulations (Leibovich and Paolucci 1980b).

Observations of bubble clouds suggest that Langmuir circulation can affect air-sea gas exchange. Wave breaking and heavy rain provide uniformly distributed bubble sources at the sea surface (Thorpe and Hall 1980). With a bottom-mounted, side-scan sonar, Thorpe (1982) found that higher concentrations of bubbles are formed under the windrows rather than between them. These bubble clouds are carried to great depth by the downwelling jet under convergence zone. They are used as indictors of the Langmuir circulation in field observations (Zedel and Farmer 1992). Furthermore, by analyzing a numerical model that accounts for the turbulent diffusion of bubbles from the free surface, bubble rise and dissolution, and advection by Langmuir circulations, Thorpe (1984) concluded that the effective turbulent diffusivity with the effects

of Langmuir circulation included is up to twice as that due to turbulence alone. Therefore, the enhancement of turbulent mixing by Langmuir circulation can indirectly influence the gas exchange (Crawford and Farmer 1987, Faller and Perini 1984).

Langmuir circulations also play a role in the heat transfer in the upper ocean. Due to the diurnal variation of ocean surface temperature, a warm layer of water tends to form at the surface during midday, and a cool layer during nighttime. Thorpe and Hall (1982) observed in Loch Ness that, when Langmuir circulations are present, temperature anomalies develop in the downwelling regions. Weller *et al.* (1985) arrived at the same conclusion. During their measurements from the research platform FLIP, they found positive temperature anomalies during the daytime and negative anomalies during nighttime, both correlated with surface streaks formed with the surface markers. Furthermore, Smith *et al.* (1987) noticed that the stratification developed in the absence of Langmuir circulations can be rapidly destroyed by the powerful mixing induced by Langmuir circulation. All of these observations indicate that Langmuir circulations enhance heat transfer in the mixed layer.

Langmuir circulation also intensifies the mixing of the windward momentum. Since the windward and downwelling velocity components are strongly correlated, Langmuir circulation is potentially an efficient transporter of the momentum deposited in the thin surface layer by wave breaking (Pollard 1977b). Gordon (1970) estimated that for a Langmuir circulation with a maximum downwelling of $4cm/s$ and average upwelling of $1.5cm/s$ and a current anomaly of $2cm/s$, the resulting Reynolds stress is more than sufficient to transport all the momentum input by the wind ($5m/s$) downwards. Weller and Price (1988) confirmed the correlation between the downwelling and windward velocities. With measurements at great depth, they showed that the downwelling and windward flows are much larger than Gordon's estimate. This is further supportive of the conclusion that the momentum redistributed by Langmuir circulation and turbulence combined is much greater than that by the wind shear turbulence alone.

It is also believed that the distribution of phytoplankton is influenced by Langmuir circulation (Evans and Taylor 1980, Hamner and Schneider 1986). Weller *et al.* (1985) stated that the vertical velocities induced by Langmuir circulation are greater than

the terminal velocity of phytoplankton. Hence, this helical flow can redistribute the phytoplankton, changing the irradiance they experience and thus their rate of photosynthesis.

Faller and Auer (1988) pointed out that Langmuir circulation contributes to horizontal dispersion. Films (Faller and Perini 1984) and oil spills (Thorpe 1995) on the surface are frequently observed to collect into parallel, narrow bands, which may slowly coalesce to form longer streaks with larger spacing. This process provides an effective mechanism for dispersion (Farmer and Li 1995).

Observations have found that Langmuir circulations that extend to the thermocline (Leibovich 1983). It has therefore been suggested that Langmuir circulation might influence the formation, sustenance and erosion of the thermocline. Langmuir himself believed that " *the helical vortices set up by wind apparently constitute the essential mechanism by which the epilimnion is produced*". Lele (1985) has studied the formation and deepening of thermocline numerically. Li and Garrett (1997) also demonstrated the rapid deepening in their simulations. These studies have been reinforced by the field observations by Smith (1998). He discovered that initially, the depth of the mixed layer increases rapidly, and later slows down later. After that, Langmuir circulation may maintain and even slowly extend the mixed layer.

1.2 Review of Related Work

Many studies have been conducted on Langmuir circulation. Early reviews were written by Faller (1971), Pollard (1977b), and Leibovich (1983). Rapid progress has been made since then in field observation, laboratory experiment and numerical simulation. Here, only studies relevant to this work are presented below.

1.2.1 Theoretical Work

Numerous ideas concerning the mechanism of creation of Langmuir circulation have been proposed. Early hypotheses include the effects of surface films (Welander 1963, Kraus 1967), correlation with atmospheric vortices (Woodcock and Wyman 1946),

pure irrotational wave effects (Stewart and Schmitt 1968, Faller 1969), thermal convection (Csanady 1965), Ekman layer instability (Faller 1964, Gammelsrod 1975) and preferential wave breaking (Garrett 1976). However, each of these mechanisms has been shown to be incorrect on theoretical and/or experimental grounds.

The most promising theory to date is the Craik-Leibovich theory. It was first proposed by Craik and Leibovich (1976) based on concepts suggested by Craik (1970) and Leibovich and Ulrich (1972). It assumes the motion of the upper layer of water consists of a nearly irrotational wave field and a weaker rotational current and asserts that the formation of Langmuir circulation is due to the non-linear interaction between surface waves and the wind-driven current. In Craik and Leibovich (1976), a quasi-steady system was solved. It focused on the development of the Langmuir circulation and did not compute the wind-driven current. This was extended by Leibovich (1977b), who treated both the Langmuir circulation and the wind driven current in an unsteady flow as a single system. This theory was later extended further by Leibovich (1977a) to include the effects of stratification. With the key assumption of disparate time scales, *i. e.* the time scale of Langmuir circulation evolution is much larger than a wave period, and the wave period is much larger than the time scale of small-scale turbulence, multiple time scale averaging was applied to the Navier-Stokes equations, resulting in the Craik-Leibovich equations. These equations are the generic Navier-Stokes equations altered by a "vortex forcing" term, $u_s \times \omega$, where u_s is the Stokes drift of the irrotational wave fields and ω the vorticity of rotational current. It is expected in the ocean and in lakes that the shape of the wave is unaffected by the mean current. Thus the Stokes drift can be computed *a priori.*

Following the original derivation, the Craik-Leibovich equations were rederived by Leibovich (1980) and Craik (1985) using the generalized Lagrangian mean theory by Andrews and McIntyre (1978), and later by Holm (1996) using an averaged Hamilton principle.

According to the Craik-Leibovich theory, vortex forcing exerts a torque on the water and produces Langmuir circulation in either of two ways. The first is referred as the CL1 mechanism. It assumes the wave field is highly directional in the spanwise direction. The resulting Stokes drift creates periodic vortex torque, which directly

forms the roll motions. The assumption of phase-locked, crossed wave fields is the weakest point of this mechanism, as this state is very unlikely to occur in the sea.

The second mechanism, known as CL2, generates the convective motion from the instability of the mean current. It is more promising than CL1 and was first proposed by Craik (1977). It works as follows (Gnanadesikan 1996): Spanwise perturbation of the streamwise current creates vertical vorticity of both signs. The vertical vorticity is then bent by the exponentially decaying Stokes drift thus forming longitudinal vortices of alternating signs. The rate of the tilting is determined by the Stokes drift shear. These counter rotating vortices in turn twist the spanwise vorticity of the mean current into the vertical direction, reinforcing the horizontal perturbation. The rate of this strengthening depends on the mean current shear. Hence, the growth rate of the convective motion goes as the geometric mean of the Stokes shear and the mean current shear.

1.2.2 Stability Studies

The CL2 mechanism was explored further by Craik (1977) for unstratified flows and by Leibovich (1977a) for stratified flows. Mathematically, for linear profiles of the Stokes drift and the mean current, the linearized problem is similar to the Bénard instability for unstratified flow, and to the double diffusive thermosolutal problem for stratified flow. Based on this analogy, Craik (1977) and Leibovich (1977a) estimated (but did not compute) the conditions for marginal stability and reported that a wide range of typical conditions found in the ocean are highly unstable. Furthermore, they computed the growth rate for inviscid flow. The finite depth, unstratified case was studied by Craik, and the infinite depth, stratified case was investigated by Leibovich. Although both studies found all the wavenumbers to be unstable, which is not true for viscous case, the validity of the instability mechanism for producing Langmuir circulation has been demonstrated.

Leibovich and Paolucci (1980a, 1981) studied the CL2 instability for a viscous, stratified flow in a domain of infinite depth, with a zero surface stress at time zero and a finite, constant surface stress afterwards. The Stokes drift profile was that of a irrotational Stokes wave, and the mean current was the unsteady similarity solution

of the Rayleigh problem. Both linear stability and energy stability analysis were carried out. The results showed that the linear and energy stability limits are close. Leibovich and Paolucci also pointed out that the creation of two dimensional roll motions are favored, as observed in the ocean. The spanwise wavenumber for the most unstable mode was also calculated.

For stratified flows with finite depth, Lele (1985) performed the linear stability analysis for a non-slip bottom boundary conditions and variable Stokes drift gradients. The same problem for unstratified flow was solved by Garg *et al.* (1992) in an attempt to compare with the experiment results of Nepf (1992). In both cases, finite critical wavenumbers were reported.

Both linear and weakly nonlinear analyses of a stratified, zero-stress bottom flow have been carried out by Leibovich *et al.* (1989). With both linear mean current and Stokes drift, the mathematical problem is strictly analogous to the double diffusion problem. Their numerical simulations, performed parallel with the analysis, were in error and were later corrected by Cox *et al.* (1992b, 1992a). Cox *et al.* also extended the linear Stokes profile to a more real profile with an exponentially decay. Multiple bifurcation were obtained, resulting in equilibrium states of either traveling wave or steady state type. This is consistent with observed Langmuir circulations, which is either persistent or drift in the spanwise direction.

The stability analyses mentioned above are all for two dimensional problems. Streamwise invariance is assumed. Leibovich and Tandon (1993) studies three dimensional Langmuir circulations. They investigated stratified flows with non-slip bottom boundaries. Linear Stokes drift and constant top stress were applied. From the linear stability analysis, they showed that for unstratified flow, steady two dimensional rolls are preferred. For stratified flow, however, the most unstable modes are weakly three dimensional, with windrow angles slightly off the wind direction.

Recently, secondary instability in Langmuir circulation was studied out by Tandon and Leibovich (1995b). It has been observed that for both stratified and unstratified flows, two dimensional Langmuir circulations are subject to three dimensional instabilities. Traveling waves in the wind direction appear in the Langmuir circulations. Therefore, the windrows deviate from the streamwise direction by small angles.

It should be noticed that these stability analyses deal with the states near marginal stability and the non-linearity. The goal is to investigate the requirements for instability and the flow structures associated with response of the parameter spaces. Since in the real ocean and lakes, the flow is highly supercritial, full non-linear simulations should be performed.

1.2.3 Field Observations

Field measurement of Langmuir circulations is a complicated and difficult task. Velocity and temperature must be obtained at an array of locations designed specifically to capture Langmuir circulation. Visual guidance is also important. Averaging over a large number of samples obtained under similar conditions is required to reconstruct the coherent motion. Furthermore, environmental conditions and information about the surface wave must be determined simultaneously. With all these difficulties, it is not surprising that, at this date, few good data sets are available.

Orientation and Horizontal Scales

The spacing and orientation of Langmuir circulations can be identified visually by the windrows formed by floating substances such as foam, debris and seaweed, or by the surface-temperature anomalies seen in infrared photographs. Langmuir (1938) reported that the windrows are roughly aligned with wind. Faller (1964) discussed a tendency for consistent deviation of the surface streaks to the right of the wind at an angle of approximately 13 degrees. This conclusion was partially supported by Katz *et al.* (1965), who found similar angles to Faller's in four out of six experiments. Ichiye *et al.* (1985) also observed similar deviations ranging from 0 to 12 degrees for most cases. However, rather small deviation angles have been observed by Welander (1963) in the ocean. Myer (1971) and Kenny (1977) found the surface streaks were aligned with the wind within 3 degrees in Lake George and Lake of the Woods, respectively, showing no systematic deflection of Langmuir circulations.

The spacing between windrows ranges from $2m \sim 25m$ in lakes and $2m \sim 300m$ in oceans. For example, Langmuir (1938) observed that streaks were mainly $5m \sim 25m$ apart in Lake George, depending on the season of the year. Harris and Lott (1973)

found that cell spacings were around $3m$ to $4m$ in Lake Ontario. In the ocean, larger scales occur. Langmuir (1938) reported parallel lines of massive collections of seaweed $100m$ to $200m$ apart. In the ocean near Bermuda, Assaf *et al.* (1971) showed from aerial photographs that the largest spacing of the convergence zones was about $280m$.

It has been suggested that the horizontal spacing scales with the depth of the mixed layer. Scott (1969) reported that the streak spacing correlates with the depth of thermocline, and so did Kenny (1977). Langmuir (1938) found that the row spacing of the surface streaks is larger in October and November, when the thermocline is deeper and smaller in May and June, when the themocline is shallower. During the cruise of MILDEX (MIxed Layer Dynamics EXperiment), Smith *et al.* (1987) found with the Doppler sonar from the FLIP platform that the Langmuir circulation spacing is about three times the depth of the mixed layer. This feature persisted for a period of two hours, while the mixed layer depth changed from $40m$ to $60m$. This aspect ratio is confirmed by Weller and Price (1988), who found values ranging from $2.5 \sim 3.5$. Smith (1992) later provided a slightly different ratio for weak stratification conditions in the mixed layer. During the experiments in SWAPP (Surface WAve Process Program), he observed the growth of Langmuir circulations in the Pacific Ocean. Within an hour following a sudden change of wind, the Langmuir circulation spacing increased at a speed of $40cm/s$, while the density measurement indicated the mixed layer deepened at a rate of $20cm/s$. Therefore, he concluded that the Langmuir cell is almost square with an aspect ratio of unity.

Vertical Penetration

In experiments in Lake Ladoga, Filatov *et al.* (1981) found that the penetration depth of Langmuir circulation is proportional to wind speed and inversely proportional to stratification. For stronger and more persistent cell motions in deep water, however, it is suggested that the vertical penetration of Langmuir circulations is limited by the first significant thermocline.

Observations by Langmuir (1938) showed that the small umbrellas used to measure the mean currents gradually drifted under a streak $5m$ below the surface, but did not at $10m$ depth. From this it can be inferred that the depth of the cellular motion is a

small multiple of $5m$, comparable to the mixed layer depth.

Weller and Price (1988) provided a more complete picture. From the measurements performed on the FLIP platform, they found that the Langmuir circulations are more active in the upper half of the mixed layer. The longitudinal and transverse velocities in Langmuir circulations gradually decay with depth. Near the thermocline, the flow is significantly influenced by the strong stratification and is too weak to be detected.

Spacing Hierarchies and Y Junctions

Between the well-formed, long windrows with the largest horizontal spacing, there exist numerous shorter, elongated, less well-defined streaks, as observed by Langmuir (1938) in both the ocean and Lake George. Multiple scales have also been observed by other researchers. Assaf *et al.* (1971), for example, also stated that the largest cells ($280m$ in spacing) coexist with cells of small to medium sizes (approximately $5m$ to $35m$).

Scott *et al.* (1969) discovered the small-scale motions are temporary, disappearing quickly after the wind dies. Furthermore, they tend to coalesce to form longer bands with larger scales. By distributing computer cards on the ocean surface, Smith *et al.* (1987) found that smaller cells gradually merge to form bigger ones. Weller and Price (1988) observed similar processes, with the cards initially forming shorter lines of several meters in length and spacing, then being carried into longer lines of tens of meters long and $10 \sim 40m$ apart, and finally forming one or two lines approximately $100m$ apart. When new cards were scattered, young cells with short convergence lines formed between the streaks already formed, and the same migration process from small-scale motion to large repeated, as also reported by Harris and Lott (1973).

The consolidation of surface markers implies a dynamic cascade from small scale to large scale. Smith (1992) showed that as the flow evolves, the energy of the once dominant small scales vanishes and moves to the large scale motions, indicating a inverse energy cascade of the kind commonly found in two dimensional turbulence.

In addition, the upscale cascade is carried out by the amalgamation of pairs of convergence bands, as shown in the sonographs by Thorpe (1992) and Farmer and Li (1995), forming the so-called "Y Junctions".

Vertical Velocity

Early measurements of the velocity in Langmuir circulations were made near the surface. Langmuir (1938) used aluminum plates ballasted for neutral buoyancy and measured the descent velocities of $2 \sim 3m/s$ under streaks and upwelling velocities of $1 \sim 1.5m/s$. These devices were later used by Harris and Lott (1973). Filatov *et al.* (1981) performed measurements in Lake Ladoga with "Sutcliff" floats, horizontal plates attached to buoyant vertical poles first used by Sutcliff *et al.* (1963). Filatov *et al.* gave a nonlinear fit of the downwelling speed to the wind speed, with the coefficient depending on the air-sea temperature difference. Leibovich (1983) summarized some of these measurements. He divided the data sets into two groups, one from Filatov *et al.*, and the other from Sutcliff *et ai.* and Harris and Lott, and fit each set with a linear relation: $w^d_{down} = 0.0025U^d_w$ and $w^d_{down} = 0.0085U^d_w$, respectively, where w^d_{down} denotes the dimensional downwelling velocity, and U^d_w the dimensional wind speed. These two relations produce an approximate range of the downwelling velocity in Langmuir circulations.

Weller and Price (1988) deployed Vector Measuring Current Meters (VMCMs) from the research platform FLIP and were able to obtain velocity measurements further below from the surface at depths of approximately $10m \sim 165m$. Since the upwelling speed was smaller, they mainly discussed the results of the downwelling velocity. The picture emerged showed that there exists a subsurface maximum of the downwelling speed. The strongest downwelling velocity occured between $6m$ and $20m$ depth, when the mixed layer depth was $40m$ to $60m$. Therefore, the early results made near the surface underestimated the downwelling velocity of Langmuir circulations. The data obtained are rather scattered, with the maximum downwelling velocity up to $30cm/s$, but with more values lying in the range of $5cm/s$ to $10cm/s$. Nevertheless, the data showed a general trend of increased downwelling velocity with stronger wind, supporting the proportionality proposed by Leibovich (1983).

Horizontal Velocity

Flow visualizations showed that the downwind velocity varies across Langmuir circulations. Langmuir (1938) laid a thin cord perpendicular to the wind direction. After about 10 minutes, the straight cord deformed into well-defined waves, being displaced forward in the streaks and backward out of them, indicating that the downwind velocity is greater in the convergence zone than in the divergence zone. This "current anomaly" was confirmed by Gordon (1970) and Assaf *et al.* (1971), who observed the sinusoidal frontier of dye in the ocean. The difference between the downwind velocity at the convergence and divergence zones was reported to be in the range of $1cm \sim 17cm$ (Pollard 1977b).

Measurements deeper in the water from the platform FLIP (Smith *et al.* 1987, Weller and Price 1988) revealed stronger downwind currents at mid-depth of the mixed layer than near the surface. They are correlated with the convergence zone, with a magnitude comparable to the downwelling velocity. The downwind velocity was estimated generally in the range of $15cm/s \sim 30cm/s$, with the maximum value up to $40cm/s$ (Weller and Price 1988).

1.2.4 Laboratory Studies

Laboratory experiments have been performed to investigate the generation of Langmuir circulations. Faller (1969) was the first to demonstrate Langmuir circulations can be established by waves and current only. Neither the waves generated mechanically nor the sheared current produced by slow draining of the shallow tank alone caused roll motions. However, by introducing waves on the sheared current, he obtained vigorous convective cells. Furthermore, the circulations produced are much stronger than the thermal convection organized by shear; thus the latter is not a necessary condition to generate Langmuir circulations.

Since then, numerous experiments have been conducted to study the wave current interaction mechanism, especially to verify the later-developed Craik-Leibovich theory (Craik and Leibovich 1976, Craik 1977, Leibovich 1977b, Leibovich 1977a). Experiments designed to test the CL1 mechanism have been reported (Faller 1978, Faller and Cartwright 1983, Mizuno 1985). When a carefully produced crossed-wave

pattern was imposed on a shear flow, well organized longitudinal cells were readily seen. The shear was generated by blowing a light wind over the surface. When the wind direction was reversed, the direction of Langmuir circulations reversed as well, in agreement with the CL1 theory.

Faller and Caponi (1978) generated Langmuir circulations by blowing wind over the water surface. However, the resulting wave field was rather complex. Structures similar to the crossed-wave pattern coexist with other wave forms. Thus, the experiment could not distinguish between the CL1 and CL2 mechanisms.

The CL2 mechanism was further tested by Faller and Perini (1984), who produced a unidirectional wave with a mechanical wave generator and a mean current with a moving surface film. With the aid of dye streaks, cell activity was observed. Nepf and Monismith (1991) further studied the CL2 mechanism with a combination of mechanical waves and a narrow flume. In this flow, the vertical vorticity from the sidewall boundary layers was rotated by the Stokes drift from the wave motion. Longitudinal rolls were produced. Furthermore, reversal of the wave direction changed the downwelling zone at the center of the channel into an upwelling zone, as predicted by the CL2 mechanism. However, the experiment only partially verified the CL2 mechanism. Since the sidewalls provided a permanent source of vertical vorticity, the feedback component of the CL2 mechanism, in which the vertical vorticity associated with the spanwise perturbation is reinforced by the Langmuir circulations, was not confirmed.

In an effort to verify this feature of the CL2 mechanism, Nepf *et al.* (1995) utilized a wider channel and placed curved screens upstream of the wave maker to produce a mean sheared current. With this arrangement, the initial vertical vorticity was generated via spanwise perturbation of the mean current, as required by the CL2 mechanism. Both positive and negative shear were created. The idea was to test whether negative sheared current inhibits the generation of Langmuir circulations. However, it was found that longitudinal vortices were produced equally well with positive, negative, or even no imposed shear. The formation of Langmuir circulations was more correlated to the steepness of the wave. When a wave breaks at the surface, cells developed. Otherwise, they did not appear. Nepf *et al.* (1995) suggested

that wave breaking eliminates the negative shear near the surface, allowing longitudinal vorticity to form via the CL2 mechanism. These vortices are then maintained through the interactions with the bottom boundary layer, where a strong positive shear develops. In addition, Monismith and Magnaudet (1998) proposed that wave breaking might also play an important role in generating wave drift. Evidence shows that waves generated mechanically appear to be the Gerstner waves that produce no wave drift. Wave breaking allows Stokes drift to form, and thus Langmuir circulations are produced.

Recently, Melville *et al.* (1998) performed experiments on the Langmuir circulations generated by the instability of a wind-driven surface shear layer. However, the experiments did not confirm the assumptions of the CL2 theory in that the wind-driven current was of the same order as the phase speed of the wave, which is a $\mathcal{O}(1)$ quantity instead of the $\mathcal{O}(\epsilon^2)$ current of CL theory, where ϵ denotes the surface wave slope.

Laboratory studies have confirmed the characteristics of Langmuir circulations found in field observations. Nepf (1992) observed that the cell spacing (shown by floating beads) is about 1.5 to 3 times the channel height. Faller and Caponi (1978) found the maximum spacing to depth ratio between 2.5 to 3.5. Upscale energy cascading was also found by Faller and Caponi (1978). In agreement with Weller and Price (1988), Nepf and Monismith (1991) observed that the maximum downwelling velocity occurs just above the half depth of the channel. Furthermore, vigorous mixing induced by Langmuir circulations has also been seen. Faller and Perini (1984) found that the mean streamwise velocity at the surface decreases sharply after the onset of instabilty, showing the enhancement of vertical momentum exchange. Nepf (1992) also observed that the Langmuir circulations erase the shear in the mean current, producing a more uniform profile.

1.2.5 Numerical Simulations

Numerical simulations of the fully non-linear process of the generation and evolution of Langmuir circulations have based on solution of the Craik-Lebovich equations in a rectangular domain. Wind stress is modeled by streamwise stress applied at the top

surface and the wave-current interactions with the vortex forcing term.

Leibovich and Radhakrisnan (1977) performed a numerical study based on the CL1 mechanism. They simulated an unsteady, two dimensional problem in a domain invariant in the streamwise direction. They assumed the flow to be infinitely deep, and of constant density and eddy viscosity. A crossed-wave pattern with a pair of wave trains propagating at equal and opposite angles to the wind direction, which produces a spanwise-periodic Stokes drift, was included. The width of the domain was determined by the periodicity of the wave pattern. The top stress was turned on at time zero and longitudinal vortices developed and deepened with time. Downwelling occurs at the location of the minimum Stokes drift and upwelling where the Stokes drift is maximum. Current anomalies similar to those observed in the field were also predicted. Furthermore, with careful selection of parameters, they produced a maximum downwelling velocity comparable to field observation.

A similar problem was solved later by Leibovich and Paolucci (1980b), who studied the instability CL2 mechanism. The computational setup was the same as that of Leibovich and Radhakrishnan (1977), except that the spanwise dimension was comparable to the most unstable wavelength. A spanwise uniform Stokes drift was included in place of the crossed-wave field. Stratification was also included, but only as a passive scalar (Leibovich 1983). The Langmuir circulations obtained qualitatively resemble the solutions by Leibovich and Radhakrishnan (1977). In addition, a cell merging process, in which the small scale perturbations cascade to larger ones, was discovered.

Leibovich and Lele (1982) improved Leibovich and Paolucci's (1980b) results for the stratified case. Starting with a constant initial temperature gradient, they observed the transformation to a uniform temperature profile in the well mixed region. More interestingly, a dynamically evolving layer with a strong temperature gradient forms below the Langmuir circulations. It resembles the thermocline deepening in the ocean.

Li and Garrett (1993) conducted two dimensional CL (2DCL) simulations in a domain with finite depth. The flow was assumed to have constant eddy viscosity and no stratification. A no-slip condition was applied at the bottom so that the flow can

reach a steady state. Two counter rotating Langmuir cells formed after a cell merging process, which Li and Garrett claimed to be much different from vortex pairing in two dimensional process. They also showed that the strength of the Langmuir circulations, represented by the maximum downwelling velocity at the steady state, depends on the Langmuir number $La = (\nu\kappa_x/u_*^d)^{3/2}(S/u_*^d)^{-1/2}$, and the ratio S/u_*^d. For small La:

$$\frac{w_{down}^d}{u_*^d} = 0.72(S/u_*^d)^{\frac{1}{3}} La^{-\frac{1}{3}} \tag{1.1}$$

where S is the characteristic Stokes drift equal to a half its the surface value. κ_x is the wavenumber of the surface wave, ν the eddy viscosity, u_*^d the dimensional shear velocity at the top. Furthermore, with parameters typical of a fully developed sea, their model predicted a maximum downwelling velocity comparable to the observed magnitude, but a weaker downwind jet. Calculations were performed in domains of different spanwise-vertical aspect ratios, but no major differences were found in the results.

Surface heat flux and stratification were added to the 2DCL model by Li and Garrett (1995, 1997). The effects of surface cooling are found to be less important than wave-current interaction for typical sea conditions. Simulations of a flow with a constant buoyancy frequency N revealed that Langmuir circulations play a critical role in mixed layer deepening if the velocity difference across the base of the mixed layer $\Delta u < 0.01U_w^d$, with U_w^d the wind speed. The longitudinal vortices first create a homogeneous layer. This mixed layer deepens rapidly by the action of the Langmuir circulation and stops when the depth reaches $H \simeq 10u_*^d/N$, or when the buoyancy jump at the base (Price *et al.* 1986) reaches about $50u_*^{d2}/H$.

Langmuir circulations in a three dimensional domain with weak vortex forcing have been simulated by Tandon and Leibovich (1995b). Constant eddy viscosity was assumed and the domain was of finite depth with a no-slip bottom wall. The selection of streamwise and spanwise dimensions was guided by linear and second order instability analysis (Tandon and Leibovich 1995a). As predicted by the secondary instability, no steady state with two dimensional, longitudinal rolls is reached. Instead, the flow shows a traveling wave propagating in the streamwise direction at the final quasi-steady state. With higher vortex forcing, the traveling wave further loses

stability, giving rise to three dimensional, oscillating Langmuir circulations.

Large eddy simulations of Langmuir circulations in turbulent flow have been carried out by Skyllingstad and Denbo (1995) and McWilliams *et al.* (1997) based on the Craik-Leibovich theory. In both models, multiple processes were incorporated simultaneously, including vortex forcing, surface cooling, stratification, and the effects of the Coriolis force. The domain extends from the ocean surface to below the thermocline. The radiation boundary condition used at the top boundary of atmospheric models (Klemp and Duran 1983) was employed at the bottom of their domain. The results show a rich structure with horizontal scales increasing with depth. The dominant coherent structures are longitudinal streaks that are deviate to the right of the wind direction due to the Coriolis force. Unlike Skyllingstad and Denbo (1995), McWilliams *et al.* (1997) incorporated Stokes drift effects into the Coriolis term, and thus predicted deviation angle of the streaks as large as 45°, much larger than that predicted by Skyllingstad and Denbo. The streaks intensify near the surface within a layer of thickness of the e-folding scale of the Stokes drift and undergo occasional merging at "Y" junctions. Larger scale Langmuir circulations were found with conditional averaging (McWilliams *et al.* 1997). Compared to cases without vortex forcing, the Langmuir circulations in the turbulent flow greatly enhance the vertical mixing. Skyllingstad and Denbo (1995) showed that the entrainment rate of heat flux is almost doubled when vortex forcing is included.

All the simulations above solved Craik-Lebovich equations in a rectangular domain. Mobley (1977) attempted to study the CL1 mechanism in a wavy domain by solving the full Navier-Stokes equations, but failed to find Langmuir circulations. McDonald (1994) made an effort to explore the CL2 mechanism in a flow beneath a propagating wave. However, stability problems and difficulties with the spectral method used for a curvilinear system made the calculation a formidable task, preventing him from testing the CL2 mechanism.

1.3 Motivation, Approach and Objectives

As shown above, the Craik-Leibovich theory has been used to describe Langmuir circulations. Although predictions of LES and laminar simulations based on the Craik-Leibovich equations are roughly in agreement with observations, many questions remain unanswered.

The key assumption of the Craik-Leibovich theory is that of disparate time scales. That is, the time scale of Langmuir circulation evolution is assumed to be much longer than a wave period, and the wave period is assumed to be much longer than the time scale of small-scale turbulence. No test has been made to verify these fundamental assumption.

Furthermore, the Craik-Leibovich theory abstracts the effects of the wave motion into the Stokes drift, a drift induced by inviscid flow. In the viscous case, however, Longuet-Higgins (1953) showed that there exists another current caused by the wavy boundary layer under the surface, *i. e.* the Eulerian mean flow. It is of second order in wave slope, the same magnitude as the wind-driven current required by the Craik-Leibovich theory. Craik (1985) suggested the Eulerian mean flow is unstable in typical sea conditions and can lead to Langmuir circulations without any additional stress. No previous simulation took the Eulerian mean flow into account. Whether it should be included in the Craik-Leibovich theory needs to be addressed.

Since, in the Craik-Leibovich equations, the wave field interacts with the mean current solely through the vortex forcing term, the wave field is not included in the results. Clearly, the question of how Langmuir circulations modify and are modified by the wave field cannot be resolved with the Craik-Leibovich theory.

In this work, three dimensional numerical simulations are performed for flows under a wavy surface, which propagates at a constant speed over an otherwise rectangular domain. The shape of the wave is that of a second order Stokes wave and its speed is the corresponding phase speed predicted by theory. The wind-driven current is produced by a tangential stress on the wavy surface. We assume the wave shape remains unchanged. The coordinate system moves with the wave at the phase speed. Thus, the shape of the domain is fixed in time.

The full Navier-Stokes equations are solved in a curvilinear coordinate system.

No averaging is used. The kinetic and dynamic boundary conditions are applied at the wavy surface. A modified version of the fractional step method of Zang *et al.* (1994) for a generalized curvilinear coordinate is used as the numerical method. An orthogonal transformation is employed to map the physical wavy domain into a rectangular computational domain. The orthogonality of the transformation significantly simplifies the simulation.

Both laminar and turbulent cases are examined. For turbulent cases, large eddy simulation with a dynamic subgrid scale model is used. As these are the first simulation of Langmuir circulations in a wavy domain, we consider the simplest case. A no-slip boundary condition is imposed at the bottom wall. Periodic boundary conditions are applied in the lateral directions. No scalar transport due to surface cooling or stratification is incorporated. The Coriolis force is neglected.

The goals of this work are to study the mechanism and dynamics of Langmuir circulation, and to verify whether the wave-current interactions generate Langmuir circulations in the way predicted by the Craik-Leibovich theory. In particular, the objectives are:

- To develop a computational model capable of capturing the flow structures due to the interactions of surface wave and wind-driven current;
- To study the structure and properties of Langmuir circulations;
- To evaluate the effects of the Eulerian mean flow on wave-current interactions;
- To assess the influences of Langmuir circulation on the wave field, and the modulation of the wave on Langmuir circulations.
- To investigate the cell merging process;
- To evaluate the contribution of Langmuir circulations to vertical mixing by comparing the flows with Langmuir circulations with a regular open channel flow;
- To justify the averaging in the Craik-Leibovich theory by comparing CL simulations with wavy simulations.

1.4 Layout of the Dissertation

The rest of the thesis is organized as follows. In chapter 2, we present the mathematical bases for simulating a generalized three dimensional turbulent flow under a wavy surface. This is followed by a discussion of the numerical methods in chapter 3. In chapter 4, two dimensional wave motion under a free surface is studied. Both inviscid and viscous solutions are obtained. Chapter 5 examines the laminar wavy flow. Langmuir circulation structure and properties are studied, Eulerian mean flow effects are evaluated, and comparisons between the wavy case and the Craik-Leibovich theory are made. Langmuir turbulence in a wavy domain is presented in chapter 6, together with a simulation based on the Craik-Leibovich theory, and a simulation of open channel turbulent Couette flow. In addition to analyzing the characteristics of Langmuir turbulence, the limit of validity of the Craik-Leibovich theory is discussed and the mixing due to Langmuir circulations is evaluated. Finally, conclusions and future work are discussed in chapter 7.

Chapter 2

Mathematical Formulation

2.1 Introduction

In this dissertation, two sets of governing equations are used: the Navier-Stokes equations and the Craik-Leibovich equations. The Navier-Stokes equations are solved in both Cartesian and curvilinear coordinate systems. The Craik-Leibovich equations are solved in a Cartesian system.

The Craik-Leibovich equations resemble the Navier-Stokes equations except that they have an extra source term due to averaging over a wave period. The boundary conditions applied to the flow in a curvilinear system are more complex. For this reason, the Navier-Stokes equations in a curvilinear coordinate system are chosen as the typical case in this chapter and the next. The physical problem is three dimensional turbulent flow under a wavy surface. The differences in the governing equations and the boundary conditions for other cases will be presented later.

The governing equations and boundary conditions are first presented in a Cartesian system in section 2.2. The filtered equations for large eddy simulation and the turbulence model used are given in sections 2.3 and 2.4, respectively. In section 2.5, the equations are transformed into a curvilinear coordinate system. Finally, in section 2.6, statistical equations for turbulent flows are presented.

2.2 Governing Equations and Boundary Conditions

The physical domain for the flow under a wavy surface is sketched in Figure 2.1. The wavy top surface has the form of a second order Stokes wave. The other surfaces are flat. The flow is treated in a coordinate system moving at a constant speed equal to the phase speed of a propagating, non-deforming wave. Thus the shape of the domain remains fixed in time. The flow is viscous, incompressible, and of constant density.

It is driven by the surface wave propagation and a tangential stress applied on the top surface. Gravity is the only body force. The Coriolis force is neglected.

The flow is non-dimensionalized using the half mean depth of the domain, h, as the length scale and a characteristic Stokes drift velocity, $S = \epsilon^2 C_w^d/2$, as the velocity scale, where $\epsilon = a\kappa_x^d$ and $C_w^d = \sigma^d/\kappa_x^d$ represent the slope and the phase speed of the Stokes wave, respectively, with a as the wave amplitude, σ^d the radian frequency and κ_x^d the wavenumber of the Stokes wave, where the superscript d denotes a dimensional quality. The non-dimensional quantities are:

$$(x_i, \eta_s, L_x, L_y) = (\frac{x_i^d}{h}, \frac{{\eta_s}^d}{h}, \frac{L_x^d}{h}, \frac{L_y^d}{h}) \tag{2.1}$$

$$(u_i, C_w) = (\frac{u_i^d}{S}, \frac{C_w^d}{S}) \tag{2.2}$$

$$t = \frac{t^d S}{h} \tag{2.3}$$

$$p = \frac{p^d}{\rho^d S^2} \tag{2.4}$$

$$\tau_* = \frac{\rho^d (u_*^d)^2}{\rho^d \nu S/h} \tag{2.5}$$

$$(\kappa_x, \kappa_y, \mu) = ({\kappa_x}^d h, {\kappa_y}^d h, \mu^d h) \tag{2.6}$$

$$Re_* = \frac{u_*^d h}{\nu}, \quad Re_s = \frac{Sh}{\nu} \tag{2.7}$$

where x_1, x_2, and x_3 lie in the streamwise, spanwise and vertical direction of the domain, respectively. The domain extent is represented by:

$$0 \le x_1 \le L_x, \quad 0 \le x_2 \le L_y, \quad -1 \le x_3 \le 1 + \eta_s \tag{2.8}$$

where η_s is the height of the wave (Whitham 1974):

$$\eta_s = \frac{\epsilon}{\kappa_x} \cos(\kappa_x x_1) + \frac{\epsilon^2 \mu}{{\kappa_x}^2} \cos(2\kappa_x x_1) \tag{2.9}$$

and

$$\mu = \frac{\kappa_x}{2} \coth(2\kappa_x) \left[1 + \frac{3}{2\sinh^2(2\kappa_x)} \right] \tag{2.10}$$

In the above equations, μ is the amplitude parameter of the second component of the wave, u_i is the x_i-velocity component, t is time, p represents the modified pressure (hydrostatic component subtracted), C_w denotes the phase speed of the wave, τ_s represents the tangential stress at the top surface and κ_y represents the wavenumber of the spanwise periodicity.

After the nondimensionalization, the Navier-Stokes equations can be written in Einstein summation form as:

$$\frac{\partial u_i}{\partial x_i} = 0 \tag{2.11}$$

$$\frac{\partial u_i}{\partial t} + \frac{\partial u_i u_j}{\partial x_j} = -\frac{\partial p}{\partial x_i} + \frac{1}{Re_s}\frac{\partial^2 u_i}{\partial x_j \partial x_j} \tag{2.12}$$

Boundary Conditions

Periodic boundary conditions are used in both the x_1 and x_2 directions. It is justified if the domain is large enough to allow periodicity not to affect the results. For flows with Langmuir circulations developed under a wavy surface, as in this case, L_x and L_y should also be multiples of the surface wavelength in the streamwise direction and the Langmuir circulation wavelength in the spanwise direction, respectively. The selection of the physical domain size in the simulation will be discussed in chapter 3.

A no-slip condition is imposed on the bottom wall, which, in a moving coordinate system, carries the boundary conditions:

$$u_1 + C_w = u_2 = u_3 = 0 \tag{2.13}$$

These conditions are suitable for Langmuir circulations formed in a shallow lake or a laboratory flume.

On the upper surface of the domain, two types of conditions are specified: kinematic and dynamic boundary conditions. The former condition states that a particle on the wavy surface remains on the surface. The latter imposes the conservation of momentum on the air-water surface.

Kinematic Boundary Condition

According to Mei (1983), the kinematic condition can be written as:

$$\frac{\partial \eta_s}{\partial t} = u_3 - u_1 \frac{\partial \eta_s}{\partial x_1} - u_2 \frac{\partial \eta_s}{\partial x_2} \tag{2.14}$$

since η_s is a function of x_1 only, equation 2.14 can be simplified to:

$$u_3 = u_1 \frac{\partial \eta_s}{\partial x_1} \tag{2.15}$$

Dynamic Boundary Condition

Consider a curvilinear coordinate system (η^1, η^2, η^3) that is fitted to the wavy top, with η^1 being the tangential coordinate on the surface in the streamwise direction, η^2 the spanwise coordinate; and η^3 the normal coordinate. If the inertia of the surface is negligible, the dynamic boundary condition requires that the normal stress, $\tau_{\eta^3\eta^3}$, and the tangential stresses, $\tau_{\eta^1\eta^3}$ and $\tau_{\eta^2\eta^3}$ be continuous across the air-water surface. The detail derivation of the dynamic boundary condition in a general curvilinear system can be found in Scriven (1960). For a water wave with a constant tangential stress applied along η^1 direction, the dynamic boundary conditions are:

$$P = P_{air} + \tau_{\eta^3\eta^3} \tag{2.16}$$

$$\tau_{\eta^1\eta^3} = \tau_{air} = Re_*^2/Re_s \tag{2.17}$$

$$\tau_{\eta^2\eta^3} = 0 \tag{2.18}$$

where P is the total pressure that includes the hydrostatic components. It has been assumed that surface tension and the viscosity of the air are negligible.

For real water waves, all three dynamic boundary conditions (equations 2.16 to 2.18) must be satisfied. The shape of the wave changes with time, thus the surface height is one of the unknowns to be determined. In the present study, as a first approximation, the shape of the top wavy surface is fixed and is a second order Stokes wave. As suggested by Nepf (1992), the assumption of a second order Stokes wave is reasonable, at least for waves generated in the laboratory. Furthermore, this

assumption saves a substantial amount of computational effort.

However, with this assumption, the three dynamic boundary conditions (equation 2.16 to 2.18) can not be satisfied simultaneously. If the tangential stresses are specified, then the normal stress condition can not require that the air side pressure is a constant. Extra normal stress are needed to maintain the wave shape (Craik 1982). Thus, in the present study, only the two tangential stress conditions are specified explicitly:

$$\tau_{\eta^1\eta^3} = Re_*^2/Re_s \tag{2.19}$$

$$\tau_{\eta^2\eta^3} = 0 \tag{2.20}$$

The pressure is determined implicitly from the momentum and continuity equations on the boundaries.

2.3 Filtered Governing Equations and Boundary Conditions

In large eddy simulation, only the large scale motions of the flow are computed explicitly. These components are called the resolved motion and are obtained via a filtering process, defined as:

$$\overline{f}(x_1, x_2, x_3) = \int_D \prod_{i=1}^{3} G_i(x_i, x_i') f(x_1', x_2', x_3') dx_1' dx_2' dx_3' \tag{2.21}$$

where D denotes the whole domain and G_i is the filter function. The filter can be Gaussian or sharp cutoff type used in spectral methods (Piomelli *et al.* 1987) or, as in this dissertation, a box filter which is appropriate when finite volume or finite difference methods are used. In this case, G_i is unity within a grid volume and zero elsewhere.

When applying the filtering process to the governing equations, one important issue is to decide whether filtering and differentiation commute. Ghosal and Moin (1993) proposed an alternative definition of filtering and showed that filtering and

differentiation operations can commute to second order accuracy in the grid width. Using this property, one can derive the filtered Navier-Stokes equations:

$$\frac{\partial \overline{u}_i}{\partial x_i} = 0 \tag{2.22}$$

$$\frac{\partial \overline{u}_i}{\partial t} + \frac{\partial \overline{u}_i \overline{u}_j}{\partial x_j} = -\frac{\partial \overline{p}}{\partial x_i} + \frac{1}{Re_s}\frac{\partial^2 \overline{u}_i}{\partial x_i^2} - \frac{\partial q_{ij}}{\partial x_j} \tag{2.23}$$

where q_{ij} is the anisotropic part of the subgrid-scale stress tensor, $\tau_{ij} = \overline{u_i u_j} - \overline{u}_i \overline{u}_j$, which represents the effects of the subgrid motions. The isotropic part has been lumped with the pressure. The reason for splitting the subgrid stress into two parts is that only the anisotropic part is modeled explicitly by the subgrid model described in section 2.4.

The periodic boundary conditions are unchanged by the filtering process. The boundary conditions at the bottom surface become:

$$\overline{u}_1 + C_w = \overline{u}_2 = \overline{u}_3 = 0 \tag{2.24}$$

The filtered kinematic and dynamic boundary conditions are:

$$\overline{u}_3 = \overline{u}_1 \frac{\partial \eta_s}{\partial x_1} \tag{2.25}$$

$$\overline{\tau}_{\eta^1 \eta^3} = \frac{Re_*^2}{Re_s} \tag{2.26}$$

$$\overline{\tau}_{\eta^2 \eta^3} = 0 \tag{2.27}$$

In equation 2.25, it has assumed that

$$\overline{u_1 \frac{\partial \eta_s}{\partial x_1}} = \overline{u}_1 \frac{\partial \eta_s}{\partial x_1} \tag{2.28}$$

It is not difficult to prove, with the aid of Taylor expansions, that, if the wave shape is smooth enough, with the box filter used in this study, the assumption 2.28 results in a second order error.

2.4 Subgrid Turbulence Model

First proposed by Deardorff (1970), the basic concept of large eddy simulation (LES) is to explicitly compute the resolved motion and to model the effect of the subgrid scales. LES is an effective tool for simulating turbulent flows. Since the momentum transport is carried by large, energy-containing eddies, the computed turbulent flows are less sensitive to the accuracy of the model in LES than Reynolds averaged calculations.

The widely used model in LES was proposed by Smagorinsky (1963):

$$q_{ij} = -2\nu_t \overline{S}_{ij} \tag{2.29}$$

where q_{ij} is the anisotropic part of the subgrid-scale stress tensor, τ_{ij}, ν_t is eddy viscosity, and $\overline{S}_{ij}$ is the strain-rate tensor:

$$\nu_t = C\overline{\Delta}^2|\overline{S}|, \quad \overline{S}_{ij} = \frac{1}{2}(\frac{\partial \overline{u}_i}{\partial x_j} + \frac{\partial \overline{u}_j}{\partial x_i}), \quad |\overline{S}| = (2\overline{S}_{ij}\overline{S}_{ij})^{1/2} \tag{2.30}$$

where C is the parameter to be determined; $\overline{\Delta}$ is the filter size. The reason why the anisotropic part of the subgrid stress tensor (which is trace-free) is used in the left hand side of equation 2.29 is that the right hand side of the equation is trace free for incompressible flow. This equation can be derived in a number of ways, one of which is to assume that the smallest resolved scales are in the inertial subrange (Ferziger 1998) and to set the energy transfer from the large eddies to the small eddies equal to the energy dissipation rate in the small scales.

The dynamic subgrid model (DSM) developed by Germano (1991) is used in this dissertation. In the DSM, the coefficient C in the above equations is determined through a dynamic process described below.

We apply a second test-scale filter with size $\widetilde{\overline{\Delta}} > \overline{\Delta}$ to the grid-scale filtered equations 2.22 and 2.23. The subgrid scale stress that needs to be modeled in this process is:

$$T_{ij} = \widetilde{\overline{u_i u_j}} - \widetilde{\overline{u}}_i \widetilde{\overline{u}}_j \tag{2.31}$$

This stress tensor is related to the original τ_{ij} through the so-called Germano identity:

$$\mathcal{L}_{ij} = \mathcal{T}_{ij} - \tilde{\tau}_{ij} \tag{2.32}$$

where $\mathcal{L}_{ij}$ is essentially the Leonard stress:

$$\mathcal{L}_{ij} = \widetilde{\overline{u}_i \overline{u}_j} - \tilde{\overline{u}}_i \tilde{\overline{u}}_j \tag{2.33}$$

If we assume the subgrid stresses $\mathcal{T}_{ij}$ and τ_{ij} are approximated by the model given by equation 2.29 with the same coefficient C, the anisotropic part of $\mathcal{T}_{ij}$ is modeled by:

$$Q_{ij} = -2C\tilde{\overline{\Delta}}^2 |\tilde{\overline{S}}| \tilde{\overline{S}}_{ij} \tag{2.34}$$

where

$$\tilde{\overline{S}}_{ij} = \frac{1}{2}\left(\frac{\partial \tilde{\overline{u}}_i}{\partial x_j} + \frac{\partial \tilde{\overline{u}}_j}{\partial x_i}\right), \quad |\tilde{\overline{S}}| = (2\tilde{\overline{S}}_{ij}\tilde{\overline{S}}_{ij})^{1/2} \tag{2.35}$$

Now we substitute equations 2.29 and 2.34 into equation 2.32. This results in:

$$\mathcal{L}_{ij} = -2C\overline{\Delta}^2 M_{ij} \tag{2.36}$$

where

$$M_{ij} = (\tilde{\overline{\Delta}}^2/\overline{\Delta}^2)|\tilde{\overline{S}}|\tilde{\overline{S}}_{ij} - \widetilde{|\overline{S}|\overline{S}_{ij}} \tag{2.37}$$

Since both sides of equation 2.36 (except C) can be computed from the resolved field in LES, C can be determined. However, because C is a scalar and $\mathcal{L}_{ij}$, M_{ij} are tensors, C is over-determined by equation 2.36. Germano suggested solving this problem by contracting equation 2.36 with $\overline{S}_{ij}$. This approach was later improved by Lilly (Lilly 1992) who calculated the model coefficient C in a least square manner:

$$C\overline{\Delta}^2 = -\frac{\mathcal{L}_{ij}M_{ij}}{2M_{ij}M_{ij}} \tag{2.38}$$

The dynamic subgrid model has been successfully applied to LES of transitional and turbulent channel flows (Germano *et al.* 1991) and to both compressible and incompressible isotropic turbulence (Moin *et al.* 1991). It has shown several desirable features. First, it automatically produces a decaying coefficient of C near a wall. Second, for laminar flow, the dynamic subgrid model also exhibits the correct behavior. Third, it allows back scattering in turbulent flows through negative eddy viscosity, a process observed in DNS (Piomelli *et al.* 1991).

Unfortunately, one of the major problems this model suffers from is the instability caused by large negative C, which results in a large negative eddy viscosity (Cabot 1991). A large eddy viscosity generally results from a small denominator in equation 2.38. This happens when little energy is carried by the resolved high wavelength eddies (Ferziger 1998) and can result in a long correlation time of C (Lund *et al.* 1993). Several methods have been proposed to cure this problem.

One method is to simply clip the eddy viscosity to the negative of the molecular viscosity, $-\nu$. That is, if $\nu_t < -\nu$, set $\nu_t = -\nu$. This approach, though somewhat *ad hoc*, can prevent the total viscosity from being negative.

An alternative is averaging. Prior to computing the parameter C, the equation 2.38 is averaged to produce:

$$C\overline{\Delta}^2 = -\frac{< \mathcal{L}_{ij} M_{ij} >}{2 < M_{ij} M_{ij} >} \tag{2.39}$$

where <> means averaging over a spatial direction to which the flow is homogeneous. Garg (1996) applied this approach successfully in his stratified channel flow simulations.

For flows with less homogeneity, Piomelli (1992) cures the negative eddy viscosity by a combined averaging in both time and a local spatial region. The size of the spatial region is big enough to smooth the parameter variation but smaller than the scale of inhomogeneity.

In this thesis, a combination of the first two approaches has been implemented. The third approach to be implemented in future work.

2.5 Transformed Governing Equations and Boundary Conditions

The filtered equations and the boundary conditions (equation 2.22 to equation 2.27), combined with the turbulence model described in section 2.4, form a closed system. To solve this system numerically, the wavy physical domain in the Cartesian system (x_1, x_2, x_3) is transformed into a rectangular computational box in a curvilinear system (ξ^1, ξ^2, ξ^3). The discretizations are performed in the computational domain. As pointed out by Zang (1994), this approach enables us to treat the boundary conditions accurately and conveniently. In order to prevent extra terms from being generated by the transformation, only the independent variables are transformed. The Cartesian velocity components remain as the dependent variables in the transformed domain (Shyy and Vu 1991).

In the present study, an orthogonal transformation is used. Compared with a non-orthogonal transformation, it simplifies the numerical problem greatly. The detailed form of this orthogonal transformation will be given in Chapter 3. The rectangular computational domain after the transformation has unity grid spacing in all directions and is represented by:

$$0 \leq \xi^1 \leq ni-2, \quad 0 \leq \xi^2 \leq nj-2, \quad 0 \leq \xi^3 \leq nk-2 \tag{2.40}$$

Where ni, nj, and nk are the numbers of grid points used in the streamwise, spanwise, and vertical direction in the curvilinear system, respectively, including the two ghost points employed in each direction for boundary condition implementation. The two surfaces in the streamwise direction of the physical domain are mapped into $\xi^1 = 0$ and $\xi^1 = ni-2$, respectively. Likewise, $\xi^2 = 0$ and $\xi^2 = nj-2$ represent the physical boundaries in the streamwise direction; and $\xi^3 = 0$ and $\xi^3 = nk-2$ the bottom and top surfaces. The ghost point approach will be discussed in section 3.2.

Applying the chain rule of derivatives to equations 2.22 and 2.23, we have:

$$\frac{\partial}{\partial x_j} = \frac{\partial \xi^m}{\partial x_j}\frac{\partial}{\partial \xi^m} \tag{2.41}$$

Then we multiply the resulting equations by the inverse of the Jacobian $J^{-1} = det(\frac{\partial x_i}{\partial \xi^m})$ and utilize the identity:

$$\frac{\partial}{\partial \xi^m}(J^{-1}\frac{\partial \xi^m}{\partial x_i}) \equiv 0 \tag{2.42}$$

Then we obtain the transformed governing equations in "Strong-Conservation-Law-Form":

$$\frac{\partial \overline{U}^m}{\partial \xi^m} = 0 \tag{2.43}$$

$$\frac{\partial J^{-1}\overline{u}_i}{\partial t} + \frac{\partial \overline{F}_i^m}{\partial \xi^m} = \overline{S}_i \tag{2.44}$$

where $\overline{U}^m$ is the volume flux in the ξ^m direction and G^{mn} is called the "skewness tensor". They are defined as:

$$\overline{U}^m = J^{-1}\frac{\partial \xi^m}{\partial x_j}\overline{u}_j \tag{2.45}$$

$$G^{mn} = J^{-1}\frac{\partial \xi^m}{\partial x_j}\frac{\partial \xi^n}{\partial x_j} \tag{2.46}$$

One of the valuable properties of the skewness tensor is that, for an orthogonal transformation, such as the one used in this study, the off-diagonal terms of G^{mn} are identically zero.

The terms $\overline{F}_i^m$ and $\overline{S}_i$ on the right hand side of equation 2.44 are:

$$\overline{F}_i^m = \overline{U}^m\overline{u}_i + J^{-1}\frac{\partial \xi^m}{\partial x_i}\overline{p} - (\nu_t + \frac{1}{Re_s})G^{mn}\frac{\partial \overline{u}_i}{\partial \xi^n}, \quad (m = n) \tag{2.47}$$

$$\overline{S}_i = J^{-1}\frac{\partial \xi^m}{\partial x_j}\frac{\partial \xi^n}{\partial x_i}\frac{\partial \nu_t}{\partial \xi^m}\frac{\partial \overline{u}_j}{\partial \xi^n} \tag{2.48}$$

where the turbulence model presented in equation 2.29 has been applied.

After the transformation, the periodic boundary conditions in the streamwise and spanwise directions now apply to the boundaries in the computational domain. The bottom boundary conditions in equation 2.24 are applied on the surface $\xi^3 = 0$.

The kinematic boundary condition in equation 2.25 can be written in a simpler

form in the curvilinear system as follows. Substitute equation 2.25 into the definition of $\overline{U}^3$ in equation 2.45, the volume flux on the top boundary becomes:

$$\overline{U}^3 = J^{-1}\overline{u}_1(\frac{\partial \xi^3}{\partial x_1} + \frac{\partial \xi^3}{\partial x_3}\frac{\partial \eta_s}{\partial x_1}) \tag{2.49}$$

Since the top surface is represented by $\xi^3 = nk - 2$ in the curvilinear system, and ξ^3 is obtained by a transformation of the following form:

$$\xi^3 = f(x_1, x_3) \tag{2.50}$$

where $x_3 = 1 + \eta_s(x_1)$ at the surface, the top surface shape can be written as:

$$\xi^3 = f(x_1, 1 + \eta_s(x_1)) = nk - 2 \tag{2.51}$$

Taking the derivative of equation 2.51 with respect to x_1 results in:

$$\frac{\partial \xi^3}{\partial x_1} + \frac{\partial \xi^3}{\partial x_3}\frac{\partial \eta_s}{\partial x_1} = 0 \tag{2.52}$$

By substituting equation 2.52 into equation 2.49, the kinematic boundary condition now becomes:

$$\overline{U}^3 = 0 \tag{2.53}$$

This equation implies that the normal flux at the top surface is zero. This guarantees global conservation of mass: there is no flux across the bottom boundary; the fluxes across the boundaries in streamwise direction cancel out due to the periodic boundary condition and so do the fluxes in the spanwise direction. Thus the total mass accumulation in the domain is zero.

The tangential stresses in equation 2.26, $\overline{\tau}_{\eta^1\eta^3}$, becomes $\overline{\tau}_{\xi^1\xi^3}$ in the current curvilinear system. According to Goldstein (1952), the non-dimensional tangential stress can be written as:

$$\overline{\tau}_{\eta^1\eta^3} = \overline{\tau}_{\xi^1\xi^3} = \frac{h_1}{h_3}\frac{\partial}{\partial \xi^3}(\frac{\overline{u}(1)}{h_1}) + \frac{h_3}{h_1}\frac{\partial}{\partial \xi^1}(\frac{\overline{u}(3)}{h_3}) \tag{2.54}$$

where h_α ($\alpha = 1,3$) is the scaling factor, defined as the ratio of the distance to the coordinate difference if an infinitesimal displacement is made in ξ^α direction. For orthogonal transformation, $h_\alpha = \sqrt{g^{\alpha\alpha}}$ (no summation on α) (Aris 1989), where g^{ij} is related to the skewness tensor G^{ij} defined in equation 2.46 by:

$$g^{ij} = G^{ij}/J^{-1} \tag{2.55}$$

$\overline{u}(\alpha)(\alpha = 1,3)$ in equation 2.54 is the physical component of the resolved velocity in ξ^α direction in the curvilinear system (Note that it is different from $\overline{u}_\alpha$ in the Cartesian system). It can be computed from the contravariant velocity (Aris 1989) :

$$\overline{u}(\alpha) = h_\alpha \overline{V}^\alpha \tag{2.56}$$

The contravariant velocity $\overline{V}^\alpha$ is connected to the volume flux $\overline{U}^\alpha$ defined in equation 2.45 as:

$$\overline{V}^\alpha = \overline{U}^\alpha/J^{-1} \tag{2.57}$$

Therefore, the dynamic boundary condition in equation 2.26 now becomes:

$$\sqrt{\frac{G^{33}}{G^{11}}}\frac{\partial}{\partial\xi^3}(\frac{\overline{U}^1}{J^{-1}}) + \sqrt{\frac{G^{11}}{G^{33}}}\frac{\partial}{\partial\xi^1}(\frac{\overline{U}^3}{J^{-1}}) = \frac{Re_*^2}{Re_s} \tag{2.58}$$

Since the kinematic boundary condition requires $\overline{U}^3$ to be identically zero along the top surface, where $\xi^3 = nk - 2$, the second term of the left hand side in the above equation reduces to zero. Thus the dynamic boundary condition specified in equation 2.26 becomes:

$$\sqrt{\frac{G^{33}}{G^{11}}}\frac{\partial}{\partial\xi^3}(\frac{\overline{U}^1}{J^{-1}}) = \frac{Re_*^2}{Re_s} \tag{2.59}$$

Similarly, the dynamic boundary condition specified in equation 2.27 becomes:

$$\frac{\partial}{\partial\xi^3}(\frac{\overline{U}^2}{J^{-1}}) = 0 \tag{2.60}$$

2.6 Statistical Equations

Turbulent flows are usually described in terms of the mean properties and the fluctuations. This is achieved by decomposing each variable into mean and fluctuating components. The mean component of a variable ϕ is represented as $< \phi >$. The angular brackets denote ensemble averaging, which means time averaging for turbulent flows that reach a statistical steady state, and averaging over homogeneous directions if there are any. The fluctuating component is denoted as ϕ'' and is the difference between the instantaneous value and the mean value, $\phi - < \phi >$. Obviously, the operation of emsemble average and those of addition and differentiation commute.

In the present study, statistics are collected from the turbulent flow based on the mean momentum equations and the resolved Reynolds stress equations.

The mean continuity and momentum equations are obtained by applying ensemble averaging to the filtered equations 2.22 and 2.23:

$$U_{i,i} = 0 \tag{2.61}$$

$$U_{i,t} + (U_i U_j)_{,j} = - < \overline{p} >_{,i} + \tau^m_{ij,j} + \tau^{sgs}_{ij,j} + \tau^r_{ij,j} \tag{2.62}$$

In the above equations, a comma followed by an index implies a partial derivative in the spatial direction specified by the index. U_i is the mean velocity component in x_i direction, defined as:

$$U_i = < \overline{u}_i > \tag{2.63}$$

The corresponding fluctuation components are:

$$u''_i = \overline{u}_i - U_i \tag{2.64}$$

$$p'' = \overline{p} - < \overline{p} > \tag{2.65}$$

τ^m_{ij}, τ^{sgs}_{ij} and τ^r_{ij} on the right hand side of equation 2.62 represent the ensemble averaged stress due to molecular viscosity, the ensemble averaged subgrid-scale stress

(anisotropic part), and the resolved Reynolds stress, respectively:

$$\tau_{ij}^{m} = 2/Re_s < \overline{S}_{ij} > \quad (2.66)$$

$$\tau_{ij}^{sgs} = - < q_{ij} >= 2 < \nu_t \overline{S}_{ij} > \quad (2.67)$$

$$\tau_{ij}^{r} = - < u_i'' u_j'' > \quad (2.68)$$

And the total stress, τ_{ij}^{total} is the summation of the above three components.

If we subtract the mean momentum equations 2.61 and 2.62 from the instantaneous equations 2.22 and 2.23, we obtain the continuity and momentum equations for the fluctuating component. We multiply the momentum equation for u_i'' by u_j'' and multiply the momentum equation for u_j'' by u_i'' and then add the resulting two equations. After applying ensemble averaging, we obtain the transport equation for the resolved Reynolds stress:

$$< u_i'' u_j'' >_{,t} = C_{ij} + P_{ij} + T_{ij} + \Pi_{ij} + \phi_{ij} + D_{ij} + \varepsilon_{ij} + T_{ij}^{sgs} + \varepsilon_{ij}^{sgs} \quad (2.69)$$

where the terms at the right hand side are defined as follows:

$C_{ij} = -U_k < u_i'' u_j'' >_{,k}$	Mean velocity transport
$P_{ij} = -(U_{i,k} < u_k'' u_j'' > + U_{j,k} < u_k'' u_i'' >)$	Production rate
$T_{ij} = - < u_i'' u_j'' u_k'' >_{,k}$	Turbulent transport rate
$\Pi_{ij} = -(< p'' u_j'' >_{,i} + < p'' u_i'' >_{,j})$	Pressure transport rate
$\phi_{ij} = 2 < p'' S_{ij}'' >$	Pressure strain redistribution
$D_{ij} = \frac{1}{Re_s} < u_i'' u_j'' >_{,kk}$	Viscous diffusion rate
$\varepsilon_{ij} = -\frac{2}{Re_s} < u_{i,k}'' u_{j,k}'' >$	Viscous dissipation rate
$T_{ij}^{sgs} = -(< q_{ik}'' u_j'' > + < q_{jk}'' u_i'' >)_{,k}$	SGS transport rate
$\varepsilon_{ij}^{sgs} =< q_{ik}'' u_{j,k}'' > + < q_{jk}'' u_{i,k}'' >$	SGS dissipation rate

where $q_{ij}'' = q_{ij} - < q_{ij} >$ and $S_{ij}'' = \overline{S}_{ij} - < \overline{S}_{ij} >$ are the fluctuating components of the subgrid-scale stress and the resolved strain-rate tensor, respectively.

The above statistical equations are written in the Cartesian coordinate system. To calculate each term numerically in a curvilinear system, the chain rule in equation 2.41 needs to be applied.

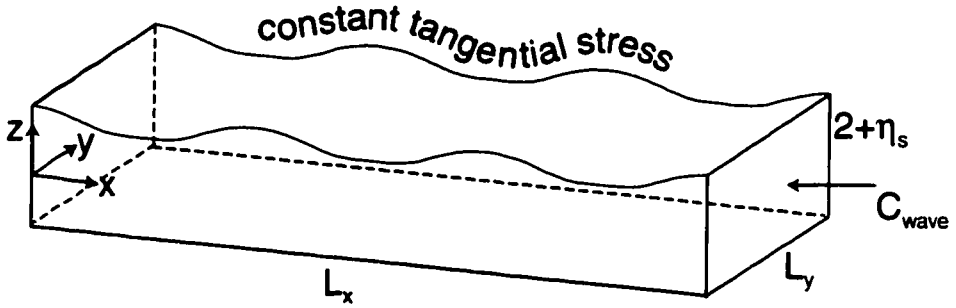

Figure 2.1: A sketch of the domain for 3D wavy flow.

Chapter 3

Numerical Methods and Implementation Issues

3.1 Introduction

The numerical method is adapted from the finite volume approach developed by Zang *et al.* (1994). Two sets of variables are employed on a non-staggered grid layout: the velocity and pressure components at the center of a control volume, and the contravariant volume fluxes on the surfaces of the control volume. With the non-staggered grid, a substantial saving in computational memory for the metric terms is achieved relative to the staggered-grid approach. At the same time, the accuracy of the algorithm is maintained by avoiding averaging of metric terms. By using the contravariant fluxes, the pressure Poisson equation is derived in a manner similar to that in the staggered grid approach. It guarantees mass conservation to machine zero at every time step.

In the present study, both the kinematic and the dynamic boundary conditions on a wavy surface are incorporated into Zang's algorithm. Several modifications are made. First, in Zang's method, central differencing is used for the spatial discretization except for the convective term, where a quadratic upstream interpolation scheme, QUICK (1979), is applied to improve the stability. However, as pointed out by Ferziger and Perić (1997), upstream differential methods introduce false diffusion, whereas central difference schemes do not. Thus, central differencing is used for all spatial discretizations here. Second, in Zang's method, the three dimensional multigrid method is used to solve the pressure Poisson equation. In the present case, the grid stretching used in the vertical direction adversely affects the speed of convergence. This problem is solved by applying multigrid method only in the lateral directions, with the vertical direction solved implicitly. Third, the code has been rewritten in a

more modular way and has been optimized further for the specific cases studied.

The layout of this chapter is as follows. In section 3.2, the grid generation and metric term computation are presented; In section 3.3, the selections of the domain size and the grid spacing are described . The discretization of the governing equations and the fractional step method used by Zang *et al.* (1994) are summarized in section 3.4. The discretization of the boundary conditions for the wavy domain is derived in section 3.5, The overall solution procedure is presented in section 3.6. Finally, implementation issues are discussed in section 3.7.

3.2 Grid Generation

3.2.1 Coordinate Transformation

The physical domain shown in Figure 2.1 is first transformed into a rectangular domain in space (η^1, η^2, η^3). The dimensions of the domain in the streamwise and spanwise directions are the same as of the physical domain, whereas the domain depth becomes $2 - 0.5\epsilon^2/\kappa_x \coth(2\kappa_x)$, where κ_x is the wave number and ϵ is the wave slope. The transformation is:

$$\begin{aligned} x_1 &= \eta^1 + \frac{\epsilon}{\kappa_x}\frac{\sin(\kappa_x\eta^1)\cosh[\kappa_x(1+\eta^3)]}{\sinh(2\kappa_x)} + \\ &\quad \epsilon^2\left[\frac{\mu}{{\kappa_x}^2} + \frac{\coth(2\kappa_x)}{2\kappa_x}\right]\frac{\sin(2\kappa_x\eta^1)\cosh[2\kappa_x(1+\eta^3)]}{\sinh(4\kappa_x)} \qquad (3.1) \\ x_2 &= \eta^2 \qquad (3.2) \\ x_3 &= \eta^3 + \frac{\epsilon}{\kappa_x}\frac{\cos(\kappa_x\eta^1)\sinh[\kappa_x(1+\eta^3)]}{\sinh(2\kappa_x)} + \\ &\quad \epsilon^2\left[\frac{\mu}{{\kappa_x}^2} + \frac{\coth(2\kappa_x)}{2\kappa_x}\right]\frac{\cos(2\kappa_x\eta^1)\sinh[2\kappa_x(1+\eta^3)]}{\sinh(4\kappa_x)} - \epsilon^2\frac{\coth(2\kappa_x)}{2\kappa_x} \qquad (3.3) \end{aligned}$$

Since the wave height is constant in the spanwise direction, nothing is done to x_2. The transformation on x_1 and x_3 is orthogonal because it satisfies the Cauchy-Riemann conditions:

$$\frac{\partial x_1}{\partial \eta^1} = \frac{\partial x_3}{\partial \eta^3}, \quad \frac{\partial x_1}{\partial \eta^3} = -\frac{\partial x_3}{\partial \eta^1} \qquad (3.4)$$

The discretization is then performed in (η^1, η^2, η^3) space. Uniform grids are used in both streamwise and spanwise directions. Non-uniform grids with a hyperbolic tangential stretch (Piomelli *et al.* 1987) are used in the vertical direction. This distributes more grid points near the bottom and the top surfaces, where viscous boundary layers need to be resolved.

For implementation convenience, the domain in (η^1, η^2, η^3) space is transformed again into the final computational space (ξ^1, ξ^2, ξ^3), in which the grids are uniformly distributed in each direction with unity spacing. The ghost point approach is employed to implement the boundary conditions. This method can be described with the aid of the one-dimensional sketch shown in Figure 3.1. There are ni grids in ξ^1 direction. The computational nodes ($i = 1$ to ni) are located at the centers of the grid cells. The boundaries of the physical domain are mapped to the east surfaces of the first and the $(ni-1)$st grids, with the coordinates $\xi^1 = 0$ and $\xi^1 = ni - 2$, respectively. The coordinate of the ith node is $\xi^1 = i - 1.5$. The first and last nodes are the ghost points that lie outside the physical domain; and the rest of nodes are inside the physical domain. The same layout also applies to the ξ^2 and ξ^3 directions. The advantage of this approach is that no special treatment of the spatial discretization is needed near the boundaries.

The transformation from (ξ^1, ξ^2, ξ^3) space to (η^1, η^2, η^3) space is:

$$\eta^1 = \frac{\xi^1}{ni-2} L_x \tag{3.5}$$

$$\eta^2 = \frac{\xi^2}{nj-2} L_y \tag{3.6}$$

$$\eta^3 = \frac{1}{\alpha}\left(1 - \frac{\epsilon^2}{4\kappa_x}\coth(2\kappa_x)\right)\tanh\left[\tanh^{-1}(\alpha)\left(\frac{2\xi^3}{nk-2} - 1\right)\right] + \frac{\epsilon^2}{4\kappa_x}\coth(2\kappa_x) \tag{3.7}$$

where ni, nj, and nk are the numbers of grids in the ξ^1, ξ^2 and ξ^3 directions, respectively; and α $(0 \leq \alpha \leq 1)$ is the parameter for the grid stretching in the ξ^3 direction.

3.2.2 Computation of Metric Terms

The coordinate transformation is reflected in the governing equations and boundary conditions by the metric terms. For a non-orthogonal transformation, a set of 16 metric terms needs to be calculated (Zang *et al.* 1994). They are: 1 inverse of the Jacobian J^{-1}, 9 surface metric terms $J^{-1}\frac{\partial \xi^m}{\partial x_i}$ and 6 non-trivial elements of the symmetric skewness metric tensor G^{mn}. For the orthogonal transformation in section 3.2.1, only the three diagonal elements of G^{mn} are non-zero. Since the wave shape does not vary in the spanwise direction, only 5 of the 9 surface metric terms are non-trivial. Therefore, the storage is needed for a set of $1+3+5=9$ metric terms. Furthermore, due to the two-dimensionality of the surface wave, the metric terms can be stored in a two dimensional array of size $(ni \times nk)$ instead of a three dimensional array of size $(ni \times nj \times nk)$.

The inverse of Jacobian and the non-trivial surface metric terms can be written in terms of $\frac{\partial x_i}{\partial \xi^m}$ as follows:

$$J^{-1} = \frac{\delta x_2}{\delta \xi^2}\left(\frac{\delta x_1}{\delta \xi^1}\frac{\delta x_3}{\delta \xi^3} - \frac{\delta x_1}{\delta \xi^3}\frac{\delta x_3}{\delta \xi^1}\right) \tag{3.8}$$

$$J^{-1}\frac{\partial \xi^1}{\partial x_1} = \frac{\delta x_2}{\delta \xi^2}\frac{\delta x_3}{\delta \xi^3}, \quad J^{-1}\frac{\partial \xi^1}{\partial x_3} = -\frac{\delta x_2}{\delta \xi^2}\frac{\delta x_1}{\delta \xi^3}, \tag{3.9}$$

$$J^{-1}\frac{\partial \xi^3}{\partial x_3} = \frac{\delta x_2}{\delta \xi^2}\frac{\delta x_1}{\delta \xi^1} \quad J^{-1}\frac{\partial \xi^3}{\partial x_1} = -\frac{\delta x_2}{\delta \xi^2}\frac{\delta x_3}{\delta \xi^1}. \tag{3.10}$$

$$J^{-1}\frac{\partial \xi^2}{\partial x_2} = J^{-1}/\frac{\delta x_2}{\delta \xi^2} \tag{3.11}$$

The symbol δ denotes a finite difference approximation. It is found in the right hand side of above equations, because all the metrics are computed using central differencing rather than analytical values. Numerically computed metric terms guarantee that the metric identity in equation 2.42 is satisfied to machine accuracy. This important condition is necessary for the derivatives in the transformed equations to vanish when the physical variable is uniform (Thompson *et al.* 1985).

The non-trivial skewness metric terms can be calculated from their definitions:

$$G^{11} = J^{-1}\left(\frac{\partial \xi^1}{\partial x_1}\frac{\partial \xi^1}{\partial x_1} + \frac{\partial \xi^1}{\partial x_3}\frac{\partial \xi^1}{\partial x_3}\right) \tag{3.12}$$

$$G^{22} = J^{-1}\frac{\partial \xi^2}{\partial x_2}\frac{\partial \xi^2}{\partial x_2} \tag{3.13}$$

$$G^{33} = J^{-1}(\frac{\partial \xi^3}{\partial x_1}\frac{\partial \xi^3}{\partial x_1} + \frac{\partial \xi^3}{\partial x_3}\frac{\partial \xi^3}{\partial x_3}) \tag{3.14}$$

where the right hand sides of the above equations can be calculated using equations 3.8 to 3.11.

The definitions of the two sets of the variables, *i. e.*, the velocity components and pressure at the center of the control volume, and the contravariant volume fluxes on the surfaces, require that the metric terms to be calculated at different locations. For a control volume, J^{-1} denotes the value at the center of the control volume; $J^{-1}\frac{\partial \xi^1}{\partial x_1}$, $J^{-1}\frac{\partial \xi^1}{\partial x_3}$ and G^{11} are the values at the east surface; $J^{-1}\frac{\partial \xi^2}{\partial x_2}$ and G^{22} at the front surface; and $J^{-1}\frac{\partial \xi^3}{\partial x_1}$, $J^{-1}\frac{\partial \xi^3}{\partial x_3}$ and G^{33} at the north surface.

3.3 Domain Size and Grid Spacing Selections

Given the limitations of the number of grid points allowed by the available computer power, the choice of the grid locations should be optimized based on the physical properties of the flow. The grid size has to be small enough to resolve the important flow structures and the resolved flow should contain as much energy as possible. On the other hand, the domain has to be big enough to include the largest turbulent coherent structures, so that the periodic boundary conditions (chapter 2) will not affect the numerical results.

For the three dimensional turbulent flow under a wavy surface in the present study, the grid selection depends on the properties of both the turbulence and the Langmuir circulations.

In order to use periodic boundary conditions in the lateral directions, the streamwise and the spanwise dimensions should be multiples of the wavelength of the Stokes wave and the Langmuir circulation, respectively. These two wavelengths are determined according to the typical field observations of Langmuir circulations (Smith 1992, Smith *et al.* 1987). In the present study, the nondimensional wavenumbers of the Stokes wave and the Langmuir circulations, normalized by the half mean

depth of the domain, h, are:

$$\kappa_x = 1.5, \quad \kappa_y = 1.56 \tag{3.15}$$

Further details of the physical parameter selections will be given in chapter 6.

The periodicity lengths in the lateral directions are also guided by the biggest turbulent structures observed in the experiments by Comte-Bellot (1963) and the DNS simulations by Kim *et al.*(1987) of turbulent channel flows. Both the experiment data and the DNS results show that the correlation of the velocity fluctuations between two points vanishes beyond a streamwise distance of $3.2h$ and a spanwise distance of $1.6h$. Thus, a domain with approximately $6.4h$ in streamwise direction and $3.2h$ in spanwise direction would justify the use of the periodic boundary conditions. Therefore, in the turbulent wavy case, three wavelengths of the surface wave and one wavelength of the Langmuir circulation are chosen as the domain size:

$$L_x = 3\frac{2\pi}{\kappa_x} = 12.56, \quad L_y = \frac{2\pi}{\kappa_y} = 4 \tag{3.16}$$

In choosing the grid size, one has to consider the thickness of the viscous sublayers and the turbulent structures formed in the vicinity of the bottom non-slip wall that are known as longitudinal streaks (Comte-Bellot 1963, Kim *et al.* 1987, Handler *et al.* 1993). In addition, the structures due to the wave motion, such as the thickness of the viscous wavy boundary and the thickness of the downwelling zone of the Langmuir circulations, should also be taken into consideration.

The thickness of the viscous sublayer under the top surface is around 5 ν/u_* units, where u_* is the friction velocity at the top surface, and ν the molecular viscosity. On the other hand, the thickness of the wavy boundary layer is given by:

$$\delta_w^d = \sqrt{\frac{2\nu}{C_w^d {\kappa_x}^d}} \tag{3.17}$$

where C_w^d and ${\kappa_x}^d$ are, respectively, the dimensional phase speed and the wavenumber of the surface wave. As will be shown in chapter 6, for the turbulent wavy case, the nondimensional wavy boundary layer thickness (based on h) is $\delta_w = 0.009$. In wall

units, the wavy boundary layer thickness is $\delta_w^+ = 0.009 Re_* = 0.9$, where $Re_* = \frac{u_* h}{\nu} = 100$ for a typical 3D wavy turbulent case.

Hyperbolic tangential stretching is applied in the vertical direction (section 3.2). In equation 3.7, larger α distributes more grids near the top and bottom boundaries. In this study, 64 grids are used between the two boundaries, with $\alpha = 0.98$. As a result, the first grid is 0.15 wall unit away from the boundary; the largest grid near the centerline is 7 wall units; there are 3 grids inside the wavy boundary layer and 9 grids inside the viscous sublayer.

From the experiments (Comte-Bellot 1963), the longitudinal streaks have an average spacing of 100 wall units in the spanwise direction, and an average length of 440 wall units in the streamwise direction. Therefore, for the turbulent wavy cases under study, where $Re_* = 100$, the nondimensional average streak spacing and length (based on h) are, respectively:

$$\lambda_2 = \frac{100}{Re_*} = 1, \quad \lambda_1 = \frac{440}{Re_*} = 4.4 \tag{3.18}$$

Assume that at least 4 points are needed to resolve each streak, then, with uniform grids in the lateral directions, the minimum numbers of grids in the streamwise and the spanwise direction (including 2 ghost points) are:

$$ni_{min} = \frac{L_x}{\lambda_1} \times 4 + 2 = 14, \quad nj_{min} = \frac{L_y}{\lambda_2} \times 4 + 2 = 18 \tag{3.19}$$

Li and Garrett (1993) solved two dimensional Craik-Leibovich equations and performed a scaling study on the Langmuir circulations. They suggested dividing each Langmuir circulation into four regions, as shown in Figure 3.2: (1) a narrow downwelling region of spanwise thickness $\delta^d_{downwelling} \sim \mathcal{O}\left(La^{1/2}\lambda^d_x\right)$ between the two counter-rotating Langmuir circulations, (2) a surface boundary layer region of vertical thickness $\delta^d_s \sim \mathcal{O}\left(La^{1/2}\lambda^d_y\right)$ beneath the surface wave, (3) a corner region that is the intersection of the first two regions, and (4) an advection region that is the rest of the Langmuir circulation. In the above expressions, λ^d_x and λ^d_y are the (dimensional) wavelength of the surface wave and the Langmuir circulation, respectively, and La is the laminar Langmuir number. The definition of the Langmuir number will be

discussed in chapter 5, in which our modification to the Langmuir number used by Li and Garrett is present.

For the turbulent wavy case, $La \sim 4 \times 10^{-4}$. Therefore, the nondimensional thicknesses (based on h) of the downwelling zone and the surface boundary layer are:

$$\delta_{downwelling} = 0.083, \quad \delta_s = 0.08 \tag{3.20}$$

In wall units, the thickness of the surface boundary layer is $\delta_s^+ = 0.08 Re_* = 8.0$. Thus the surface boundary layer is thicker than the viscous sublayer, which is well resolved with the stretched grids. For the narrow downwelling zone, however, assuming at least 4 grids are needed to resolve it. Then, with a uniform grid, the minimum number of the spanwise grids (including the 2 ghost points) is:

$$nj_{min} = \frac{L_y}{\delta_{downwelling}} \times 4 + 2 = 202 \tag{3.21}$$

In addition, because three wavelengths of the surface wave are included in the domain. each wavelength needs a reasonable number of grids to resolve the flow motion beneath it.

Summing up all the information, for uniform grids in the lateral directions, the following values of ni and nj are recommended:

$$ni = 66 \quad nj = 202 \tag{3.22}$$

However, due to the limitation of the computational resource for this study, the numbers of grids in the lateral directions are chosen as:

$$ni = nj = 66 \tag{3.23}$$

including the 2 ghost points in each direction. Thus, for the turbulent wavy case, the downwelling zone of the Langmuir circulation cannot be resolved at this stage. Nevertheless, McWilliams *et al.* (1997) suggested that the downwelling zone is broaden by the turbulent mixing. Thus, we expects that the problem caused by the number of grid points in the spanwise direction is not serious.

3.4 Numerical Discretization

3.4.1 Temporal Discretization

For time advancement, the convective term is treated explicitly with the Adam-Bashforth scheme. The viscous diffusive term is advanced with the Crank-Nicolson scheme. The motivation of treating the viscous term implicitly is to remove the severe time-step restriction of an explicit scheme, caused by the refined grids near the wall. For the current numerical method, the maximum time step is determined by the CFL condition:

$$CFL = max\left[(|\overline{U}^1| + |\overline{U}^2| + |\overline{U}^3|)\frac{\Delta t}{J^{-1}}\right]_{\xi^1,\xi^2,\xi^3} < \overline{C} \sim 1 \tag{3.24}$$

Experimentation with the code showed that practically the maximum CFL number is around 0.4.

3.4.2 Spatial Discretization

For spatial discretization, central differencing is used. The values of the velocity components and pressure on a cell surface are obtained with linear interpolation (second order accurate). Since the grids are all of size unity in computational space, the form of the first and second order partial derivatives in the governing equations can be written: (with ξ^1 direction as an example)

$$(\frac{\delta f}{\delta \xi^1})_i = f_{i+\frac{1}{2}} - f_{i-\frac{1}{2}} \tag{3.25}$$

$$(\frac{\delta}{\delta \xi^1}(g\frac{\delta f}{\delta \xi^1}))_i = g_{i+\frac{1}{2}}(f_{i+1} - f_i) - g_{i-\frac{1}{2}}(f_i - f_{i-1}) \tag{3.26}$$

where the subscript i implies the value is evaluated at the center of the ith grid, and the subscript $i + \frac{1}{2}$ the value on the east surface of the ith grid.

3.4.3 Fractional Step Method

The transformed equations and the boundary conditions developed in chapter 2 are solved with a fractional step method that closely follows the derivation by Zang *et al.* (1994) for a generalized curvilinear system, an extension to the one developed by Kim and Moin (1985), who stated that the overall method achieves a second order accuracy in both space and time.

Three steps are involved:

1. Predictor step.

   In this step, the velocity field is predicted without the constraints of the continuity equation or the pressure term:

$$(I - \frac{\Delta t}{2J^{-1}} D_3)\Psi_i = \frac{\Delta t}{J^{-1}}[\frac{3}{2}C_i^{(n)} - \frac{1}{2}C_i^{(n-1)} + D_I(\overline{u}_i^{(n)}) + \overline{S}_i^{(n)}] \quad (3.27)$$

$$(I - \frac{\Delta t}{2J^{-1}} D_2)\Phi_i = \Psi_i \quad (3.28)$$

$$(I - \frac{\Delta t}{2J^{-1}} D_1)(u_i^* - \overline{u}_i^{(n)}) = \Phi_i \quad (3.29)$$

   where the ADI (Alternate Direction Implicit) method has been used. Ψ_i and Φ_i are the intermediate variables for the ADI method. The superscript (n) means the nth time step; and

$$D_\alpha = \frac{\delta}{\delta \xi^\alpha}\left[(\frac{1}{Re_s} + \nu_t)G^{\alpha\alpha}\frac{\delta}{\delta \xi^\alpha}\right] \quad (3.30)$$

   where $\alpha = 1, 2, 3$, with no summation on α.

$$C_i = -\frac{\delta}{\delta \xi^m}(\overline{U}^m \overline{u}_i) \quad (3.31)$$

$$D_I(\cdot) = \frac{\delta}{\delta \xi^m}\left[(\frac{1}{Re_s} + \nu_t)G^{ml}\frac{\delta}{\delta \xi^l}\right](\cdot), (m = l) \quad (3.32)$$

$$\overline{S}_i = J^{-1}\frac{\delta \xi^m}{\delta x_j}\frac{\delta \xi^l}{\delta x_i}\frac{\delta \nu_t}{\delta \xi^m}\frac{\delta \overline{u}_j}{\delta \xi^l} \quad (3.33)$$

   The numerical boundary conditions for equation 3.27 on the top and bottom

surfaces are from LeVeque and Oliger (1981):

$$\Psi_i = (\overline{u}_i^{(n)} - \overline{u}_i^{(n-1)}) + \Delta t \frac{\delta \xi^m}{\delta x_i} \frac{\delta \phi^{(n)}}{\delta \xi^m} \tag{3.34}$$

where ϕ is the pseudo-pressure defined in the next step.

Periodic boundary conditions are used for equations 3.28 and 3.29.

2. Pressure Poisson equation.

The pseudo-pressure is computed:

$$\frac{\delta}{\delta \xi^m}\left(G^{ml}\frac{\delta \phi^{(n+1)}}{\delta \xi^l}\right) = \frac{1}{\Delta t}\frac{\delta U^{*m}}{\delta \xi^m}, (m = l) \tag{3.35}$$

where U^{*m} is the intermediate volume flux defined on the cell surface. It is computed as:

$$U^{*m} = J^{-1}\frac{\partial \xi^m}{\partial x_j} u_j^* \tag{3.36}$$

The relation between the pressure $\overline{p}$ and the pseudo-pressure ϕ is:

$$\frac{\delta}{\delta \xi^m}\left(J^{-1}\frac{\delta \xi^m}{\delta x_i}\overline{p}\right) = \left(I - \frac{\Delta t}{J^{-1}} D_I\right)\frac{\delta}{\delta \xi^m}\left(J^{-1}\frac{\delta \xi^m}{\delta x_i}\phi\right) \tag{3.37}$$

3. Corrector step.

The intermediate velocities, u_i^* and U^{*m}, are corrected to get the true velocities.

For the Cartesian velocity defined on the cell center:

$$\overline{u}_i^{(n+1)} = u_i^* - \frac{\Delta t}{J^{-1}}\frac{\delta}{\delta \xi^m}\left(J^{-1}\frac{\delta \xi^m}{\delta x_i}\phi^{(n+1)}\right) \tag{3.38}$$

For the volume flux defined on cell surface:

$$\overline{U}^{m(n+1)} = U^{*m} - \Delta t\left(G^{ml}\frac{\delta \phi^{(n+1)}}{\delta \xi^l}\right), (m = l) \tag{3.39}$$

The pressure Poisson equation was derived by Zang *et al.* (1994) in a similar way as for a staggered-grid layout. A "compact" numerical operator results from discretizing the Laplacian operator in the Poisson equation. The volume fluxes obtained at this step satisfy the continuity equation 2.43 to machine accuracy.

To solve the pressure Poisson equation 3.35, periodic boundary conditions are used in the streamwise and spanwise directions. At the vertical boundaries, U^{*3} in the right hand side of equation 3.35 is replaced by $U^{3(n+1)}$ according to equation 3.39. Because central differencing is used, this substitution results in cancellation of the term $G^{33}\frac{\delta\phi^{(n+1)}}{\delta\xi^3}$ defined on the boundary. This is equivalent to applying Neumann boundary conditions at this boundary.

With the Neumann and periodic boundary conditions, the discretized Poisson equation needs to satisfy the compatibility condition, which requires the summation of the source term on the right hand side of equation 3.35 over the whole domain to be machine zero, which is essentially the global mass conservation. Since the actual volume fluxes $U^{3(n+1)}$ are used in the vertical boundaries, the global mass conservation is guaranteed.

However, these boundary conditions cause the pressure Poisson equation to be singular, because any contant field is a solution. This problem can be cured by subtracting the mean value from the pseudo-pressure field at each time step.

3.5 Boundary Condition Discretization

The boundary conditions listed in the last section, equation 3.34 and the Neumann condition for the pressure Poisson equation, are derived from the specific numerical techniques. They are only indirectly related to the actual physical boundary conditions, and thus are called numerical boundary conditions. To find the final values of the Cartesian velocities and pseudo-pressure at the ghost points at each time step, the physical boundary conditions are needed. Furthermore, the volume fluxes also need to be specified on the boundaries. That is, $\overline{U}^1$ needs to be specified on the boundaries in the streamwise direction; $\overline{U}^2$ on the boundaries in the spanwise direction; and $\overline{U}^3$ on the boundaries in the vertical direction.

In the streamwise and spanwise directions, periodic boundary conditions are used. Therefore, ghost point values for a variable, ψ, which denotes the Cartesian velocities or the pseudo-pressure, can be computed as:

$$\psi_{1,j,k} = \psi_{ni-1,j,k}, \quad \psi_{ni,j,k} = \psi_{2,j,k} \tag{3.40}$$

$$\psi_{i,1,k} = \psi_{i,nj-1,k}, \quad \psi_{i,nj,k} = \psi_{i,2,k} \tag{3.41}$$

The boundary values of $\overline{U}^1$ and $\overline{U}^2$ can be calculated according to equation 2.45, where the Cartesian velocities are obtained by interpolating the values of the ghost point and the interior point immediately next to the boundary.

In the vertical direction, ghost point values of the pseudo-pressure are obtained implicitly from the interior points values according to the momentum equations:

$$\frac{\delta\phi^{(n+1)}}{\delta\xi^3} = -\frac{1}{\Delta t G^{33}}(\overline{U}^{3(n+1)} - \overline{U}^{*3}) \tag{3.42}$$

where $\overline{U}^{3(n+1)}$ is zero at both top and bottom surfaces. It is zero at the top surface due to the kinematic boundary condition, equation 2.53; it is also zero at the bottom surface because $\overline{u}_3 = 0$ and $J^{-1}\frac{\partial\xi^3}{\partial x_1} = 0$ there.

All that is left to calculate are the ghost point values of the Cartesian velocities at the top and the bottom surfaces. It is straightforward to discretize the bottom boundary condition, equation 2.24, to get the Cartesian velocities at the ghost points. But at the top surface, both the kinematic and dynamic boundary conditions are needed to solve for the ghost point values of the Cartesian velocities.

Consider a control volume immediately beneath the top surface, as shown in Figure 3.3. Let us label values at the center of the control volume with subscript P, values at the ghost point in the control volume above it with subscript N, and values on the boundary between the two control volumes with subscript n. The kinematic and dynamic boundary conditions in equation 2.53, 2.59, and 2.60 are discretized using central differencing:

$$(\frac{\partial\xi^1}{\partial x_1})_N\overline{u}_{1N} + (\frac{\partial\xi^1}{\partial x_3})_N\overline{u}_{3N} = (\frac{\partial\xi^1}{\partial x_1})_P\overline{u}_{1P} + (\frac{\partial\xi^1}{\partial x_3})_P\overline{u}_{3P} + \frac{Re_*^2}{Re_s}\sqrt{\frac{G_n^{11}}{G_n^{33}}}$$

$$= b_1 \tag{3.43}$$

$$(\frac{\partial \xi^3}{\partial x_1})_n \overline{u}_{1N} + (\frac{\partial \xi^3}{\partial x_3})_n \overline{u}_{3N} = -\left[(\frac{\partial \xi^3}{\partial x_1})_n \overline{u}_{1P} + (\frac{\partial \xi^3}{\partial x_3})_n \overline{u}_{3P}\right]$$

$$= b_2 \tag{3.44}$$

$$(\frac{\partial \xi^2}{\partial x_2})_N \overline{u}_{2N} = (\frac{\partial \xi^2}{\partial x_2})_P \overline{u}_{2P} \tag{3.45}$$

By solving these three equations, the ghost point values are obtained:

$$\overline{u}_{2N} = \left[(\frac{\partial \xi^2}{\partial x_2})_P / (\frac{\partial \xi^2}{\partial x_2})_N\right] \overline{u}_{2P} \tag{3.46}$$

$$\begin{pmatrix} \overline{u}_{1N} \\ \overline{u}_{3N} \end{pmatrix} = \frac{1}{(\frac{\partial \xi^1}{\partial x_1})_N (\frac{\partial \xi^3}{\partial x_3})_n - (\frac{\partial \xi^1}{\partial x_3})_N (\frac{\partial \xi^3}{\partial x_1})_n} \begin{pmatrix} (\frac{\partial \xi^3}{\partial x_3})_n & -(\frac{\partial \xi^1}{\partial x_3})_N \\ -(\frac{\partial \xi^3}{\partial x_1})_n & (\frac{\partial \xi^1}{\partial x_1})_N \end{pmatrix} \begin{pmatrix} b1 \\ b2 \end{pmatrix} \tag{3.47}$$

where all the metric terms here are computed directly at the corresponding location and not by interpolation.

3.6 Overall Solution Procedure

The overall solution procedure for one time step $(n+1)$ is as follows:

1. Compute the CFL number from equation 3.24, adjust the time step such that the CFL number is less than the specified criterion.

2. Compute the eddy viscosity from the turbulence model (section 2.4).

3. Solve equation 3.27 of the predictor step in ξ^3 direction for Ψ_i at all the interior nodes, using the boundary condition 3.34.

4. Solve equation 3.28 of the predictor step in ξ^2 direction for Φ_i at all the interior nodes, using periodic boundary condition.

5. Solve equation 3.29 of the predictor step in ξ^1 direction for $u_i^* - \overline{u}_i^{(n)}$ at all the interior nodes, using periodic boundary condition.

6. Compute the intermediate Cartesian velocity, u_i^*, at all the interior nodes. Update the ghost point values of u_i^* in the streamwise and spanwise directions

using the periodic boundary conditions.

7. Compute U^{*m} from u_i^* on all the control volume surfaces within the boundaries, and on the boundary surfaces in the streamwise and spanwise directions using periodic boundary conditions.

8. Compute the source term of the pressure Poisson equation 3.35, using $U^{3(n+1)}$ instead of U^{*3} on the top and bottom boundaries.

9. Solve the pressure Poisson equation 3.35 for the pseudo-pressure, $\phi^{(n+1)}$, at all the interior points, using Neumann boundary conditions on the top and bottom boundaries and periodic boundary conditions in the streamwise and spanwise directions.

10. Update the ghost point values of the pseudo-pressure, using periodic boundary conditions in the streamwise and spanwise directions, and the physical boundary condition 3.42 for the top and bottom boundaries.

11. Correct the Cartesian velocity components at all the interior points using equation 3.38.

12. Correct the volume fluxes at all the surfaces within the boundaries and on the boundary surfaces on the streamwise and spanwise directions, using equation 3.39.

13. Update the Cartesian velocity components at the ghost points. Apply boundary condition 2.24 at the bottom surface, equations 3.46 and 3.47 at the top boundary; and periodic conditions in streamwise and spanwise directions.

14. Update the volume flux, $\overline{U}^{3(n+1)}$, to be zero on the top and bottom surfaces, as derived in section 3.5.

15. Compute Ψ_i on the top and bottom surfaces for the next time step, using equation 3.34 with the Cartesian velocity from last (n) and the current $(n+1)$ steps and the pseudo-pressure from the current time step.

3.7 Implementation Issues

In chapter 2 and the previous sections in this chapter, the formulation and numerical methods were given for a turbulent flow under a wavy surface. In this section, the development of the computational model is discussed.

3.7.1 Overview of the Computational Code

The computational code is designed and constructed for the following five types of problems:

1. Two dimensional wavy case (2Dwavy). This simulates the flow in a domain with a wavy top and flat surfaces as the other boundaries. Navier-Stokes equations are solved. The flow is driven by the second order Stokes wave propagating on the top of the domain and a tangential stress applied along its surface.

2. Two dimensional rectangular case (2DCL). This models a flow driven by the vortex force derived by Craik and Leibovich. Craik-Leibovich equations are solved. The problem is assumed to be invariant in the streamwise direction, and the numerical domain is a spanwise-vertical plane but all the three velocities are non-trivial. The initial base flow for this case is a streamwise mean current, which can be either linear or input by the user. The Stokes drift in the vortex force is derived from the wave theory (Phillips 1977). Both laminar flow and two dimensional turbulent flow (created via a specified eddy viscosity) can be simulated.

3. Three dimensional wavy flow (3Dwavy). This problem is similar to the two dimensional wavy flow except that streamwise variations are also considered.

4. Three dimensional channel flow with Craik-Leibovich forcing (3DCL). This is an extension to the two dimensional rectangular case, with considerations of the streamwise variations.

5. Three dimensional open channel flow (3DOChan). This case simulates a flow in a rectangular domain driven by the tangential force on the top surface. Navier-Stokes equations are solved.

For all the three dimensional cases, either laminar flows or turbulent flows can be modeled with the code. The turbulence model used is the dynamic subgrid scale model described in section 2.4.

The first two cases are used mainly for code validation. The 2Dwavy case is tested against Longuet-Higgins' theory (1953). The 2DCL case is compared with the linear stability study performed by Garg *et al.* (1992) using the Craik-Leibovich theory. The 3Dwavy case is for the direct study of wave-current interactions. A couple of major production runs are performed for both laminar and turbulent cases.

Steady state results from the 2Dwavy cases are also used as the initial base flows for the 3Dwavy flows. Random white noise of small magnitude is imposed on the base flow. The simulation results are analyzed to elucidate the underlying physics of the 3D flow structures.

To study the effects of the wave on the turbulent flow, an open channel flow without waves is simulated. The 3D open channel case is constructed to be as close to the 3Dwavy case as possible to facilitate comparison.

The limit of the validity of the Craik-Leibovich theory are tested by comparing the 3Dwavy simulations with the results from 2DCL runs, which are mainly for the laminar cases, and the solutions from the 3DCL runs, which includes turbulent models. The base flows of the CL cases are the Stokes drift and the mean current, which is caused by both the wave-induced Eulerian mean flow and the stress imposed on the top surface. Infinitesimal random noise is used as the initial perturbations. The effects of turbulence on Langmuir cells are also studied.

3.7.2 Modularization, Vectorization, and Audit Routines

The computer codes are designed to balance performance and flexibility. There are two types of codes, one is two dimensional, and the other three dimensional. Separating these two codes makes each of them simpler to read and maintain and yields improved performance and better reliability. Moreover, computational memory can

be saved in the two dimensional cases compared with Zang's code (Zang *et al.* 1994), which has been used in both two dimensional and three dimensional problems. Each code has a single interface that allows the various flow scenarios described in section 3.7.1. Therefore, wavy cases, CL cases, and open channel cases can be simulated with the same code, with minor changes to the input files.

Vectorization and modularization are two other major concerns. With the vector architecture of the Cray J90 in the Environment Fluid Mechanics Lab at Stanford, a single instruction can carry out operations on a string of data. Techniques such as loop inversion and non-vectorization loop segmentation are used to vectorize the code as much as possible. With $64 \times 64 \times 64$ grids[1], the Navier-Stokes solver for the 3Dwavy cases achieves approximately 60 Megaflops on a single CPU, compared with the peak 200 Megaflops per CPU of the Cray J90. If it were run on a Cray C90, whose peak performance is 1 Gigaflops, and if the performance is scalable, the code would run at 300 Megaflops, a good speed for a Navier-Stokes solver.

Some basic blocks such as the pressure Poisson solver, the tridiagonal solver, and the metric term generator are built in stand-alone fashion. Their implementations are totally separate from the main module, the Navier-Stokes solver. They interact with the main module through application programming interfaces. Therefore, the user of the main module does not need to know the detailed implementations behind the interfaces. It is also easier for the code developer in that each basic block can be tested alone, and if new algorithms are to be used in a basic block, the implementation can be changed just within that module without affecting the rest of the code.

The computational model has been tested thoroughly. Each of the subroutines and modules is validated with an audit routine. The audit routines were developed separately from the subroutines. Such tests, although time consuming, are very efficient in finding subtle problems in the implementation that might otherwise corrupt the data slowly and show up only after a very long run time.

[1]The default notation of grid points does not include the ghost points.

3.7.3 Poisson Solver Modification for Grid Stretching

A three dimensional multigrid method (Perng 1990) is used in Zang's algorithm to solve the pressure Poisson equation. The solution is obtained with a V-cycle structure that contains several levels of grids. An approximate solution of the pressure field is first obtained on the finest grid, with one to two iterations of a line-by-line Gauss-Seidel method, called the "smoother". Then the error in the current solution is "restricted" to the next coarser grid, where a Poisson equation for the pressure correction is solved with one to two iterations of the smoother. This process continues until the correction is obtained on the coarsest grid. Then, the correction is "prolonged" to the next fine grid, where the solution on the fine grid is corrected. This process is continued until the corrected pressure is obtained at the finest grid.

If uniform grid is used in all directions, the above multigrid method can achieve fast convergence. However, the vertically stretched grid used in this study introduces variation of the numerical coefficients in the vertical direction and greatly slows down the convergence of the multigrid method. The more the grid is stretched, the slower the convergence rate is.

We define the stretching ratio of a vertically stretched grid as:

$$\gamma = max \left[\frac{max(\Delta z_{k+1}, \Delta z_k)}{min(\Delta z_{k+1}, \Delta z_k)} \right]_k \tag{3.48}$$

where Δz_k is the grid size of the kth grid in the physical domain. Experimentation showed that γ should be less than 1.2 (Zang 1993).

To make the effectiveness of the Poisson solver less dependent on the stretching ratio, the three dimensional multigrid method is changed to a two dimensional multigrid method in the lateral directions, where uniform grids are used. A vertically implicit line-by-line Gauss-Seidel smoother is used with the two dimensional multigrid method at each grid level. That is, in the Gauss-Seidel method, the terms arising from boundary conditions are kept on the left hand side of the equations so that boundary conditions in the vertical direction are also treated implicitly.

α in equation 3.7	stretching Ratio (γ)	V-cycles Modified Method	V-cycles 3D Multigrid
0.01	~ 0	8	9
0.70	1.03	8	12
0.95	1.10	9	26
0.98	1.15	10	38

Table 3.1: Comparison of the modified method and the three dimension multigrid method of Poisson solver. Poisson equation 3.49 with random noise as the source term is solved. 64 x 64 x 64 grid is used. All runs converges with the residue to be less than 10^{-6} times the norm of the source term.

The modified algorithm has been evaluated using the Poisson equation:

$$\frac{\partial^2 \phi}{\partial x^2} + \frac{\partial^2 \phi}{\partial y^2} + \frac{\partial^2 \phi}{\partial z^2} = f \tag{3.49}$$

Uniform grids are used in the lateral directions. Hyperbolic tangential stretching given by equation 3.7 is used in the vertical direction. Several types of the source term, f have been tried, all leading to similar conclusions. The modified algorithm is compared with the three dimensional multigrid method in table 3.1 for the case in which f is random noise. Periodic boundary conditions are used in the lateral directions, and Neumann boundary conditions are used on the top and bottom surfaces. The mean value of the source term f has been subtracted to satisfy the compatibly condition (section 3.4). With the same convergence criterion, the number of V-cycles needed for the three dimensional multigrid method to converge increases dramatically with the stretching ratio. With uniform grid in vertical direction, the Poisson solver converges in only 9 V-cycles; with stretching ratio 1.15, however, 38 V-cycles are needed. On the other hand, the modified algorithm depends less on the stretching ratio, and the Poisson solver converges within approximately the same number of V-cycles.

3.8 Summary

An orthogonal transformation has been used to transform the physical wavy domain into a rectangular computational domain. The orthogonal transformation and the two dimensionality of the surface wave enable us to save a great deal of the computational storage for the metric terms and to simplify the numerical problem.

With the available computational resources, the selection of domain size for the three dimensional turbulent case is guided by the periodicity of the surface wave and the Langmuir circulation, as well as the two point correlation from the experiments on turbulent channel flow. The goal is to make to domain size large enough that the periodicity imposed in the lateral directions does not affect the results.

The grid is chosen to resolve the viscous sublayer and the viscous wavy boundary layer in the vertical direction. The streak structure formed near the bottom wall and the downwelling zone thickness of Langmuir circulation determine the selection of the grid spacing in the lateral directions.

The numerical method used here is adapted from the fractional step method by Zang *et al.* (1994) for a generalized curvilinear system, with the Adam-Bashforth scheme for the convective terms and the Crank-Nicolson scheme for the viscous terms. Central differencing is used for all the spatial discretizations. Second order accuracy is achieved in both space and time.

The way the pressure Poisson equation is formulated guarantees that mass conservation is satisfied at each time step. With the stretched grid in the vertical direction, the Poisson equation is solved with a two dimensional multigrid method in the lateral directions, combined with vertically implicit line-by-line Gauss-Seidel smoother.

The computational code is written in a modularized way, with the basic blocks such as the pressure Poisson solver built in a stand-alone fashion. The code for the two dimensional cases are separate from that for the three dimensional cases to improve both readability and performance. Each type of code simulates the wavy case and the rectangular cases with Craik-Leibovich equations with a uniform interface. All the computational codes are fully vectorized and tested thoroughly.

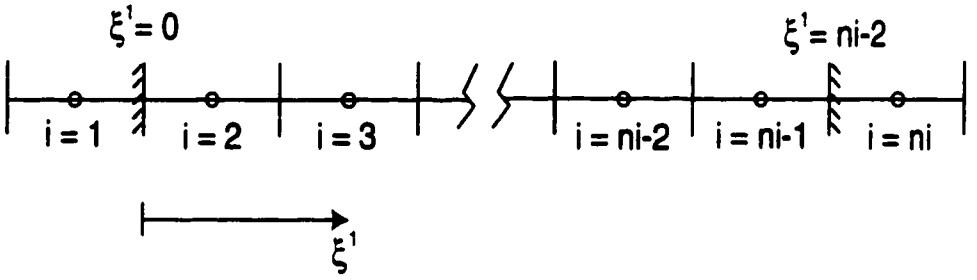

Figure 3.1: Sketch of the ghost point approach.

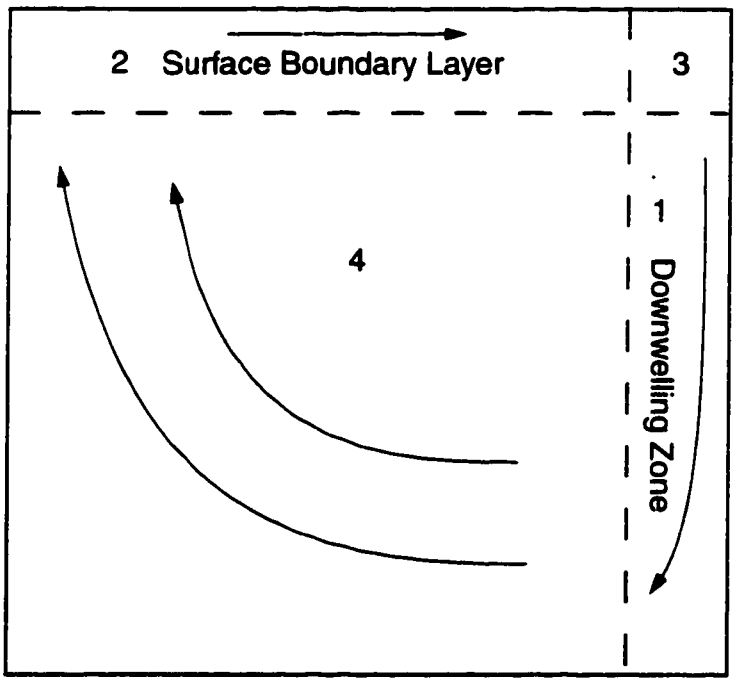

Figure 3.2: Sketch of the four subregions of a Langmuir cell. (After Li and Garrett (1993))

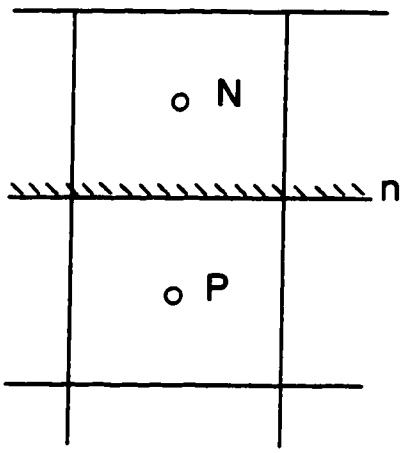

Figure 3.3: Sketch of a control volume near top surface.

Chapter 4

Two Dimensional Flows Under a Free Wavy Surface

4.1 Introduction

In this chapter, two dimensional flow under a surface gravity wave is studied. Since this is an old subject on which research has continued for over 200 years, no attempt is made to summarize the full range of the knowledge. The goals here are to develop solutions, both analytical and numerical, for flows under a specific non-deforming surface wave and to study the important flow properties related to the generation of Langmuir circulations.

Analytical solutions have been developed for inviscid flow, which are valid as a first approximation when the wave Reynolds number is high enough for viscous forces to be neglected. The inviscid theory of surface waves was pioneered by Stokes (1847), who developed the equation for the shape of a progressive wave in water of finite depth. The Stokes wave has been widely utilized to predict many observed wave phenomena and in the design of offshore platforms. It will be used in this work as the typical surface wave.

Traditionally, a periodic wave flow field is obtained by solving equations for incompressible, irrotational flow with kinematic and dynamic boundary conditions at the free surface and an impermeability condition at the bottom. The dependent variables are expanded in power series around the mean wave height. For example, the velocity field and the dispersion relation for the flow under a first order Stokes wave, *i. e.* a sinusoidal wave, has been given by Phillips (1977). Although the solutions obtained from the power series expansion are valid only below the trough, they are often used to obtain the flow field up to the wave crest. The error in doing so is of third order of the wave slope.

McDonald (1994) solved the flow under a second order Stokes wave in a transformed coordinate system. His transformation is non-orthogonal and fitted to the wave boundary. No power series approximation is needed. Thus, the solutions obtained are valid in the whole domain.

In the first half of this chapter, an analytical solution of the inviscid flow under a second order Stokes wave is developed using a method similar to McDonald's. The orthogonal transformation developed in chapter 3 is used, leading to a much simpler stream function. Furthermore, since both the analytical wave field and the numerical solutions are obtained in the same transformed coordinate system, it is convenient for making the comparisons and for examining the interactions between the wave and Langmuir circulations.

In the inviscid field, the velocity is periodic. No mean current exists in an Eulerian system. However, from a Lagrangian point of view, as first predicted by Stokes (1847), the fluid particles have open orbits. This creates the so-called Stokes drift that plays a major role in the Craik-Leibovich theory.

For real water waves, however, Longuet-Higgins (1953) elaborated that molecular viscosity, no matter how small its magnitude, causes another Eulerian mean drift. Just outside the bottom thin boundary layer, there exists a constant second order mean drift velocity. Similarly, just as below the surface boundary layer, there is a second order mean gradient of drift velocity. These lead to a second order Eulerian mean current.

In the Craik-Leibovich theory (1976), only the contribution of the Stokes drift is considered. Craik (1982) did a scaling analysis and showed that the Eulerian mean flow alone can lead to Langmuir circulations. Flows with wind stress have stronger mean currents and, thus, are more unstable to the disturbances that generate Langmuir circulations. The effects of the Eulerian mean flow is studied in this work.

In the second half of this chapter, a periodic viscous two dimensional flow is simulated numerically. The flow is under a rigid progressive second order Stokes wave and has a flat, no-slip bottom boundary. The Eulerian mean flow obtained is compared with the second order asymptotic solution predicted by Longuet-Higgins (1953). The simulation also serves as a validation of the implementation of the free surface

boundary condition presented in chapter 3.

The layout of this chapter is as follows. In section 4.2, the analytical solution for inviscid flow under a second order Stokes wave is presented. The velocity and pressure fields up to second order in the wave slope are calculated. Also, the dispersion relation up to first order is derived from the dynamic boundary condition. In section 4.3, numerical simulation of a viscous two dimensional wavy flow is carried out. The computation of the drift velocity of a fluid particle is discussed. Comparisons are made between the predicted drift and Longuet-Higgins' solution (1953), and between the flow field and the first order solution of Phillips (1977). A summary is presented in section 4.4.

4.2 Analytical Study of Inviscid Flows

4.2.1 Formulation

The formulation for two dimensional inviscid flow is similar to that presented in chapter 2 except that the flow is now two dimensional and the viscous term is zero. As in chapter 2, the coordinate system is moving at the phase speed of the rigid surface wave. Thus the wave shape becomes stationary. Unlike the viscous case, the rigid surface wave is not an approximation for the inviscid flow because there is no viscous dissipation and hence no wave damping.

Figure 4.1 illustrates the flow domain. It is one wavelength long in the streamwise direction, and $2h$ high from the bottom to the mean wave height in the vertical direction. A different non-dimensionalization from that of chapter 2 is used here. All the variables are non-dimensionalized using a velocity scale, U, the half height, h, and the time scale h/U:

$$(x_1, x_3, \eta_s, \eta^1, \eta^3) = (\frac{{x_1}^d}{h}, \frac{{x_3}^d}{h}, \frac{{\eta_s}^d}{h}, \frac{{\eta^1}^d}{h}, \frac{{\eta^3}^d}{h}) \tag{4.1}$$

$$(u_1, u_3, C_w) = (\frac{{u_1}^d}{U}, \frac{{u_3}^d}{U}, \frac{C_w^d}{U}) \tag{4.2}$$

$$(\kappa_x, \mu) = ({\kappa_x}^d h, \mu^d h) \tag{4.3}$$

$$P = \frac{P^d}{\rho^d U^2} \tag{4.4}$$

$$\psi = \frac{\psi^d}{Uh} \tag{4.5}$$

$$Fr = \frac{U}{\sqrt{gh}} \tag{4.6}$$

where the superscript d denotes a dimensional quality; x_1 and x_3 denote the streamwise and vertical directions, respectively; u_1 and u_3 are the corresponding velocity components in the moving system; η_s, κ_x and μ are variables associated with the shape of the Stokes wave, as defined in Equations 2.9 and 2.10; $C_w^d = \frac{\sigma}{\kappa_x}$ is the phase speed of the wave; η^1 and η^3 are the coordinates in the transformed domain, respectively; P is the pressure, including the hydrostatic part; ρ^d is the density of the fluid; g is the gravity; ψ is the stream function in the moving system; and, finally, Fr is the Froude number.

The inviscid flow is governed by the Euler equations:

$$u_1 = \frac{\partial \psi}{\partial x_3} \tag{4.7}$$

$$u_3 = -\frac{\partial \psi}{\partial x_1} \tag{4.8}$$

$$\frac{\partial^2 \psi}{\partial {x_1}^2} + \frac{\partial^2 \psi}{\partial {x_3}^2} = 0 \tag{4.9}$$

$$u_1 \frac{\partial u_1}{\partial x_1} + u_3 \frac{\partial u_1}{\partial x_3} = -\frac{\partial P}{\partial x_1} \tag{4.10}$$

$$u_1 \frac{\partial u_3}{\partial x_1} + u_3 \frac{\partial u_3}{\partial x_3} = -\frac{\partial P}{\partial x_3} - \frac{1}{Fr^2} \tag{4.11}$$

where

$$0 \le x_1 \le \frac{2\pi}{\kappa_x}, \quad -1 \le x_3 \le 1 + \eta_s \tag{4.12}$$

The boundary conditions for the above equations are impermeability at the bottom surface and the dynamic boundary conditions at the top surface. The kinematic boundary condition is equation 2.15. The dynamic boundary conditions are given in

equation 2.16 to equation 2.18, which are, for inviscid flow, simplified to:

$$P = P_{air} \tag{4.13}$$

For convenience, we set P_{air} to zero and rewrite the kinematic boundary condition in terms of the stream function, the boundary conditions become:

$$\frac{\partial \psi}{\partial x_1} = 0 \qquad \text{on} \quad x_3 = -1 \tag{4.14}$$

$$-\frac{\partial \psi}{\partial x_1} = \frac{\partial \psi}{\partial x_3}\frac{\partial \eta_s}{\partial x_1} \qquad \text{on} \quad x_3 = 1 + \eta_s \tag{4.15}$$

$$P = 0 \qquad \text{on} \quad x_3 = 1 + \eta_s \tag{4.16}$$

$$\phi(x_1, x_3) = \phi(x_1 + \frac{2\pi}{\kappa_x}, x_3) \tag{4.17}$$

where ϕ denotes any variable from the set $\{u_1, u_3, P, \psi\}$.

The orthogonal transformation of chapter 3 is used. It is represented by equations 3.1 and 3.3. With this transformation, the left boundary of the original domain is mapped into $\eta^1 = 0$, the right boundary is transformed into $\eta^1 = \frac{2\pi}{\kappa_x}$, The top surface becomes $\eta^3 = 1$, and the bottom surface is mapped into $\eta^3 = -1 + \epsilon^2 \frac{\coth(2\kappa_x)}{2\kappa_x}$. Notice that the mean domain depth in the transformed domain has decreased by $\epsilon^2 \frac{\coth(2\kappa_x)}{2\kappa_x}$. As will be shown in section 4.2.6, this is due to the Stokes drift over the depth of the flow.

Using the chain rule for derivatives, the relation between $\frac{\partial \eta^m}{\partial x_i}$ and $\frac{\partial x_i}{\partial \eta^m}$ can be derived as:

$$\frac{\partial \eta^1}{\partial x_1} = \frac{\partial \eta^3}{\partial x_3} = J\frac{\partial x_1}{\partial \eta^1} \tag{4.18}$$

$$\frac{\partial \eta^1}{\partial x_3} = -\frac{\partial \eta^3}{\partial x_1} = J\frac{\partial x_3}{\partial \eta^1} \tag{4.19}$$

and the derivatives in the Cartesian system become:

$$\frac{\partial}{\partial x_1} = J\frac{\partial x_1}{\partial \eta^1}\frac{\partial}{\partial \eta^1} - J\frac{\partial x_3}{\partial \eta^1}\frac{\partial}{\partial \eta^3} \tag{4.20}$$

$$\frac{\partial}{\partial x_3} = J\frac{\partial x_3}{\partial \eta^1}\frac{\partial}{\partial \eta^1} + J\frac{\partial x_1}{\partial \eta^1}\frac{\partial}{\partial \eta^3} \tag{4.21}$$

$$\frac{\partial^2}{\partial {x_1}^2} + \frac{\partial^2}{\partial {x_3}^2} = J(\frac{\partial^2}{\partial {\eta^1}^2} + \frac{\partial^2}{\partial {\eta^3}^2}) \tag{4.22}$$

where J is the Jacobian, defined as:

$$J = \frac{1}{(\frac{\partial x_1}{\partial \eta^1})^2 + (\frac{\partial x_3}{\partial \eta^1})^2} \tag{4.23}$$

Two handy metric terms that will be used extensively later are defined as:

$$A = J\frac{\partial x_1}{\partial \eta^1}, \qquad B = J\frac{\partial x_3}{\partial \eta^1} \tag{4.24}$$

A perturbation method is used to obtain analytical solutions. The dependent variables and the metric terms are expanded to the powers of the wave slope:

$$\phi = \phi_0 + \epsilon\phi_1 + \epsilon^2\phi_2 + \mathcal{O}\left(\epsilon^3\right) \tag{4.25}$$

where ϕ denotes any variable from the set $\{\psi, u_1, u_3, P, C_w, A, B\}$.

From the definitions of A and B, their coeffcients can be derived as:

$$A_0 = 1 \tag{4.26}$$

$$A_1 = -\frac{\cos(\kappa_x\eta^1)\cosh[\kappa_x(1+\eta^3)]}{\sinh(2\kappa_x)} \tag{4.27}$$

$$A_2 = -\frac{2\mu}{\kappa_x}\frac{\cos(2\kappa_x\eta^1)\cosh[2\kappa_x(1+\eta^3)]}{\sinh(4\kappa_x)} + \frac{1}{2\sinh^2(2\kappa_x)} \tag{4.28}$$

$$B_0 = 0 \tag{4.29}$$

$$B_1 = -\frac{\sin(\kappa_x\eta^1)\sinh[\kappa_x(1+\eta^3)]}{\sinh(2\kappa_x)} \tag{4.30}$$

$$B_2 = -\frac{2\mu}{\kappa_x}\frac{\sin(2\kappa_x\eta^1)\sinh[2\kappa_x(1+\eta^3)]}{\sinh(4\kappa_x)} \tag{4.31}$$

4.2.2 Velocity Field

As seen from equation 4.22, the Laplacian operator is preserved by the orthogonal transformation. Therefore, equation ?? becomes:

$$\frac{\partial^2\psi}{\partial\eta^{1^2}} + \frac{\partial^2\psi}{\partial\eta^{3^2}} = 0 \tag{4.32}$$

Furthermore, the orthogonal transformation leads to a simple solution for the stream function of the flow:

$$\psi = -C_w\eta^3 \tag{4.33}$$

Obviously, this solution satisfies the Laplace equation 4.32. It must also satisfy, to second order, the boundary conditions in equations 4.14, 4.15, and 4.17. In the transformed coordinate system, these boundary conditions become:

$$C_w J\frac{\partial x_3}{\partial\eta^1} = 0 \qquad \text{on} \quad \eta^3 = -1 + \epsilon^2\frac{\coth(2\kappa_x)}{2\kappa_x} \tag{4.34}$$

$$-C_w J\frac{\partial x_3}{\partial\eta^1} = -C_w J\frac{\partial x_1}{\partial\eta^1}\frac{\partial\eta_s}{\partial x_1} \qquad \text{on} \quad \eta^3 = 1 \tag{4.35}$$

$$\phi(\eta^1,\eta^3) = \phi(\eta^1 + \frac{2\pi}{\kappa_x},\eta^3) \tag{4.36}$$

Since the left hand side of equation 4.34 is C_wB, and from equations 4.29 and 4.30, we know that $B_0 \equiv 0$ and that $B_1 = 0$, to second order, at $\eta^3 = -1 + \epsilon^2\frac{\coth(2\kappa_x)}{2\kappa_x}$. Thus, equation 4.34 is satisfied to second order.

With the arguments given in chapter 2 (equations 2.51 and 2.52), we obtain

$$\frac{\partial\eta_s}{\partial x_1} = -\frac{\partial\eta^3}{\partial x_1}\Big/\frac{\partial\eta^3}{\partial x_3} \tag{4.37}$$

Substituting this equation into equation 4.35 and using equations 4.20 and 4.21, we find that equation 4.35 is satisfied.

Since η^3 is periodic, the stream function satisfies Equation 4.36. Therefore, the simple function in Equation 4.33 is the solution for the inviscid flow to second order accuracy in the wave slope.

Notice that if the coefficient of η^3 is changed, the resulting function would also satisfy both the Laplace equation and the boundary conditions. However, with a propagating surface whose displacement is of first order, one should expect the velocity to also be of first order in magnitude. The zeroth order velocity should be zero when observed in a fixed system. In the moving system used here, the zeroth order streamwise velocity must be C_{w0}. Thus, the coefficient of the stream function must be C_w.

The stream function demonstrates that the lines of constant η^3 are inviscid streamlines. This property of our orthogonal transformation makes it much easier to interpret numerical results in the mapped coordinates.

With this stream function, the velocity field can be obtained as follows:

$$u_1 = -C_w A, \quad u_3 = -C_w B \tag{4.38}$$

It will be shown in section 4.2.5 that C_{w1} is zero. Therefore, using equations 4.26 to 4.31, the velocity field is:

$$u_{10} = -C_{w0} \tag{4.39}$$

$$u_{11} = C_{w0}\frac{\cos(\kappa_x\eta^1)\cosh[\kappa_x(1+\eta^3)]}{\sinh(2\kappa_x)} \tag{4.40}$$

$$u_{12} = C_{w0}\frac{2\mu}{\kappa_x}\frac{\cos(2\kappa_x\eta^1)\cosh[2\kappa_x(1+\eta^3)]}{\sinh(4\kappa_x)} - C_{w0}\frac{1}{2\sinh^2(2\kappa_x)} \tag{4.41}$$

$$u_{30} = 0 \tag{4.42}$$

$$u_{31} = C_{w0}\frac{\sin(\kappa_x\eta^1)\sinh[\kappa_x(1+\eta^3)]}{\sinh(2\kappa_x)} \tag{4.43}$$

$$u_{32} = C_{w0}\frac{2\mu}{\kappa_x}\frac{\sin(2\kappa_x\eta^1)\sinh[2\kappa_x(1+\eta^3)]}{\sinh(4\kappa_x)} \tag{4.44}$$

4.2.3 Zeroth Order Pressure Field

Substituting equations 4.20, 4.21 and 4.38 into the momentum equations results in the governing equations for the pressure field:

$$C^2(A^2+B^2)\frac{\partial A}{\partial \eta^1} = -A\frac{\partial P}{\partial \eta^1} + B\frac{\partial P}{\partial \eta^3} \tag{4.45}$$

$$C^2(A^2+B^2)\frac{\partial B}{\partial \eta^1} = -B\frac{\partial P}{\partial \eta^1} - A\frac{\partial P}{\partial \eta^3} - \frac{1}{Fr^2} \tag{4.46}$$

The boundary conditions are:

$$P = 0 \quad \text{on} \quad \eta^3 = 1 \tag{4.47}$$

and periodic boundary conditions in the η^1 direction.

The pressure field can be calculated by expanding the above equations and boundary conditions into powers of the wave slope, as was done for the other quantities earlier.

The zeroth order equations for the pressure are:

$$\frac{\partial P_0}{\partial \eta^1} = 0 \tag{4.48}$$

$$\frac{\partial P_0}{\partial \eta^3} = -\frac{1}{Fr^2} \tag{4.49}$$

To satisfy the boundary condition $P_0 = 0$ at $\eta^3 = 1$, the zeroth order pressure must be:

$$P_0 = \frac{1}{Fr^2}(1-\eta^3) \tag{4.50}$$

which represents the hydrostatic pressure.

4.2.4 First Order Pressure Field

The first order momentum equations are:

$$\frac{\partial P_1}{\partial \eta^1} = -{C_{w0}}^2\frac{\partial A_1}{\partial \eta^1} - \frac{B_1}{Fr^2} \tag{4.51}$$

$$\frac{\partial P_1}{\partial \eta^3} = -{C_{w0}}^2\frac{\partial B_1}{\partial \eta^1} + \frac{A_1}{Fr^2} \tag{4.52}$$

Solving these equations gives:

$$P_1 = \{C_{w0}{}^2\cosh[\kappa_x(1+\eta^3)] - \frac{1}{Fr^2\kappa_x}\sinh[\kappa_x(1+\eta^3)]\}\frac{\cos(\kappa_x\eta^1)}{\sinh(2\kappa_x)} + D \qquad (4.53)$$

where D is a constant.

For P_1 to be zero at $\eta^3 = 1$, D must be zero and

$$C_{w0}{}^2 = \frac{1}{Fr^2\kappa_x}\tanh(2\kappa_x) \qquad (4.54)$$

This is the dispersion relation that specifies the wave speed to zeroth order.

4.2.5 Second Order Pressure Field

The equations for the second order pressure are obtained in a similar way:

$$\frac{\partial P_2}{\partial \eta^1} = -C_{w0}{}^2(\frac{\partial A_2}{\partial \eta^1} + A_1\frac{\partial A_1}{\partial \eta^1} + B_1\frac{\partial B_1}{\partial \eta^1}) + \frac{2A_1B_1 - B_2}{Fr^2} - 2C_{w1}\frac{\partial A_1}{\partial \eta^1} \qquad (4.55)$$

$$\frac{\partial P_2}{\partial \eta^3} = -C_{w0}{}^2(\frac{\partial B_2}{\partial \eta^1} + A_1\frac{\partial B_1}{\partial \eta^1} - B_1\frac{\partial A_1}{\partial \eta^1}) + \frac{B_1{}^2 - A_1{}^2 + A_2}{Fr^2} - 2C_{w1}\frac{\partial B_1}{\partial \eta^1} \qquad (4.56)$$

The solution to this system is:

$$\begin{aligned} P_2 = {} & C_{w0}{}^2\left\{\frac{2\mu}{\kappa_x}\frac{\cosh[2\kappa_x(1+\eta^3)]}{\sinh(4\kappa_x)} - \frac{1}{4\sinh^2(2\kappa_x)}\right\}\cos(2\kappa_x\eta^1) - \\ & \frac{1}{2Fr^2\kappa_x}\left\{\frac{2\mu}{\kappa_x}\frac{\sinh[2\kappa_x(1+\eta^3)]}{\sinh(4\kappa_x)} + \frac{\sinh[2\kappa_x(1+\eta^3)]}{2\sinh^2(2\kappa_x)}\right\}\cos(2\kappa_x\eta^1) - \\ & C_{w0}{}^2\frac{\cosh[2\kappa_x(1+\eta^3)]}{4\sinh^2(2\kappa_x)} - C_{w0}{}^2\frac{1}{2\sinh^2(2\kappa_x)} + \\ & 2C_{w1}\frac{\cosh[\kappa_x(1+\eta^3)]}{\sinh(2\kappa_x)}\cos(\kappa_x\eta^1) + E \end{aligned} \qquad (4.57)$$

where E is a constant.

The only way for the pressure to be zero to second order at the top surface is that the following conditions be satisfied:

$$C_{w0}{}^2 = \frac{1}{Fr^2\kappa_x}\tanh(2\kappa_x) \qquad (4.58)$$

$$C_{w1} = 0 \tag{4.59}$$

$$E = {C_{w0}}^2 \left\{ \frac{1}{2\sinh^2(2\kappa_x)} + \frac{\cosh(4\kappa_x)}{4\sinh^2(2\kappa_x)} \right\} \tag{4.60}$$

Notice that the dispersion relation for the second order flow field (equation 4.58) is the same as for the first order flow field (equation 4.54). The first order contribution to the phase speed of the propagating wave, C_{w1}, is zero. This agrees with results presented by Whitham (1974).

4.2.6 Discussion

Equation 4.41 indicates that there exists a second order Eulerian mean velocity in the transformed coordinates, with the average taken along first order inviscid stream lines. If the stream function is transformed to Cartesian coordinates, one obtains the following stream function:

$$\begin{aligned} \psi &= -C_w \eta^3 \\ &= -C_{w0} x_3 + C_{w0} \frac{\epsilon}{\kappa_x} \frac{\cos(\kappa_x x_1)\sinh[\kappa_x(1+x_3)]}{\sinh(2\kappa_x)} \\ &\quad + C_{w0}\epsilon^2 \left[\frac{\mu}{{\kappa_x}^2} - \frac{\coth(2\kappa_x)}{2\kappa_x} \right] \frac{\cos(2\kappa_x x_1)\sinh[2\kappa_x(1+x_3)]}{\sinh(4\kappa_x)} \end{aligned} \tag{4.61}$$

Thus the velocity field in the Cartesian system contains no Eulerian mean flow to second order. This is consistent with McDonald's (1994) solution.

Although the Eulerian mean flow is zero, there exists a second order Lagrangian mean flow, namely the Stokes drift, generated because the orbits of the fluid particles are not closed. Imagine a vertical line of fluid particles at time zero. After a wave period, it will be bent forward due to the Stokes drift, u_s, which Longuet-Higgins (1953) showed to be:

$$u_s = \epsilon^2 C_w \frac{\cosh[2\kappa_x(1+x_3)]}{2\sinh^2(2\kappa_x)} \tag{4.62}$$

Integrating equation 4.62 from the bottom surface $x_3 = -1$ to the mean wave height, $x_3 = 1$, we obtain the averaged Lagrangian volume flux (per unit length in

the spanwise direction) as $\epsilon^2 C_w \frac{\coth(2\kappa_x)}{2\kappa_x}$. This corresponds to the depth deficit in the orthogonal transformation that was mentioned in section 4.2.1. The explanation is as follows. We know that between two streamlines, $\psi = \psi_1$ and $\psi = \psi_2$, with $\psi = \psi_1$ at the top, the volume flux (per unit length in the spanwise direction) from left to the right is $\psi_1 - \psi_2$. In this case, the stream function is $\psi = -C_w \eta^3$ (equation 4.33). Since the bottom surface is represented by $\eta^3 = -1 + \epsilon^2 \frac{\coth(2\kappa_x)}{2\kappa_x}$ and the top surface by $\eta^3 = 1$, the volume flux is $-C_w(2 - \epsilon^2 \frac{\coth(2\kappa_x)}{2\kappa_x})$. The term $-2C_w$ is due to the moving coordinate. So the net flux is $\epsilon^2 C_w \frac{\coth(2\kappa_x)}{2\kappa_x}$ and is induced by Stokes drift.

From Equation 4.57, a second order depth-varying average pressure (averaged over a wave length in the wave propagation direction) appears in the transformed system. This term cannot be canceled by inverting the transformation to write the zeroth and the first order pressure fields in the Cartesian coordinate system. Therefore, in the Cartesian system, there also exists a second order depth-varying average pressure:

$$P_{avg} = \epsilon^2 {C_{w0}}^2 \frac{\cosh[2\kappa_x(1 + x_3)]}{4\sinh^2(2\kappa_x)} \tag{4.63}$$

This agrees with the results given by Phillips (1977).

4.3 Numerical Simulations of Viscous Flows

4.3.1 Simulation Setup

Geometry

The simulation domain for the two dimensional wavy case is the same as for the two dimensional inviscid case as is shown in Figure 4.1. It is one wavelength long in the streamwise direction. The height of the domain is $2h$.

Governing Equations and Boundary Conditions

The flow is driven by the rigid wave propagating at the top. The surface wave provides no tangential stress, but requires a contribution from the normal stress to maintain the wave shape. The governing equations and boundary conditions are similar to

Name	ϵ	κ_x	Re_s
Set1	0.05	3.0	0.075, 0.15, 0.3, 0.6, 1.2, 2.4
Set2	0.1	3.0	0.075, 0.15, 0.3, 0.6, 1.2, 2.4
Set3	0.2	3.0	0.075, 0.15, 0.3, 0.6, 1.2, 2.4
Set4	0.1	1.5	0.075, 0.15, 0.3, 0.6, 1.2, 2.4
Set5	0.1	2.25	0.075, 0.15, 0.3, 0.6, 1.2, 2.4

Table 4.1: Cases studied for two dimension flows with a free wavy surface.

those for the three dimensional wavy cases presented in chapter 2. The same non-dimensionalizations are used, with equations 2.11 and 2.12 as the governing equations, equation 2.13 as the bottom boundary conditions, equations 2.15 and 2.19 as the top boundary conditions, where $Re_* = 0$, and periodic boundary conditions are used in the streamwise (x_1) direction. The only difference is that the flow studied here is two dimensional in the (x_1, x_3) plane and $u_2 = 0$.

Case Definitions

The state of the flow is dependent on three parameters: the Reynolds number, Re_s, the wavelength of the surface wave, κ_x, and the slope of the surface wave, ϵ. Table 4.1 lists the cases simulated for studying the effects of these three parameters.

The existance of the molecular viscosity gives rise to an oscillatory boundary layer under the wavy surface. The thickness of the boundary layer is $\delta_w^d = \sqrt{2\nu/(C_w^d \kappa_x{}^d)}$, as shown by Phillips (1977). There also exists a boundary layer near the bottom surface with similar thickness. In deep water waves, as in the cases treated in this study, the bottom boundary layer is not very important.

64×64 grids are used in all these cases. Uniform grids are used in the streamwise direction. The grids are vertically stretched using equation 3.7, with $\alpha = 0.98$. This achieves a minimum grid size of approximately $0.0015h$, allowing 5 points inside the thinnest boundary layer, which occurs in the case with $\epsilon = 0.05, \kappa_x = 3.0$, and $Re_s = 2.4$.

The initial field for the simulations is a uniform flow with velocity equal to the negative phase speed of the surface wave. Each case was run for $3 \sim 4$ characteristic

time scales, defined as $t^d = (2h)^2/\nu$, by which time the flow reaches a steady state. This is achieved by monitoring the change on the total mean current induced by the flow (see section 4.3.4) to be less than 1% over a period of t^d.

4.3.2 Vorticity Field

The spanwise vorticity contours for the case with $\epsilon = 0.1, \kappa_x = 1.5, Re_s = 0.075$ are plotted in Figure 4.2. The top boundary layer can be clearly identified; in it, the vorticity is oscillatory and of first order. This vorticity occupies a thickness of $0.5h$, which is comparable with the characteristic boundary layer thickness, $\delta^d \sim 0.3h$. Below the top boundary layer, the vorticity is distributed more uniformly and of second order in magnitude. A weak bottom boundary layer with slightly higher vorticity can also be observed.

Phillips (1977) showed that the vorticity to the first order at the wavy surface is:

$$\omega_2^d = -2\epsilon C_w^d {\kappa_x}^d \cos(\kappa^d \eta^{1^d}) \tag{4.64}$$

Figure 4.3 compares this profile with that from the numerical simulation for the case with $\epsilon = 0.1, \kappa_x = 1.5, Re_s = 0.075$. The numerical results in fair agreement with the linearized theory. However, the linearized theory gives a maximum at the wave trough while the numerical results have a local minimum there and two local maxima nearby. This shows the influence of higher order terms, as expected, because the numerical results include components of all orders, while the linearized theory only gives the first order approximation to the vorticity.

4.3.3 Velocity Field

Figure 4.4 shows the velocity vectors for the case with $\epsilon = 0.1, \kappa_x = 1.5, Re_s = 0.075$. These vectors are observed in the fixed coordinate system. From the velocity near the top surface, the forward surface (with negative wave slope) is moving upwards and the backward surface (with positive wave slope) is moving downward, illustrating the propagation of the wave from the left to the right. The vertical velocity decreases monotonically from the top surface to the bottom surface as in the inviscid solution

(section 4.2.2). Also like the inviscid flow, the fluid moves forward at the crest and backward at the trough of the surface wave. However, the maximum negative velocity is much smaller than that of the positive velocity in the viscous case, while in the inviscid flow, the maximum magnitudes are equal. The streamwise velocity is largest in the top boundary layer.

This increased streamwise velocity is evident in Figure 4.5, which gives the streamwise velocity profile of the inviscid and viscous solutions. The profile is given on the line of constant η^3 closest to $x = L_x/4$. The figure shows an increase of streamwise velocity with vertical coordinate, with a jump of the slope beyond $z = 0.5h$. This is due to the high vorticity in the top boundary layer. Figure 4.5 also shows a large discrepancy between the viscous field and the inviscid solutions and reveals the existence of a net positive mean Eulerian current in the viscous case, as predicted by Longuet-Higgins (1953). Furthermore, the mean current is almost linear between the top and the bottom boundary layers as also suggested by Longuet-Higgins' analysis. Due to the positive Eulerian mean flow, the magnitudes of the positive and negative streamwise velocity are unequal, as noted above.

The vertical velocity in the viscous and inviscid cases are presented in Figure 4.6. It can be seen that, unlike the streamwise velocity, the vertical velocity distribution in viscous case does not deviate much from the inviscid solution.

4.3.4 Computation of Wave Drift

In this section, we will describe the method of calculating the drift velocity of a fluid particle in the wavy flow. In other parts of this thesis, Eulerian description is used. But if particle motion is of interest, the Lagrangian description is more appropriate.

We calculate the drift velocity in the fixed Cartesian coordinate system. Three coordinate systems are used: the fixed Cartesian coordinate system, (X_1, X_3), in which the surface wave is propagating, the moving Cartesian system, (x_1, x_3), in which the surface wave is stationary, and the transformed curvilinear coordinate system, (ξ^1, ξ^3), in which the computation is done. The relation between the fixed and moving

Cartesian system is:

$$x_1 = X_1 - C_w t \tag{4.65}$$
$$x_3 = X_3 \tag{4.66}$$

Suppose that, at time t_0, a particle is located at (X_{10}, X_{30}), and at time t, the particle moves to (X_1, X_3). Then:

$$\frac{dX_1}{dt} = U_{1l}(X_{10}, X_{30}, t) \tag{4.67}$$
$$\frac{dX_3}{dt} = U_{3l}(X_{10}, X_{30}, t) \tag{4.68}$$

where (U_{1l}, U_{3l}) is the Lagrangian velocity of the particle. Since at time t, the particle is located at (X_1, X_3), the Lagrangian velocity is related to the Eulerian velocity (U_{1e}, U_{3e}), by the following equations:

$$U_{1l}(X_{10}, X_{30}, t) = U_{1e}(X_1, X_3, t) \tag{4.69}$$
$$U_{3l}(X_{10}, X_{30}, t) = U_{3e}(X_1, X_3, t) \tag{4.70}$$

In the moving systems, the Eulerian velocity becomes:

$$U_{1e}(X_1, X_3, t) = u_{1e}(x_1, x_3) + C_w \tag{4.71}$$
$$U_{3e}(X_1, X_3, t) = u_{3e}(x_1, x_3) \tag{4.72}$$

where (u_{1e}, u_{3e}) is the Eulerian velocity in the moving system, and (x_1, x_3) the corresponding location of (X_1, X_3) in the moving system according to equation 4.65 and 4.66. u_{1e} and u_{3e} are functions of (x_1, x_3) only since the flow reaches steady state in the moving coordinate system.

Let (ξ^1, ξ^3) be the mapped location of (x_1, x_3). Then (u_{1e}, u_{3e}) is essentially the velocity (u_1, u_3) obtained at (ξ^1, ξ^3) from the numerical simulation. Therefore,

$$\frac{dX_1}{dt} = u_1(\xi^1, \xi^3) + C_w \tag{4.73}$$

$$\frac{dX_3}{dt} = u_3(\xi^1, \xi^3) \tag{4.74}$$

where

$$\xi^1 = \xi^1(x_1, x_3) = \xi^1(X_1, X_3, t) \tag{4.75}$$

$$\xi^3 = \xi^3(x_1, x_3) = \xi^3(X_1, X_3, t) \tag{4.76}$$

Given the initial position of a particle, (X_{10}, X_{30}), the drift velocity of the particle is calculated by advancing equations 4.73 and 4.74 over one wave period using a second order Runge-Kutta method, and then dividing the displacement of the particle by the elapsed time.

The only problem left is to find the velocity $(u_1(\xi^1, \xi^3), u_3(\xi^1, \xi^3))$ of a particle located at (X_1, X_3) in the fixed coordinate system at time t. It is computed as follows:

1. Calculate the location in the moving system, (x_1, x_3), from equations 4.65 and 4.66. For some values of (X_1, X_2, t), x_1 might be out of the domain of $(0, L_x)$ in which the numerical solution is provided. Since periodic boundary condition is used in the streamwise direction, multiples of L_x can be added to x_1 to make it within the range.

2. Solve the coordinate transformation given in chapter 3 to find (ξ^1, ξ^3) numerically. A steepest descent method is used here. Due to numerical error, the location in the transformed coordinate system might be out of the range of $(0, ni-2)$ for ξ^1, and $(0, nk-2)$ for ξ^3. Approximation is then used: if ξ^1 is out of range, the closest boundary value (0 or $ni-2$) is used; if ξ^3 is out of range, call the results for that particle to be invalid. At the end of the procedure, only results for the valid particles are used to compute the drift velocity profile. For the drift velocity profile obtained in this thesis, the influence of this approximation is found to be small, since very few particles near the surface have ξ^3 out of range.

3. Interpolate the velocity (u_1, u_3) for the point (ξ^1, ξ^3) from the numerical field. A second order accurate scheme is used.

4.3.5 Stokes Drift

As mentioned in section 4.2.6, an inviscid irrotational wave generates a second order (in wave slope) drift, known as Stokes drift. To validate the drift computation described in section 4.3.4, the inviscid flow field is used as an input for the calculation. As shown in Figure 4.7, the inviscid propagating wave induces a net drift that decays exponentially with the depth. In Figure 4.7, the Lagrangian drift computed using the method in section 4.3.4 and the Stokes drift from equation 4.62 are compared. Remarkable agreement is found between the two profiles. The results confirm the correctness of both the drift computation method and the implementation of this method in the computer code.

4.3.6 Eulerian Mean Flow

We showed in sections 4.3.2 and 4.3.3, that the vorticity in the top boundary layer penetrates downward and introduces a mean current in the flow, *i. e.*, the Eulerian mean flow. In section 4.3.4 we discussed the method of calculating the drift of a fluid particle in a two dimensional wave field. We now will examine the Eulerian mean flow formed in two dimensional viscous flow under the wave conditions summarized in Table 4.1.

It is important to note that the drift computed with the method from section 4.3.4 is the total drift that contains both Stokes drift and the Eulerian mean flow. To obtain the Eulerian mean drift, the Stokes drift component must be subtracted from the total drift. For example, Figure 4.8 presents the total drift, the Stokes drift and the Eulerian mean flow for the case with $\epsilon = 0.1, \kappa_x = 1.5, Re_s = 0.075$. It demonstrates that the Eulerian mean flow is of the same order as the Stokes drift. It is also obvious that since the Stokes drift decays exponentially with the characteristic depth of $1/(2\kappa_x) = 0.3$, the Eulerian mean flow is very close to the total drift below this depth.

For an unbounded channel with a periodic wave propagating on the top, Longuet-Higgins (1953) first derived the leading order (in wave slope) component of the Eulerian mean flow in the limit of infinite Reynolds number. For deep water wave, it is a

linear function and is independent of Reynolds number:

$$u_e^{dLH} = 2\epsilon^2 C_w^d \kappa_x{}^d (x_3^d + h) \tag{4.77}$$

The Eulerian mean flow from the simulation is dependent on the Reynolds number and includes the components of all orders. We calculated the gradient of our Eulerian mean flow via a linear curve-fit to the drift below the wave boundary layer and the characteristic depth of $1/(2\kappa_x)$, whichever is bigger. If we normalize this gradient with the slope of the Eulerian mean flow predicted by Longuet-Higgins, equation 4.77, the result, u_e/u_e^{LH}, should be close to but not equal to unity, and should be a function of ϵ, κ_x, and Re_s. This is clearly true as shown by Figures 4.9 and 4.10, which present the normalized gradients for all the wave conditions studied.

As shown in both figures, for fixed wave slope and wave length, the normalized drift increases with Re_s. Figure 4.9 shows the effects of wave slope on the normalized Eulerian mean flow. A smaller wave slope produces an Eulerian mean flow closer to the second order analytical solution by Longuet-Higgins. With the same amount of differences in wave slope, the resulting discrepancies in the normalized drift are comparable. Thus, we can conclude that the third order Eulerian mean flow makes a major contribution to the discrepancy.

Figure 4.10 depicts the influence of wave number on u_e/u_e^{LH}. The three curves present cases with the same wave slope but different surface wave length. Since, for fixed wave slope and Reynolds number, the decrement in u_e/u_e^{LH} is proportional to that in the wave number, it is apparent that, to the first order at least, u_e/u_e^{LH} is a linear function of κ_x.

Based on the above observation, we propose the following simple approximation:

$$\frac{u_e}{u_e^{LH}} = 1 - C_1 \epsilon \kappa_x (Re_s)^{C_2} \tag{4.78}$$

Curve fitting gives $C_1 = 0.5, C_2 = -0.3$.

The fitted data are shown in Figure 4.11. The vertical axis value plotted is $\frac{u_e}{u_e^{LH}} + 0.5\epsilon\kappa_x(Re_s)^{-0.3}$. All the results are very close to unity, except for the case with the highest wave slope $\epsilon = 0.2$, which have the greatest influence of the fourth order

terms.

4.4 Summary

A second order accurate solution of the velocity field and the pressure field for the inviscid flow under a second order Stokes wave has been obtained. The dispersion relationship up to second order is derived from the flow field by imposing the dynamic boundary condition. The first order wave propagation speed is zero.

Using a coordinate system moving at the wave propagation speed and an orthogonal transformation greatly simplifies the results. Because no linearization of the boundary conditions is used, the flow field obtained in this study is valid throughout the whole domain under the wavy surface.

From the inviscid solution, no Eulerian mean flow exists to second order under the wave in laboratory coordinates. However, there is a second order Lagrangian mean flow, the Stokes drift. A second order depth-varying mean pressure is also found from the analytical solution.

The viscous flow under the same propagating wave as in the inviscid case is simulated numerically for deep water waves. The numerical results reveal an oscillating top boundary layer under the surface wave and a weaker boundary layer near the bottom. The vorticity inside the top boundary layer is of first order and agrees with Phillips' (1977) linearized results for spanwise vorticity along the top surface.

The velocity field shows that, unlike the inviscid flow, the magnitude of the streamwise positive velocity is greater than that of the negative velocity; this is caused by the net Eulerian mean flow. The Eulerian mean flow is of second order and has a linear profile, as suggested by Longuet-Higgins (1953).

Therefore, associated with the viscous wave field, there are two kinds of mean currents: the exponentially depth-decaying Lagrangian Stokes drift and the linear Eulerian mean flow. The Eulerian mean flow introduces an extra shear in the water column. Even though no tangential stress is exerted on the surface, a fluid element "feels" a tangential stress generated by the viscous wavy boundary layer above. This contribution to the wave-induced effects has not been included in the Craik-Leibovich

(1976) theory, and will be studied in the following chapters.

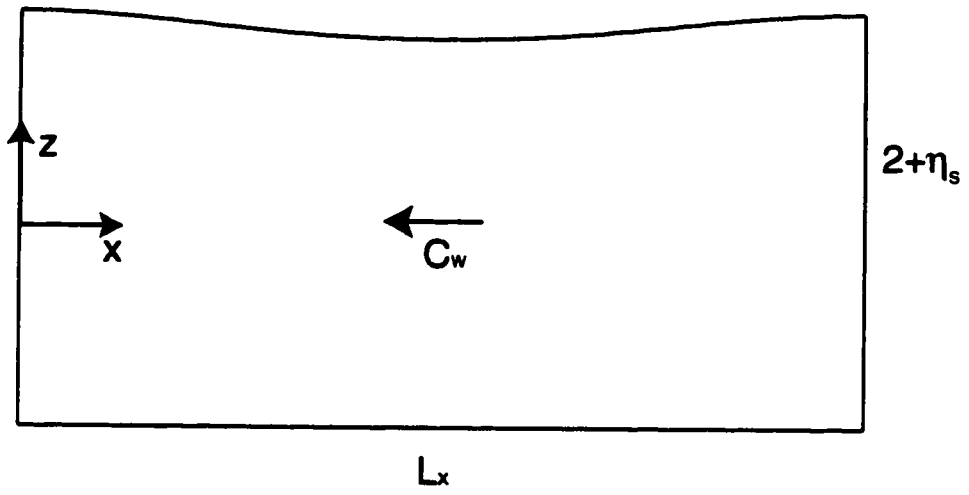

Figure 4.1: A sketch of the 2D wavy flow.

Figure 4.2: 2Dwavy free surface case, with $\epsilon = 0.1, \kappa_x = 1.5, Re_s = 0.075$. Spanwise vorticity contours. (normalized by S/h)

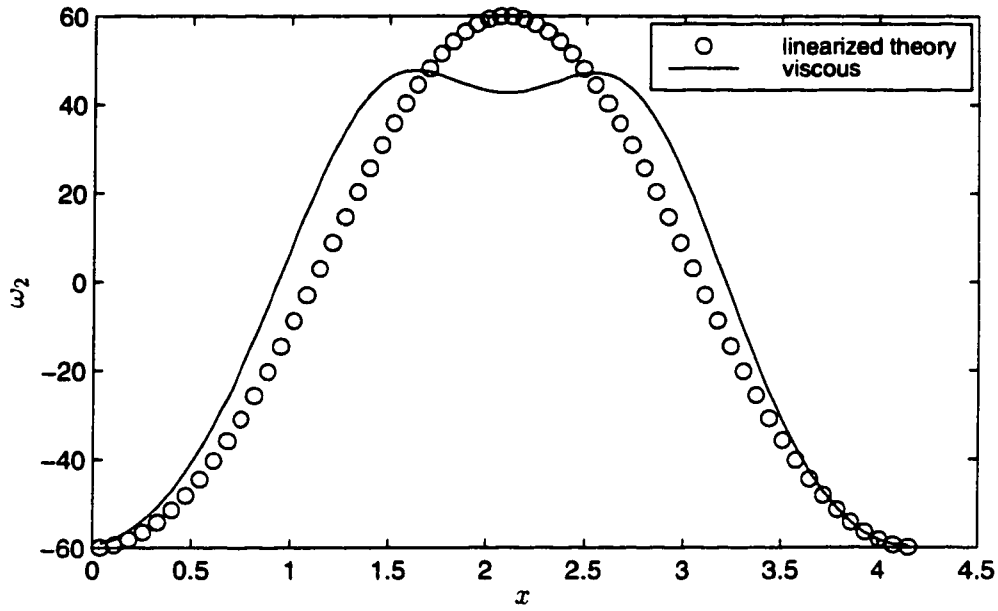

Figure 4.3: 2Dwavy free surface case, with $\epsilon = 0.1, \kappa_x = 1.5, Re_s = 0.075$. Spanwise vorticity profile at the top surface, compared with the linearized theory. (ω_2 normalized by S/h, x normalized by h)

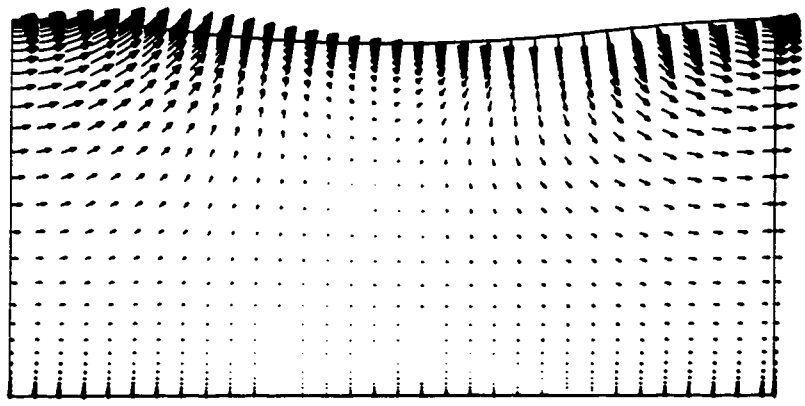

Figure 4.4: 2Dwavy free surface case, with $\epsilon = 0.1, \kappa_x = 1.5, Re_s = 0.075$. Velocity vectors.

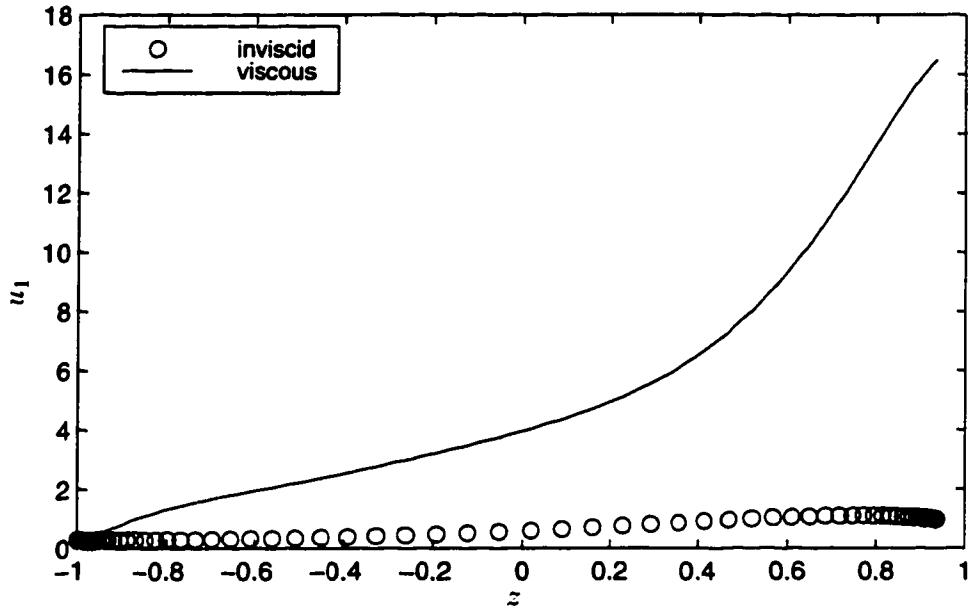

Figure 4.5: 2Dwavy free surface case, with $\epsilon = 0.1, \kappa_x = 1.5, Re_s = 0.075$. Streamwise velocity profile near $x = L_x/4$, compared with the inviscid case. (velocity normalized by S, z normalized by h)

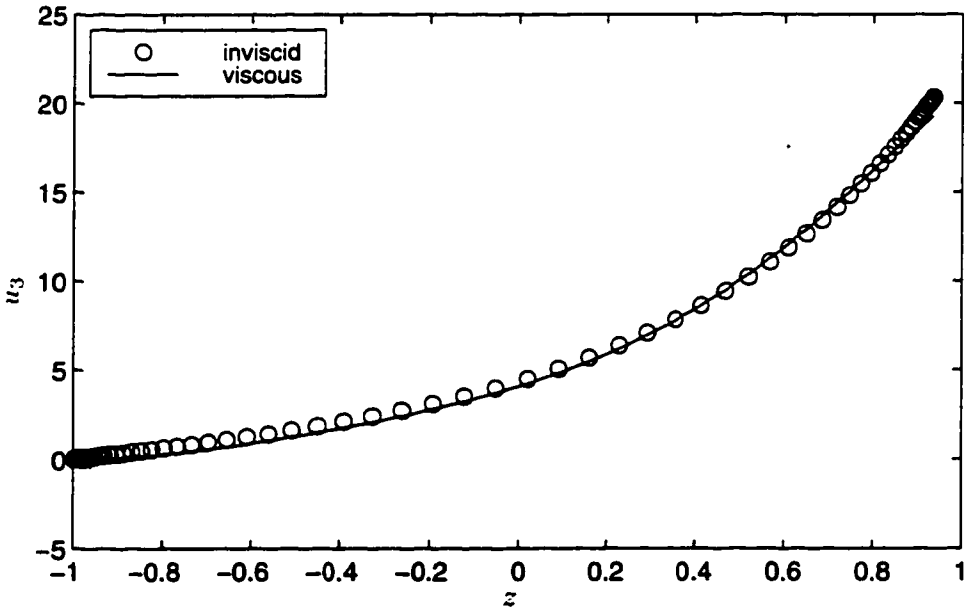

Figure 4.6: 2Dwavy free surface case, with $\epsilon = 0.1, \kappa_x = 1.5, Re_s = 0.075$. Vertical velocity profile near $x = L_x/4$, compared with the inviscid case. (velocity normalized by S, z normalized by h)

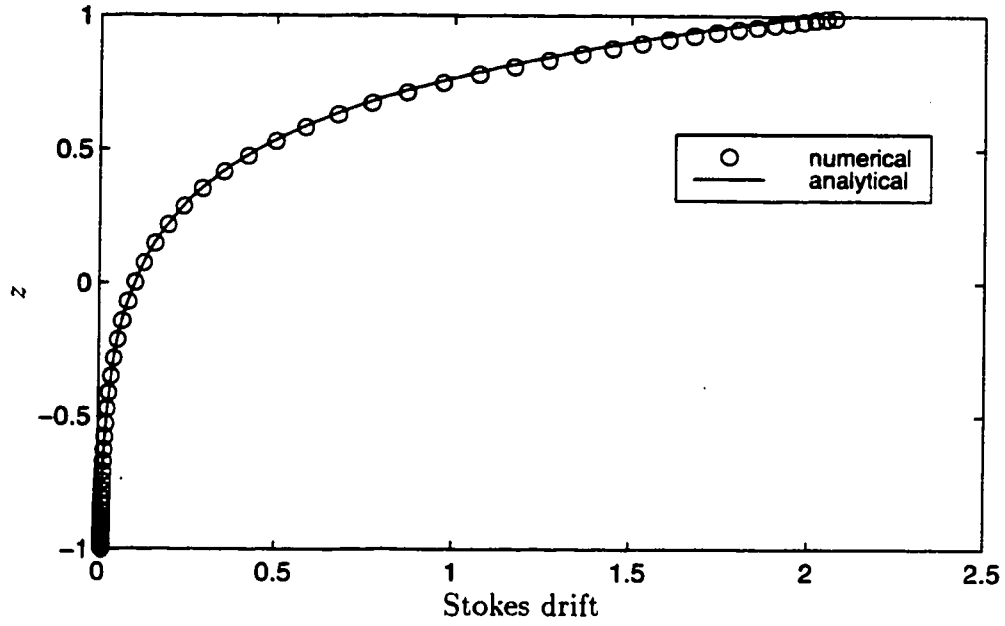

Figure 4.7: Comparison of the numerically computed Stokes drift from the inviscid field and the analytical Stokes drift. (drift normalized by S, z normalized by h)

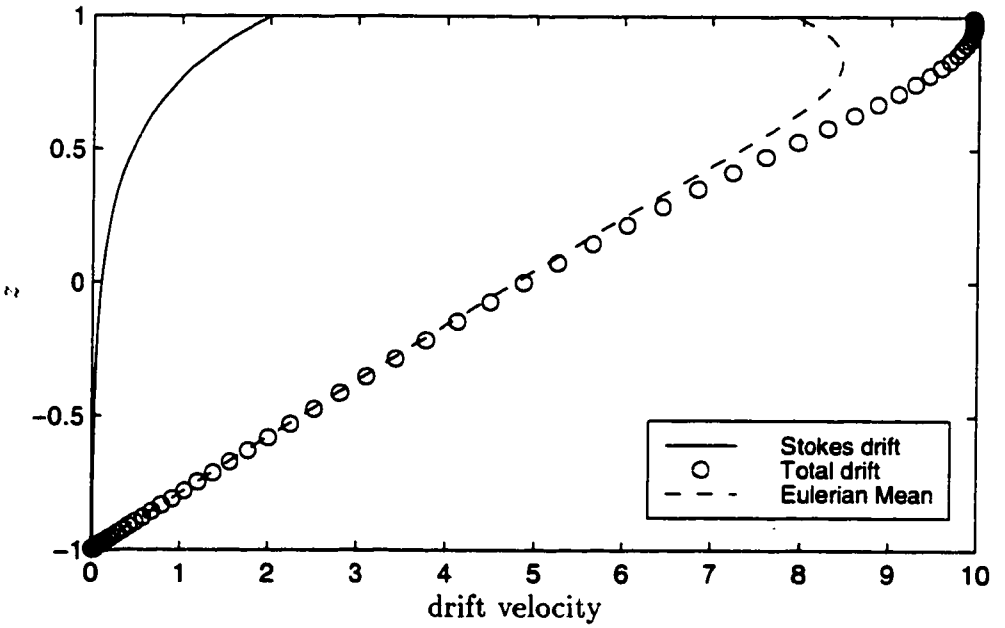

Figure 4.8: 2Dwavy free surface case, with $\epsilon = 0.1, \kappa_x = 1.5, Re_s = 0.075$. Drift velocities. (velocity normalized by S, z normalized by h)

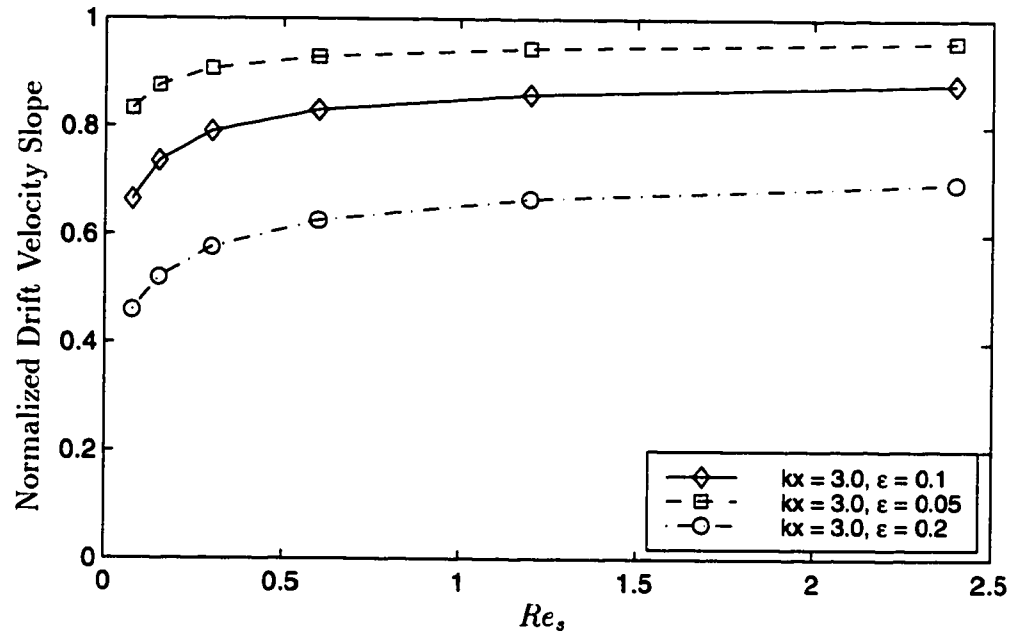

Figure 4.9: 2Dwavy free surface cases. Effects of the wave slope on the Eulerian mean flow.

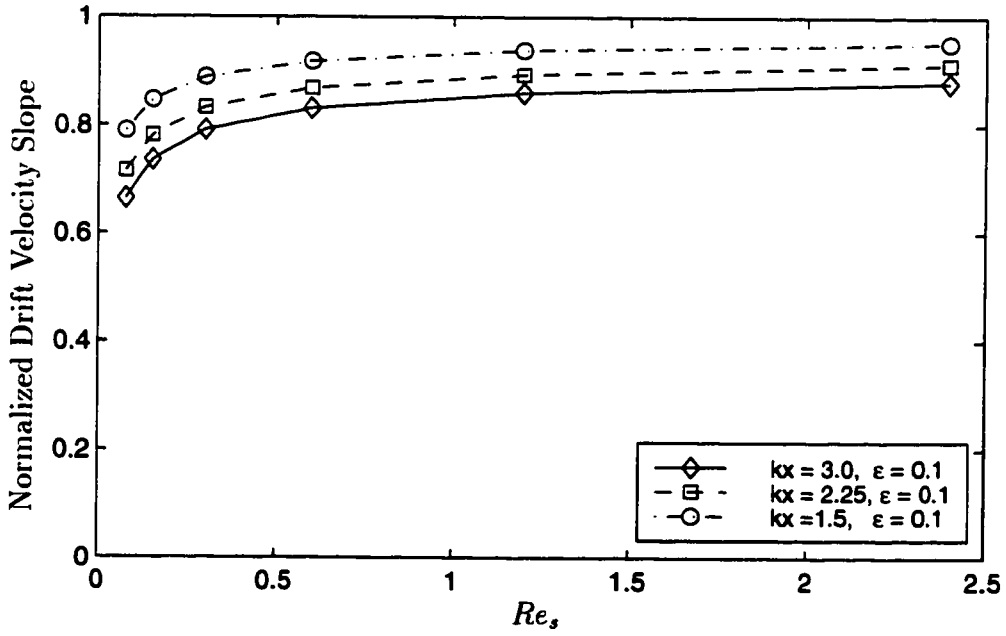

Figure 4.10: 2Dwavy free surface cases. Effects of the wave number on the Eulerian mean flow.

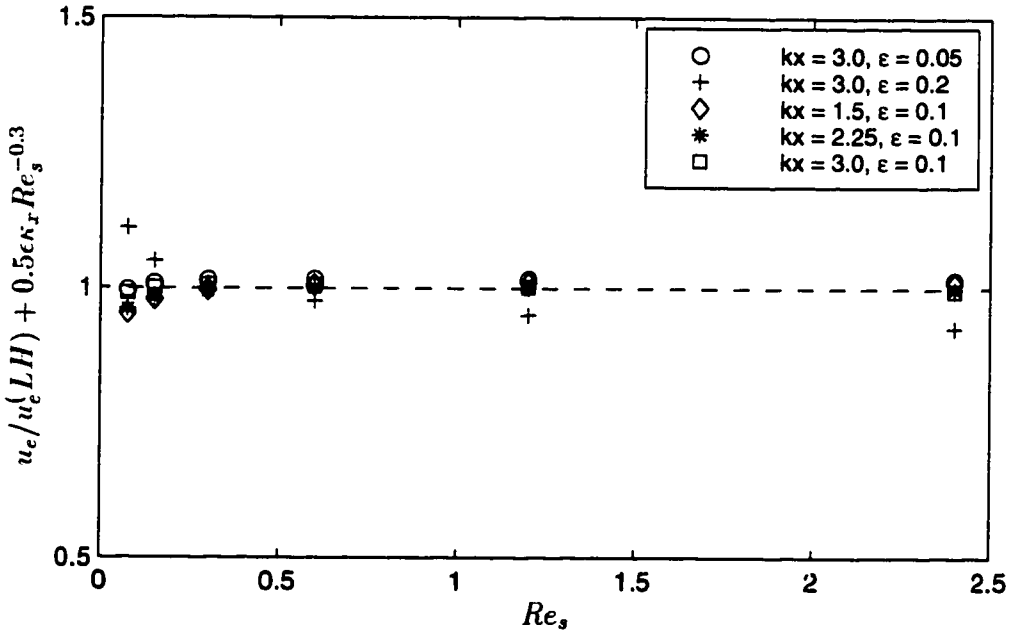

Figure 4.11: 2Dwavy free surface cases. Fitted data for the Eulerian mean flow.

Chapter 5

Simulations of Langmuir Circulations in Flows with Constant Eddy Viscosity

5.1 Introduction

In the last chapter two components of the wave field important to Langmuir circulation were studied: the wave-induced Stokes drift and Eulerian mean flow. This chapter examines the interactions between the surface wave and wind-driven current in a flow of constant eddy viscosity. In particular, the following issues are addressed: the structure and properties of Langmuir circulations, the cell merging process in Langmuir circulation evolution, the effects of the Eulerian mean flow, and the justification of the averaging used in the Craik-Leibovich theory.

Langmuir circulations with constant eddy viscosity have been studied numerically by other researchers (Leibovich and Paolucci 1980b, Li and Garrett 1993), who integrated the Craik-Leibovich equations in a spanwise-vertical plane. The effect of the wave induced viscous stress was not considered. The structure of the predicted Langmuir circulations is qualitatively close to field observations (Scott *et al.* 1969, Smith *et al.* 1987, Weller and Price 1988). Furthermore, both simulations predict a cell merging process that corresponds to the observed "Y junctions" (Thorpe 1992, Farmer and Li 1995) and an upscale energy cascade (Weller and Price 1988). It has been suggested by Faller and Auer (1988) that this process is analogous to the inverse energy cascade in two dimensional turbulence with the amalgamation of like-sign vortices. On the other hand, Li and Garrett (1993) claimed only cancellation of the opposite-signed vortices occurs.

This chapter presents results of a 2D simulation carried out by solving the Craik-Leibovich equations (2DCL) with vortex forcing similar to that used by Li and Garrett. However, in contrast to Li and Garrett, we find that the cell merging is more like the inverse energy cascade in two dimensional turbulences (Melander *et al.* 1988); very little opposite-signed vortex cancellation is observed.

There also exist some quantitative disagreements between the field observation and the simulations by Li and Garrett (1993) and Leibovich and Paolucci (1980b). Li and Garrett examined two aspects of the motion, the maximum downwelling velocity under the convergence line and the pitch, defined as the ratio of surface downwind jet velocity to the maximum downwelling velocity. Although the maximum downwelling velocity is within the range of the observations, the pitch they obtained, $0.37 \sim 0.49$, is smaller than the value observed by Weller and Price (1988), $1.33 \sim 8$. Leibovich and Paolucci (1980b) argued that their downwelling jet agrees well with observations (Scott *et al.* 1969). However, from their Figures 14 and 15, which correspond to the case with reasonable downwelling velocity, a pitch of 0.33 can be derived, which is in the same range as those obtained by Li and Garrett (1993). In this study, by including the effects of the wave stress due to the Eulerian mean flow, we obtain both a downwelling velocity and a pitch that are closer to observations.

As mentioned in chapter 1, in the Craik-Leibovich theory the Navier-Stokes equations are averaged over a time scale longer than both the longest wave period and the turbulence time scale (Leibovich 1977b). The assumption behind this averaging, that of disparate time scales, is hardly discussed. The results presented in this chapter address validity of this averaging for laminar flows using a 3D simulation of a flow under a propagating wave (3Dwavy). No averaging is used, *i. e.* the full Navier-Stokes equations are solved. The results are compared with those from the Craik-Leibovich theory, obtained via a 2DCL simulation. Good agreement is achieved if the Eulerian mean flow is included in the 2DCL case. The averaging is thus justified.

Section 5.2 presents the Craik-Leibovich equations and the boundary conditions used in the 2DCL simulations. Section 5.3 describes the initial conditions and the input parameters in both 2DCL and 3Dwavy cases. The numerical method for the 2DCL case is also briefly discussed. Section 5.4 validates the computer code by

comparing a 2DCL simulation of weak vortex forcing with linear stability analysis (Garg *et al.* 1992). The structure and properties of Langmuir circulations are also examined. In section 5.5, a 2DCL simulation with moderate vortex forcing is carried out and the characteristics of Langmuir circulation are further studied. The cell merging process is discussed and the effect of Eulerian mean flow effects is investigated. Section 5.6 presents the 3Dwavy simulation. The modulation of Langmuir circulation by the surface wave is demonstrated. Section 5.7 compares the Craik-Leibovich theory with the 3Dwavy results to verify the disparate time scale assumption. Finally, section 5.8 summarizes the results.

5.2 The Craik-Leibovich Equations and Boundary Conditions

5.2.1 The Craik-Leibovich Equations

We consider open channel flow with a two dimensional surface wave. Since the surface wave effects have already been abstracted by the Craik-Lebovich theory into the Stokes drift, the physical domain for the simulation based on Craik-Leibovich equations contains no surface wave. The domain is a rectangular box with the same length and width as the wavy channel, and depth equal to the mean channel height, $2h$. The wind driven current is modelled by applying a constant streamwise stress, $\rho^d u_*^{d2}$, on the flat top surface.

In this study, there is no stratification and the Coriolis force is neglected. Using the same notation as in chapter 2 (see equations 2.1 to 2.7) and non-dimensionalizing scales, (*i. e.* the characteristic Stokes drift velocity, S, as the velocity scale, and the half depth of the domain as the length scale) as in section 2.2, the non-dimensional Craik-Leibovich equations become:

$$\frac{\partial u_i}{\partial x_i} = 0 \tag{5.1}$$

$$\frac{\partial u_i}{\partial t} + \frac{\partial (u_i u_j)}{\partial x_j} = -\frac{\partial p}{\partial x_i} + \frac{1}{Re_s}\frac{\partial^2 u_i}{\partial x_j \partial x_j} + \varepsilon_{ijk} u_{sj} \omega_k \tag{5.2}$$

These equations closely resemble the Navier-Stokes equations 2.11 and 2.12, but an extra vortex force term, $\varepsilon_{ijk}u_{sj}\omega_k$, appears in the momentum equation, where ε_{ijk} is the permutation tensor; u_{si} is the x_i Stokes drift component; $\omega_i = \varepsilon_{ijk}\frac{\partial u_k}{\partial x_j}$ is the x_i vorticity component, where x_1, x_2, and x_3 lie in the streamwise, spanwise and vertical directions, respectively.

A monochromatic Stokes wave propagating in the streamwise direction is used as the surface wave. Therefore, the nondimensional Stokes drift takes the form:

$$(u_{s1}, u_{s2}, u_{s3}) = (u_s, 0, 0) \tag{5.3}$$

$$u_s = \epsilon^2 C_w \frac{\cosh[2\kappa_x(1+x_3)]}{2\sinh^2(2\kappa_x)} = \frac{\cosh[2\kappa_x(1+x_3)]}{\sinh^2(2\kappa_x)} \tag{5.4}$$

In this chapter, for those simulations based on the Craik-Leibovich equations, only two dimensional cases are considered. The flow is assumed to be x_1-independent, *i. e.* $\frac{\partial}{\partial x_1} = 0$. All the three velocity components are computed on a spanwise-vertical plane, whose extent is represented by:

$$0 \le x_2 \le L_y = \frac{2\pi}{\kappa_y}, \quad -1 \le x_3 \le 1 \tag{5.5}$$

With this simplification, the two dimensional Craik-Leibovich equations become:

$$\frac{\partial u_2}{\partial x_2} + \frac{\partial u_3}{\partial x_3} = 0 \tag{5.6}$$

$$\frac{\partial u_1}{\partial t} + \frac{\partial (u_2 u_1)}{\partial x_2} + \frac{\partial (u_3 u_1)}{\partial x_3} = \frac{1}{Re_s}\left(\frac{\partial^2 u_1}{\partial x_2 \partial x_2} + \frac{\partial^2 u_1}{\partial x_3 \partial x_3}\right) \tag{5.7}$$

$$\frac{\partial u_2}{\partial t} + \frac{\partial (u_2 u_2)}{\partial x_2} + \frac{\partial (u_3 u_2)}{\partial x_3} = -\frac{\partial p}{\partial x_2} + \frac{1}{Re_s}\left(\frac{\partial^2 u_2}{\partial x_2 \partial x_2} + \frac{\partial^2 u_2}{\partial x_3 \partial x_3}\right) + u_s \frac{\partial u_1}{\partial x_2} \tag{5.8}$$

$$\frac{\partial u_3}{\partial t} + \frac{\partial (u_2 u_3)}{\partial x_2} + \frac{\partial (u_3 u_3)}{\partial x_3} = -\frac{\partial p}{\partial x_3} + \frac{1}{Re_s}\left(\frac{\partial^2 u_3}{\partial x_2 \partial x_2} + \frac{\partial^2 u_3}{\partial x_3 \partial x_3}\right) + u_s \frac{\partial u_1}{\partial x_3} \tag{5.9}$$

5.2.2 Boundary Conditions

Periodic boundary conditions are used in the spanwise direction. At the bottom wall, a non-slip boundary condition is imposed. At the top surface, boundary conditions include non-permeability, constant streamwise stress and zero spanwise stress. The

boundary conditions can be written as:

$$u_1 = u_2 = u_3 = 0 \qquad \text{on} \quad x_3 = -1 \tag{5.10}$$

$$u_3 = \frac{\partial u_2}{\partial x_3} = 0 \qquad \text{on} \quad x_3 = 1 \tag{5.11}$$

$$\frac{\partial u_1}{\partial x_3} = \frac{Re_*^2}{Re_s} \qquad \text{on} \quad x_3 = 1 \tag{5.12}$$

$$\psi(0, x_3, t) = \psi(L_y, x_3, t) \tag{5.13}$$

where Re_* is the Reynolds number based on the friction velocity due to wind stress and the half depth of the channel. ψ is a general variable that denotes any velocity component, u_i, or the pressure, p.

5.3 Initial Conditions, Input Parameters and Numerical Methods

As was mentioned in section 5.1, this chapter contains both 2DCL and 3Dwavy simulations. For the 3Dwavy cases, the governing equations and boundary conditions have been presented in chapter 2, and the numerical method in chapter 3. For the 2DCL cases, the governing equations and boundary conditions were described in the last section. This section examines the initial conditions and input variables for both types of simulations, and the numerical method for the 2DCL cases.

5.3.1 Initial Conditions

The initial conditions consist of a mean flow and a perturbation field. In 2DCL cases, the initial mean flow is fully developed Couette flow which satisfies the no-slip condition at the bottom and the constant stress condition at the top. For the 3Dwavy simulation, the initial mean flow is a steady two dimensional wavy field from another simulation in a streamwise-vertical plane, with the same surface wave and top tangential stress, and periodic streamwise conditions.

Three dimensional random noise is added to initial mean field. The magnitude

of the perturbations is very small ($\mathcal{O}(10^{-4})$). For 2DCL cases with weak Craik-Leibovich forcing, eigenfunctions with small magnitude from linear stability analysis (Garg *et al.* 1992) can be used as the input. It has been found that neither the growth rate nor the final steady state depend on the form of the initial perturbations, but the flow with white noise perturbations has a longer transient stage. Furthermore, numerical tests show that even without any perturbation, the numerical error would destabilize the flow and produce Langmuir circulation. Here, only results with random initial perturbation are presented.

5.3.2 Input Parameters

The input parameters for the 3Dwavy case are the Reynolds number based on the friction velocity due to wind stress, Re_*, which represents the strength of the wind; the Reynolds number based on the Stokes drift velocity, Re_s, which indicates the sea state (see equation 2.7 for detailed definitions); the wavenumber of the surface wave, κ_x: the wavenumber of spanwise periodicity that determines the width of the domain, κ_y: and the wave slope, ϵ.

The 2DCL simulation, on the other hand, needs only $Re_*, Re_s, \kappa_x, \kappa_y$ as input. The wave slope, ϵ, does not show up in the governing equations (equations 5.6 to 5.9) or the boundary conditions (equations 5.10 to 5.13). It serves as a parameter for post-processing the results (output parameter), such as computing how many wave periods correspond to a given non-dimensional time.

5.3.3 Numerical Methods

The discretization method used for 3Dwavy cases was applied to the 2DCL cases, with the following modifications:

- The physical domain for the 2DCL cases is rectangular. Thus the transformation from the physical domain to the computational domain with unity grid spacing is from a Cartesian system to another Cartesian system, and the cross terms in the metric tensors reduce to zero.

- Since the governing equations for the 2DCL cases have a vortex term not in the Navier-Stokes equations, this source term is added in the first predictor step in the fractional step method 3.4.3.

- Because the 2DCL cases are x_1-independent, the last predictor step of the ADI method is omitted. Only the spanwise and vertical volume fluxes are needed. Furthermore, the pressure Poisson equation becomes two dimensional, and is solved using the 2D multigrid method.

5.4 2D Simulation with Weak Vortex Forcing

In this section we focus on a 2DCL simulation with weak vortex forcing that is just above the critical condition from linear stability theory (Garg *et al.* 1992). This simulation not only enables us to study the formation and basic characteristics of Langmuir circulation, but also allows us to further validate our computer code by comparing the numerical results with linear stability analysis.

5.4.1 Linear Stability Theory

Garg *et al.* (1992) performed a linear stability analysis for the 2DCL problem presented in section 5.2. Their approach was similar to that used by Leibovich *et al.* (1989), in which normal mode solution to the linearized equations was introduced:

$$\psi = \Psi(x_3)e^{i\varpi t + i\kappa_y x_2} \tag{5.14}$$

where ψ is a general function that can be either the the streamwise perturbation velocity or streamfunction of the spanwise vertical motion. Ψ is its amplitude, $\varpi = \varpi_r + i\varpi_i$ is a complex frequency and κ_y represents the wavenumber of the Langmuir circulation. A sixth order eigenvalue problem in ϖ was formed and solved numerically using a collocation technique based on Chebyshev polynomials. The computer code by Garg *et al.* takes the following inputs: the profiles of the initial wind driven current and the Stokes drift, which could be arbitrary depth-varying functions, κ_y, and a

Rayleigh number, $R = \sqrt{Re_s Re_*^2}$. It calculates the eigenvalue, ϖ, which contains the growth rate, $|\varpi_i|$.

Definition of the Langmuir Number

The Rayleigh number used above is the inverse of the Langmuir number, La, defined as:

$$La = (\frac{S u_*^{d2} h^3}{\nu^3})^{-1/2} = (Re_s Re_*^2)^{-1/2} \tag{5.15}$$

Note that the definition here is slightly different from the definition proposed by Leibovich (Leibovich 1977b), because we use h as the length scale instead of $1/\kappa_x$.

The Langmuir number represents the ratio of the viscous force to the vortex force. The vortex force consists of contributions from both the wind-driven current and the surface wave induced Stokes drift. The relative strength of the two is determined by the ratio Re_*^2/Re_s.

From Longuet-Higgins (1953) (see chapter 4) we know that a fluid particle under a propagating surface wave actually "feels" two types of shear: one induced by the wind stress and the other by the stress generated by the viscous wavy boundary layer above, which is responsible for the Eulerian mean flow. For this reason, we suggest that the mean shear should include flows driven by both the wind and wave stresses. Therefore, instead of using Re_*, we propose a generalized effective Reynolds number, Re_{*eff}, and modify the Langmuir number:

$$La = (\frac{S u_{*eff}^{d2} h^3}{\nu^3})^{-1/2} = (Re_s Re_{*eff}^2)^{-1/2} \tag{5.16}$$

When the effect of the Eulerian mean flow is not considered, $Re_{*eff} = Re_*$. When the Eulerian mean flow is taken into account, however, Re_{*eff} describes the total shear a fluid particle "feels". For laminar flow, the Eulerian mean flow can be estimated from equation 4.77. Thus the effective Reynolds number can be derived:

$$Re_{*eff}^2 = \frac{u_{*eff}^{d2} h^2}{\nu^2} = \frac{u_*^{d2} h^2}{\nu^2} + \frac{4 S \kappa_x{}^d h^2}{\nu} = Re_*^2 + 4\kappa_x Re_s \tag{5.17}$$

With this modification, we shall replace Re_s in our 2DCL case and linear stability theory with Re_{seff}, and u_s with u_{seff}.

Reduction of the Input Parameters

One more issue we would like to discuss here is the non-dimensionalization. As mentioned in section 5.3.2, if we use S and h as the velocity and length scales, a 2DCL simulation needs four input parameters: Re_s, Re_{seff}, κ_x, and κ_y.

Li and Garrett (1993) and Leibovich and Paolucci (1980b) utilized $(Re_{seff}u_{seff})$ as the streamwise velocity scale, which is different from the vertical and spanwise velocity scale, $(\sqrt{Re_s}u_{seff})$, and the Stokes drift velocity scale, S. The advantage is that the number of input parameters is reduced to three if h is the length scale. They are: La, κ_x, and κ_y. The ratio of the streamwise and vertical velocity scales is an output parameter. This non-dimensionalization was also used by Garg *et al.* (1992).

The important implication is that if two flows have the same La, κ_x, and κ_y, then they have the same flow structure and the quantitative flow fields are related.

We have derived the relationship between our non-dimensional variables and those by Garg *etal*, denoted by the subscript "G", as:

$$u_1 = u_{1G}\frac{Re_{seff}^2}{Re_s} \tag{5.18}$$

$$u_2 = u_{2G}\frac{Re_{seff}}{\sqrt{Re_s}} \tag{5.19}$$

$$u_3 = u_{3G}\frac{Re_{seff}}{\sqrt{Re_s}} \tag{5.20}$$

$$t = t_G\frac{\sqrt{Re_s}}{Re_{seff}} \tag{5.21}$$

$$\varpi = \varpi_G\frac{Re_{seff}}{\sqrt{Re_s}} \tag{5.22}$$

The above equations are useful in relating flows with the same La, κ_x and κ_y, but different Re_s and Re_{seff}. They will be used in the next section when we examine the effects of Eulerian mean flow.

Stability Diagram

We have run the stability code of Garg *et al.* (1992) with our profiles of the initial mean current (linear) and Stokes drift (Equation 5.4). Figure 5.1 shows the stability diagram for a surface wave with $\kappa_x = 1.5$. This is similar to the figure generated by Leibovich and Paolucci (1981) for a flow with infinite depth. The solid line is the neutral stability curve, *i. e.* the locus of all the points in the (κ_y, La^{-1}) plane for which the growth rate, $|\varpi_i|(\kappa_y, La^{-1})$, is zero. It is constructed by searching for the κ_y that, for a given La^{-1}, produces $|\varpi_i| = 0$. The curve gives the critical $La_{cr}^{-1} = 6.65$, below which the flow is stable to all the disturbances.

The dashed line is the locus of points with maximum growth rate. It is plotted by searching for the κ_y that generates the greatest growth rate of given La^{-1}. Furthermore, the real part of ϖ for these unstable modes is always zero, *i. e.*, $\varpi_r = 0$. Therefore, the Langmuir circulation obtained should be a stationary pattern of motion, *i. e.* no oscillatory modes occur.

5.4.2 2DCL Simulation

Calculation Setup

The computational parameters for the 2DCL case are given in table 5.1. We consider a surface with wave slope $\epsilon = 0.1$ and wavenumber $\kappa_x = 1.5$, which gives a deep water wave. We also selected inverse Langmuir number $La^{-1} = 7.0$, slightly higher than La_{cr}^{-1} for $\kappa_x = 1.5$, so that the assumptions of linear stability are valid. From the stability diagram, Figure 5.1, the most unstable spanwise mode is $\kappa_y = 1.06$, for which the maximum growth rate, $|\varpi_i| = 0.01885$. We set $Re_{*eff}^2 = Re_s = 7.0$ for this case. From equation 5.18 to equation 5.22, it is easy to show that, with our selection of Re_{*eff} and Re_s, the nondimensional variables from our simulation have the same values as those in Garg *et al.* (1992). This makes it easier to compare our 2DCL simulation with stability theory.

The size of computation domain is 2 in depth and $2\pi/\kappa_y$ in width. A 64×64 uniform grid is used. As will be shown later, this has reasonable resolution.

Name	ϵ	κ_x	κ_y	Re_s	Re_{*eff}	La^{-1}
2DCLW	0.1	1.5	1.06	7.0	$\sqrt{7.0}$	7.0

Table 5.1: Computation parameters for 2DCL case with weak vortex forcing.

Numerical Results

Figure 5.2 shows the contours of the streamwise vorticity at different times. At $t/T = 76$, where T denotes the wave period (Figure 5.2(a)), the streamwise vorticity is very weak. Modes of instability higher than the final wavenumber appear but they are eventually absorbed by the dominant mode and two counter-rotating Langmuir cells are formed (Figure 5.2(b)(c)) which persist and grow until a steady state is reached.

The final steady state field is shown in Figures 5.3 and 5.4. The former gives the contours of the streamwise vorticity, and the latter plots the spanwise-vertical velocity vectors and streamwise velocity contours. Figure 5.3 shows that a pair of Langmuir has developed over three quarters of the depth. Near the bottom wall, the streamwise vorticity changes sign. This is due to the viscous wall boundary layer there. The Langmuir cells are asymmetric, as observed in the field (Leibovich 1983). Moreover. the gradient of the vorticity is greater near the top surface because the vortex force is bigger there.

Two big recirculation zones are seen in Figure 5.4. They correspond to the opposite signs vortices seen in Figure 5.3. Close to the mid-width and the right end of the domain, where the streamwise vorticity changes sign, there exist a divergence zone and a convergence zone, respectively. Since the cores of the Langmuir vortices are closer to the convergence region, the downwelling flow under the convergence zone is stronger than the upwelling beneath the divergence zone. This property of Langmuir circulation is also observed in the field (Weller and Price 1988, Smith *et al.* 1987).

The steady state vertical velocity profiles at the convergence and the divergence zones are plotted *vs.* depth in Figure 5.5. The maximum downwelling velocity is located just above mid-depth, in agreement with observation (Weller and Price 1988,

Nepf and Monismith 1991). At steady state, the maximum downwelling velocity exceeds the maximum upwelling velocity by $\sim 50\%$

Figure 5.6 gives the surface streamwise velocity profile in the spanwise direction. The wind-directed surface current has its peak value at convergence zone. This is another observed characteristic of Langmuir circulations (Langmuir 1938, Assaf *et al.* 1971, Gordon 1970), and is called the "current anomaly" (Leibovich 1983).

The surface value of the spanwise velocity component is shown as a function of the spanwise coordinate in Figure 5.7. Its magnitude is anti-symmetric about the convergence line, which is located near $x_2 \sim 5.8$. The largest surface sweep velocity is found at approximately one-half the distance between the downwelling region and upwelling region.

5.4.3 Comparison with Linear Stability Theory

Figure 5.8 presents the comparison of the 2DCL simulation with linear stability theory. It plots the development of the spanwise kinetic energy of the perturbation as a function of time. In the 2DCL case, the initial perturbation is amplified exponentially at the beginning after an initial adjusting period. The flow field then equilibrates to a steady state due to non-linearity. From linear stability theory, the growth rate for the velocity is predicted to be 0.01885. Since the kinetic energy is the square of the spanwise velocity, its growth rate should be twice that or, 0.0377. For comparison, a line with slope 0.0377 is also plotted. It shows that the growth rate of the perturbation, 0.0369, is in good agreement with linear stability analysis.

5.4.4 Grid Study

A grid resolution study has performed for the 2DCL case. Figure 5.9 plots the error in the growth rate of the 2DCL cases compared with that obtained from the stability analysis. It shows that with an increase of the grid number in each direction, the error decreases in second order fashion. This indicates that the numerical method used is second order accurate in space, as expected.

In sum, the results indicated the correctness of our computational model.

5.5 2D Simulation with Moderate Vortex Forcing

This section performs a 2DCL simulation with moderate vortex forcing. In the first subsection, the computational parameters are selected. The evolution of Langmuir circulation is then discussed in the second subsection. The third subsection examines Langmuir circulation structures and properties. Finally, the effects of the Eulerian mean flow are explored in the fourth subsection.

5.5.1 Parameter Estimation and Calculation Setup

First, we shall evaluate the importance of the Eulerian mean flow, compared with the wind driven current. Since the Eulerian mean flow profile is given by equation 4.77, we can estimate the ratio of the shear induced by the wind-driven current to that by the Eulerian mean flow, β:

$$\beta = \frac{u_*^{d2}}{4\nu_t \kappa_x^d S} = \frac{u_*^{d2}}{2\nu_t \epsilon^2 \sigma^d} \tag{5.23}$$

where σ^d is the dimensional radial frequency of the surface wave; ν_t the eddy viscosity, u_*^d the friction velocity, and ϵ the wave slope.

In field observations, u_*^d is usually assessed from the wind speed with an empirical drag formulation (Smith 1988, Jones 1985). A typical surface stress in MILDEX (Smith *et al.* 1987, Weller and Price 1988) is $\tau_w = \rho^d u_*^{d2} = 0.2 N/m^2$, corresponding to a wind speed of $10 \sim 15 m/s$. This gives $u_* = 0.014 m/s$. A representative eddy viscosity from ocean subgrid parameterization is $\nu_t = 4 \times 10^{-3} m^2/s$ (Skyllingstad and Denbo 1995). For a characteristic ocean wave with wave slope $\epsilon = 0.1$ (Smith 1992, Weller and Price 1988) and wave period $T = 2\pi/\sigma^d = 4s$, we obtain:

$$\beta \simeq 1 \tag{5.24}$$

Therefore, the wind-induced stress is comparable to the wave induced stress.

Obviously, the value of β is sensitive to the estimate of the eddy viscosity. A more accurate evaluation of the wave stress would use the eddy viscosity near the

surface. However, we have poor understanding of this issue. As an approximation, we estimate the near-surface eddy-viscosity as $\nu_t = u_*^d z_0^d$, where z_0 is the length scale of turbulent eddies near the top. A good candidate for this length scale is the roughness ($\mathcal{O}(10^{-1}m)$) proposed by Craig (1996). Therefore, $\nu_t \sim 1.4 \times 10^{-3} m^2/s$, which is of the same order of magnitude as the bulk eddy viscosity above.

Furthermore, we have examined the experimental data on both mechanical and wind waves by Cheung (1985) and have calculated the near-surface eddy viscosity from the ratio of surface stress to the mean shear near the top. Although the computation of the mean velocity gradient is pretty rough, (In the data, the velocity near the surface sometimes decreases as it approaches the surface! We have to use points further down) the near-surface eddy viscosity is approximately fitted to $0.5 Re_{*s}^{1.5}$, where $Re_{*s} = u_*^{d2}/\sigma^d \nu$ is the Reynolds number based on the length scale u_*^d/σ^d, as shown in Figure 5.10. Using the parameters for the field condition as discussed ealier, we obtain $Re_{*s} = 125$ and $\nu_t \sim 0.7 \times 10^{-3} m^2/s$, supporting our previous estimates. Nevertheless, the experiments of both Craig (1996) and Cheung (1985) have wave breaking, which induces extra shear and may adversely affect our estimate of the eddy viscosity. Further experimental studies are needed to accurately determine the wave stress importance.

For the simulation, we chose the domain depth to be $25m$, a typical mixed layer depth in the Pacific Ocean off the California coast, as shown in MILDEX (Smith *et al.* 1987, Weller and Price 1988). The surface wavenumber is selected as $\kappa_x = 2.0$, corresponding to a wave length of $40m$. The wave slope is set to $\epsilon = 0.1$. We also set the wave number in the spanwise direction to $\kappa_y = 1.57$, which gives an aspect ratio of the Langmuir circulation around 1.0, as proposed by Smith (1992). Li and Garrett (1993) argued in the ocean, the Langmuir number is in the range of $0.0004 \sim 0.004$ ($0.001 \sim 0.01$ with their definition). We pick $La = 0.007$, which allows the magnitude of the vortex force to be physically reasonable, yet with a viscous force large enough to justify the constant eddy viscosity assumption. This case also corresponds to the case studied by Li and Garrett (1993), in which $La = 0.02$ according to their definition, permiting comparison of our simulation with their results.

In the case including Eulerian mean flow effects, we use $Re_s = 36$ and $Re_* = 17$.

Name	ϵ	κ_x	κ_y	Re_s	Re_{*eff}	La^{-1}
2DCLM	0.1	2.0	1.57	36	24	144

Table 5.2: Computation parameters for 2DCL case with moderate vortex forcing.

This produces a ratio of the wind-driven stress to the Eulerian mean flow stress, $\beta = Re_*^2/4\kappa_x Re_s$, of approximately unity. From equation 5.17, with Re_s, Re_*, and κ_x selected, we have $Re_{*eff} = 24$.

The computational parameters for this case are summarized in table 5.2.

The domain size is 2 in depth and $2\pi/\kappa_y$ in width. A 64×64 grid is used. The grid is stretched vertically with $\alpha = 0.98$ (see section 3.2) to put more points in the top and bottom boundary layers. A uniform grid is used in the horizontal direction.

As mentioned in section 3.3, according to Li and Garrett (1993), the important length scales in this case are the thicknesses of the surface boundary layer and the narrow downwelling zone. They are: $\delta_s \sim \mathcal{O}\left((La^{1/2}2\pi/\kappa_y)\right) \sim 0.26$, and $\delta_{downwelling} \sim \mathcal{O}\left((La^{1/2}2\pi/\kappa_x)\right) \sim 0.34$, respectively. With the above grid, we have approximately 18 points in the surface boundary layer and 6 in the downwelling zone. Thus we expect that the resolution is adequate.

5.5.2 Evolution of Langmuir Cells

Cell Merging Process

The evolution of the streamwise vorticity is illustrated in Figures 5.11 to 5.13. Small longitudinal vortices appear first. Then they merge into bigger cells. This process continues until two big counter-rotating Langmuir circulations are formed at the steady state.

The cell merging has been observed in field as well as in laboratory experiments. For example, during their Flip cruises, Weller and Price (1988) found that the computer cards they distributed on the ocean surface first merged into short lines with several meters long, and several meters apart. Later, these short lines join each other to form lines up to tens meters long, with $10 \sim 40$ meters spanwise intervals. This

coalescence was carried further. Long lines of computer cards that are approximately 100 meters apart appeared. Furthermore, if new cards were scattered, the merging process repeated, indicating the existence of a hierarchy of scales on the ocean surface. This process has also been seen by Thorpe (1992), Farmer and Li (1995) in their observations of bubble clouds generated by wave breaking. Adjacent bubble bands formed by Langmuir circulations tend to combine to form a "Y junction".

Faller and Auer (1988) suggested that the Y junctions are formed via a inverse energy cascade similar to that in two dimension turbulence. As mentioned by Melander *et al.* (1988), in two dimensional turbulence, vortices of the same sign tend to amalgamate into bigger vortices if they are close enough together. A pair of vortices of opposite signs, if they are located near an upwelling region, do not merge but move apart. This process is due to the free surface. The surface can be represented by image vortices rotating in the sense opposite to the actual vortices and brings together a pair that is responsible for downwelling. This process is not observed in the homogenuous turbulence. A pair of opposite sign vortices at a downwelling zone tends to sink as a dipole. Thorpe (1992) proposed that besides like-sign vortex amalgamation vortices of opposite signs are "squeezed" by their neighboring vortices and thus cancel due to turbulent diffusion.

We note that in two dimensional turbulence, dissipation is rather weak because there is relatively little contact area between the large vortices. Recall that dissipation is, in the end, a diffusive process and the lack of contact area gives it little fluid to operate on.

Li and Garrett (1993) argued that only the counter rotating vortex cancellation process appears in Langmuir circulation in their simulation. No vortex merging was observed. However, detailed observations were not reported. From the time sequences shown in their paper, one can observe that three vortices pairs become two, but can not see how it happens. McWilliams *et al.* (1997) found that in their large eddy simulation with three dimensional Craik-Leibovich equations (3DCL) that like-sign vortex amalgamation and opposite-signed vortex suppression occur.

From the time sequences of our 2DCL simulation, shown in Figures 5.11 to 5.13, we found that the cell merging process resembles two dimensional turbulence. The

differences are due to the free surface effects mentioned above and the existance of stretching and compression in the third dimension that causes the circulation of an individual vortex not to be conserved.

The streamwise vorticity grows from the small initial disturbance due to the Craik-Leibovich forcing. Shortly after the flow starts to evolve, at $t/T = 212$, three pairs of counter rotating vortices can be clearly identified (Figure 5.11(a)). This state is not stable. As the second and third vortices from the left grow stronger, the first and the fourth vortices are pushed downward (Figure 5.11(b)). Later (Figure 5.11(c)) at $t/T = 308$, the first and the fourth vortices seen in Figure 5.11(a) are pushed down further, while a bigger pair of vortices is formed at the top of the domain through same-sign amalgamation: the second vortex combines with the sixth one (recall the periodic boundary condition), and the third vortex with the fifth one.

The vortex pair at the top in Figure 5.11(c) forms an upwelling zone near the left boundary and a downwelling zone close to the right side. The upwelling zone is marked by a transition from the positive (red) to negative vorticity (blue), and the downwelling zone is marked by a transition from negative to positive vorticity. The vortex cores near the downwelling zone sink as a dipole, pairing with the two vortices beneath them. The lower red cell in Figure 5.11(c) moves around the big blue cell above it. During this process the red cell goes all the way to the top and grows, splitting the big blue vortex into a strong negative vortex at the right, and a weaker on to the left, which might be destroyed later by viscous cancellation. The lower blue vortex in Figure 5.11(c) moves around the big red cells above. It moves upwards and is weakened and trapped beneath the bigger positive vortex. This process is shown in Figures 5.11(d) to 5.11(e).

Compared with Figure 5.11(c), which only has one pair of vortices at the top, smaller scales are regenerated in Figure 5.11(e) through the vortex splitting process. As a result, two pairs of vortices are found near the surface. The stronger vortices on the right drive each other away from the upwelling zone, as shown in Figure 5.11(f). The other sides of these two vortices collide near the left side (Figure 5.12(a)) and squeeze and push down the weaker vortex pairs between them. In the mean time, the bottom boundary layer starts to develop.

After $t/T = 415$, these processes are repeated. The two counter rotating vortices sink as a dipole (Figure 5.12(b)), while the weaker red vortex below them moves upward and the big blue one is split into two cells. (Figure 5.12(c)). Next, the two strong cells propel each other from the upwelling and bump together near the downwelling zone, pushing the weaker vortex pair between them downward (Figures 5.12(d) and 5.12(e)). No vortex cancellation is observed during this process. In Figures 5.12(d) and 5.12(e), the big blue vortex pushes down the weaker red one on its right, and then "gobbles up" the weak green cell, while the weaker red one merges with the stronger red vortex.

From $t/T = 573$ (Figure 5.12(f)) to $t/T = 842$ (Figure 5.13(e)), another cycle occurs with processes similar to those described above, while the bottom boundary layer increases in strength. Finally two large Langmuir circulations that cover most of the domain remain. After that, the Langmuir circulations oscillate back and forth in the spanwise direction until steady state is reached.

In conclusion, we have observed like-sign vortex amalgamation, vortex splitting, opposite-signed vortex pairs being driven apart near the upwelling zone, and sinking as a dipole at the downwelling zone. We have also seen the weaker opposite-signed vortices squeezed by neighboring stronger vortex pairs. Unlike two dimensional homogeneous turbulence, the Craik-Leibovich forcing acts as a source of vortex growth and might transfer energy from one vortex to another. However, unlike the claims of Li and Garrett (1993) and Thorpe (1992), we find very little, if any, vortex cancellation. We believe that further growth of the vortices is inhibited by the layer depth. To show this conclusively, we would need to do a simulation in a larger domain.

Velocity Field Development

The merging process described above is also reflected in the development of the velocity field. In Figure 5.14, the profiles of surface downwind velocity as a function of spanwise direction are plotted at different times. At $t/T = 212$, three maxima and three minima are found. The three maxima mark the current anomalies that occur at the downwelling zones between vortex pairs shown in Figure 5.11(a). Later, at $t/T = 516$, the three pairs of vortices become two pairs and there are only two

maxima of the downwind velocity (the dashed lines in Figure 5.14). The more distinctive peak in the left is associated with the stronger vortex pairs in Figure 5.12(c), while the weaker anomaly at the right is due to the less powerful vortex pairs. At $t/T = 516$, the cell merging process is close to finish, only one pair of counter rotating vortices is left (Figure 5.13(f)). This produces a single maximum in the downwind surface profile (the diamonds in Figure 5.14).

It is also clear in Figure 5.14 that the downwind velocity at the surface decreases with time. This is because the Langmuir circulation transports fluid with larger horizontal momentum downward from the surface, and brings fluid with lower downwind momentum up to the surface, thereby decreasing the downwind velocity near the surface.

The surface spanwise velocity profiles are illustrated in Figure 5.15 for the same times. At time zero, the spanwise disturbance is negligible. It then grows to finite amplitude as the counter rotating pairs of vortices are formed. At $t/T = 212$ there are three maxima and three minima, like the downwind velocity profile. The same is true at $t/T = 516$ and $t/T = 1060$. The downwelling zones, where current anomaly occurs, are zeros of the spanwise velocity curves. An exception occurs at $t/T = 516$ in Figure 5.15, where the weak downwelling zone on the right is not marked by zero spanwise velocity. Instead, this downwelling is indicated by an inflection point.

The development of Langmuir circulations is also illustrated in Figure 5.16, which shows the development of the kinetic energy of the spanwise velocity component. It can be observed that the initial two dimensional Couette flow is highly unstable. It gives rise to the spanwise and vertical motion that forms the Langmuir circulation. Starting from an infinitesimal initial value, the spanwise energy component increases exponentially due to the vortex forcing. After about 400 wave periods, the kinetic energy begins to oscillate and later the flow relaxes into a steady state.

5.5.3 Langmuir Circulation Structures and Properties

Flow Field at Steady State

The flow with moderate vortex forcing exhibits similar structures to those in the weak vortex forcing case discussed in section 5.4. Figure 5.17 depicts the streamwise vorticity contours at steady state. The pair of Langmuir circulations are more powerful than those in the weak forcing case (Figure 5.3). They penetrate further down into the domain, leading to thinner, stronger boundary layers near the bottom surface. Furthermore, each cell is more asymmetric, with stronger streamwise vorticity near the downwelling zone and lower vorticity near the upwelling zone.

This asymmetry causes a stronger downwind jet at the downwelling zone, as seen in Figure 5.18. From the streamwise velocity contours, it can be observed that the flow moves faster at the downwelling zone than that at the upwelling zone. As in Figure 5.4, two stronger recirculation zones develop between the upwelling and downwelling zones. The bottom boundary layers are clearly seen.

Vertical Velocities

Figure 5.19 shows the vertical velocity profiles at the convergence and divergence zones. Although it shows stronger downwelling and upwelling events compared with the weak forcing case (Figure 5.5), the location of the maximum downwelling velocity is about the same, *i. e.* just above the mid-depth of the domain. This is because that the downwelling jet cross section first converges then diverges with depth. Since the spanwise velocity in the downwelling jet is nearly zero, due to continuity, the vertical velocity should be maximum where its cross section area is minimum, *i. e.* near the mid-depth of the channel.

The downwelling jet can be better seen in Figure 5.22, where the vertical velocity profile is plotted as a function of y. Clearly, a narrow region with high downward velocity can be observed near $y = 2.5$, with a downwelling velocity about twice the upwelling velocity.

The relationship between the maximum downwelling velocity and the wind speed is one of the major items measured in field observations. Leibovich (1983) summarized

early observations (Sutcliffe *et al.* 1963, Harris and Lott 1973, Filatov *et al.* 1981) with two linear relationships that gives the range of the downwelling speed:

$$0.0025U_w^d \leq w_{down}^d \leq 0.0085U_w^d \tag{5.25}$$

where w_{down}^d denotes downwelling velocity and U_w^d the wind speed. Weller and Price (1988) pointed out that the data that gave the above relation were obtained very near the surface and thus underestimated the downwelling. From their measurements at locations further below the water surface, the downwelling velocity is greater than the values suggested by equation 5.25. For a wind speed of $5m/s$ to $15m/s$, the maximum downwelling velocity observed ranges from $0.15m/s$ to $0.26m/s$. Furthermore, the data are scattered and can not be fit with a simple linear relation. From their Figure 23, w_{down}^d/U_w^d is between 0.025 and 0.03.

From Figure 5.19, we have a maximum downwelling velocity as $w_{down} = w_{down}^d/S = 2.37$. A relationship between the characteristic Stokes drift, S, and the wind speed has been suggested by Li and Garrett (1993) as:

$$S = 0.008U_w^d \tag{5.26}$$

Thus we find that our maximum downwelling velocity is $w_{down}^d = 0.019U_w^d$. This within the range predicted by Weller and Price (1988).

Downwind Velocities

The downwind "squirts" seen in the field (Smith *et al.* 1987, Weller and Price 1988) have been predicted by simulations. As shown in Figure 5.21, the downwind velocity profile at the top surface has a narrow peak above the downwelling zone, which is located at $y \simeq 2.5$. The downwind velocity reaches its minimum value at the upwelling region, located at $y \simeq 0.7$. The slow fluid particles that emerge from the upwelling zone accelerate in the downwind direction while being swept toward the convergence zone.

The downwind velocity profiles in the spanwise direction change with the depth. For example, in Figure 5.22, the spanwise profile of the downwind velocity is shown

at the depth where maximum downwelling occurs. Besides the downwind jet, there is a confined region of reduced downwind velocity at the upwelling zone. It is formed by the slower fluid that is convected upward by the Langmuir circulation.

The difference of the downwind velocities at the downwelling and upwelling zones is plotted in Figure 5.23. Two subsurface maxima are found, with one near the bottom of the domain and the other near the surface, which leads to a negative vertical shear of the downwind velocity. This has been confirmed by field observations (Weller and Price 1988, Smith *et al.* 1987).

Weller and Price (1988) also found that the magnitude of the velocity in the downwind jet is comparable to the downwelling velocity. This feature is represented by Li and Garrett's (1993) variable "pitch", denoted by Pt, the ratio of the surface jet strength to the maximum downwelling velocity. According to Weller and Price (1988), the maximum downwind velocity can be up to $0.4m/s$. They also found a maximum downwelling velocity of $0.3m/s$, although downwelling velocities in the range $0.05 \sim 0.1m/s$ were very common. Since the maximum downwind jet of $0.4m/s$ was subsurface, we believe it is more appropriate to define the pitch as the ratio of the maximum downwind jet strength below the surface to the maximum downwelling velocity. That is:

$$Pt = (u_{1downwelling} - u_{1upwelling})_{max}/(u_{3downwelling})_{max} \tag{5.27}$$

From the data collected by Weller and Price (1988), it can be inferred that Pt is in the range of $1.33 \sim 8$. From our computation, we have a maximum downwind jet velocity of 3.63 at $z = 0.82$ (Figure 5.23), and a maximum downwelling velocity of 2.37 at $z = 0.25$. Thus the pitch we get is: $Pt = 1.53$, which is within the observed range. However, the measurements were made under turbulent conditions while the simulations are of laminar flow. Thus the comparisons should not be taken too seriously. See chaper 6 for the turbulent case.

Spanwise Velocities

The surface sweeping velocity profile is shown in Figure 5.24. As in the weak vortex force case, the maximum surface sweeping velocity is achieved about half way between

the convergence zone and the divergence zone, although it is much stronger than in the weak vortex forcing case in Figure 5.7. The same property was also discovered by Leibovich and Paolucci (1980b).

Mixing of Horizontal Momentum

The mixing effects associated with Langmuir circulation are clearly demonstrated in Figure 5.25. It shows the vertical profiles of the spanwise averaged downwind velocity at the beginning and at the steady state. With the powerful convective motion of the Langmuir cells, the initial linear profile becomes a well-mixed uniform profile for the fluid column between the top and bottom boundary layers.

5.5.4 Effects of the Eulerian Mean Flow

To study the effects of the Eulerian mean flow, we consider another 2DCL case without the Eulerian mean flow. This case has the same surface wave (κ_x, ϵ), the same spanwise periodicity (κ_y), and the same vortex force (La). The only difference is that it has a different combination of Re_s and Re_{*eff} from the 2DCL with the Eulerian mean flow. Corresponding to Li and Garrett (1993), S/u_* is typically 5. Thus we select $R\epsilon_s = 80.4$ and $Re_* = Re_{*eff} = 16.08$. This both satisfies the above condition and produces the same La as in the 2DCL case with the Eulerian mean flow.

As shown in section 5.4.1, the two flows are similar. Furthermore, the two flows are related by Garg's nondimensional variables, given by equations 5.18 to 5.22. Therefore, the two flow patterns should be the same. With equations 5.18 to 5.22, one can derive the flow field for the case without the Eulerian mean flow from that with the Eulerian mean flow via Garg's nondimensional variables.

The results are presented in Table 5.3, which compares of the 2DCL results with the field observation by Weller and Price (1988). The two parameters used in last subsection are examined. Clearly, the case with the Eulerian mean flow effects produces better results, especially for the pitch, which, without the Eulerian mean flow, is far below the range observed in the field. With the Eulerian mean flow effects, a reasonable pitch value is achieved. Again, one should be cautious about comparing measurements in a turbulent flow with laminar simulations.

	Pitch (Max. Downwind Jet Strength /Max. Downwelling Vel)	Max. Downwelling Vel / Wind Speed
Experiment (Weller and Price 1988)	$1.33 \sim 8.0$	$0.0025 \sim 0.03$
2DCL With Eulerian Mean Flow	1.53	0.019
2DCL Without Eulerian Mean Flow	0.71	0.009

Table 5.3: 2DCL case with $La^{-1} = 144, \kappa_x = 2.0, \kappa_y = 1.57$. Comparison of the numerical results with the field observations for cases with and without the effects of the Eulerian mean flow.

5.6 3D Simulation in a Wavy Domain with No Explicit Vortex Forcing (3Dwavy)

The simulations in the previous two sections integrate the Craik-Leibovich equations in a rectangular domain. In this section, a flow under a second order propagating Stokes wave is studied by solving the full Navier-Stokes equations. The results will be used to validate the key assumption of the Craik-Leibovich theory in the next section.

5.6.1 Calculation Setup

Table 5.4 summarizes the parameters used in the 3Dwavy simulation. We study a deep water wave with $\kappa_x = 1.5$ and $\epsilon = 0.1$. In subsection 5.5.1, we showed that the stress due to the wind induced current is comparable to that of the Eulerian mean flow in a fully developed sea. In order to satisfy this condition Re_s and Re_* are chosen as 7.0 and 6.0, respectively. This combination of parameters gives an effective Reynolds number of $Re_{*eff} = 8.83$. According to our definition (equation 5.16), the Langmuir number is 0.04. The other parameter, κ_y, is set to 2.1, the preferred spanwise wavenumber obtained from linear stability theory (Garg *et al.* 1992). This simulation corresponds to a scenario that might happen in a fully developed sea.

The domain size is $2\pi/\kappa_x$ in length, $2\pi/\kappa_y$ in width, and 2 in depth. A $64 \times 64 \times 64$

Name	ϵ	κ_x	κ_y	Re_s	Re_*	La^{-1}
3DwavyL1	0.1	1.5	2.1	7.0	6.0	23.4

Table 5.4: Computation parameters for 3Dwavy case with constant eddy viscosity.

computational grid is used. Uniform grids are used in the lateral directions, while hyperbolic tangential stretch with $\alpha = 0.98$ is used in the vertical direction.

In this case, three important length scales exist: the wavy boundary layer thickness, δ_w, the thickness of the surface boundary layer due to Langmuir circulation, δ_s, and the downwelling zone thickness, $\delta_{downwelling}$. With the latter two estimated by Li and Garrett (1993), the three length scales are written as:

$$\delta_w \sim \mathcal{O}\left(\sqrt{2\nu/(C_w^d \kappa_x^d h^2)}\right) \sim 0.03 \tag{5.28}$$

$$\delta_s \sim \mathcal{O}\left(La^{1/2} 2\pi/\kappa_y\right) \sim 0.6 \tag{5.29}$$

$$\delta_{downwelling} \sim \mathcal{O}\left(La^{1/2} 2\pi/\kappa_x\right) \sim 0.9 \tag{5.30}$$

Therefore, the surface boundary layer due to Langmuir circulations is thicker than the wavy boundary layer. With the above grid, we can achieve reasonable resolution: about 6 points inside the wavy boundary layer and 18 points in the downwelling zone.

The code is run on the Cray J90 in the Environmental Fluid Mechanics Laboratory at Stanford. Since it requires thousands wave periods for the Langmuir circulation to reach steady state, and the computational time step is limited by the CFL criterion described in section 3.4, it takes about 30 days for this case on a single CPU.

5.6.2 Numerical Results

Flow Development and Vorticity Field

The initial 2D wavy flow obtained from a separate 2D simulation is perturbed by small random noise of magnitude of $\mathcal{O}(10^{-4})$. As expected, the flow is highly unstable. As shown in Figure 5.26, the magnitude of the spanwise motion grows exponentially right from the beginning. The spanwise kinetic energy undergoes an overshoot at $t/T \sim$

300, then settles into a steady state. The same overshoot has also been observed by other researchers (Leibovich and Radhakrishnan 1977, Leibovich and Paolucci 1980b, Li and Garrett 1993), and in the 2DCL case in the last section (See Figure 5.16).

The evolution of the streamwise vorticity is illustrated in Figures 5.27 and 5.28. The streamwise vorticity field starts from weak white noise (Figure 5.27($t = 0$)). At time $t = 127T$, there are four counter-rotating cells near the top surface. Their vorticity increases with time and they deepen. At $t = 245T$ (Figure 5.28), the four cells have merged into two larger cells, which continue to evolve until they reach the final steady state as shown in Figure 5.28 ($t = 1512T$).

The flow development process is similar to the 2D simulation based on the Craik-Leibovich equations. Furthermore, the Langmuir circulations in the 3Dwavy simulation resembles those in the 2DCL calculations, compared with Figures 5.3 and 5.17. As depicted in Figure 5.28 ($t = 1512T$), at steady state, two counter rotating vortices occupy most of the domain under the wavy surface, and a thin boundary layer is formed at the bottom.

Unlike the 2DCL simulations, however, the Langmuir circulations in this case are embedded in a wavy flow. As seen in Figure 5.29, which plots the spanwise vorticity contours, the propagating wave generates an oscillatory, confined wavy boundary layer under the top surface, and a thin, oscillatory bottom boundary layer as well. The contours on a streamwise vertical plane resemble those from a 2Dwavy simulation (see Figure 4.2), indicating that the wave field structure has not been changed much by the Langmuir circulations.

Comparing Figure 5.29 with Figure 5.28 ($t = 1512T$), it is obvious that the spanwise vorticity is one order of magnitude stronger than the Langmuir circulation. This confirms the assumption in the Craik-Leibovich theory that the wavy field is of first order in wave slope and the Langmuir circulation is of second order.

The vertical vorticity contours are presented in Figure 5.30. As expected from the CL2 mechanism in the Craik-Leibovich theory (Leibovich 1983), the Langmuir cell with positive streamwise vorticity has positive vertical vorticity, and vice versa. Thus, the 3Dwavy simulation supports the hypothesis in the Craik-Leibovich theory that Langmuir circulations are formed by the interaction of the Stokes drift and the

mean flow.

The structure of the vertical vorticity field also shows the existence of the current anomaly, as reported in experiments (Langmuir 1938, Weller and Price 1988). Figure 5.30 displays a strong vortex pair near the top surface, and another pair near the bottom (recall the periodic boundary condition in the spanwise direction). The signs of these vortices indicate that near the top surface, the streamwise (downwind) velocity is higher at the downwelling zone than in the neighboring area; near the bottom wall, the downwind velocity is lower at the upwelling zone.

Streamwise and Vertical Velocities

The vertical velocity is dominated by the wave field. As seen in Figure 5.31(a), on a streamwise-vertical plane, the vertical velocity exhibits a sinusoidal-like variation in the streamwise direction and rapid decay with depth. This is characteristic of a two dimensional wavy field as discussed in chapter 4.

The first order wave field is modified by the second order Langmuir circulation. In Figure 5.31(b), the variation of the vertical velocity in the spanwise direction is presented. At the trough of the surface wave, where there is no vertical motion due to the wave, a region of negative vertical velocity marking the downwelling zone can be clearly identified near midpoint in the spanwise direction. The upwelling zone is marked by the region of positive vertical velocity. The maximum downwelling velocity occurs above the mid-depth of the domain, in agreement with the 2DCL simulations in the previous sections and field observations (Weller and Price 1988, Smith *et al.* 1987). At the forward slope ($x = 1/4L_x$), where the vertical wave motion is large, the effect of the Langmuir circulation bends the positive vertical velocity contours upwards at the downwelling zone, and tilts them downwards near the upwelling zone. At the backward slope ($x = 3/4L_x$), where the wave motion is downward, Langmuir circulation causes the negative contour to be bent downward at the downwelling zone and upward at the upwelling zone.

The streamwise velocity is shown in Figure 5.32. In Figure 5.32(a), the properties of a two dimensional wavy field, *i. e.*, the sinusoidal variation along the streamwise direction and the fast decay with the depth, are evident. However, the maximum

forward velocity is greater than the maximum backward velocity, implying that there is a mean current superimposed on the wave field, which will be discussed in the next section.

The current anomaly (Leibovich 1983, Langmuir 1938, Weller and Price 1988) is shown in Figure 5.32(*b*), where the spanwise variation of the downwind velocity is given. At the downwelling, the positive contour lines are bent downward at the forward and backward slopes of the surface wave, while the negative contour lines are pushed upward at the trough. This indicates that the downwind velocity at downwelling zone is greater than that at the upwelling zone.

Modulation by the Surface Wave

As discussed in the last subsection, the Langmuir circulation modifies the wave field. On the other hand, the wave field also modulates the Langmuir cells in the streamwise direction.

As an example, Figure 5.33 depicts the iso-surface of the streamwise vorticity with magnitude of 2.25. The variation of the shape of the Langmuir circulations along the streamwise direction can clearly be seen. The vortex tubes contract under the forward slope of the surface wave and expand under the backward slope, showing the Langmuir circulations are affected by the wave motion. A closer look of the streamwise variation is given in Figure 5.34, which shows the streamwise vorticity contours on the streamwise vertical plane of the center of one of the Langmuir cells. The maximum streamwise vorticity occurs slightly to the right of the trough.

Due the influence of the wave motion, the convective motion of the Langmuir circulation may be hard to identify at some phases of the surface wave. Figures 5.35 to 5.38 compare the velocity vectors and the streamwise velocity contours at different streamwise locations. Near the crest and trough of the wave, where the vertical velocity of the wave field is close to zero, two counter rotating Langmuir cells can be recognized (Figure 5.38 and 5.36). On the forward and backward slopes, however, the wave field contains vertical motion. As seen in Figures 5.35 and 5.37, the second order Langmuir circulation is hidden by the first order wave motion and can not be detected. Therefore, to measure the Langmuir circulation in experiments,

Name	ϵ	κ_x	κ_y	Re_s	Re_{*eff}	La^{-1}
2DCLL1E	0.1	1.5	2.1	7.0	8.83	23.4

Table 5.5: Computation parameters for the 2DCL comparison case with 3DwavyL1.

averaging of the data over several wave periods, such as those used in the Flip cruises (Weller and Price 1988, Smith *et al.* 1987, Weller *et al.* 1985), is essential.

5.7 Comparison of 3Dwavy Simulation and Craik-Leibovich Theory

The basic assumption of the Craik-Leibovich theory, the disparate time scales, is verified by comparing our 3Dwavy results with those obtained from a 2DCL simulation based on the Craik-Leibovich equations.

The computational parameters of the 2DCL case are listed in table 5.5. The 2DCL case has the same κ_x, κ_y, Re_s and La as the 3Dwavy flow. The base flow of the 2DCL case contains a Stokes drift determined by the surface wave and a linear mean current with the same slope as that under the top boundary layer in 3Dwavy case. Thus, the current incorporates the effects of both the wind stress and the Eulerian mean flow. The effective stress Reynolds number from the total shear stress, Re_{*eff}, is 8.83. A 64×64 uniform computational grid is used.

Figure 5.39 shows the growth of the spanwise kinetic energy integrated over the whole domain for both the 3Dwavy and the 2DCL cases. To make the two cases comparable, the values shown for the 2DCL case are the product of the integral of the kinetic energy over the two dimensional domain of the 2DCL case and the streamwise length of the 3Dwavy domain. It can be observed that after an initial adjustment period, the perturbations in both flow grow at essentially the same rate. Afterwards, the kinetic energy overshoots about the same amount in both cases and then relaxes to approximately the same final value. The difference of the initial adjustment pattern of the kinetic energy might be caused by an incorrect initial guess of the pressure field in either cases or the initial conditions.

Figure 5.40 compares the streamwise vorticity field between the 3Dwavy and 2DCL cases. The contours for the 3Dwavy case are obtained via streamwise averaging along the inviscid streamlines. The contours of the 2DCL case have been phase-shifted in the spanwise direction so that the downwelling occurs at the same spanwise location as in the 3Dwavy case. This phase shift makes no difference since periodic boundary conditions are used. It can be observed that the vorticity fields in the two cases are nearly identical.

The same situation also applies to the velocity field, as shown in Figure 5.41. The streamwise velocity contours from the two cases closely resemble each other. Since a stretched grid is used for the 3Dwavy case and a uniform grid for the 2DCL case, the flows are hard to compare quantitatively in this plane.

In Figure 5.42, the profile of vertical velocity with depth are depicted at the upwelling and downwelling regions. Excellent agreement is achieved between the 3Dwavy and 2DCL cases.

Figure 5.43 presents the downwind velocity profiles at the top surface for the 3Dwavy and 2DCL cases. The profile of the 2DCL case has been phase-shifted to make the comparison. The current anomalies at the top surface are alike. Close resemblance is also observed in the profiles of the downwind jet strength, as shown in Figure 5.44. Both cases predict subsurface maxima of the downwind jet, as in field observations (Weller and Price 1988, Smith *et al.* 1987).

As final evidence of the remarkable success of the Craik Leibovich theory, both cases give almost identical mixing effects of Langmuir circulation on the streamwise momentum. In Figure 5.45, horizontally averaged streamwise velocity profiles are displayed. Compared to the initial linear mean current, the horizontally averaged mean current exhibits a region of uniform velocity caused by the mixing due to the convective Langmuir circulation.

The comparison of the 3Dwavy and the 2DCL cases indicates that the flow obtained by integrating the Navier-Stokes equations directly matches the Craik-Leibovich theory with remarkable precision. Both predict the characteristics of Langmuir circulations similar to those observed in field. Therefore, the averaging used in Craik-Leibovich theory is justified. Again, the difficulty of comparing laminar and

turbulent flows should raise a caution flag.

5.8 Summary

Langmuir circulations in a flow with constant viscosity have been studied with two dimensional simulations based on the Craik Leibovich theory and three dimensional simulations that use a wavy top surface.

The computer code has been validated by the comparison of the numerical results for a weak vortex forcing case with the linear stability theory.

To account for the Eulerian mean flow effects, we suggest that the conventional Langmuir number must be modified to:

$$La = (Re_s Re_{*eff}^2)^{-1/2} \tag{5.31}$$

where Re_s is the Reynolds number based on the characteristic Stokes drift velocity and the half depth of the domain, and Re_{*eff} a effective Reynolds number based on the half domain depth and the friction velocity due the both the wind stress and the Eulerian mean flow induced stress. We estimate that the wave stress is comparable to the wind stress. However, the ratio of these two stress highly depends on the eddy viscosity near the top surface, which need to be further studied in experiment.

Both types of simulations predict the correct characteristics of the Langmuir circulations. In the 2DCL simulation with carefully selected parameters, from the time sequences of the streamwise vorticity evolution, we found that the cell merging process resembles the inverse energy cascade in two dimensional turbulence. Vortex pairing and splitting processes are observed. Very limited vortex cancellation of the type suggested by Li and Garrett (1993) is found.

Eulerian mean flow effects are important in predicting the correct quantitative properties of Langmuir circulations. With the Eulerian mean flow, the 2DCL simulation with the Eulerian mean flow effects gives values of the maximum downwelling velocity and the pitch that lie within the range of field observations (Weller and Price 1988, Smith *et al.* 1987). Without it, the pitch predicted is far below the observed value. Thus the effects of the Eulerian mean flow need to be included in the Craik-Leibovich

theory, which is achieved by including the wave stress in the total stress at the top surface.

The key assumption of the Craik-Leibovich theory, disparate time scales, is examined by performing a 3Dwavy simulation of a flow under a propagating wavy surface using the full Navier-Stokes equations. Without averaging, Langmuir circulations found in the simulation coexist with the wave field and are modulated by the surface wave. Averaged in the streamwise direction, the 3Dwavy results are in excellent agreement with those from the calculation based on the Craik-Leibovich theory with the Eulerian mean flow effect included. Thus, the results both have verified the key assumption of the Craik-Leibovich theory and have confirmed the correctness of our 3D computer code for the flow under a wavy surface. Indeed, the validity of the Craik-Leibovich theory under the condition for which it was derived has been demonstrated.

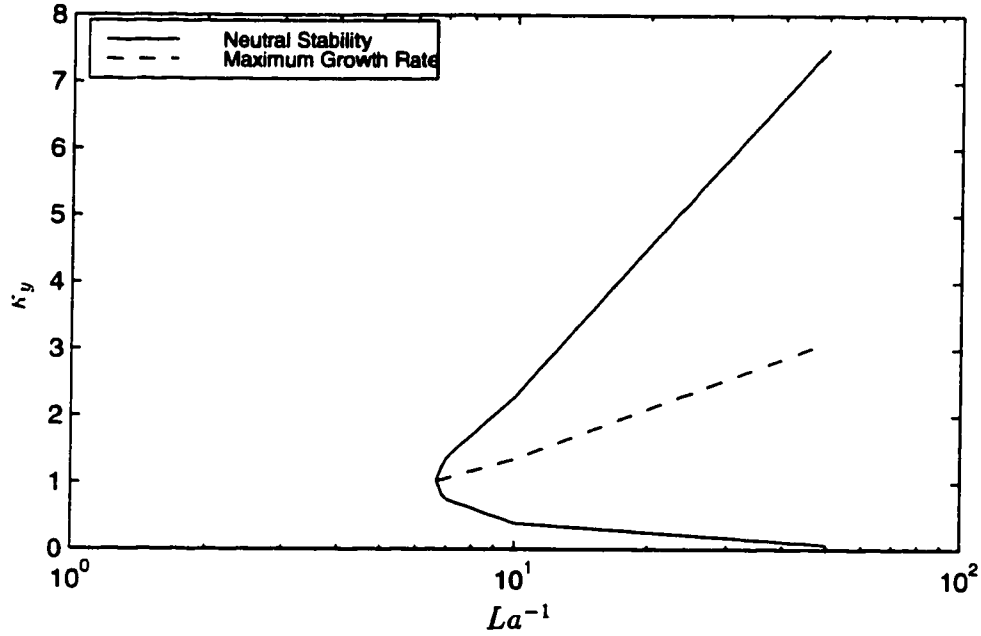

Figure 5.1: Stability Diagram for $\kappa_x = 1.5$.

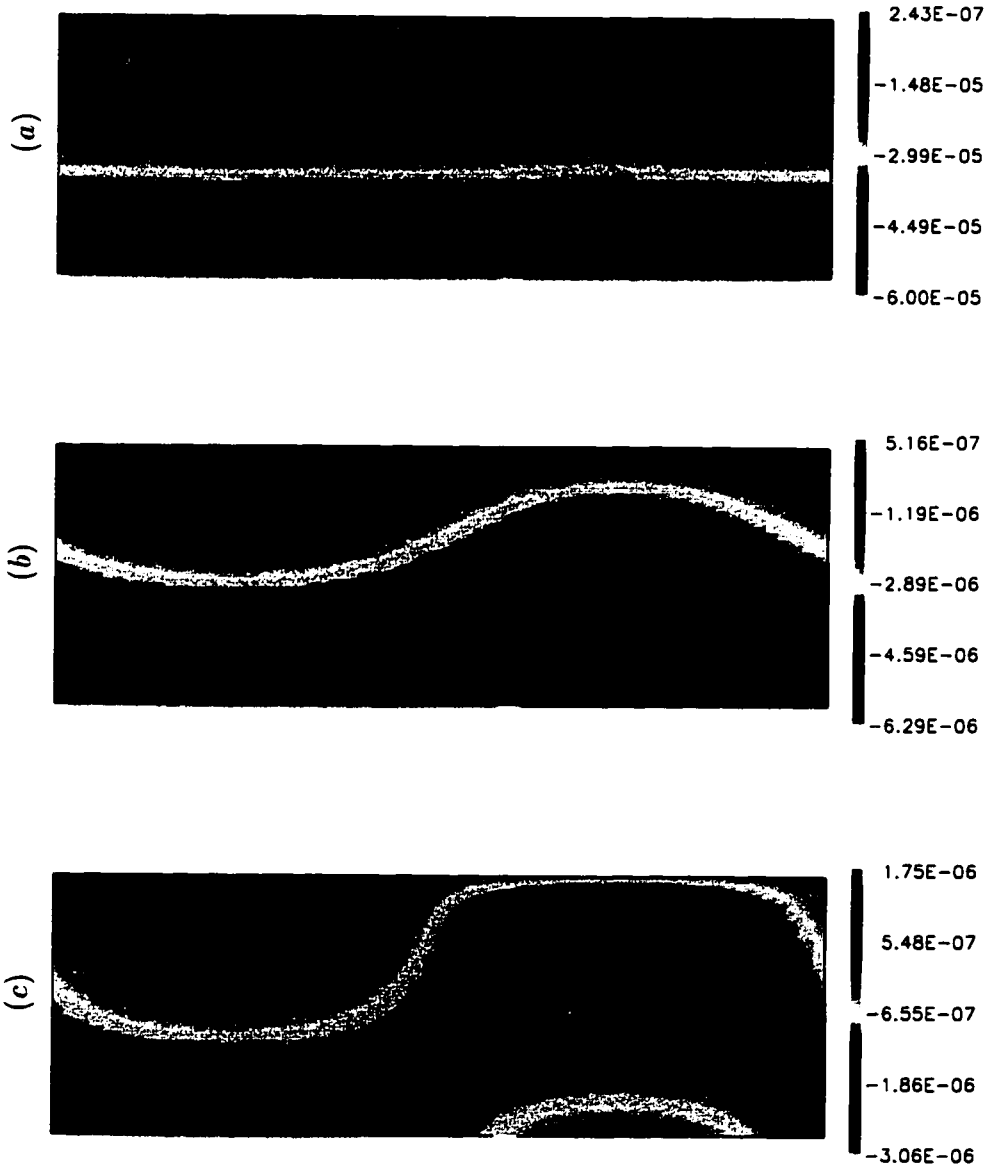

Figure 5.2: 2DCLW with $La = 1/7, Re_s = 7, \kappa_x = 1.5, \kappa_y = 1.06$. Development of streamwise vorticity (normalized by S/h). $(a) : t/T = 76, (b) : t/T = 1241, (c) : t/T = 1910$

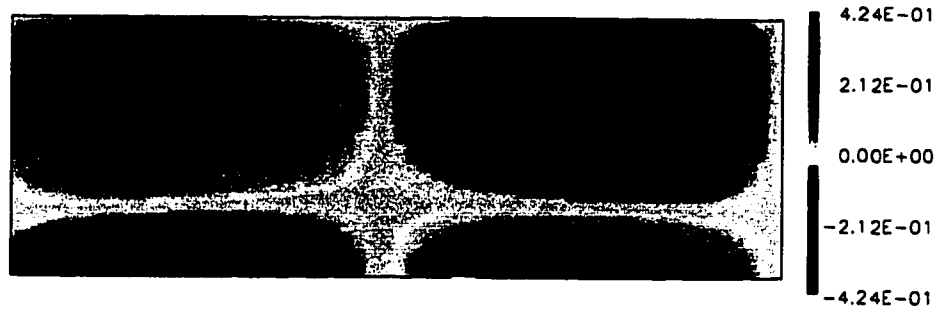

Figure 5.3: 2DCLW with $La = 1/7, Re_s = 7, \kappa_x = 1.5, \kappa_y = 1.06$. Streamwise vorticity (normalized by S/h) at steady state.

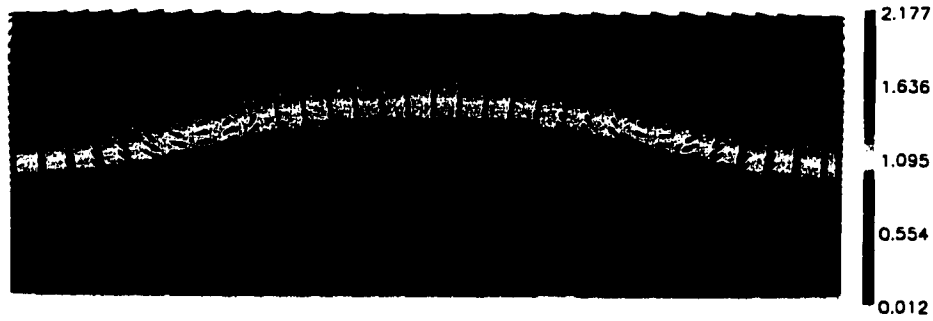

Figure 5.4: 2DCLW with $La = 1/7, Re_s = 7, \kappa_x = 1.5, \kappa_y = 1.06$. Velocity vectors and streamwise velocity contours (normalized by S) at steady state.

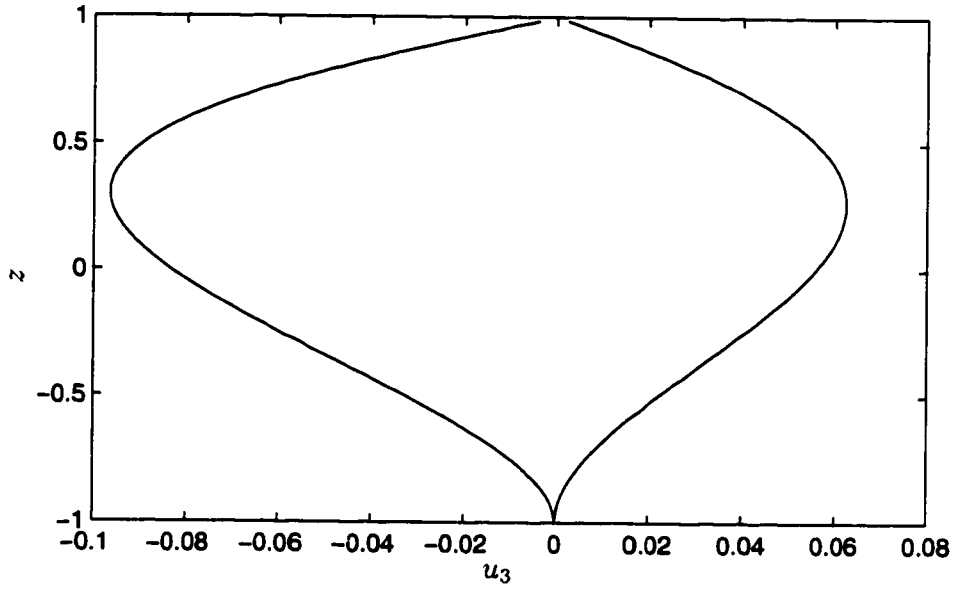

Figure 5.5: 2DCLW with $La = 1/7, Re_s = 7, \kappa_x = 1.5, \kappa_y = 1.06$. Vertical velocities (normalized by S) as functions of z (normalized by h) at convergence and divergence regions at steady state.

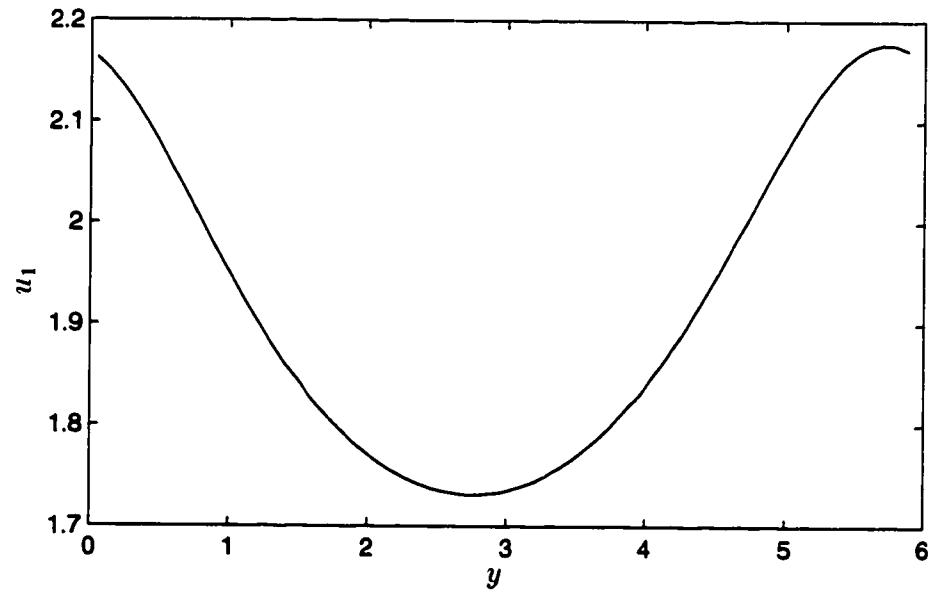

Figure 5.6: 2DCLW with $La = 1/7, Re_s = 7, \kappa_x = 1.5, \kappa_y = 1.06$. Surface downwind velocity (normalized by S) as a function of y (normalized by h) at steady state.

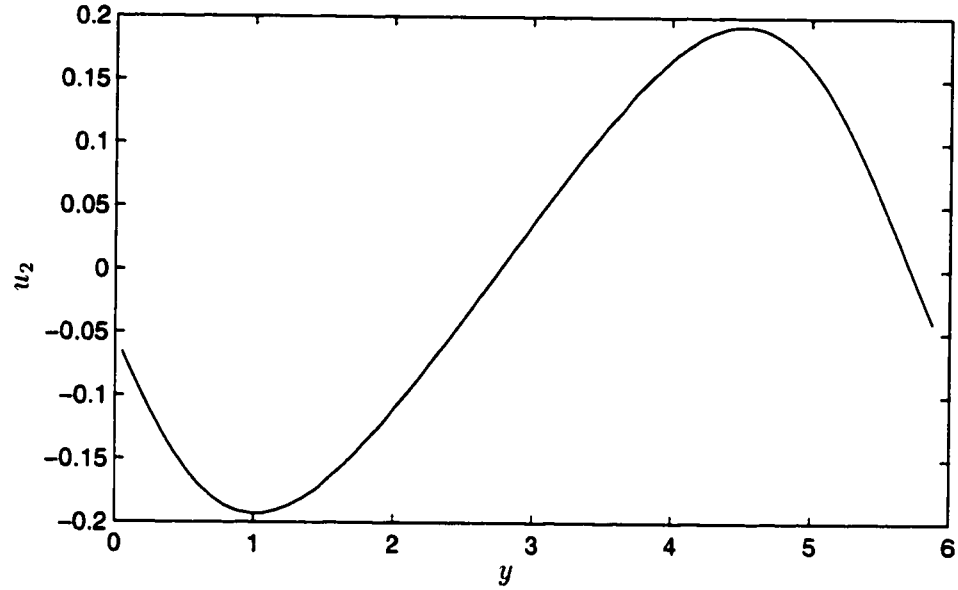

Figure 5.7: 2DCLW with $La = 1/7, Re_s = 7, \kappa_x = 1.5, \kappa_y = 1.06$. Surface sweeping velocity (normalized by S) as a function of y (normalized by h) at steady state.

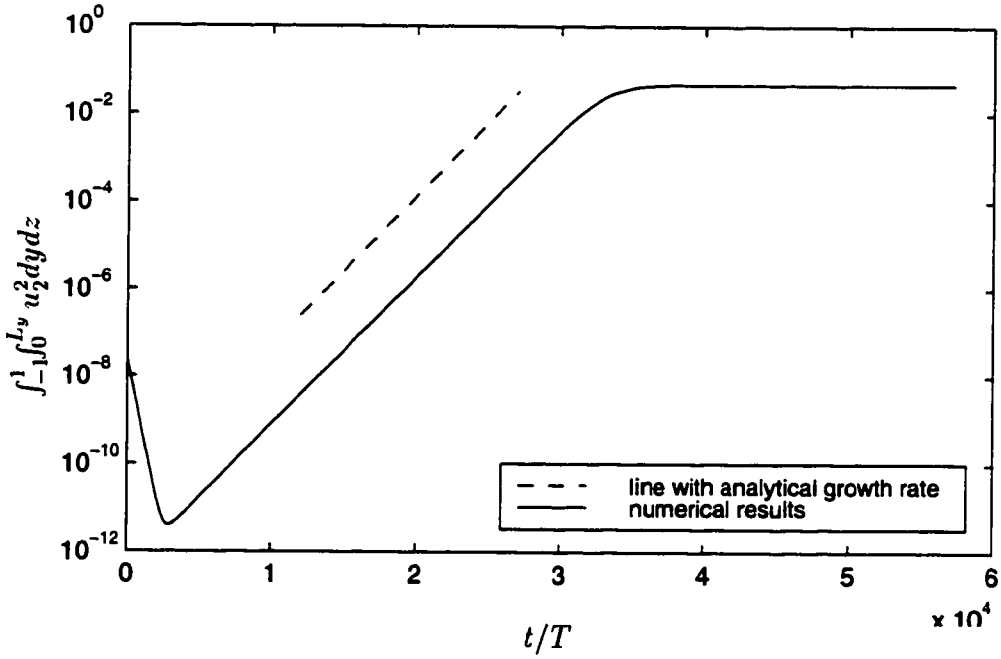

Figure 5.8: 2DCLW with $La = 1/7, Re_s = 7, \kappa_x = 1.5, \kappa_y = 1.06$. Development of kinetic energy computed from spanwise velocity (normalized by S^2) versus time. The dashed line has a slope given by linear stability theory.

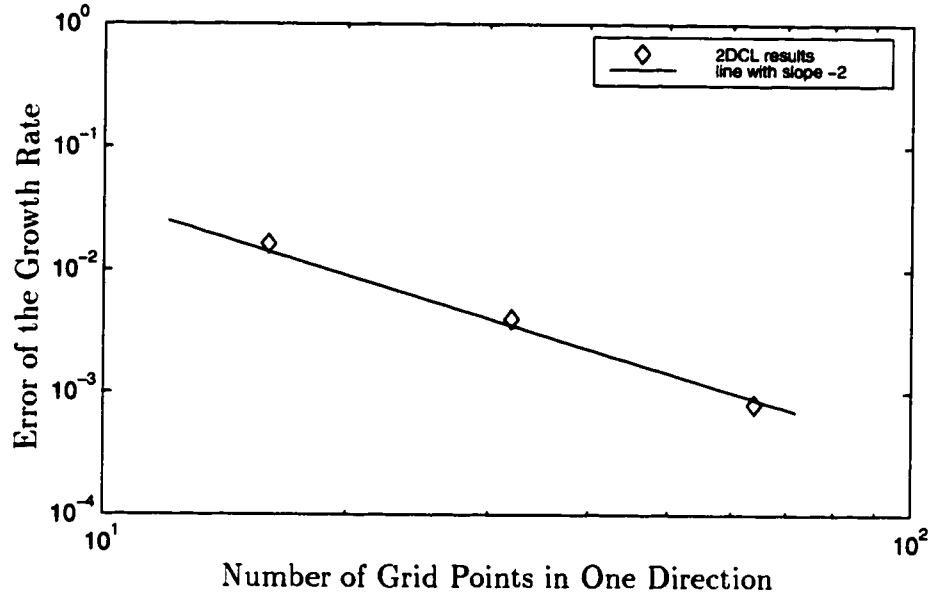

Figure 5.9: 2DCLW with $La = 1/7, Re_s = 7, \kappa_x = 1.5, \kappa_y = 1.06$. Grid Study.

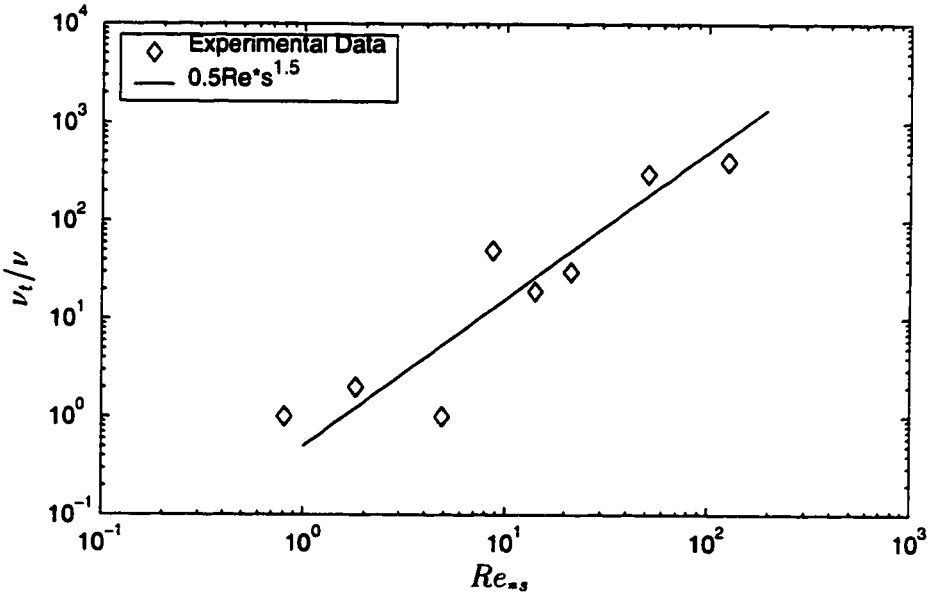

Figure 5.10: Near-surface eddy viscosity computed from Cheung (1985) as a function of $Re_{*s} = u_*^{d2}/\sigma^d\nu$.

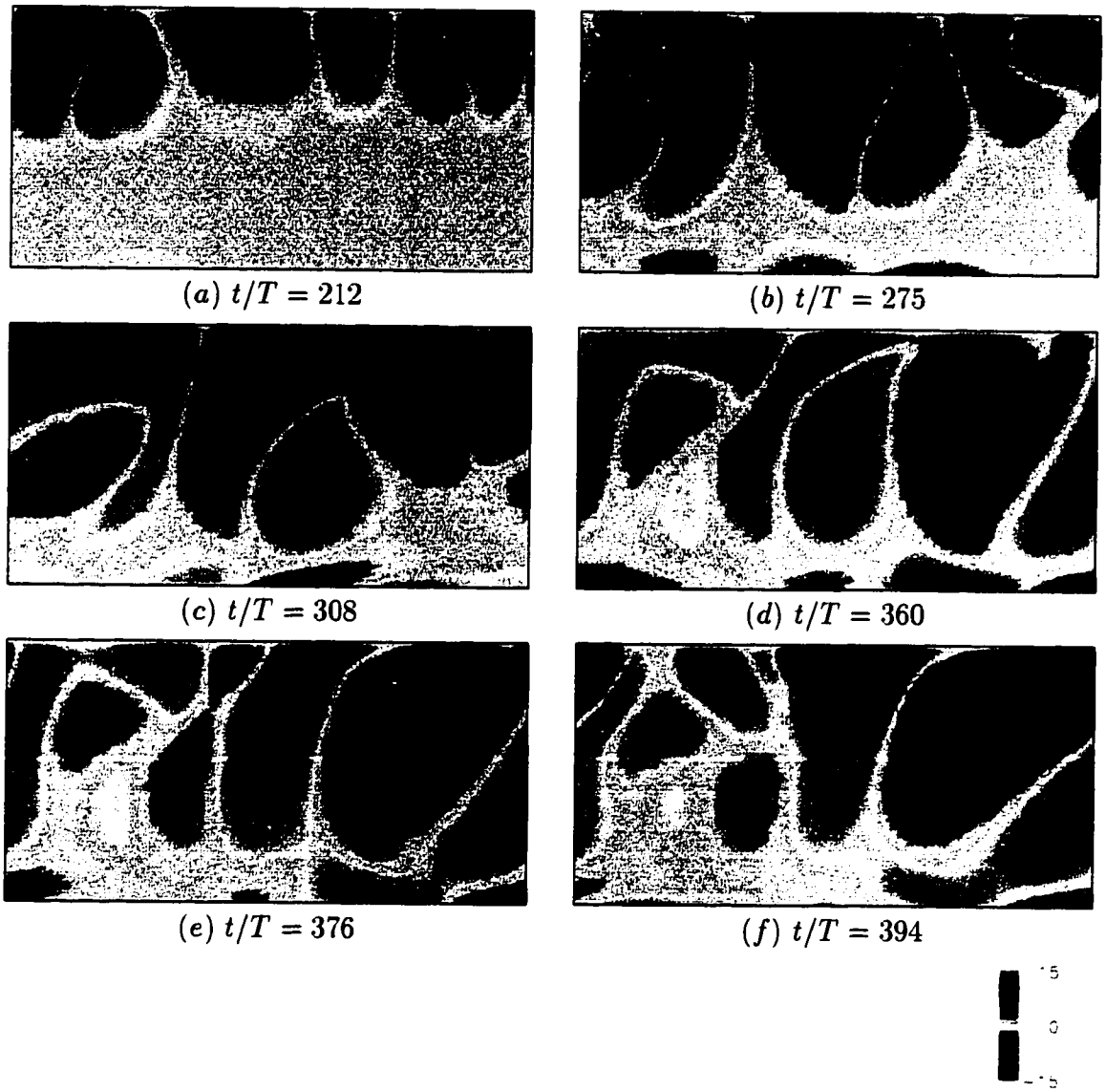

Figure 5.11: 2DCLM with $Re_{eff} = 24, Re_s = 36, \kappa_x = 2.0, \kappa_y = 1.57$. Streamwise vorticity contours (normalized by S/h) at various times. Part 1 of 3

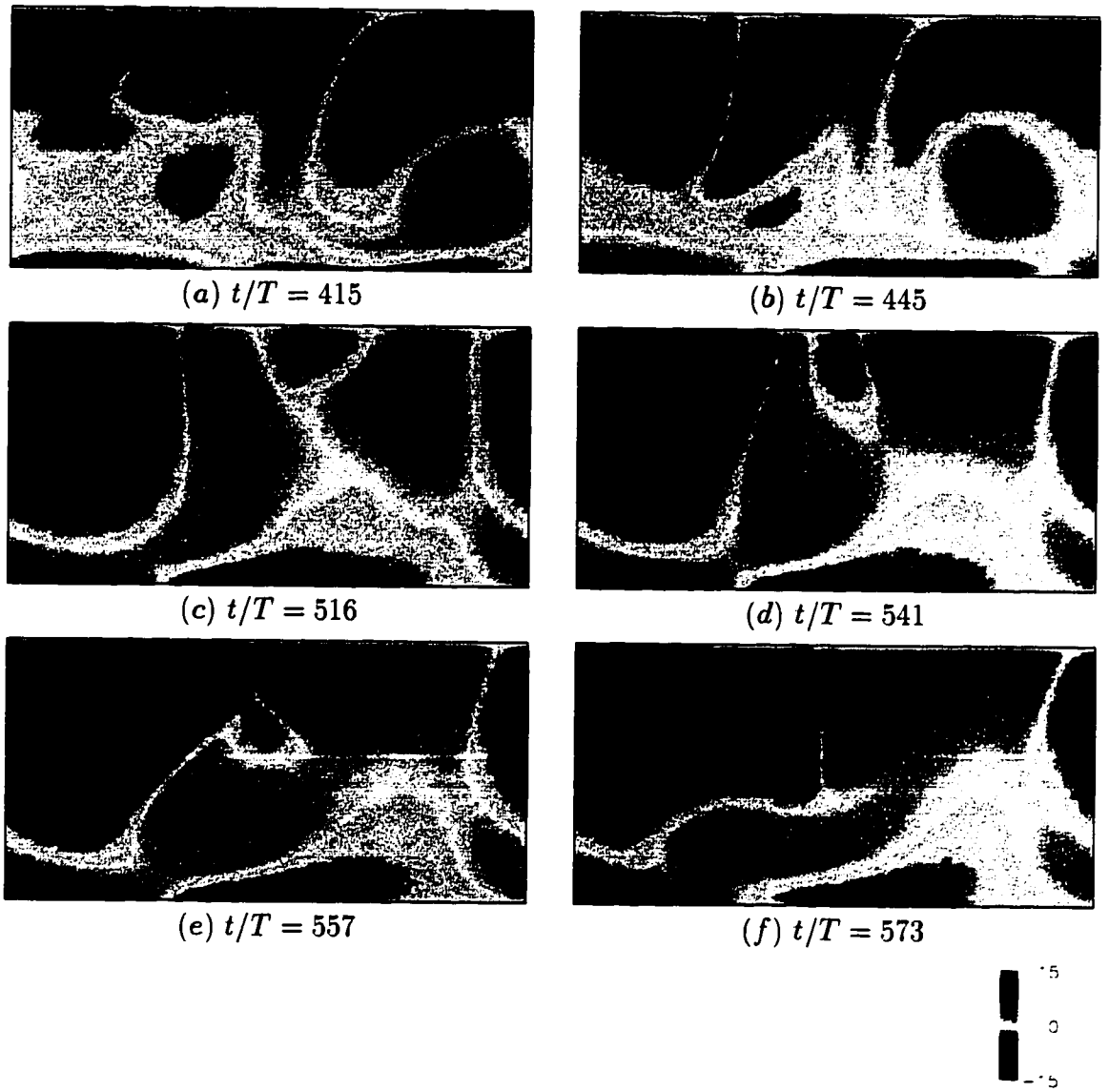

Figure 5.12: 2DCLM with $Re_{eff} = 24, Re_s = 36, \kappa_x = 2.0, \kappa_y = 1.57$. Streamwise vorticity contours (normalized by S/h) at various times. Part 2 of 3

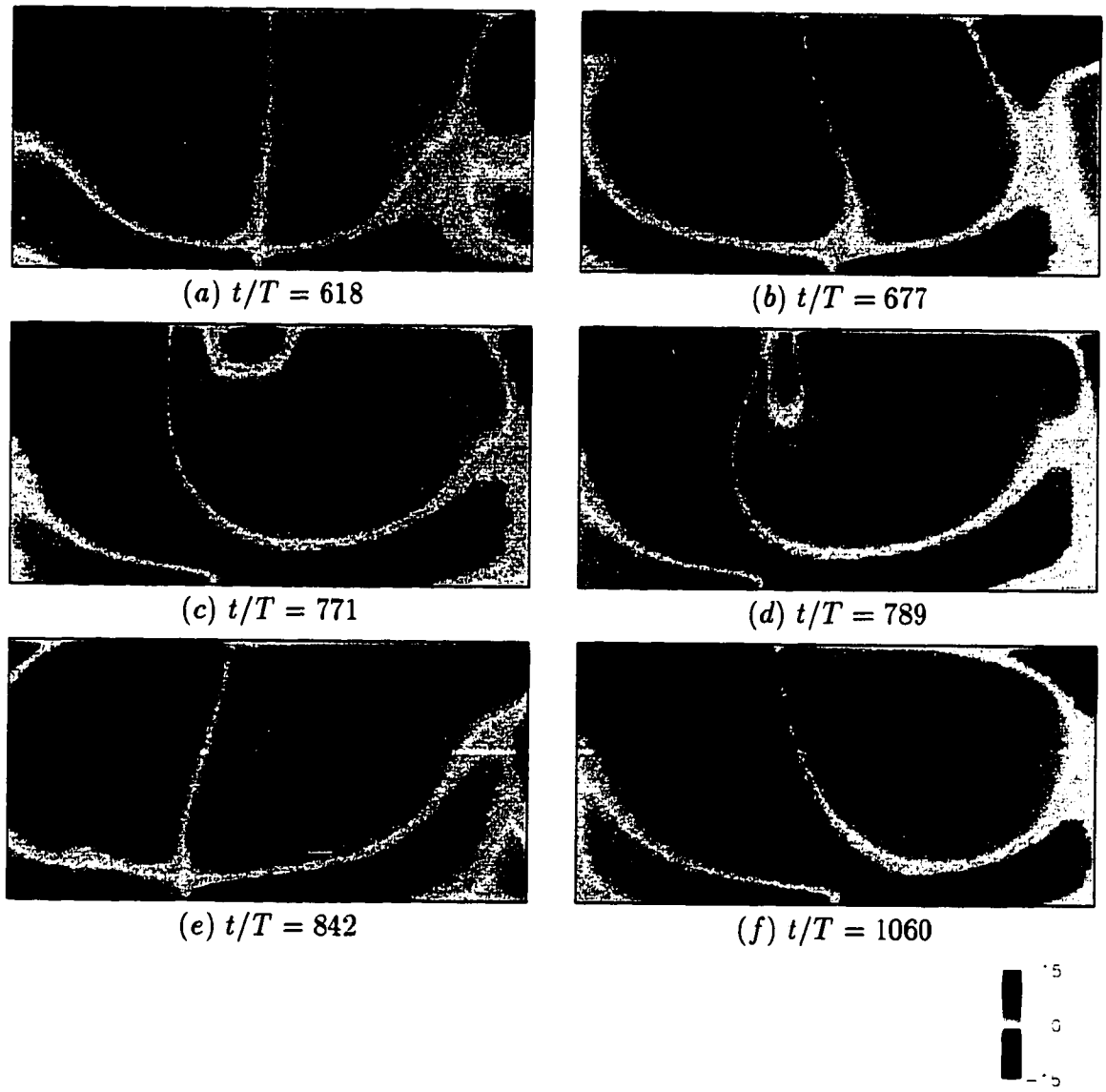

Figure 5.13: 2DCLM with $Re_{*eff} = 24, Re_s = 36, \kappa_x = 2.0, \kappa_y = 1.57$. Streamwise vorticity contours (normalized by S/h) at various times. Part 3 of 3

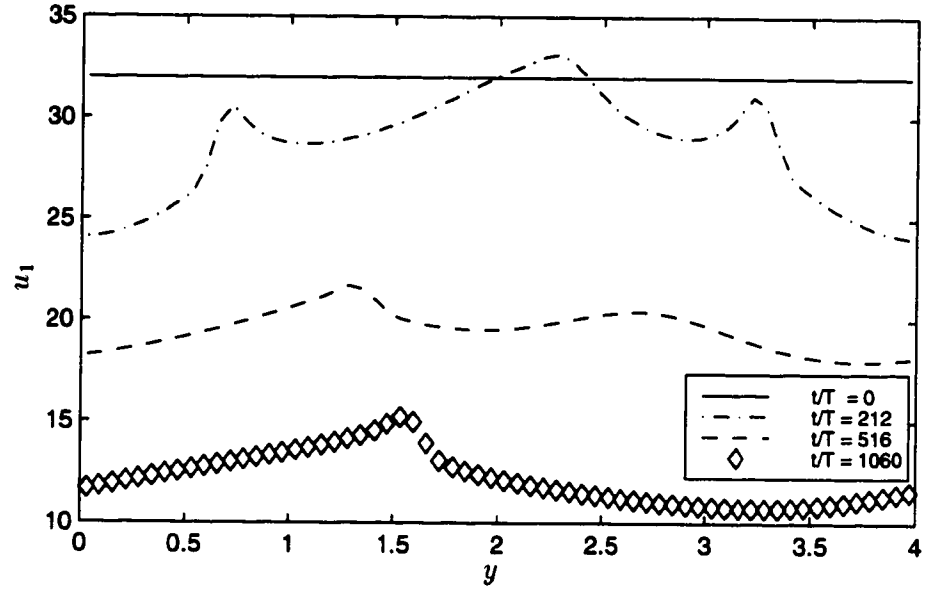

Figure 5.14: 2DCLM with $Re_{*eff} = 24, Re_s = 36, \kappa_x = 2.0, \kappa_y = 1.57$. Surface downwind velocity (normalized by S) as a function of y (normalized by h) at various times.

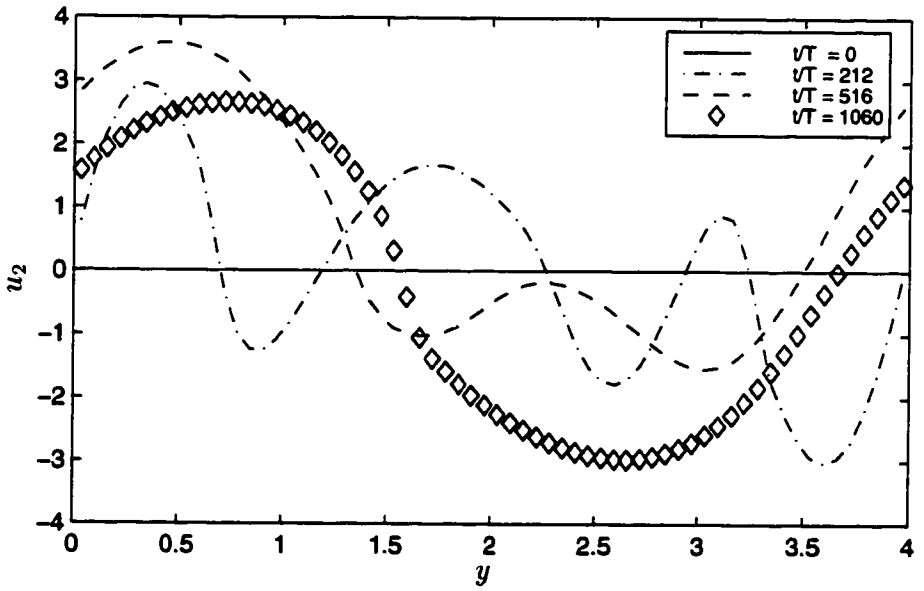

Figure 5.15: 2DCLM with $Re_{*eff} = 24, Re_s = 36, \kappa_x = 2.0, \kappa_y = 1.57$. Surface spanwise velocity (normalized by S) as a function of y (normalized by h) at various times.

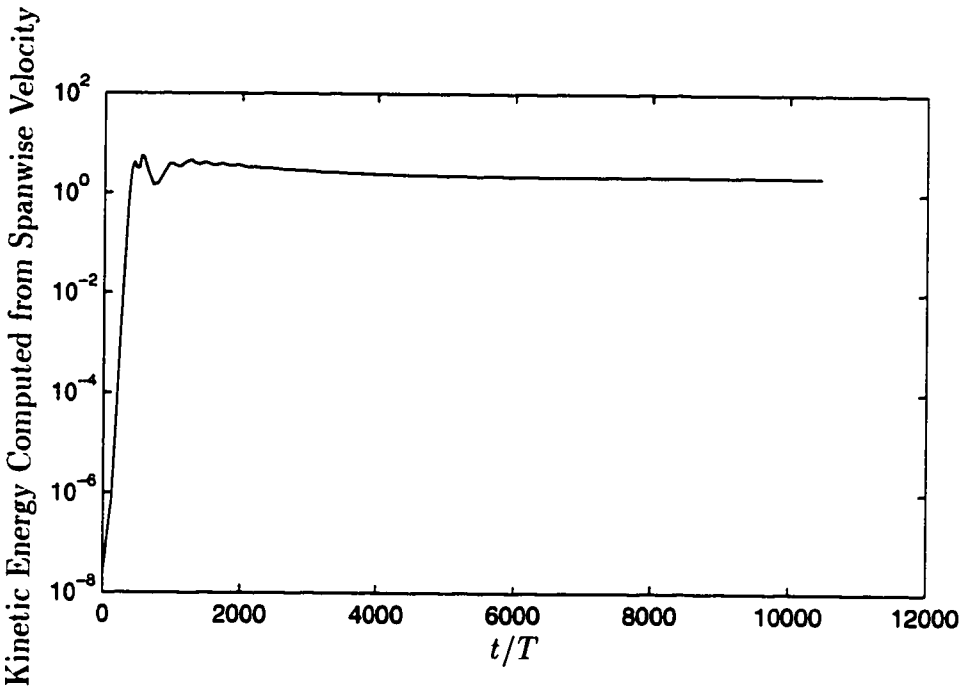

Figure 5.16: 2DCLM with $Re_{eff} = 24, Re_s = 36, \kappa_x = 2.0, \kappa_y = 1.57$. Development of kinetic energy (normalized by S^2) computed from spanwise velocity.

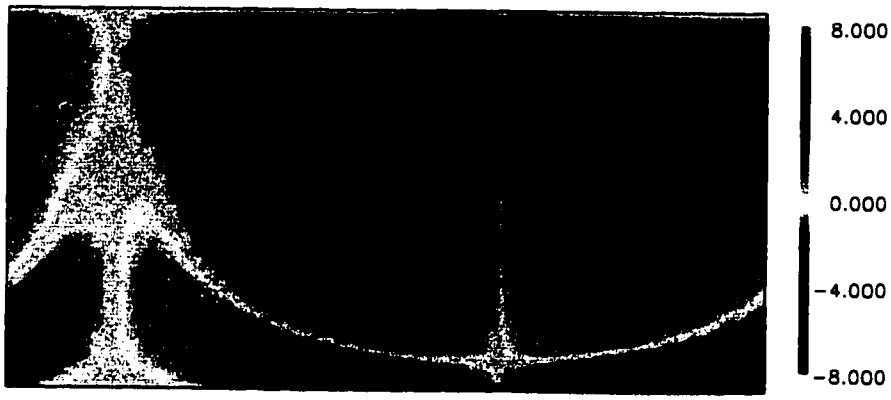

Figure 5.17: 2DCLM with $Re_{*eff} = 24, Re_s = 36, \kappa_x = 2.0, \kappa_y = 1.57$. Streamwise vorticity (normalized by S/h)at steady state.

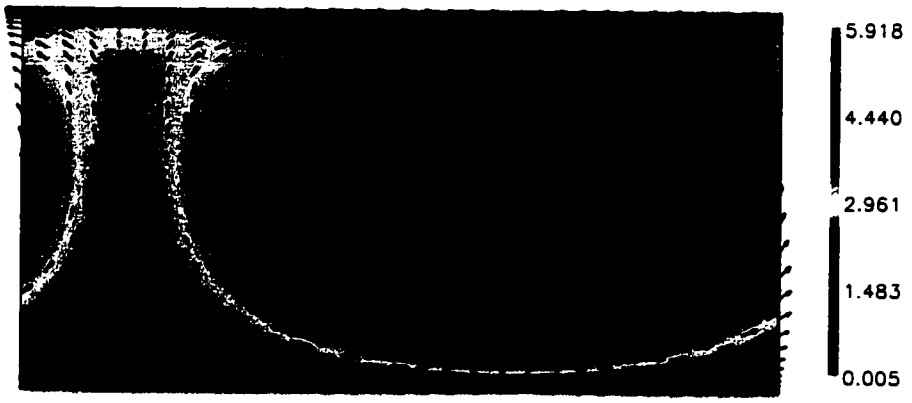

Figure 5.18: 2DCLM with $Re_{*eff} = 24, Re_s = 36, \kappa_x = 2.0, \kappa_y = 1.57$. Velocity vectors and streamwise velocity contours (normalized by S) at steady state.

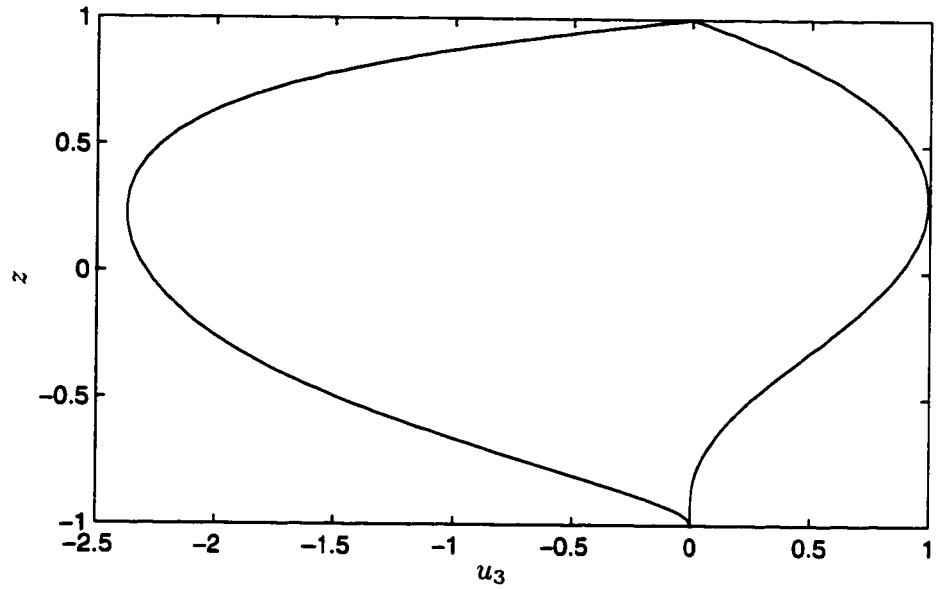

Figure 5.19: 2DCLM with $Re_{eff} = 24, Re_s = 36, \kappa_x = 2.0, \kappa_y = 1.57$. Vertical velocities (normalized by S) as functions of z (normalized by h) at convergence and divergence regions at steady state.

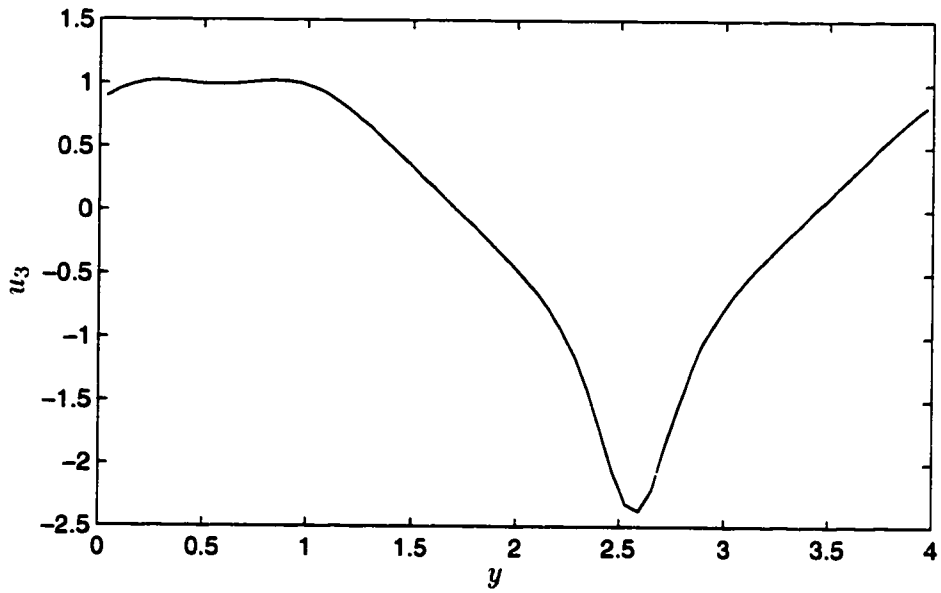

Figure 5.20: 2DCLM with $Re_{eff} = 24, Re_s = 36, \kappa_x = 2.0, \kappa_y = 1.57$. Vertical velocity (normalized by S) as a function of y (normalized by h) at the depth with maximum downwelling velocity.

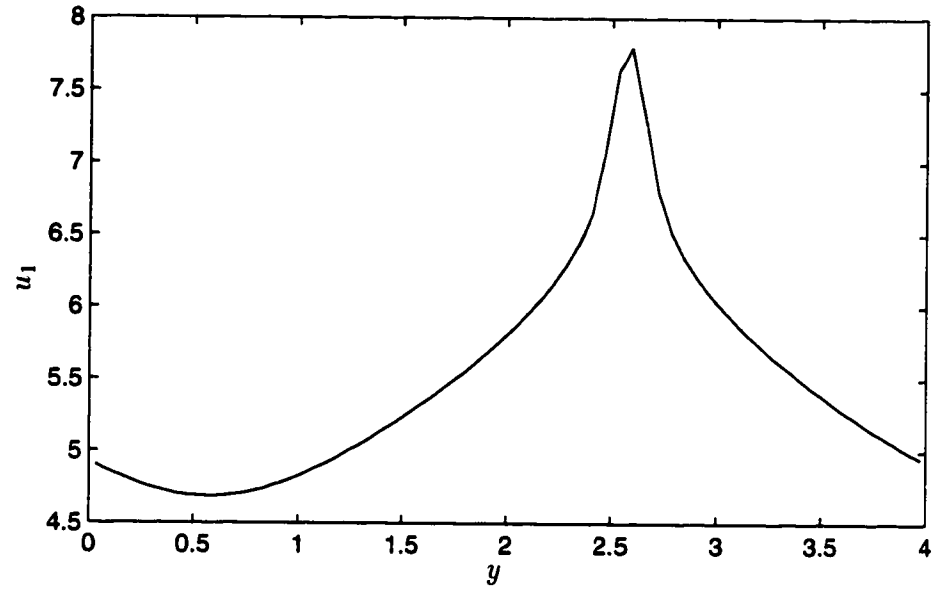

Figure 5.21: 2DCLM with $Re_{eff} = 24, Re_s = 36, \kappa_x = 2.0, \kappa_y = 1.57$. Surface downwind velocity (normalized by S) as a function of y (normalized by h) at steady state.

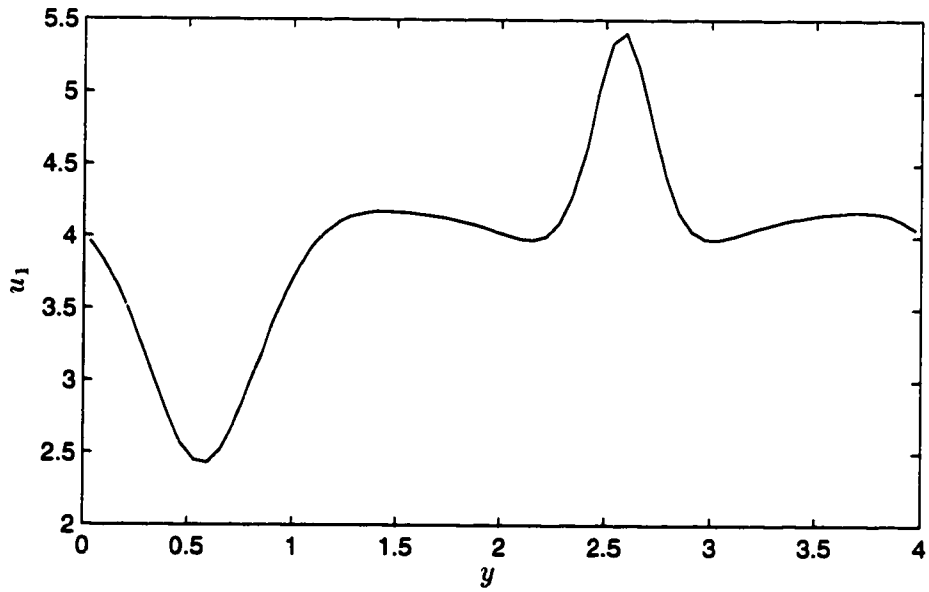

Figure 5.22: 2DCLM with $Re_{eff} = 24, Re_s = 36, \kappa_x = 2.0, \kappa_y = 1.57$. Downwind velocity (normalized by S) as a function of y (normalized by h) at the depth with maximum downwelling velocity.

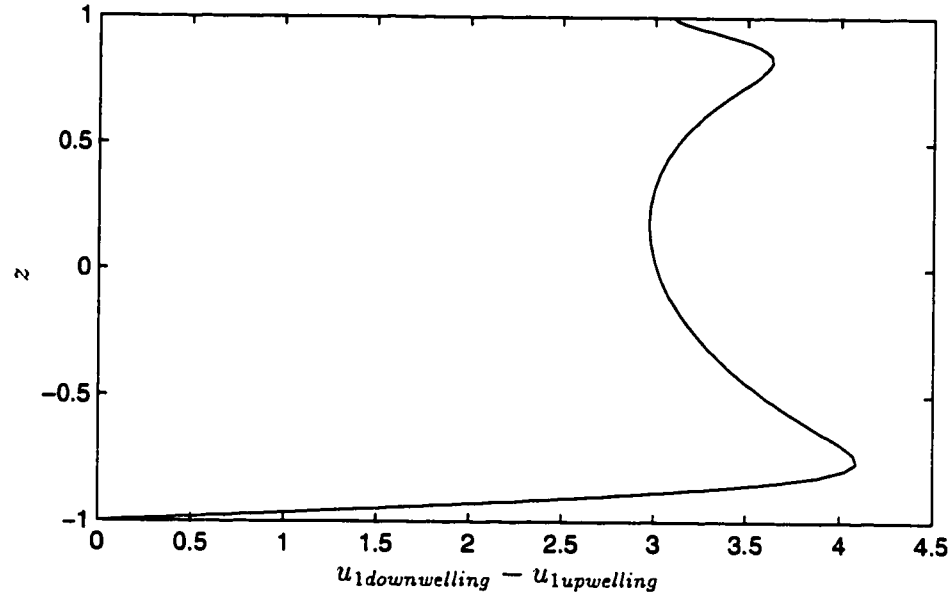

Figure 5.23: 2DCLM with $Re_{*eff} = 24, Re_s = 36, \kappa_x = 2.0, \kappa_y = 1.57$. Downwind jet strength (normalized by S) as a function of z (normalized by h) at steady state.

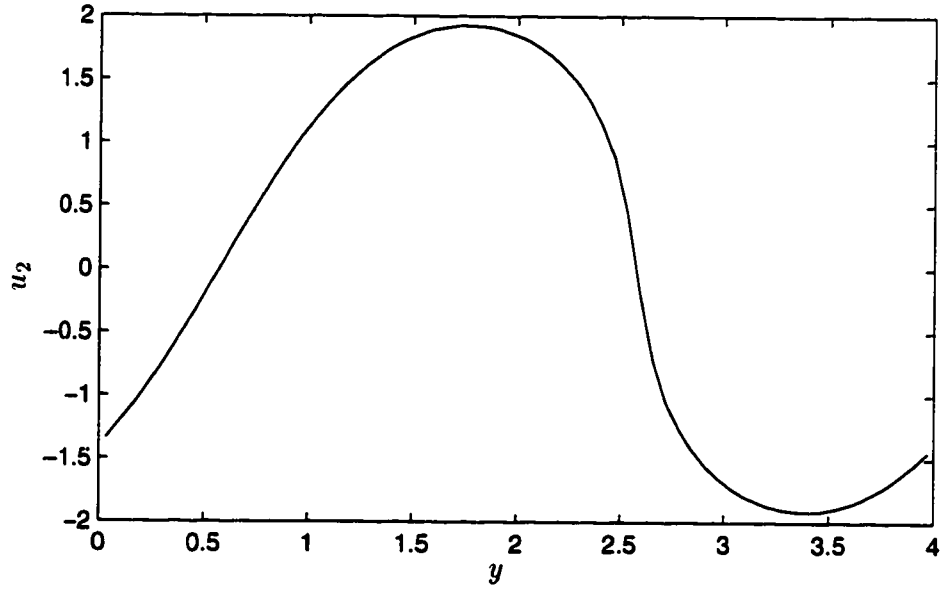

Figure 5.24: 2DCLM with $Re_{*eff} = 24, Re_s = 36, \kappa_x = 2.0, \kappa_y = 1.57$. Surface sweeping velocity (normalized by S) as a function of y (normalized by h) at steady state.

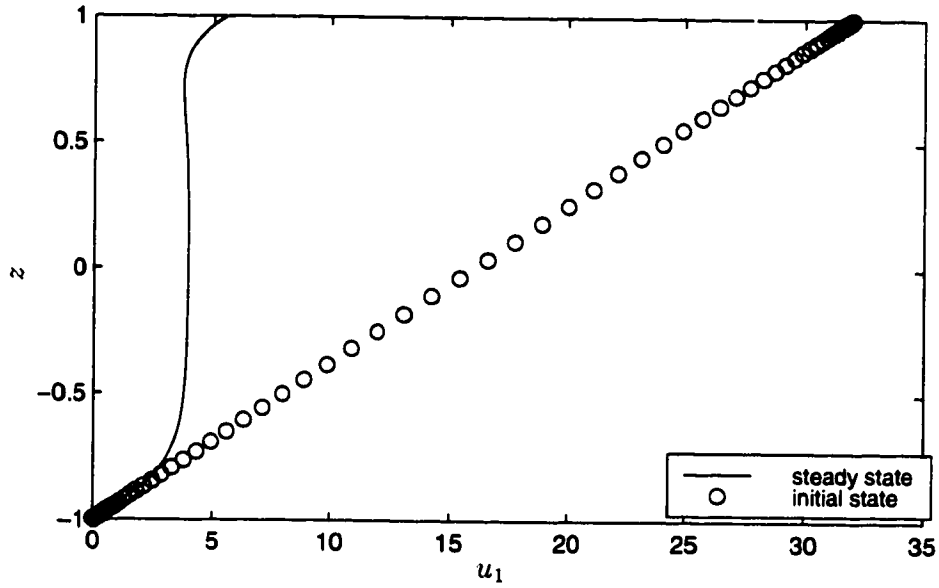

Figure 5.25: 2DCLM with $Re_{*eff} = 24, Re_s = 36, \kappa_x = 2.0, \kappa_y = 1.57$. Downwind velocity (normalized by S) averaged over spanwise direction. (z normalized by h)

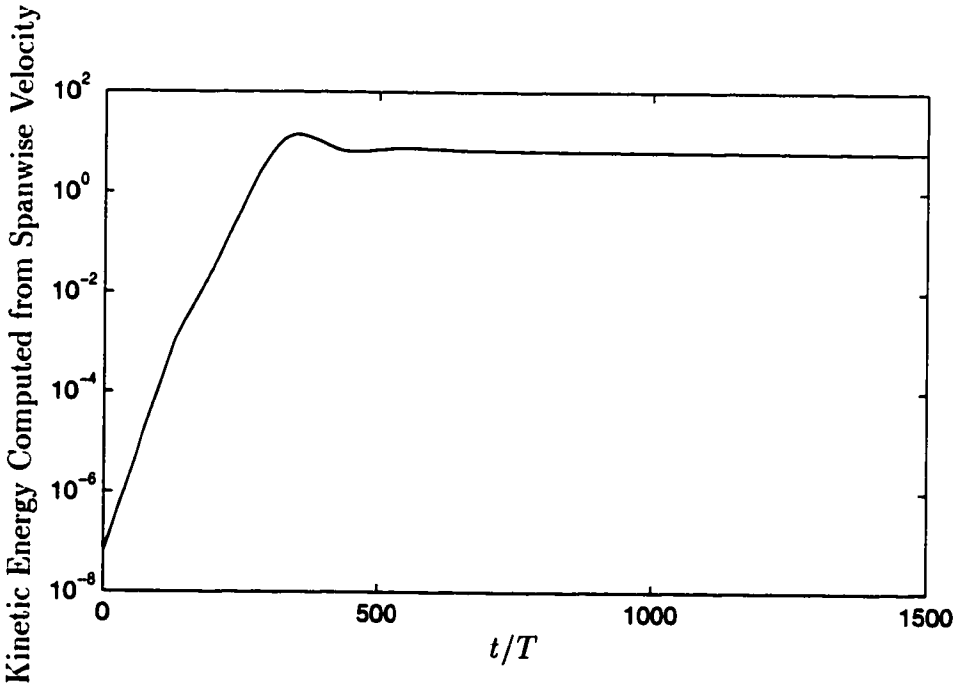

Figure 5.26: 3DwavyL1 with with $Re_* = 6.0, Re_s = 7.0, \kappa_x = 1.5, \kappa_y = 2.1, \epsilon = 0.1$. Development of kinetic energy (normalized by S^2) computed from spanwise velocity.

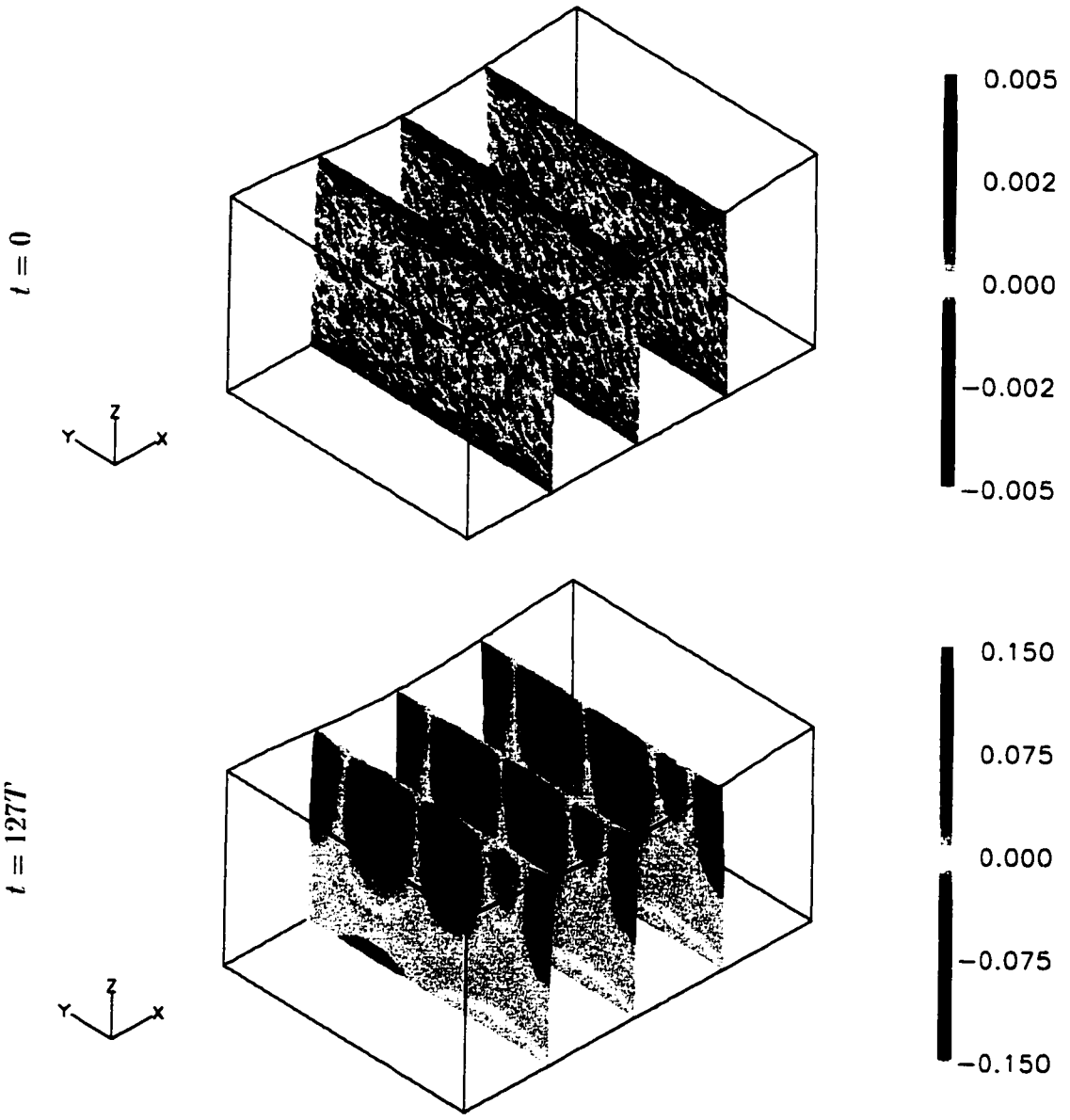

Figure 5.27: 3DwavyL1 with $Re_* = 6.0, Re_s = 7.0, \kappa_x = 1.5, \kappa_y = 2.1, \epsilon = 0.1$. Development of streamwise vorticity (normalized by S/h). Part 1 of 2.

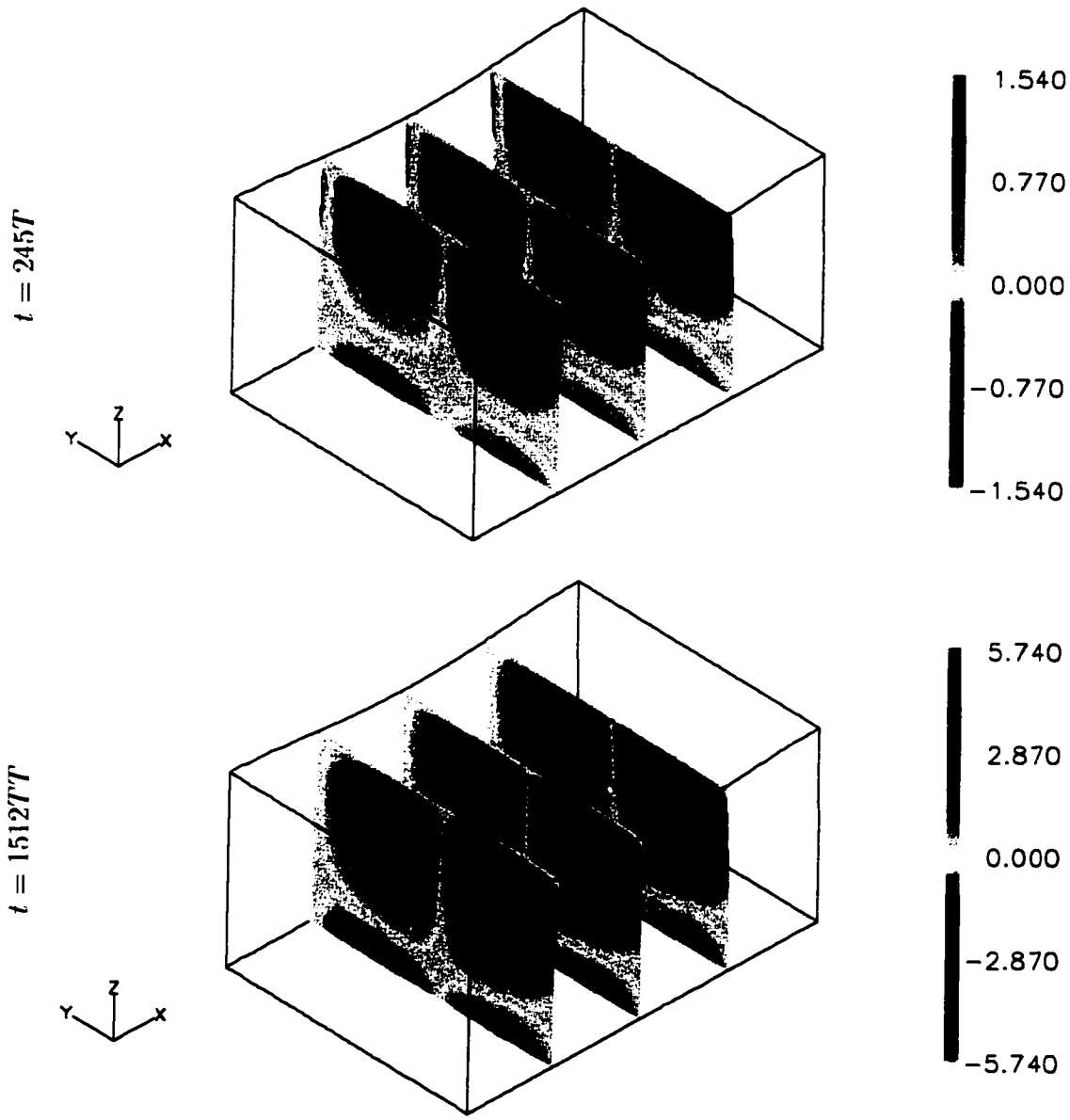

Figure 5.28: 3DwavyL1 with $Re_s = 6.0, Re_s = 7.0, \kappa_x = 1.5, \kappa_y = 2.1, \epsilon = 0.1$. Development of streamwise vorticity (normalized by S/h). Part 2 of 2.

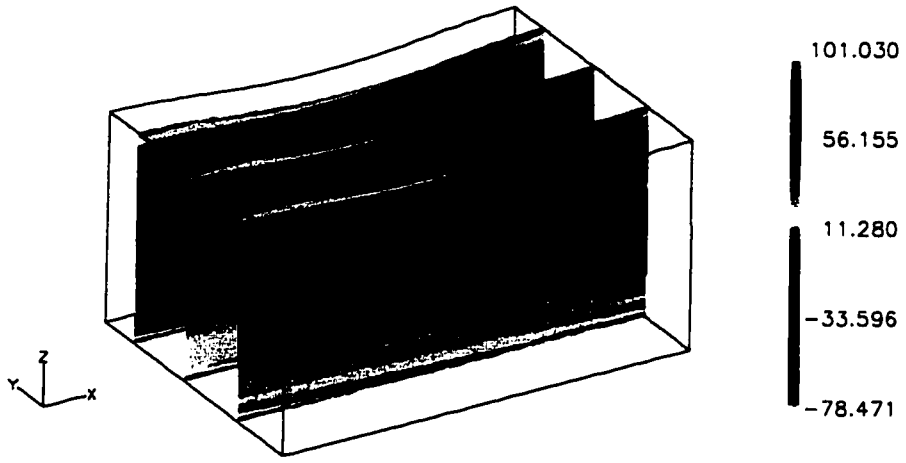

Figure 5.29: 3DwavyL1 with $Re_* = 6.0, Re_s = 7.0, \kappa_x = 1.5, \kappa_y = 2.1, \epsilon = 0.1$. Spanwise vorticity (normalized by S/h) at steady state on streamwise vertical planes.

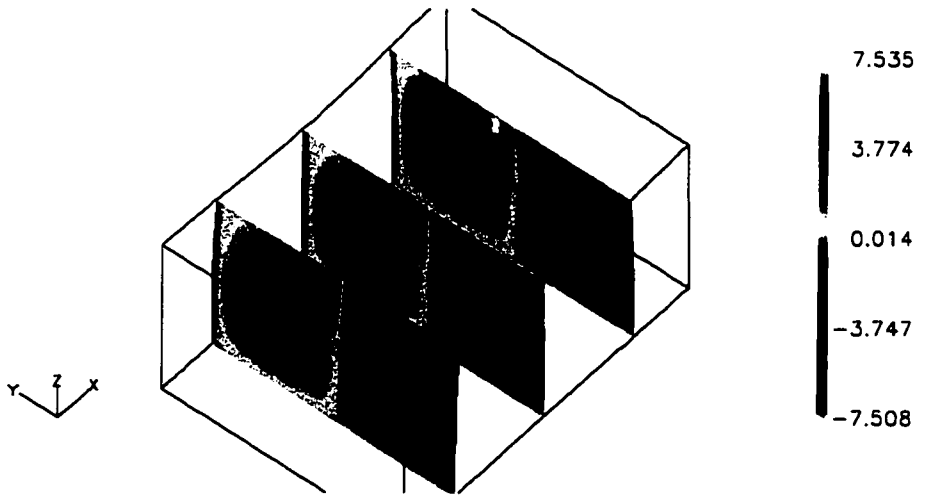

Figure 5.30: 3DwavyL1 with $Re_* = 6.0, Re_s = 7.0, \kappa_x = 1.5, \kappa_y = 2.1, \epsilon = 0.1$. Vertical vorticity (normalized by S/h) at steady state on spanwise vertical planes.

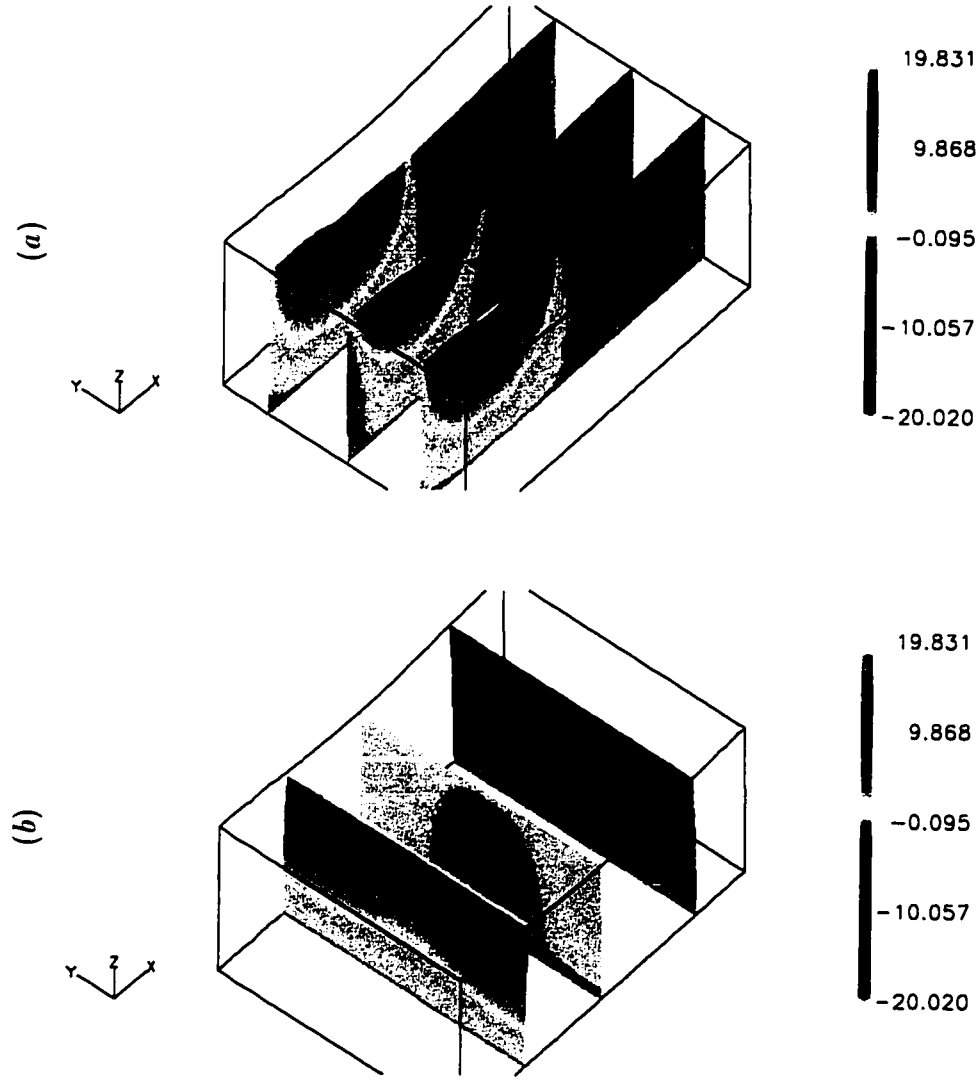

Figure 5.31: 3DwavyL1 with $Re_* = 6.0, Re_s = 7.0, \kappa_x = 1.5, \kappa_y = 2.1, \epsilon = 0.1$. Vertical velocity contours (normalized by S) at steady state.

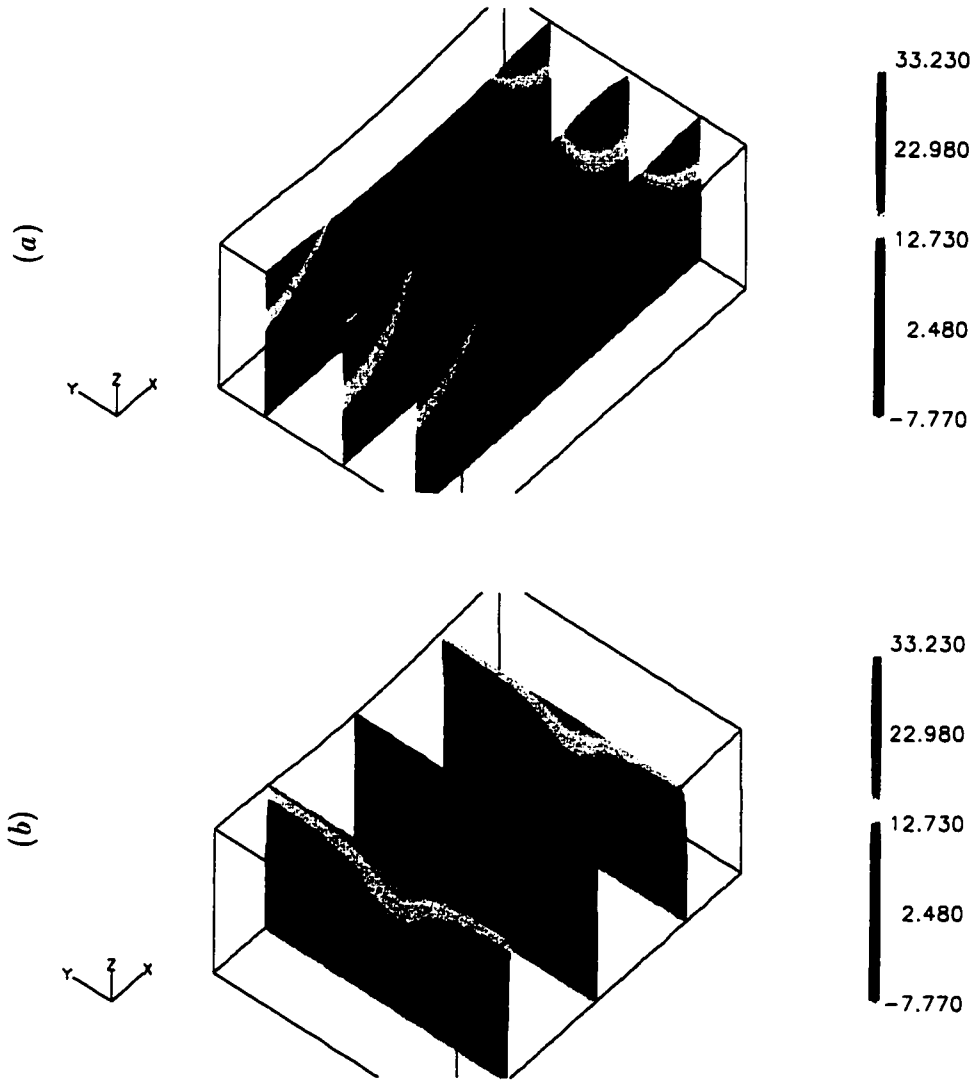

Figure 5.32: 3DwavyL1 with $Re_s = 6.0, Re_s = 7.0, \kappa_x = 1.5, \kappa_y = 2.1, \epsilon = 0.1$. Streamwise velocity contours (normalized by S) at steady state.

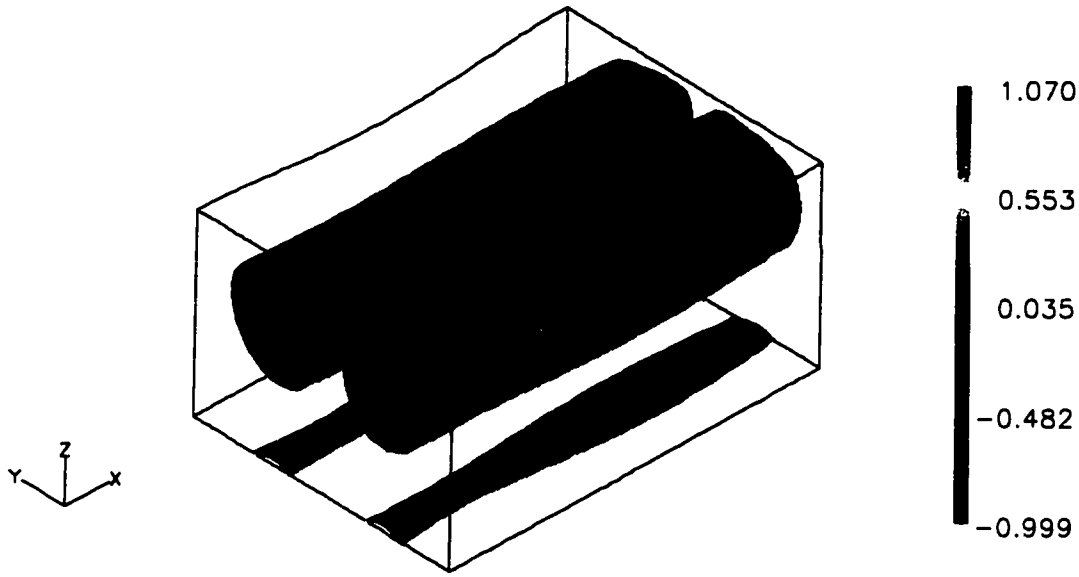

Figure 5.33: 3DwavyL1 with $Re_* = 6.0, Re_s = 7.0, \kappa_x = 1.5, \kappa_y = 2.1, \epsilon = 0.1$. Iso-surface of $\omega_1 = \pm 2.25$ (normalized by S/h). The color scale denotes the height.

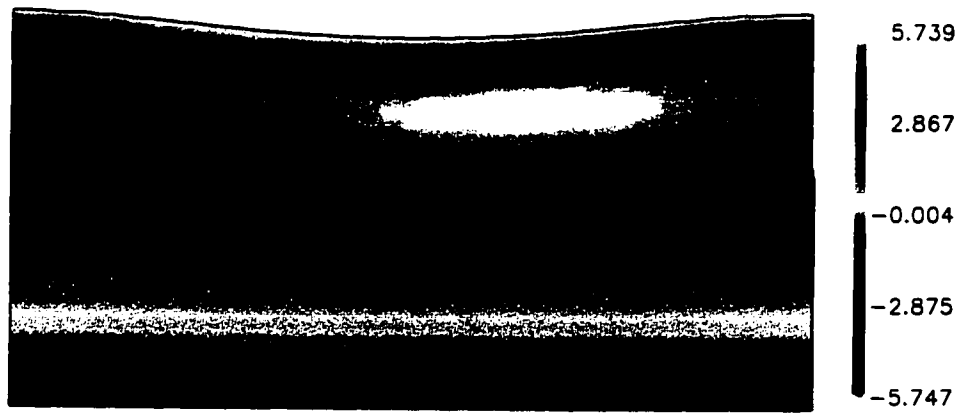

Figure 5.34: 3DwavyL1 with $Re_* = 6.0, Re_s = 7.0, \kappa_x = 1.5, \kappa_y = 2.1, \epsilon = 0.1$. Streamwise vorticity contours on the streamwise vertical plane of the center of the Langmuit cell with positive streamwise vorticity. (normalize by S/h)

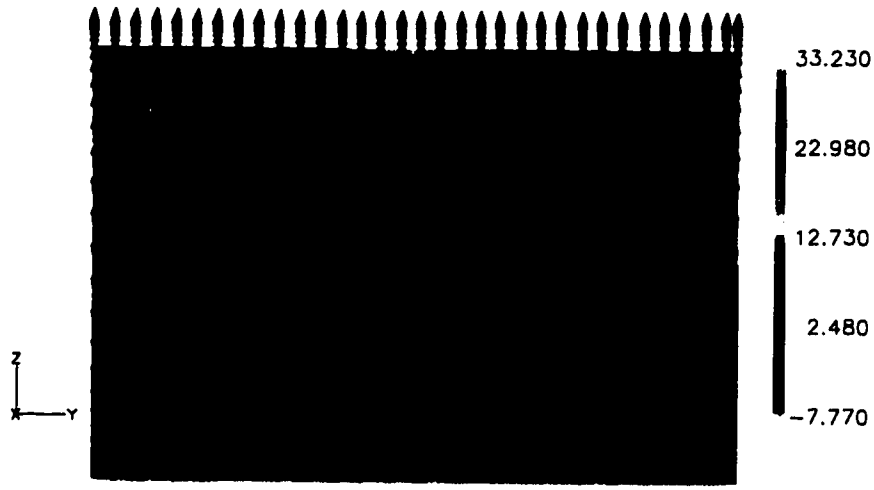

Figure 5.35: 3DwavyL1. Velocity vectors and streamwise velocity contours on a spanwise-vertical plane at forward slope of the surface wave. (contour scale normalized by S)

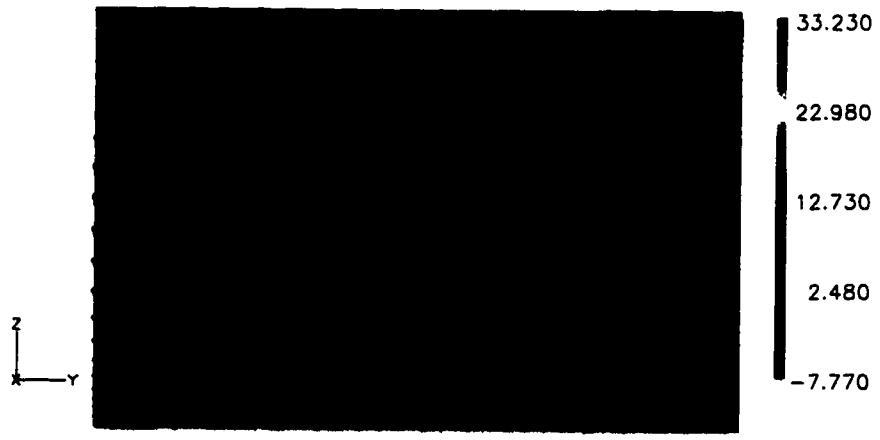

Figure 5.36: 3DwavyL1. Velocity vectors and streamwise velocity contours on a spanwise-vertical plane near the trough of the surface wave. (contour scale normalized by S)

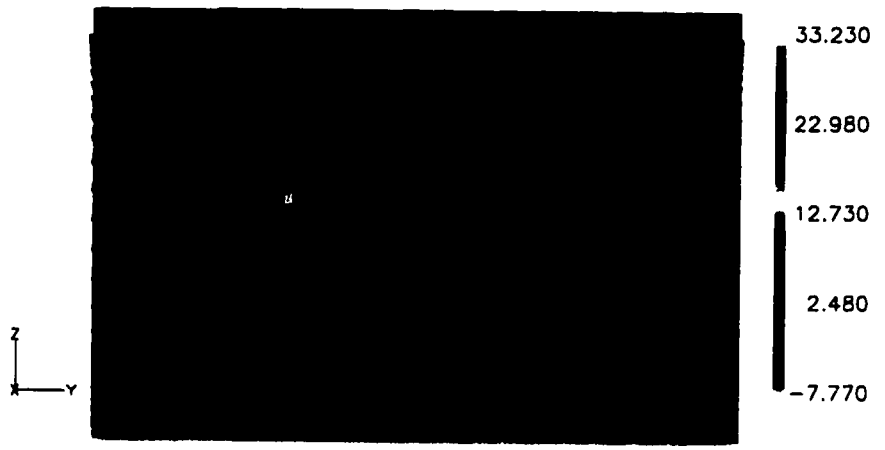

Figure 5.37: 3DwavyL1. Velocity vectors and streamwise velocity contours on a spanwise-vertical plane at backward slope of the surface wave. (contour scale normalized by S)

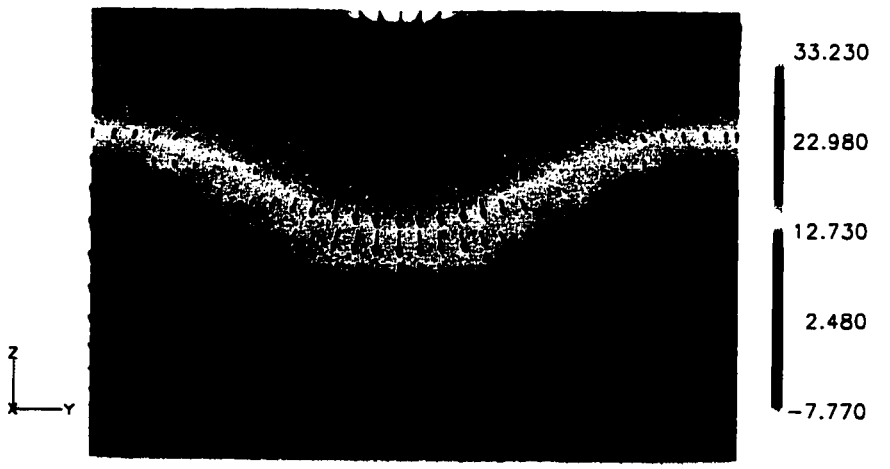

Figure 5.38: 3DwavyL1. Velocity vectors and streamwise velocity contours on a spanwise-vertical plane near the crest of the surface wave. (contour scale normalized by S)

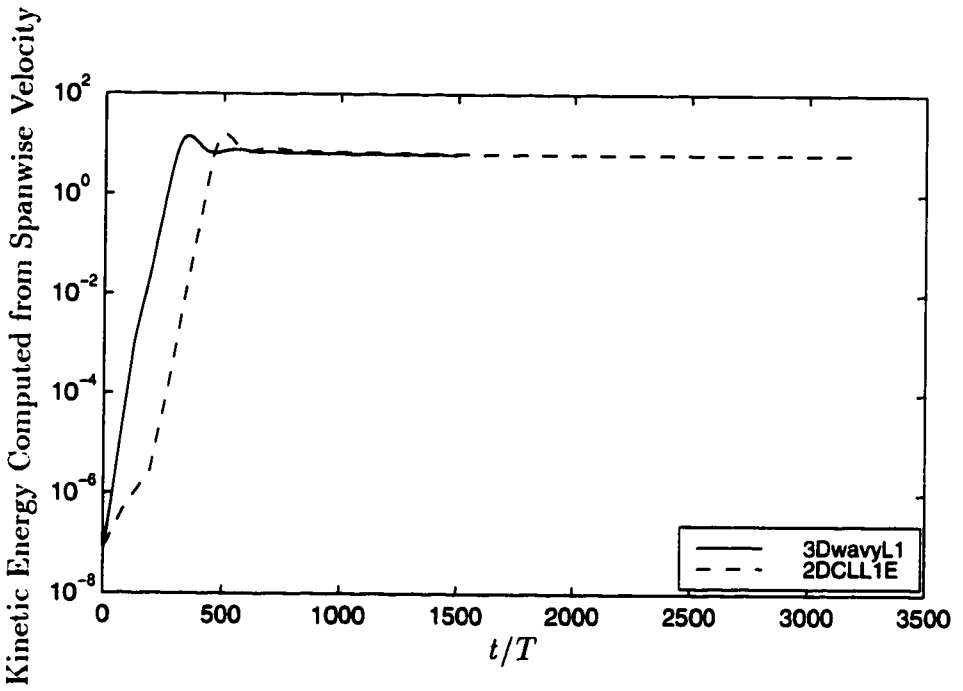

Figure 5.39: Comparison of the development of kinetic energy (normalized by S^2) computed from spanwise velocity between 3DwavyL1 and 2DCLL1E.

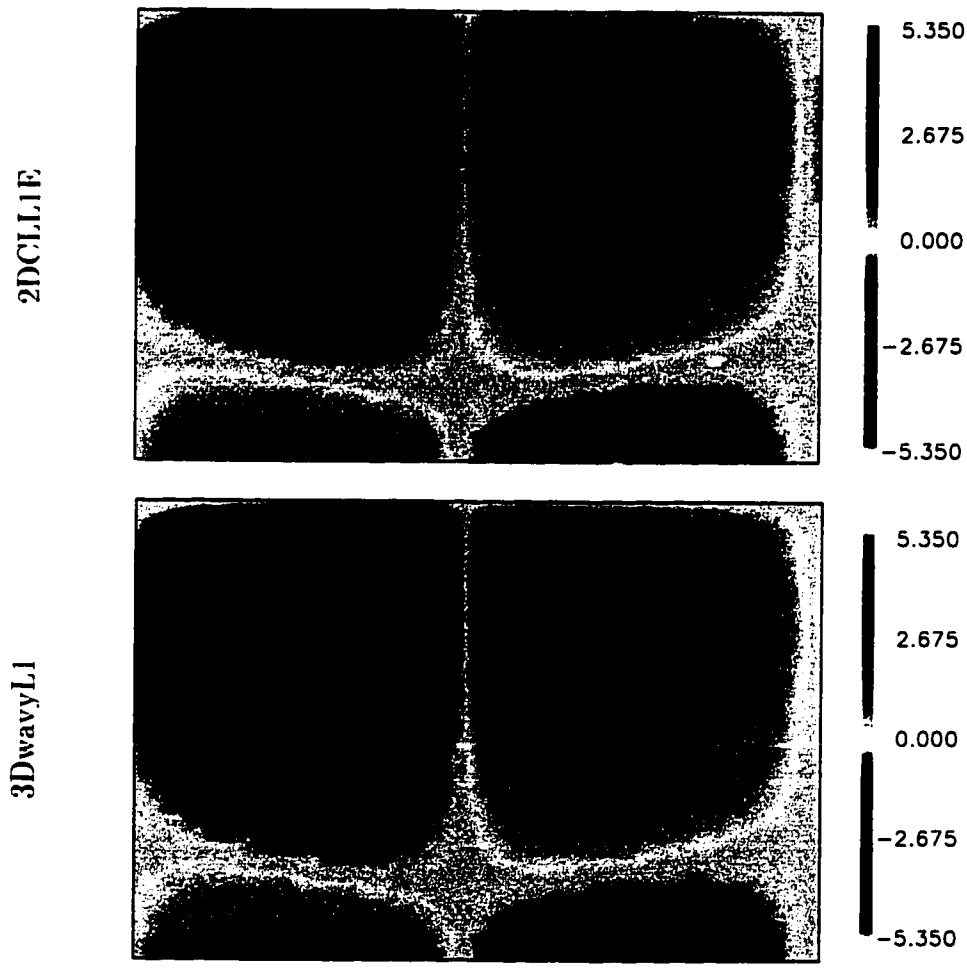

Figure 5.40: Comparison of 3DwavyL1 and 2DCLL1E. Contours of the streamwise vorticity at the spanwise vertical plane (normalized by $\frac{S}{h}$). The vorticity contours for the 3Dwavy case are obtained with streamwise averaging. The contours for the 2DCLL1E case are phase-shifted in the spanwise direction.

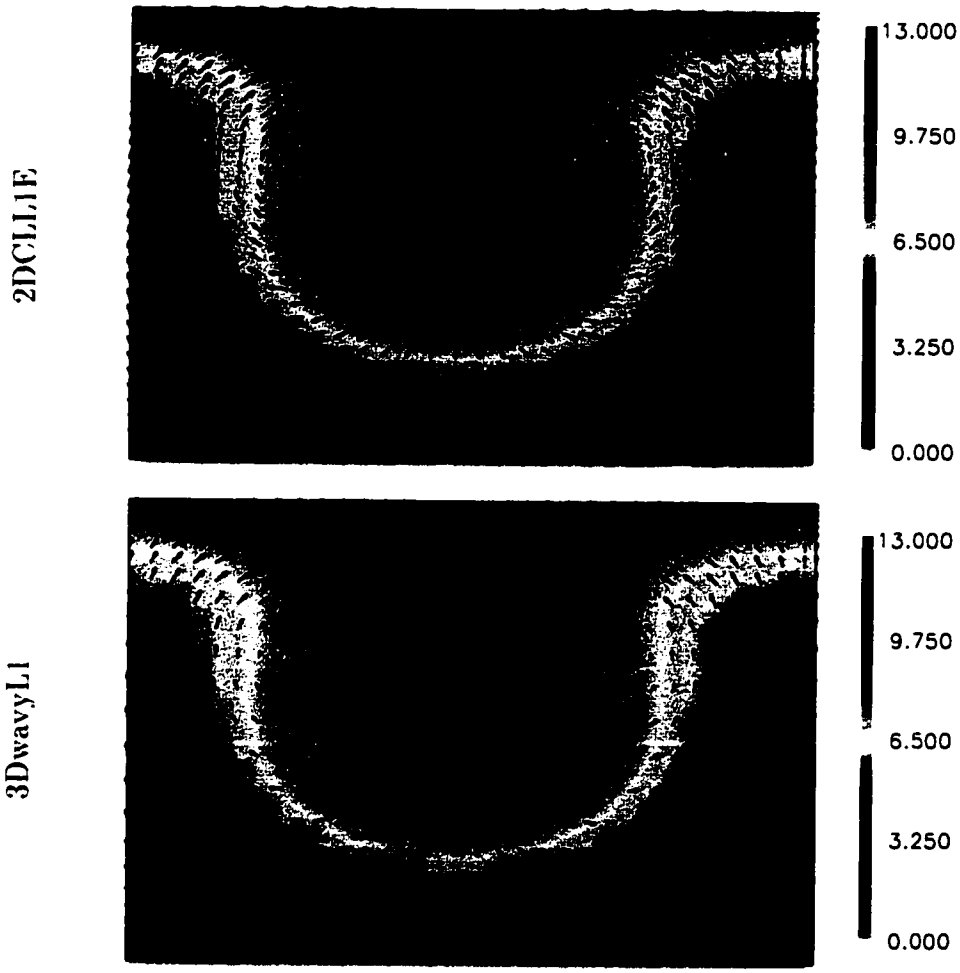

Figure 5.41: Comparison of 3DwavyL1 and 2DCLL1E. Velocity vectors and contours of the streamwise velocity at the spanwise vertical plane (normalized by S). The plot for the 3Dwavy case is obtained with streamwise averaging. The plot for the 2DCLL1E case is phase-shifted in the spanwise direction.

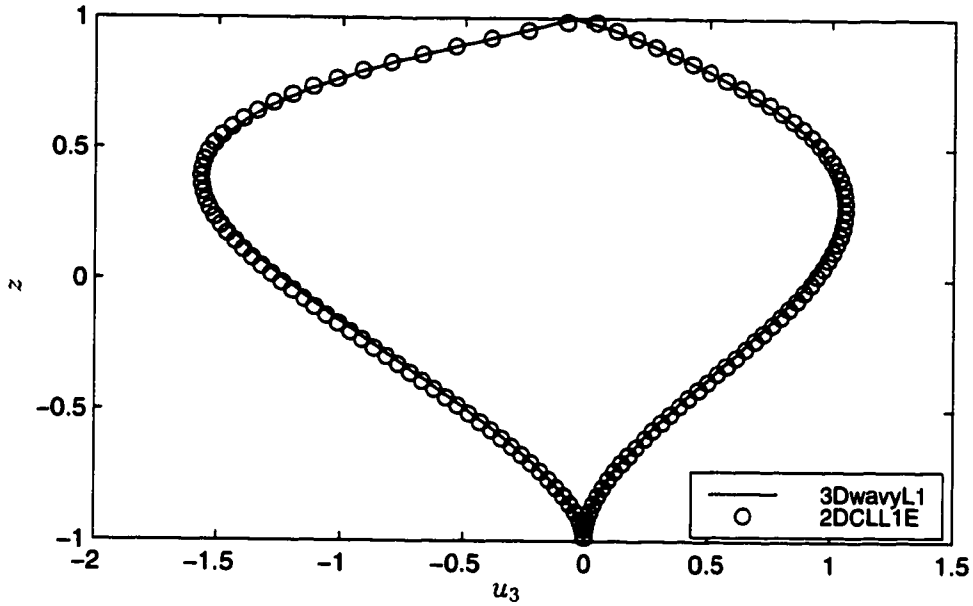

Figure 5.42: Comparison of 3DwavyL1 and 2DCLL1E. Vertical velocities (normalized by S) as functions of z (normalized by h) at upwelling and downwelling center line. The profiles for the 3DwavyL1 case are obtained by averaging in the streamwise direction.

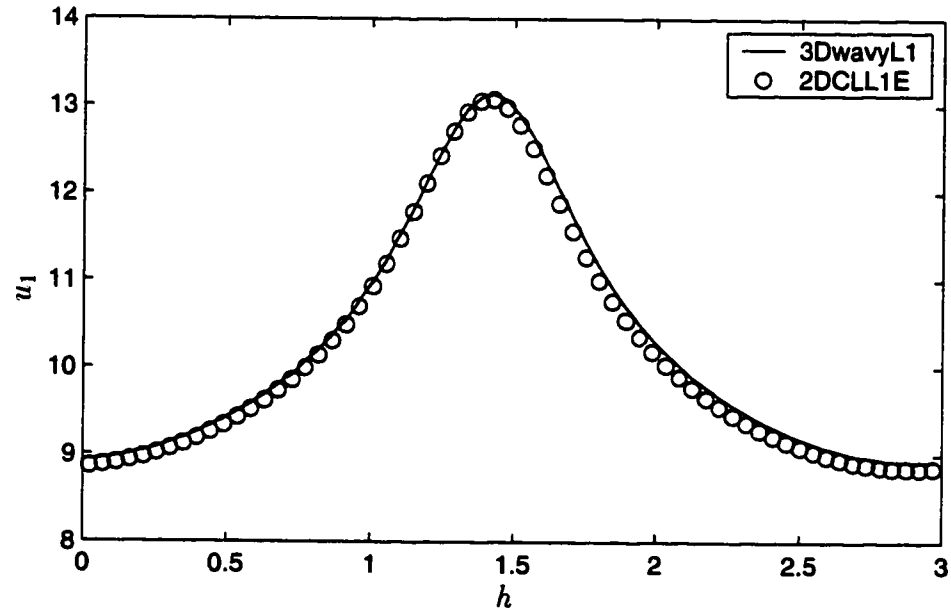

Figure 5.43: Comparison of 3DwavyL1 and 2DCLL1E. Downwind velocity (normalized by S) as functions of y (normalized by h) at the top surface. The profile for the 3DwavyL1 case is obtained by averaging in the streamwise direction. The profile for the 2DCLL1E case is phase-shifted in the spanwise direction.

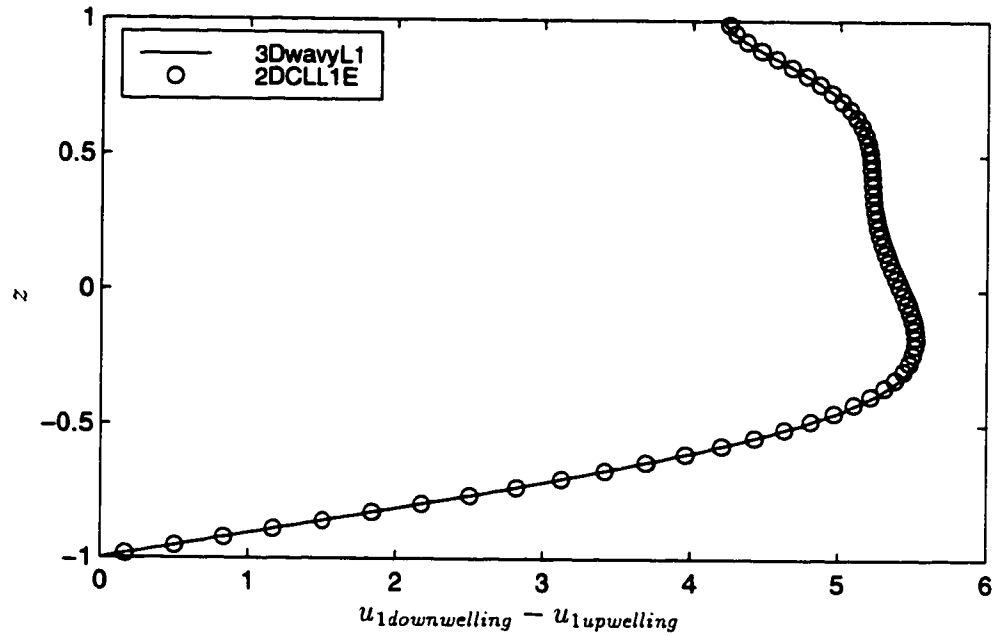

Figure 5.44: Comparison of 3DwavyL1 and 2DCLL1E. Downwind jet strength (normalized by S) as functions of z (normalized by h). The profile for the 3DwavyL1 case is obtained by averaging in the streamwise direction.

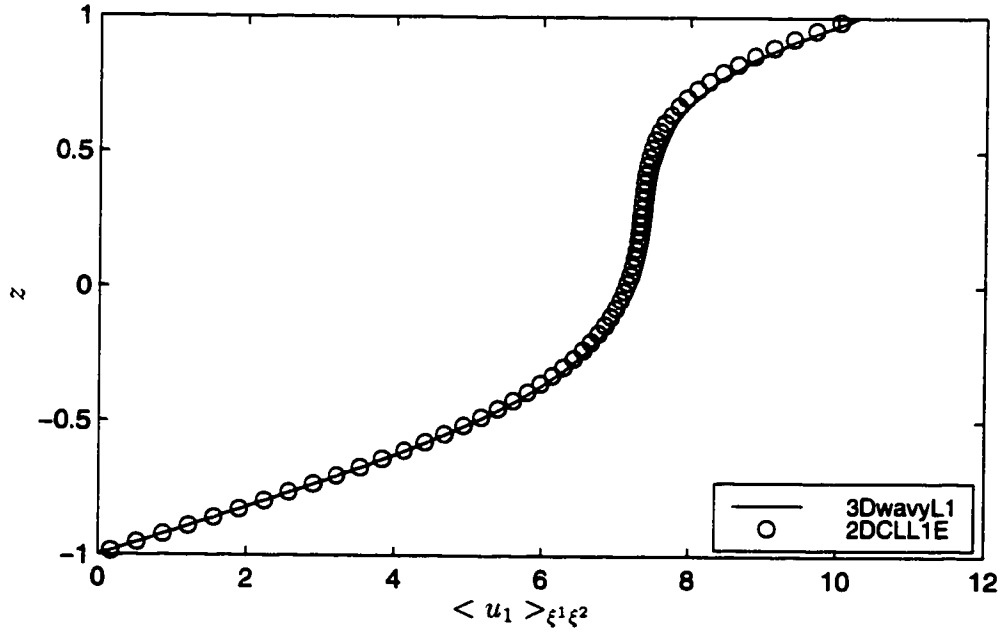

Figure 5.45: Comparison of 3DwavyL1 and 2DCLL1E. Streamwise velocity (normalized by S) averaged in the horizontal plane. (z normalized by h)

Chapter 6

Large Eddy Simulations of Langmuir Circulations

6.1 Introduction

In the previous chapter, laminar Langmuir circulations in an open channel flow with a wavy surface were investigated. In this chapter, we focus on Langmuir circulations in turbulent flows.

Recently, large eddy simulations of Langmuir turbulence have been performed by Skyllingstad and Denbo (1995) and McWilliams *et al.* (1997). Their approaches are based on the Craik-Leibovich theory. Both simulations were conducted for very complex systems, with flow domains that extend from the ocean surface to below the thermocline. The effects of the Langmuir circulations, stratification, heat transfer and Coriolis force were all incorporated. The influence of the wave field is represented by including a vortex forcing term in the momentum equations, and by combining the Stokes drift with the velocity field in the scalar advection equations. Their results show that Langmuir circulations in turbulent flow have much richer structure than in laminar flows. A continuous range of scales was observed. Langmuir circulations were found to play a key role in transport of the conserved properties.

In this chapter, we discuss large eddy simulations of Langmuir turbulence in a wavy domain (3Dwavy). The Navier-Stokes equations are solved without averaging over a wave period. To obtain a clear picture of Langmuir turbulence, it is helpful to isolate the effects of Langmuir circulation from other processes. Thus, we consider a simple case without stratification, surface heat flux, or Coriolis force. The properties and structure of Langmuir turbulence are examined.

In addition to the 3Dwavy case, a simulation based on the Craik-Leibovich theory (3DCL) is performed to extend the test of the Craik-Leibovich theory to turbulent

flows. To look at the contribution of Langmuir circulations to momentum mixing, we also compare the predicted Langmuir turbulence with those of an open channel flow (3DOChan) without waves. The effects of Langmuir circulations on the sheared mean current is discussed.

In section 6.2, an overview of the simulations in this chapter is presented. The validation of the implementation of turbulence model, the dynamic subgrid model, is described in section 6.3, followed by the flow decomposition in Section 6.4. The mean properties of the flow in the presence of Langmuir turbulence are discussed in section 6.5. Comparisons between the 3Dwavy case and the Craik-Leibovich theory, between the Langmuir turbulence and the open channel flow, and between turbulent and laminar Langmuir circulations are made. These are followed by the instantaneous field comparison of 3Dwavy, 3DCL and 3D open channel flows in section 6.6. The turbulence properties, the effects of Langmuir circulations on mixing, and the interactions between the wave, mean flow and turbulence are demonstrated in section 6.7. Finally, section 6.8 summarizes the observations.

6.2 Simulations Setup

6.2.1 Overview

Four simulations have been performed for this chapter. One is of a flow in a wavy domain. The other three are flows in rectangular domains, and are thus referred as "box cases". One of the box cases is a pressure-driven, closed channel flow (3DCChan) which is used to test the implementation of the turbulence model. Its parameter selection will be presented in the next section. This section discusses the setup of the other three cases. They are the 3Dwavy, the 3DCL and the 3DOChan cases introduced in the last section. These are stress-driven (at the top surface) flows with no externally imposed streamwise pressure gradient. Periodic boundary conditions are applied in both the streamwise and spanwise directions. Stress conditions are applied on the top surface and a no-slip boundary condition is imposed on the bottom wall. For the wavy case, the tangential stress on the top is constant, whereas for the other two box cases, streamwise stress is set to a constant. The spanwise stress on the top

is zero for all three cases.

6.2.2 Governing Equations and Numerical Methods

Because they are large eddy simulations, the equations for the 3Dwavy case and 3D open channel case are the filtered Navier-Stokes equations 2.22 and 2.23. For the 3Dwavy case, these equations are transformed into equations 2.43 and 2.44 in a curvilinear coordinate system. For the 3DCL case, the filtered equations are based on the Craik-Leibovich equations 5.1 and 5.2. They are:

$$\frac{\partial \overline{u}_i}{\partial x_i} = 0 \tag{6.1}$$

$$\frac{\partial \overline{u}_i}{\partial t} + \frac{\partial (\overline{u}_i \overline{u}_j)}{\partial x_j} = -\frac{\partial \overline{p}}{\partial x_i} + \frac{1}{Re_s}\frac{\partial^2 \overline{u}_i}{\partial x_j \partial x_j} - \frac{\partial q_{ij}}{\partial x_j} + \varepsilon_{ijk} u_{sj} \overline{\omega}_k \tag{6.2}$$

The turbulence model used is the dynamic subgrid model discussed in section 2.4. The numerical method for the 3Dwavy case were described in chapter 3. It is also applied to the box cases, except that, in the box cases, no coordinate transformation is necessary, and, for the 3DCL case, the Craik-Leibovich forcing term is added to the momentum equations.

6.2.3 Selections of Physical Parameters, Domain, and Grids

We first consider the parameter selection for the wavy case. Since no input parameter is necessary for the turbulence model, the input parameters for the turbulent 3Dwavy case are the same as for the laminar case: Re_*, Re_s, κ_x, κ_y and ϵ (see subsection 5.3.2 for the definitions).

We choose the channel depth to be a typical mixed layer depth, $25m$, of the Pacific Ocean off the California coast. We set κ_x to 1.5 to give a deep water wave. (As shown in chapter 2, the flow is non-dimensionalized with the characteristic Stokes drift velocity, S, and the half channel depth, h.) This corresponds to a monochromatic surface wave of wavelength $53m$, and a wave period of $6s$, comparable to the $4s$ wave observed by Smith (1992). Smith also observed that the aspect ratio of a Langmuir cell, defined as ratio of the half distance between adjacent convergence zones to the

depth of penetration, is approximately unity. Therefore, we set the wavelength of Langmuir circulation to $50m$, which gives $\kappa_y = 1.56$.

The gravitational acceleration is $g = 9.8m/s^2$. Therefore the phase speed of the wave is $C_w^d = \sqrt{g/\kappa_x^d}\tanh(2\kappa_x^d h)$. The parameters remaining to be determined are u_*^d, ν and ϵ.

The molecular viscosity is limited by available computer resources. Since we need to resolve the top viscous wavy boundary layer, which is usually much thinner than the bottom viscous sublayer, the computational grid is stretched vertically with a hyperbolic tangential function given by equation 3.7 that distributes more grid points near the top and bottom walls. However, the grid stretch is limited by its adverse influence on truncation error and the reduced convergence rate of the pressure Poisson solver. We select 64 grid points in the vertical direction, with a stretching parameter $\alpha = 0.98$ which corresponds to a stretching ratio of $\gamma = 1.15$, as defined in equation 3.48. With this grid, suppose we use three grid points to resolve the wavy boundary layer, then the thickness of the wave boundary layer should be at least $\delta_w = 0.009$. Since

$$\delta_w = \frac{\delta_w^d}{h} = \sqrt{\frac{2\nu}{C_w^d {\kappa_x}^d}h^2} \tag{6.3}$$

and for the surface Stokes wave, $C_w^d = \sqrt{g/\kappa_x^d}\tanh(2\kappa_x^d h)$. By substituting the values of κ_x^d, g and h, we get the minimum molecular viscosity allowed, $\nu = 7 \times 10^{-3} m^2/s$.

The Reynolds number based on the friction velocity is set to $Re_* = u_*^d h/\nu = 100$ to generate a turbulent channel flow. This gives a wind stress friction velocity, $u_*^d = 0.056m/s$.

In Langmuir turbulence, the laminar Langmuir number defined in equation 5.16 is very small. Another important parameter is the turbulent Langmuir number defined by McWilliams *et al.* (1997):

$$La_t = \sqrt{u_*^d/2S} \tag{6.4}$$

which represents the relative strength of the shear instability and the current-wave interaction. According to McWilliams *et al.* (1997), Langmuir turbulence occurs in

Input Dimensional Parameters	3DwavyT1	Input Non-dimensional Parameters	3DwavyT1	Derived Variables	3DwavyT1
$\lambda_x^d\ (m)$	53	Re_*	100	$C_w^d\ (m/s)$	9.1
$\lambda_y^d\ (m)$	50	Re_s	546	$T\ (s)$	6
$H\ (m)$	25	κ_x	1.5	$S\ (m/s)$	0.31
$a\ (m)$	2.2	κ_y	1.56	$\delta_w^d\ (m)$	0.114
$\nu\ (m^2/s)$	7×10^{-3}	ϵ	0.26	La	3.7×10^{-4}
$g\ (m/s^2)$	9.8			La_t	0.3
$u_*^d\ (m/s)$	0.056				

Table 6.1: Parameters for 3Dwavy turbulent case, 3DWavyT1. ("T" stands for turbulent.)

Name	ϵ	κ_x	κ_y	Re_s	Re_{*eff}
3DCLT1E	0.26	1.5	1.56	546	115
3DOChanT1E	0	1.5	1.56	546	115

Table 6.2: Computational parameters for the turbulent 3DCL and 3D open channel cases. ("T" stands for turbulence, "E" means the Eulerian mean flow is included.)

the regime of $La \ll 1$ and $La_t = \mathcal{O}(1)$. We choose the same turbulent Langmuir number as McWilliams *et al.* (1997) and Skyllingstad and Denbo (1995), $La_t = 0.3$. This determines the slope of the surface wave to be $\epsilon = 0.26$, a relatively large value.

From the parameters above, the characteristic Stokes drift velocity can be derived as $S = 0.5\epsilon^2 C_w^d = 0.31 m/s$.

The dimensional variables and the non-dimensional input parameters for the 3Dwavy case are summarized in Table 6.1.

We pick a domain that contains three wavelengths of the surface wave in the streamwise direction, and one Langmuir circulation wavelength in the spanwise direction, *i. e.* $(L_x, L_y, L_z) = (12.56, 4, 2)$. We use a $64 \times 64 \times 64$ grid, which is uniform in both the streamwise and the spanwise directions, and stretched in the vertical direction. The details of the domain and grid selection were discussed in section 3.3. The relatively small number of grid points is necessitated by the requirment of a long simulation.

The parameters for the two box cases are selected to match those of the 3Dwavy case. They are listed in Table 6.2. Both cases have the same physical domain size and the numerical grid as the 3Dwavy case. As we know from the previous chapter, for the 3DCL case, the wave slope is an output parameter. The open channel case does not have wave-current interaction, so the parameter Re_s is irrelevant. It is included here for the convenience of using the same code as for the other two cases. Furthermore, since neither a surface wave nor a Langmuir circulation occurs in the open channel case, the parameters κ_x and κ_y are used merely to determine the size of the domain.

As discussed in the last chapter, to compare with the 3Dwavy case, the surface stress imposed in the box cases should contain components due to both the wind stress and the Eulerian mean flow. Therefore, we use the effective Reynolds number, Re_{eff}, in the box cases. From equation 5.17, Re_{eff} is evaluated to be 115.

6.2.4 Initial Conditions

The initial flow for the 3Dwavy case is a fully developed wavy flow from 2D simulation with the same parameters. For the 3D open channel case, the simulation starts with a laminar Couette flow with the same top stress. White noise of small magnitude ($\mathcal{O}(10^{-4})$) is imposed on the initial flow. The time step is chosen as $\Delta t^d S/h = 2 \times 10^{-3}$. The maximum CFL number (defined in equation 3.24) is chosen to be 0.25 as described in chapter 3. If the CFL limit is exceeded, the time step is reduced so that $CFL = 0.25$. Since the code needed to run for thousands of wave periods for the 3Dwavy and 3DOChan cases to reach statistically steady states, it took about 40 days of CPU time on a single processor of the Cray-J90 at the Environmental Fluid Mechanics Laboratory. Using the fully developed turbulent 3D open channel flow as the initial condition for the 3DCL case, it takes about 25 days for the 3DCL case to reach equilibrium.

6.2.5 Limitations

There are some limitations that need to be kept in mind when interpreting the results. First, the bottom boundary is a simple no-slip wall. Since in the ocean, the Langmuir turbulence is actually constrained by a thermocline, the strong boundary layer near

the bottom wall in our simulation will adversely influence comparison of the numerical results with field observations. Second, we evaluated the Eulerian mean flow effects for the box cases using equation 5.17. However, this equation is valid only for the laminar case. As we will show later, the Eulerian mean flows in the box cases have been underestimated. Thus, different velocity scales are used to make meaningful comparisons. This will be further discussed in section 6.5.

6.3 Validation of the Subgrid Turbulence Model

6.3.1 Test Case Setup

The implementation of the dynamic subgrid-scale viscosity model was verified by performing a large eddy simulation of a pressure-driven turbulent channel flow.

The pressure gradient in the streamwise direction is $-\rho u_*^{d2}/h$, where ρ is the density of the fluid; h is half depth of the channel; and u_*^d is the wall shear velocity. The Reynolds number, $Re_* = u_*^d h/\nu$, is set to 180, where ν is the molecular kinematic viscosity. The streamwise and the spanwise dimensions of the computational box are chosen to be $4\pi h$, and $2\pi h$, respectively. Kim *et al.* (1987) have shown in their DNS simulation that this domain is sufficiently large to include the largest eddies in the flow.

A 64 × 64 × 64 grid is used. Uniform grids are used in both the streamwise and spanwise directions, which results in grid spacings around 35 and 17.5, respectively, in wall units scaled with u_*^d and ν. Hyperbolic tangent stretching is applied in the vertical direction such that the distance between the nearest point to the wall and the wall is approximately 0.3 wall unit on both sides and the maximum spacing is about 13 wall units. The effects of eddies smaller than the filter size are parameterized with the dynamic subgrid model.

Periodic boundary conditions are used in both lateral directions. No-slip conditions are imposed on the top and bottom walls. The initial condition is chosen to be a one dimensional streamwise mean flow perturbed with random noise. The mean profile is obtained from an empirical fit to the final mean velocity (C. Pierce, personal

communication, 1999):

$$U_1(z) = \frac{U_1^d(z)}{u_*^d} = 8.63 Re_*^{1/7}(1 - z^6) \tag{6.5}$$

where $U_1 =< \overline{u}_1 >$ presents the averaged filtered streamwise velocity scaled by the shear velocity, and <> indicates averaging over the lateral directions and time. z is the vertical coordinate scaled by h, measured from the centerline of the channel.

The time step is chosen as $\Delta t = 2.5 \times 10^{-3} h/u_*^d$, which is around 0.5 in wall units. To prevent the flow from laminarizing, a higher Reynolds number, $Re_* = 1000$, is used initially to make sure turbulence develops. The Reynolds number is reset to the original value after several thousand time steps.

Statistics are collected after the flow reaches the equilibrium state. This state is identified by the bulk mass flow rate oscillating around a constant value. The bulk mass flow rate is defined as:

$$u_{bulk} = \frac{1}{2}\int_{-1}^{1} U_1 dz \tag{6.6}$$

Once the flow reaches the equilibrium state, the statistics are collected by averaging both over horizontal planes and time. The symbol <> in the next subsection means averaging over x_1, x_2, and t.

6.3.2 Test Results

The results are compared with the direct numerical simulations of Kim *et al.* (1987). The direct simulations employed a fully spectral method (Fourier-Chebyshev) on $192 \times 129 \times 160$ grid points for the same Reynolds number. Figure 6.1 shows the comparison of the profiles of the mean streamwise velocity, $U_1^+ = U_1^d/u_*^d = U_1$, from LES and DNS. Overall the LES result agree with the DNS result. The LES mean velocity within the viscous sublayer ($z^+ \approx 0 \sim 5$) and most of the buffer layer ($z^+ \approx 5 \sim 40$) is close to the DNS profile. At the end of the buffer layer, the LES produces a slightly higher streamwise velocity than DNS. This trend continues all the way through the log-law region ($z^+ \simeq 40 - 80$). The maximum error is around 10%

and occurs near the center line. This is typical of large eddy simulations with this resolution (Garg 1996).

Figure 6.2 presents the three components of shear stress. They are the viscous stress, $\nu dU_1/dz$, the subgrid stress, $< -q_{13} >=< \nu_T S_{13} >$, and the resolved shear stress, $< -u_1'' u_3'' >$, where ν_T is the eddy viscosity in the turbulence model and S_{13} is the strain rate component. The sum of these three components is also plotted. It is a straight line as expected (its slope should be the pressure gradient). The subgrid stress is very small compared with the resolved Reynolds stress.

Figure 6.3 presents the comparison of the Reynolds shear stress from the DNS with the combined resolved and subgrid stress of LES. It shows that LES underpredicts the Reynolds shear stress for z^+ less than 40. Since the total stress has to be constant at a given vertical location, dU_1/dz must be greater than in the DNS simulation. This leads to the overprediction of U_1 as shown in Figure 6.1.

The comparison of the root mean square fluctuation velocities with the DNS simulations is shown in Figures 6.4 to 6.6. Although qualitatively in agreement with the DNS results, the LES results in a higher $\sqrt{< u_1'' u_1'' >}$, and lower $\sqrt{< u_2'' u_2'' >}$ and $\sqrt{< u_3'' u_3'' >}$. The error is largest for the vertical velocity fluctuations. This is expected since the vertical component is largely dependent on the small scales and thus is sensitive to the grid resolution. The same behavior has been observed by other researchers (Piomelli *et al.* 1987, Garg 1996).

6.4 Flow Decomposition

As was shown in the last section, the turbulence in channel flow can be decomposed into a mean flow and fluctuations. The mean flow is obtained by ensemble averaging and the fluctuation by subtracting the mean and instantaneous fields. In Langmuir turbulence, however, the mean flow contains several components: the sheared mean current, the Langmuir circulations and the wave field. Each part is obtained through a particular averaging. Hence, to have a clear picture of what quantities to compare between the simulations, we need to clarify the flow decomposition.

Table 6.3 summarizes the comparison of the flow decompositions for the three

3Dwavy	3DCL	3DOChan
no homogeneous direction	x_1 homogeneous	x_1, x_2 homogeneous
$< f >=< f >_t$	$< f >=< f >_{tx_1}$	$< f >=< f >_{tx_1x_2}$
$f = f_{MC} + f_W + f_L + f''$	$f = f_{MC} + f_L + f''$	$f = f_{MC} + f''$
$< f >_t = f_{MC} + f_W + f_L$	$< f >_{tx_1} = f_{MC} + f_L$	$< f >_{tx_1x_2} = f_{MC}$
$< f >_{t\xi^1} = f_{MC} + f_L$	$< f >_{tx_1x_2} = f_{MC}$	
$< f >_{t\xi^2} = f_{MC} + f_W$		
$< f >_{t\xi^1\xi^2} = f_{MC}$		

Table 6.3: Comparison of flow decompositions.

core cases of this chapter. In the table, f is a general, instantaneous flow variable, the symbol <> without a subscript means the ensemble average, while the same symbol with a subscript denotes an averaging over time (if t is a subscript) and/or the specified directions, The subscript 'MC' stands for mean current, 'W' for wave, and 'L' for Langmuir circulation. We will explain only the first column, which is the most general case. The other two columns can be explained in a similar way. In the wavy case. there is no homogeneous direction. Thus the ensemble average is the time average and contains the mean current, the Langmuir circulation and the wave field. Since the coordinate system is moving with the wave, the time average is also the phase average with respect to both the surface wave and the Langmuir circulation. To compare the wavy case with the box cases, as a first approximation, the flow field of the wavy case is averaged over the curvilinear coordinates, *i. e.*, the inviscid streamlines of the two dimensional wave field. If we average in both time and ξ^1, the wave component is removed. Similarly, if we average in both time and ξ^2, the Langmuir circulation component is removed. If we average over time and both the lateral directions, only the mean current is left.

The fluctuating component, f'', is defined as $f'' = f - < f >$ for all three cases. In Langmuir turbulence, f'' consists of unsteady Langmuir circulation and turbulence, whereas in open channel flow, it represents turbulence only. Since in Langmuir turbulence, turbulence properties such as the Reynolds stress are calculated from the fluctuation field, we also apply the term "turbulence" to the combination of unsteady

Langmuir circulation and true turbulence. Because average was performed over inviscid streamline in the x direction, the decomposition is not exact but it does provide a good idea of the contribution of the various components of the flow.

6.5 Mean Flow Properties

The simulations were run long enough for the flows to reach statistically steady states. This is monitored through the time evolution of bulk quantities. For Langmuir turbulence, the statistically steady state is indicated by the spanwise kinetic energy fluctuating around a constant value. In the open channel case, it is marked by the flow fluctuating with respect to a constant bulk velocity. The development of these bulk quantities is shown in Figures 6.7 and 6.8. Since two dimensional laminar flows are used as the initial conditions in the 3Dwavy and 3D open channel cases, these flows experience transition stages. The 3DCL case, on the other hand, starts from a fully developed turbulent field and the Craik-Leibovich forcing turned on at time zero. It shows a smaller change in the transition phase. Turbulent statistics are collected after the statistically steady state is reached.

6.5.1 Total Momentum Transport and Scaling

As was mentioned in Section 6.2, in order to compare the Craik-Leibovich theory with the wavy simulation, and to assess the contribution of Langmuir circulations to mixing, the three core cases of this chapter were designed to be as similar as possible. As shown in Tables 6.1 and 6.2, κ_x, κ_y and Re_s are the same in the three cases. Since the 3DOChan case has no surface wave, ϵ is zero in it. In addition, the top stresses in the box cases are estimated as the sum of the top tangential stress in the wavy case and the Eulerian-mean-flow-induced stress due to the surface wave. The purpose is to make the total horizontal momentum flux across the channel the same in all three cases.

However, when comparing the 3DCL and 3Dwavy cases, which are scaled with the same characteristic Stokes drift, S, and half channel depth, h, we found that the mean current profiles have similar shapes but different magnitudes. There is a major

difference in the stress at the bottom wall, indicating that the vertical fluxes of the streamwise momentum are different. Therefore, we need to examine the differences in the total momentum transport in the three cases; why they differ, and what to do to make an adequate comparison of the three cases.

Let us inspect the streamwise momentum equation. In the 3DCL case, the streamwise component of the Craik-Leibovich forcing in equation 6.2 is zero. Thus the momentum equation for u_1 is the same in all three cases. For the box cases, we apply an average in time and the two lateral directions. The resulting momentum equation for u_1 becomes:

$$(- < \overline{u}_1\overline{u}_3 >_{tx_1x_2} + 2\nu < \overline{S}_{13} >_{tx_1x_2} + 2 < \nu_t\overline{S}_{13} >_{tx_1x_2})_{,3} = (\tau_{avgBox})_{,3} = 0 \quad (6.7)$$

where τ_{avgBox} is the total transport of the streamwise momentum in the vertical direction. It is constant and is equal to the stresses on both the top and the bottom surfaces.

For the wavy case, equation 6.7 still holds. However, since a curvilinear system is used, averaging over horizontal planes is not defined. Instead, we average over surfaces of constant curvilinear coordinates ξ^1, ξ^2 and obtain an similar equation, which is strictly valid only at the bottom boundary, ($x_3 = -1$), where the curvilinear system reduces to a Cartesian system:

$$(- < \overline{u}_1\overline{u}_3 >_{t\xi^1\xi^2} + 2\nu < \overline{S}_{13} >_{t\xi^1\xi^2} + 2 < \nu_t\overline{S}_{13} >_{t\xi^1\xi^2})_{,3} = (\tau_{avgWavy})_{,3} = 0 \quad (6.8)$$

At other locations, the pressure gradient and the derivatives in x_1 and x_2 directions are nonzero. Thus the above equation is only an approximation. At the bottom surface, $\tau_{avgWavy}$ is equal to the total horizontal momentum transport. In the rest of the domain, $\tau_{avgWavy}$ is not the total horizontal momentum transport and is therefore not constant. Nevertheless, Equation 6.8 enables us to check whether the total momentum transport is the same in the three cases. We only need to compare the value of $\tau_{avgWavy}$ at the bottom surface in the wavy case with τ_{avgBox} in the box cases.

Figure 6.9 shows the profiles of τ_{avgBox} for the turbulent 3DCL and 3D open channel cases, together with the profile of $\tau_{avgWavy}$ for the turbulent 3Dwavy case.

In agreement with the above arguments, τ_{avgBox} is constant throughout the channel depth and is equal to the stress at the top and bottom surfaces. Furthermore, as expected, $\tau_{avgWavy}$ is not constant, especially near the top surface, where the pressure gradients in the x_1 and x_2 directions cause variation in the vertical direction. In the lower half of the channel, $\tau_{avgWavy}$ is almost constant. But the value of $\tau_{avgWavy}$ at the bottom surface is 0.08, almost twice the $\tau_{avgBox} \simeq 0.045$ of the other two box cases. Thus, the total momentum transport is the same in the 3DCL and the 3DOChan cases, but is different between the wavy case and the box cases.

On the other hand, this is not true for laminar cases. Figure 6.10 compares the profile of $\tau_{avgWavy}$ for the 3Dwavy laminar case with the estimated top stress for the 2DCL cases, which is equal to τ_{avgBox}. Obviously, at the bottom surface, the value of $\tau_{avgWavy}$ is very close to the estimated top stress, *i. e.* τ_{avgBox}.

Why is the total momentum transport different between the wavy and box cases for turbulent flows, but not for laminar flows? The reason is that the stress due to the Eulerian mean flow is not correct in the turbulent case. Recall that because a viscous wave field induces a second order Eulerian mean flow, the streamwise momentum in the wavy case is a combination of the wind-driven current and the Eulerian mean flow. On the other hand, the total momentum transport is constant vertically in the box cases and is equal to the top stress. Therefore, the top stresses in the box cases are estimates of the combination of the tangential stress of the 3Dwavy case and the stress due to the Eulerian mean flow. We used Equation 5.17 to make this estimate. However, the molecular viscosity was used in the evaluation of the Eulerian mean flow stress. This is correct for laminar flow but not valid for turbulent flow. Thus the total momentum transport rates obtained in this way are equal in the laminar flows but not in the turbulent ones[1].

A better way to have done the box cases would have been to wait for convergence of the wavy case, and use the value of $\tau_{avgWavy}$ at the bottom surface as the imposed top stress in the box cases. Due to the intensive demand on the computer resources, we ran the box cases simultaneously with the wavy case. Running the box cases after the wavy case would have been too time consuming. At the time of writing this

[1]This is something we only appreciated after the fact.

thesis, this task is planned for the near future. In this chapter, as an approximation, comparisons are made by scaling each flow with its shear velocity at the bottom surface, *i. e.* $u^d_{*wavy} = 0.28S$, and $u^d_{*CL} = u^d_{*OChan} = 0.21S$, respectively, so that the non-dimensional total streamwise momentum transport is unity for all the three cases.

6.5.2 Comparison between the 3Dwavy Simulation and Craik-Leibovich Theory

Langmuir circulations are formed in both the turbulent 3Dwavy case and the turbulent 3DCL case based on the Craik-Leibovich theory. They are revealed by the mean streamwise vorticity field as well as the mean velocity field.

Streamwise Vorticity

Figures 6.11 and 6.12 presents streamwise vorticity contours for the 3Dwavy and 3DCL cases, respectively. The contours are shown in spanwise-vertical planes at four streamwise locations. Both the instantaneous vorticity, ω_1, and the mean vorticity, $< \omega_1 >_t$ are given. From the instantaneous fields, we see that the flows exhibit rich turbulent structure. Large-scale coherent structures are hard to find in these fields. The flow patterns are chaotic and there is a continuous spectrum of length scales, as was observed in the LES 3DCL simulations of McWilliams *et al.* (1997) and Skyllingstad and Denbo (1995). When the flows are averaged locally over time, however, two large counter rotating vortices, *i. e.* Langmuir circulations, can clearly be identified. Thus, because the mean vorticity is only about a tenth of the instantaneous vorticity in magnitude, the Langmuir circulations are almost completely hidden by the instantaneous flows.

The Langmuir circulations obtained from the Craik-Leibovich theory are similar in structure to those in the wavy simulation, although the strengths are different. From Figures 6.11 and 6.12, the maximum longitudinal vorticity in the 3Dwavy case is only about 2/3 of that predicted from the Craik-Leibovich theory, *i. e.* the 3Dwavy simulation produces a weaker secondary flow than the Craik-Leibovich theory.

Velocity Field

The velocity field in the 3D wavy simulation contains a wave component but the one based on the Craik-Leibovich theory does not. Therefore the wave component of the 3Dwavy case needs to be removed to make comparisons. This is done by performing another averaging of the time averaged 3Dwavy flow. We average over the ξ^1 coordinate of the curvilinear system, *i. e.* along inviscid streamlines. In the 3DCL case, the flow is also averaged in the streamwise direction. This is done solely to increase the sample size for the ensemble average, since the flow is homogeneous in the streamwise direction. According to the flow decompositions (see Table 6.3), for the 3Dwavy and 3DCL cases, the resulting velocity field consists of the mean sheared current and the Langmuir circulations.

Figure 6.13 compares the velocity fields of the 3Dwavy and 3DCL cases. The mean currents are shown by streamwise velocity contours and Langmuir circulations by spanwise-vertical velocity vectors. The plot for the 3DCL case is phase-shifted in the spanwise direction to make the downwelling zone at the same location as in the 3Dwavy case (This is justified by the spanwise periodic boundary condition).

In both the 3Dwavy and 3DCL cases, the velocity vectors reveal two counter rotating circulations, *i. e.* Langmuir cells, with upwelling and downwelling zones between them. Near the top of the domain, there is a boundary layer near the surface as described by Li and Garrett (1993). Near the bottom wall, the vectors show the shear boundary layer.

The mean currents in the two cases closely resemble each other. The streamwise velocity contours show a bottom shear layer with a strong velocity gradient and a well mixed zone above. The bottom boundary layer is thickened by the upward motion of slow fluid at the base of the upwelling region. Below the downwelling zone, the bottom boundary layer is "squeezed" by the high momentum fluid coming from above. A current anomaly can also be observed, the mean current has lower speed in the upwelling zone than in the downwelling zone, especially in the lower half of the channel. Furthermore, the magnitudes of the streamwise currents are also very close, showing a quantitative similarity between these two cases. The mean current will be discussed further in the next subsection.

The Langmuir circulations can be examined closely in line plots. Figure 6.14 compares the current anomalies. It plots the streamwise velocity versus the spanwise coordinate at the vertical locations where the maximum anomalies occur. The curve for the 3Dwavy case is not as smooth as the one for the 3DCL case since fewer samples are used in the ensemble average. The streamwise velocity changes more rapidly near the upwelling zone than near the downwelling zone. The maximum variation of the streamwise velocity, *i. e.* the non-dimensional strength of the downwind jet is 6 for the 3Dwavy case, and 9 for the 3DCL case.

The spanwise velocity profiles along the vertical centerlines of the Langmuir circulations are given in Figure 6.15. In both cases, the cores of the Langmuir cells, marked by the zeros of the spanwise velocity profile, are located at almost the same height, slightly above the mid-height of the channel. The bottom boundary layer thickness in the 3Dwavy case is close to that from the Craik-Leibovich theory. Furthermore, the maximum spanwise velocity at the surface is almost twice the velocity at the top of the viscous boundary layer near the bottom wall, indicating vertical asymmetry of the Langmuir circulation.

The vertical velocities at the downwelling and upwelling center lines are compared in Figure 6.16. The profiles are similar for the 3Dwavy and 3DCL cases. The maximum downwelling occurs just above the half depth of the channel, and the maximum upwelling is located slightly above maximum downwelling point. As expected, the vertical velocity gradient is zero at the bottom wall due to the impermeability boundary condition there and continuity. In addition, unlike the laminar case, the upwelling jet is more intense than the downwelling jet. In both cases, the maximum upwelling velocity is about 30% higher than the maximum downwelling speed.

As in the vorticity fields, the Langmuir circulation structures revealed by the velocity fields are qualitatively similar in the 3Dwavy and the Craik-Leibovich simulations. However, Figures 6.14 to 6.16 show that the magnitude of the downwind jet, the maximum spanwise velocity, the maximum downwelling and maximum upwelling speed in the 3Dwavy case are all approximately 2/3 of those in the 3DCL case, consistent with the vorticity ratio shown in Figures 6.11 and 6.12.

Comparison with Field Obserations

The magnitude of the maximum downwelling velocity and the pitch are compared with observations (Weller and Price 1988). For the 3Dwavy case, from Figure 6.16, the maximum downwelling velocity is $w^d_{down}/u^d_{*wavy} = 1.25$. From the relation $u^d_{*wavy} = 0.28S$ and equation 5.26, we obtain $w^d_{down} = 0.036U^d_w$, where U^d_w is the wind speed. Furthermore, from Figure 6.14, the maximum downwind jet velocity (difference of u_1 at downwelling and upwelling) is $u^d_{1downwindjet}/u^d_{*wavy} = 6$. Thus the pitch is approximately $Pt = u^d_{1downwindjet}/w^d_{down} = 4.8$. These are in rough agreement with those observed by Weller and Price (1988): $w^d_{down} \sim (0.0025 \sim 0.03)U^d_w$ and $Pt \sim (1.33 \sim 8.0)$ (see Table 5.3).

Using similar methods, the downwelling velocity and the pitch can be derived for the 3DCL case as $w^d_{down} = 0.067U^d_w$ and $Pt = 5.17$, respectively. The pitch value is within the range of observation, but the maximum downwelling velocity is overpredicted by the Craik-Leibovich theory.

6.5.3 Differences of Langmuir Circulations in Laminar and Turbulent Flows

The Langmuir circulation structure in turbulent flow is very different from that in laminar flow. In laminar flow, downwelling jet is much stronger than the upwelling jet. Figure 5.19 demonstrates that the maximum downwelling velocity is almost twice the maximum upwelling velocity. In the turbulent flow, to the contrary, the upwelling jet is stronger, as shown in Figure 6.16.

Comparing the streamwise velocity contours in Figure 6.13 for the turbulent case with Figure 5.18 for the laminar case, it is obvious that in the laminar flow, there is a downwind current anomaly near the surface, where a powerful downwind jet occurs. In the turbulent cases, however, the narrow downwind jet near the surface at the downwelling zone is dramatically reduced in strength and is hard to detect. This feature can also be observed in Figure 6.17, where the streamwise velocity as a function of depth are plotted at the downwelling and upwelling zones for both the 3Dwavy and 3DCL cases. Clearly, the current anomaly is stronger near the bottom wall than near

the top surface, whereas, as can be seen in Figure 5.23, it is of comparable strength near the two boundaries in the laminar case.

A closer look at the upwelling and downwelling zones is given in Figure 6.14, where the spanwise profiles of streamwise velocity are presented at the depth where maximum downwind jet occurs. Compared with the laminar case in Figure 5.22, a narrow dip is formed at the upwelling zone in both laminar and turbulent flows. The peak at the downwelling in Figure 5.22 is smeared out in the turbulence cases. Thus, the differences are caused by the change in the downwelling zone in turbulent flows.

The main reason for this change is the effect of turbulent mixing. As will be shown later, turbulent kinetic energy is greater at the top surface than above the bottom boundary layer. Therefore, mixing is more powerful near the surface where wave-current interactions occur. Since the downwelling is formed at the top surface, it is vigorously stirred by the turbulent mixing, and the downwelling zone is broadened and the downward speed is decreased. The upwelling jet, on the other hand, is formed near the bottom wall. Because the mixing there is weaker than near the top wall, the upwelling jet is less diffuse.

6.5.4 Langmuir Circulation Effects on the Mean Current

In this subsection, the mixing due to the Langmuir circulations is examined in terms of the mean current profiles.

Figure 6.18 compares streamwise mean velocities for the 3Dwavy, 3DCL and 3D open channel cases. The mean current is obtained by averaging in time and over horizontal planes for the box cases. In the wavy case, instead of averaging over horizontal planes, the streamwise velocity is averaged over the curvilinear coordinates in the streamwise and spanwise directions. After normalization with the friction velocity at the bottom wall, the mean currents of the two Langmuir turbulence cases are close to each other. This demonstrates the approximateness of the velocity scale selected.

This figure clearly shows that the mean current profile is greatly altered by the Langmuir circulations. In the turbulent open channel flow, shear layers develop near both the top and the bottom surfaces. In the two cases with Langmuir turbulence,

however, the vertical transport of the streamwise momentum induced by Langmuir circulations causes the mean currents to be more uniform. The efficient mixing produced by Langmuir turbulence not only erases the shear in the center of the channel, but also largely destroys the strong top shear layer.

Figure 6.19 shows the mean streamwise velocity in wall units for the turbulence Couette flow. In the viscous sublayer above the bottom wall, the mean velocity follows the $U_1^+ = z^+$ law of the wall up to $z^+ = 5$, as expected. In the logarithmic region of the lower half of the channel, the mean velocity can be fit:

$$U_1^+ = 2.5 \ln z^+ + 5.1 \tag{6.9}$$

which is the same as that obtained by Lam and Banerjee (1992). The commonly used Nikuradze logarithmic law, $U_1^+ = 2.5 \ln z^+ + 5.5$ is plotted for comparison.

In the top half of the channel, the mean velocity deficit $U_{1s}^+ - U_1^+$ is plotted as a function of the distance from the upper wall, where U_{1s} is the normalized velocity at the top surface. The mean velocity deficit is smaller than the mean velocity in the lower half wall. In the viscous sublayer, the deficit deviates from $U_{1s}^+ - U_1^+ = z^+$ after $z^+ = 3$. In the logarithmic region, the curve can be fit with:

$$U_{1s}^+ - U_1^+ = 2.5 \ln z^+ + 2.3 \tag{6.10}$$

This lower velocity deficit is caused by the boundary condition at the upper surface. Unlike the non-slip bottom wall, constant stress is specified there. While the perturbations of all components of the velocity are zero at the bottom wall, nonzero streamwise and spanwise perturbations are allowed at the top. This results in a higher Reynolds stress $- < u_1'' u_3'' >_{tx_1x_3}$ there. Since the total streamwise momentum transport is constant at any depth, the viscous stress is smaller near the top surface, thus causing the lower velocity deficit shown in Figure 6.19.

Figures 6.20 and 6.21 compare the mean currents in the Langmuir turbulence cases in wall units with that of the open channel flow. Figure 6.20 gives the mean current velocity in the lower half channel, whereas Figure 6.21 presents the mean velocity deficit in the upper half channel. Near the bottom wall, the mean current profiles in

the 3Dwavy and 3DCL cases agree with the open channel flow up to $z^+ = 10$. But the logarithmic layer of the open channel flow is replaced by a more uniform velocity distribution in Langmuir turbulence, indicating that the influence of the Langmuir circulation penetrates into the log-law region of the turbulence boundary layer. A similar alteration of near wall structure by longitudinal vortices has also been observed by Barlow and Johnston (1988) in concave boundary layers.

Near the top wall, as will be shown later, the turbulence is stronger due to Langmuir circulations. Thus, much smaller velocity deficits are obtained in both the 3Dwavy and 3DCL cases. The powerful mixing induced by the longitudinal vortices affects the mean current profiles all the way to the top surface. A more uniform mean current is produced in Langmuir turbulence.

6.5.5 Modulations of Langmuir Circulations and Wave Fields

Due to the interaction between the Langmuir circulation and the wave field, the Langmuir circulations are modulated by the wave. In turn, the wave field is altered by the Langmuir circulations.

The structure of the wave field is exhibited in Figure 6.22, which shows the spanwise vorticity profile as a function of the vertical coordinate under the trough of the wave. The top wavy boundary layer can be clearly identified. It is approximately 0.02 units thick and has about 10 grid points inside it. On the other hand, the thickness of the bottom boundary layer is about 0.18 units, almost 9 times as thick as the top boundary layer. The majority of the fluid between these two boundary layers has very little spanwise vorticity.

Figure 6.23 presents the time averaged streamwise vorticity contours at the center of one of the Langmuir cells. Clearly, it varies in the streamwise direction. The maximum streamwise vorticity is located under the trough, and is about 30% larger than the minimum vorticity under the crest.

The mean streamwise and vertical velocities averaged over time are shown in Figures 6.24 and 6.25, respectively. As in the laminar case in section 5.6, the mean flow is dominated by the first order sinusoidal wave field (see Figures 6.24(a) and 6.25(a)). Since a higher wave slope, $\epsilon = 0.26$, is used in the turbulent case, second order

components of the wave field can also be observed. The velocity decays rapidly with depth, as expected for a deep water wave. Furthermore, the mean sheared current gives rise to a non-zero mean streamwise velocity, which leads to the asymmetry in the streamwise velocity magnitude between the crest and trough in Figure 6.24(a).

The wave field is slightly altered by the second order Langmuir circulations. In the vertical velocity field shown in Figure 6.25(b), the upwelling and downwelling zones can be clearly identified at the wave crest and trough, since the vertical motion caused by wave is zero at both locations. At the slopes of the wave, however, the vertical wave velocity is non-zero. In the downwelling zone, the negative vertical velocity contours are tilted downward, and the positive contours are pushed upward. In the upwelling zone, the opposite occurs.

Figure 6.24(b) shows that, in the upwelling zone, the current anomaly induced by the Langmuir circulations bends the contours of the positive streamwise velocity upwards (see the contours at the wave crest) and contours of the negative streamwise velocity downwards (see the contours at the trough). As mentioned before, the current anomaly is very weak in the downwelling zone and the contour lines are hardly modified there.

6.6 Instantaneous Structure

The instantaneous near-surface structures of the three core cases are compared in Figures 6.26 to 6.28 as iso-surfaces of the instantaneous vorticity $\overline{\omega}_1 = \pm 6.5$. The vorticity is nondimensionalized with the shear velocity and the half channel depth. The iso-surfaces are presented in a layer near the top surface with thickness roughly equal to the e-folding depth of the Stokes drift, $1/(2\kappa_x)$. The influence of the wave and the current interaction are evident. In the 3Dwavy flow, as shown in Figure 6.26, there are longitudinally elongated streaks. They are of finite length and irregular spacing and have alternating signs of vorticity along the spanwise direction. These "streaks" cannot be normal boundary layer streaks as they are not present in the flat channel flow. Apparently they are mini-Langmuir cells about which we shall say more below. On the other hand, in the normal open channel flow case (Figure 6.28), the

iso-surfaces are less regular and organized. The ratio of the streamwise to spanwise length scales of the contours is closer to unity.

The instantaneous Langmuir circulation structure is in qualitative agreement with the sonograph obtained by Thorpe (1992). The coexistance of multiple scales of Langmuir circulations reported in field observations (Langmuir 1938, Assaf *et al.* 1971, Weller and Price 1988, Thorpe 1992) is evident. We believe that the structure seen is the result of two opposing forces. The Langmuir mechanism tends to form streaks that may coalesce with each other, increasing the distance between them. On the other hand, the turbulence breaks up the cells.

Figure 6.27 presents the same vorticity iso-surfaces for the case based on the Craik-Leibovich theory. As in the 3Dwavy flow, coherent structures can be clearly identified. Nevertheless, with a stronger mean secondary motion than in the 3Dwavy case, these streaks are more concentrated near the downwelling zone at $y \sim 0.8$. The structures seem also to have a lambda-shape, which may be due to the large shear introduced by the Craik-Leibovich theory.

The instantaneous structure varies with depth in Langmuir turbulence. Figures 6.29 and 6.30 provide the contours of instantaneous vorticity of the 3Dwavy case at four different depths in the curvilinear system. The horizontal planes are located at the centers of the four layers, each of thickness $1/(2\kappa_x)$. η^3 is the vertical coordinate in the curvilinear system, with $-1 \leq \eta^3 \leq 1$. The strong coherent longitudinal structures are concentrated in a layer of a thickness comparable to the Stokes drift decay scale near the top of the domain (Figure 6.30(a), where $\eta^3 \simeq 1 - 1/(4\kappa_x)$). With increasing depth, the magnitude of the streamwise vorticity decreases rapidly. At depth $1/(2\kappa_x)$ (Figure 6.30(b)), the streamwise oriented rolls have greater spanwise length scale but smaller streamwise length scale than at the top. This decrease of "streakiness" is also found in the plane located at another $1/(2\kappa_x)$ down, shown in Figure 6.30(a), the length of the structure has decreased. At $\eta^3 = 1 - 7/(4\kappa_x) = -0.11$ (Figure 6.30(b)), the structure is more fragmented, and the vorticity is even weaker. The diminishing of instantaneous Langmuir circulations with depth have also been reported by Skyllingstad and Denbo (1995) and McWilliams *et al.* (1997). A significant difference is that our results show no Ekman spiral of the streaks in McWilliams

et al. (1997), since the Coriolis force is not included.

6.7 Turbulence Properties and Budget

In this section, we focus on the statistical properties and budgets of Langmuir turbulence. These statistical moments are based on the ensemble averaging discussed in section 6.4.

6.7.1 Root Mean Square Fluctuations

The root mean square fluctuations of the three velocity components are presented in Figures 6.31 to 6.33 for the 3Dwavy, 3DCL, and 3DOChan cases. For the open channel case, since the turbulence is homogeneous in both lateral directions, the velocity variances are functions of z only. This is not true for the 3Dwavy and 3DCL cases. The velocity variances are functions of both y and z in the 3DCL case, and functions of x, y and z in the 3Dwavy case. Therefore, after the root mean square fluctuation fields are computed, horizontal averaging is used to produce the vertical profiles shown in these figures.

In all cases, the turbulence fluctuations reduce rapidly to zero at the bottom wall. Near the top surface, where constant shear stress is specified, both the lateral fluctuations, u''_{1rms} and u''_{2rms}, are finite while the vertical fluctuations, u''_{3rms} becomes to zero. That is, the vertical kinetic energy is redistributed into the horizontal components via the pressure redistribution. This behavior is similar to that found in the pressure-driven open channel flow by Lam and Banerjee (1992).

The velocity variance profiles for Langmuir turbulence in both the 3Dwavy and the 3DCL cases confirm the importance of the vertical scale discussed in the previous section, the e-folding depth of the Stokes drift near the top surface, $1/(2\kappa_x)$. From Figures 6.31 and 6.32, the streamwise and spanwise components of the velocity variance exhibit a sharp increase inside the e-folding depth of the Stokes drift, which is approximately 0.3 units thick. In particular, the spanwise velocity variance at the surface is almost double that at $z = 0.7$. In Figure 6.33, the vertical root mean square fluctuation reaches a peak value within the e-folding depth of the Stokes drift,

and decreases monotonically below, in agreement with McWilliams *et al.* (1997) and Skyllingstad and Denbo (1995). This vertical scale is due to the influence of the Craik-Leibovich forcing, which is responsible for the creation of the turbulence intensity in this layer.

Compared with open channel flow, Langmuir turbulence shows a greater anisotropy. Figure 6.31 shows that the streamwise velocity variance is larger in the open channel flow. In most of the domain, u''_{lrms} in the 3Dwavy case is 2/3 that in the 3DOChan case. However, as shown in Figures 6.32 and 6.33, the spanwise and vertical fluctuations are stronger in 3Dwavy case, especially in the upper half of the channel. These differences reflect the fact that secondary Langmuir circulations develop at the cost of the weakening of the streamwise motion, which is produced by the mean shear.

The profiles of the root mean square fluctuations are qualitatively similar in the 3Dwavy and 3DCL cases but all three components of the velocity variance are smaller in the 3DCL case than in the 3Dwavy case. This indicates that the Craik-Leibovich theory predicts weaker turbulence and stronger mean Langmuir circulations. This accords with our expectations. According to Monismith and Magnaudet (1998), there are three types of wave-turbulence interactions. (1) Fast turbulence has a time scale significantly smaller than the wave period. It responds quasi-steadily to the wave motion but is unable to extract much energy from the wave field. (2) Turbulence with time scales of the same order as the wave period can interact with the wave in a nonlinear fashion. (3) Slow turbulence has time scales much longer than the wave period and its response to the wave motion can be approximated by rapid distortion theory. It has been shown in Monismith and Magnaudet (1998) that the Craik-Leibovich theory assumes rapid distortion by the fast wave field of the slow Langmuir circulations. Therefore, the Craik-Leibovich theory neglects the second type of interaction and thus underestimates the turbulence intensities.

6.7.2 Energy Spectra

Figures 6.34 to 6.36 show one-dimensional energy spectra of the three velocity components at a vertical location approximately in the center of the e-folding depth of the Stokes drift. In these figures, k_y is the wave number in the spanwise direction. It can

be observed that, near the surface, the spanwise and vertical energy of all resolved scales in the 3Dwavy case are greater than that in the 3DOChan case. However, the streamwise energy in the 3Dwavy case is smaller than in the open channel flow for most length scales. This confirms the anisotropy of Langmuir turbulence as discussed in the last subsection. The smaller scales in the wavy case are due to the more intense turbulence which cascades more energy to the small scales.

These spectra also reveals that the energy in the small scale motions is weaker in the 3DCL case than in the 3Dwavy case, especially for the streamwise and spanwise energy components (Figure 6.34 and 6.35). This indicates that Craik-Leibovich theory predicts more kinetic energy in large scales. It is consistent with the instantaneous streamwise vorticity fields in Figure 6.11 and 6.12, which show larger scales near the surface in the 3DCL case than in the 3Dwavy case.

6.7.3 Reynolds Stress

The horizontally averaged Reynolds stresses, $- < u_1'' u_3'' >_{tx_1x_2}$, for the three core cases are compared in Figure 6.37. To interpret this plot, we need to look into details of the momentum transport.

As mentioned in section 6.5.1, at the statistically steady state, the total vertical transport of streamwise momentum should be constant with depth. The momentum transport consists of three parts: viscous diffusion, convective transport, and subgrid transport. For the cases under consideration, the subgrid component is very small. Also, except in the top and boundary layers, where viscous diffusion is significant, the streamwise momentum is mainly carried by the energetic convective motion. Therefore, the convective component, $- < \overline{u}_1 \overline{u}_3 >$ is dominant in most of the domain.

To estimate the total convective transport, horizontal averaging is applied. Thus $- < \overline{u}_1 \overline{u}_3 >$ becomes to $- < \overline{u}_1 \overline{u}_3 >_{tx_1x_2}$. The exception is the 3Dwavy case, where averaging is performed along the curvilinear coordinates, ξ^1 and ξ^2. As demonstrated in Figure 6.9, averaging along surfaces in the curvilinear system is a good approximation in most of the flow.

Due to the different physics of open channel flow and Langmuir turbulence, the distribution of the total convective transport among the components varies in these

cases.

The open channel flow, as discussed in section 6.4, can be decomposed into a steady, depth varying mean current and unsteady turbulence. Thus:

$$- < \overline{u}_1 \overline{u}_3 >_{tx_1x_2} = -u_{1MC}u_{3MC} - < u_1'' u_3'' >_{tx_1x_2} \tag{6.11}$$

where is subscript "MC" denotes the mean sheared current and is defined in Table 6.3. Since the mean vertical velocity, u_{3MC}, is identically zero, the total convective transport is equal to the Reynolds stress. In Figure 6.37, as expected, the Reynolds stress for the normal open channel flow is close to unity in most of the channel, except near the wall, where viscous diffusion dominates.

For the Langmuir turbulence, on the other hand, the mean flow obtained by the ensemble averaging contains an component due to the secondary Langmuir circulation. In addition, there also exists a wave component in the 3Dwavy flow. Therefore, each variable can be decomposed into three parts in the 3DCL case and four in the 3Dwavy case. Hence, the total convective term consists of nine and sixteen components for the 3DCL and 3Dwavy cases, respectively. However, some of them are zero by definition. After simplification, the convective momentum transport for the 3Dwavy case can be written as:

$$\begin{aligned} - < \overline{u}_1 \overline{u}_3 >_{t\xi^1\xi^2} \;=\; & -u_{1MC}u_{3MC} - < u_{1W}u_{3W} >_{t\xi^1\xi^2} - < u_{1L}u_{3L} >_{t\xi^1\xi^2} \\ & - < u_{1W}u_{3L} + u_{1L}u_{3W} >_{t\xi^1\xi^2} - < u_1'' u_3'' >_{t\xi^1\xi^2} \end{aligned} \tag{6.12}$$

and for 3DCL as:

$$- < \overline{u}_1 \overline{u}_3 >_{tx_1x_2} = - < u_{1L}u_{3L} >_{tx_1x_2} - < u_1'' u_3'' >_{tx_1x_2} \tag{6.13}$$

Therefore the Reynolds stresses for the 3Dwavy and 3DCL cases plotted in Figure 6.37 represent only a part of the convective transport of the streamwise momentum: that carried by the turbulence and the unsteady Langmuir circulations. The contribution of other components are given in Figure 6.38 for the 3DCL case and Figure 6.39 for the 3Dwavy case.

In the 3DCL case, the streamwise momentum transport is due to two processes, the Reynolds stress and the steady Langmuir circulations. Their sum must be unity except in the top and bottom boundary layers. In the upper half of the channel, the momentum is carried down mainly by the fluctuation field that is a combination of turbulence and unsteady Langmuir circulations. In the lower half of the channel, momentum is transported mainly via the steady Langmuir circulations.

In 3Dwavy case, besides the Reynolds stress, there exists momentum transport due to the mean current, the wave field, the Langmuir circulations, and the interaction of the wave and Langmuir circulations. They correspond to the first four terms on the right hand side of equation 6.12. According to Figure 6.39, the interaction between the wave and the Langmuir circulation produces virtually no transport of streamwise momentum. The contributions due to the mean current and the wave field are nearly zero in most of the domain and are small in a thin region near the top surface. Therefore, the streamwise momentum is transported mainly through the steady Langmuir circulations and the fluctuation field, as in the 3DCL case. The transport produced by the Langmuir circulations allows momentum to be transported deeper into the flow from the surface and produces a deeper mixed layer.

As seen in Figure 6.37, the Reynolds stress is greater in the 3Dwavy case than in the 3DCL case. Since the combined transport of the Reynolds stress and the Langmuir circulations is constant except at the top and the bottom, Langmuir circulations in the 3DCL case have to be stronger, in agreement with the discussion of the mean flow field in section 6.5.

6.7.4 Turbulent Kinetic Energy (TKE), Dissipation Rate and TKE Budgets

Comparison of horizontally averaged turbulent kinetic energy for the three core cases is presented in Figures 6.40. In the bottom boundary layer, the turbulent kinetic energy of the 3Dwavy case is similar to that in the open channel flow. In the lower half of the channel, the turbulence is weaker in the 3Dwavy flow than in the open channel flow. This is caused by the weakening of the streamwise mean current by the mixing due to the Langmuir turbulence. In the upper half of the channel, however,

the reduction in the streamwise turbulence intensity is compensated for by the spanwise and vertical turbulence generated by the wave-current interaction. This results in the turbulence kinetic energy in the 3Dwavy and the open channel cases being comparable. In the thin region very close to the top surface, the production due to the Langmuir mechanism increases rapidly and the turbulent kinetic energy of the 3Dwavy flow exceeds that of the open channel flow.

The turbulent kinetic energy profile for the 3DCL case is qualitatively similar to that for the 3Dwavy case, but the 3DCL flow is less turbulent than the 3Dwavy flow, as was shown earlier.

Figure 6.41 compares the viscous dissipation rate of the three cases. For the open channel case, the flow exhibits the law-of-the-wall behavior in both the top and bottom boundary layers, where the velocity profiles are logarithmic, as shown in section 6.5. Therefore, the dissipation due to the turbulent motion balances the turbulence production, and is scaled as the cube of the shear velocity divided by the length scale (Skyllingstad and Denbo 1995). That is:

$$\varepsilon^d = \frac{u_*^{d3}}{\kappa(h - z^d + z_0^d)} \quad \text{upper half channel} \tag{6.14}$$

$$\varepsilon^d = \frac{u_*^{d3}}{\kappa(h + z^d + z_0^d)} \quad \text{lower half channel} \tag{6.15}$$

where $\kappa = 0.4$ is von Karman's constant and z_0^d is the roughness length representing the minimum scale of the turbulent eddies (Craig and Banner 1994), and $h - z^d$ and $h + z^d$ are the distances from the top and bottom walls, respectively. The roughness length for the bottom boundary layer has been well studied (Jenter and Madsen 1989). Here we use $z_0^d = 0.1m$ for both the top and bottom boundary layers, as suggested by Craig and Banner (1994). Using the velocity scale u_*^d and the length scale h, the non-dimensional dissipation is:

$$\varepsilon = \frac{1}{\kappa(1 - z + z_0)} \quad \text{upper half channel} \tag{6.16}$$

$$\varepsilon = \frac{1}{\kappa(1 + z + z_0)} \quad \text{lower half channel} \tag{6.17}$$

where $z_0 = 0.08$. These law of the wall profiles for the dissipation are also plotted in Figure 6.41 for comparison.

It can be seen that the energy dissipation rate in the 3DOChan case decreases inversely with wall distance, supporting the law of the wall. In the bottom boundary layer, dissipation of the 3Dwavy case is close to that in the open channel flow. For the 3DCL case, since the flow is less turbulent, the energy dissipation is smaller than in the 3Dwavy case there. In the lower half of the channel, Langmuir turbulence weakens the turbulence intensity and thus the dissipation is smaller than in the open channel case. In the upper half of the channel, due to the turbulence induced by the wave-current interaction, the dissipation in Langmuir turbulence is bigger than that in the lower half of the channel and is comparable to the open channel case. While the 3DCL flow has a smaller turbulent kinetic energy than the 3Dwavy flow, the dissipation in the two cases are close to each other in most of the domain. Furthermore, the dissipation in the 3DCL case is greater than in the 3Dwavy case near the surface. This implies that the simply production-dissipation balance of turbulent kinetic energy in the open channel flow does not apply to Langmuir turbulence. As will be shown shortly, terms such as pressure transport play more important roles than viscous dissipation.

The distributions of both the turbulent kinetic energy and the viscous dissipation in a spanwise-vertical plane are highly correlated with the Langmuir circulations. Figure 6.42 and 6.43 show the contours of streamwise averaged turbulent kinetic energy and viscous dissipation, respectively. Clearly, as shown in Figure 6.42, turbulence that is generated near the top and bottom walls is convected by the Langmuir circulations and thus is concentrated in the downwelling zone near the top surface and the upwelling zone near the bottom surface. Likewise, the viscous dissipation occurs mainly near the top and bottom surfaces, and its contours are closely related to the Langmuir circulations.

For the 3Dwavy case and the open channel case, the mean budget of the turbulence kinetic energy can be derived from the Reynolds stress transport equation 2.69 by multiplying it by 0.5 and setting the subscript $i = j$, *i. e.* taking the trace of these

equations. The resulting equation is similar to equation 2.69 except that the pressure-strain term drops out:

$$< \frac{1}{2} u_i'' u_i'' >_{,t} = C + P + T + \Pi + D + \varepsilon + T^{sgs} + \varepsilon^{sgs} \tag{6.18}$$

Each term on the right hand side of this equation is half the trace of the corresponding tensor in equation 2.69. Their definitions are listed in section 2.6.

The Craik-Leibovich equations has an extra vortex force term not present in the Navier-Stokes equations. As a result, equations 2.69 and 6.18 become respectively:

$$\begin{aligned} < u_i'' u_j'' >_{,t} &= C_{ij} + P_{ij} + T_{ij} + \Pi_{ij} + \phi_{ij} + D_{ij} + \varepsilon_{ij} + T_{ij}^{sgs} + \varepsilon_{ij}^{sgs} \\ &\quad + H_{ij} \end{aligned} \tag{6.19}$$

$$< \frac{1}{2} u_i'' u_i'' >_{,t} = C + P + T + \Pi + D + \varepsilon + T^{sgs} + \varepsilon^{sgs} + H \tag{6.20}$$

where $H_{ij} = \epsilon_{ilm} u_{sl} < \omega_m'' u_j'' > + \epsilon_{jlm} u_{sl} < \omega_m'' u_i'' >$ is the production term due to the vortex forcing, with u_s as the Stokes drift velocity, and $H = 0.5 H_{ii}$.

In the open channel flow, the production term (P) is approximately balanced by the dissipation term (ε) at all depths, as shown in Figure 6.44.

In the Langmuir turbulence of the 3DCL case, although the budget is similar to the open channel flow budget in the bottom boundary layer, it is dramatically different near the top surface. This is demonstrated by Figure 6.45, where the horizontally averaged turbulent kinetic energy budget is plotted, note the different scales in Figures 6.44 and 6.45. In a layer of thickness $1/(2\kappa_x)$ near the top surface, the vortex force production rate (H) greatly exceeds the shear production of the open channel flow. It is mainly balanced by the pressure transport term (Π) in that region, and viscous dissipation (ε) is less important there. Therefore, the turbulent kinetic energy produced near the surface is transported downward by the pressure transport. Physically it is due to the pressure gradient that drives the flow away from the upwelling zone to the downwelling zone near the top surface.

The turbulent kinetic energy budget varies in the streamwise direction for the 3Dwavy case. The spanwise averaged budgets are shown in Figures 6.46 to 6.49 at the wave crest, forward slope, trough and backward slope, respectively. It can be

observed that at the wave slopes the principal terms are the production rate (P), the pressure transport term (Π) and the mean velocity transport term (C). These three terms have opposite signs at the forward and backward slopes. At the crest and trough of the wave, the magnitudes of these three terms are smaller, and viscous dissipation becomes important. Nonetheless, the dissipation profile is similar at all streamwise coordinates.

The turbulent production of the 3Dwavy case is studied in Figures 6.50 to 6.53. Figure 6.50 shows the contours of spanwise averaged turbulent production, P. It can be seen that the turbulence are mainly generated under the crest of the surface wave, as observed by Thais and Magnaduet (1996). A closer examination of the components of the production term indicates that the turbulence is mainly generated through the combined effects of wave stretching, $-(< u_1''u_1'' >_{t\xi^2} \frac{\partial <\overline{u}_1>_{t\xi^2}}{\partial x_1} + < u_3''u_3'' >_{t\xi^2} \frac{\partial <\overline{u}_3>_{t\xi^2}}{\partial x_3})$, and mean shear, $- < u_1''u_3'' >_{t\xi^2} (\frac{\partial <\overline{u}_1>_{t\xi^2}}{\partial x_3} + \frac{\partial <\overline{u}_3>_{t\xi^2}}{\partial x_1})$, as shown in Figure 6.51.

The contours of the stretching term, $-(< u_1''u_1'' >_{t\xi^2} \frac{\partial <\overline{u}_1>_{t\xi^2}}{\partial x_1} + < u_3''u_3'' >_{t\xi^2} \frac{\partial <\overline{u}_3>_{t\xi^2}}{\partial x_3})$, are presented in Figure 6.53. In isotropic turbulence, continuity requires this term to be zero. However, in this case, the wave stretching causes the flow to be anisotropic. Therefore, this production component becomes finite. Due to the periodicity of the wave motion, the production due to wave stretching alternates sign in the streamwise direction, with the turbulence gaining and losing energy to the wave field. This effect was observed by Pidgeon (1999) while investigating wave breaking.

The production component due to the shear layer, $- < u_1''u_3'' >_{t\xi^2} (\frac{\partial <\overline{u}_1>_{t\xi^2}}{\partial x_3} + \frac{\partial <\overline{u}_3>_{t\xi^2}}{\partial x_1})$, is shown in Figure 6.53. It is highly correlated with the Reynolds stress field, as shown in Figure 6.54, which is mainly generated under the wave crest. Furthermore, It can be observed that the production rate from the mean sheared motion and wave stretching are comparable, indicating that both the shear layer and the wave motion are important in producing turbulence.

Convective motion is one of the major mechanisms in redistributing turbulent kinetic energy in the 3Dwavy case. Figure 6.55 presents the spanwise averaged mean convection of the turbulent kinetic energy, C. The convective transport occurs mainly near the surface and is dominated by the sum of the streamwise component, $- < \overline{u}_1 >_{t\xi^2} \frac{\partial(1/2 <u_i''u_i'' >_{t\xi^2})}{\partial x_1}$, and the vertical component, $- < \overline{u}_3 >_{t\xi^2} \frac{\partial(1/2 <u_i''u_i'' >_{t\xi^2})}{\partial x_3}$,

as indicated in Figure 6.56. Figures 6.57 and 6.58 present the contours of the streamwise and vertical convective transport rate, respectively. The convection reaches it maximum magnitude in the thin wavy boundary layer near the surface. Furthermore, the vertical component is 180 degrees out of phase with the streamwise component. The net effects as shown in Figure 6.55 is positive convection at the forward slope and negative convection at the backward slope.

6.8 Summary

Large eddy simulations of Langmuir turbulence in a wavy domain (3Dwavy) were performed. The results were compared with ones derived from the Craik-Leibovich theory on a non-wavy domain (3DCL). In addition, to estimate the effects of the Langmuir circulations on the mixing, a numerical simulation of a stress-driven open channel flow (3DOchan) was carried out.

The turbulence model used is the dynamic subgrid scale model by Germano *et al.* (1991) with the correction by Lilly (1992). Its implementation is checked by simulating a closed channel flow and validated by the fact that the resulting mean current velocity profile, Reynolds stress and turbulence intensity agree reasonably well with the direct numerical simulation by Kim *et al.* (1987) compared with other large eddy simulations (Garg 1996).

In the wavy case, Langmuir circulations are generated by the interaction of the stress-driven mean current and the wave field, and are embedded in the irregular, chaotic instantaneous flow field. They can be clearly identified after time averaging the flow field. In the mean flow field, Langmuir cells coexist with the first order wave field. The longitudinal vortices slightly alter the wave field, and in turn, they are modulated by the surface wave. A current anomaly is observed, but it is rather weak near the top surface compared with that near the bottom boundary layer. This is due to the stirring effects of the turbulence, whose intensity is larger at the upper surface. The maximum downwelling speed and pitch compare favorably with those measured in field observations.

Compared with that in open channel flow, the mean current profile is quite different. The logarithmic region of near the bottom wall is reduced. Furthermore, the logarithmic profile near the top surface is almost entirely destroyed by the Langmuir circulations, resulting in a more uniform mean current.

The instantaneous Langmuir turbulence flow field has a rich structure that includes short, longitudinal streaks that are irregularly distributed near the top surface, in agreement with the multiple scales observed in experiments. In contrast, the open channel flow is more homogeneous in this region.

Langmuir turbulence produces greater anisotropy in the turbulence intensities than shear turbulence. Larger perturbations occur in the spanwise and vertical directions and less streamwise turbulence intensity is obtained.

In the turbulence, the momentum input due to the top shear stress is carried vertically by the Reynolds stress in the region outside the top and bottom boundary layers. In Langmuir turbulence, however, the turbulence only contributes about half of the vertical transport of streamwise momentum, with the other half due to the mean Langmuir circulations, demonstrating the critical role of Langmuir circulations in mixing. This has great implication in the modeling of upper ocean. Because standard turbulent parameterizations may only predict the momemtum transport due to shear turbulence, modifications must be made to count for the significant contribution of Langmuir circulations.

An important length scale discovered in the turbulence property profiles is the e-folding depth of the Stokes drift. Inside a top layer that scales with this depth, the turbulent kinetic energy increases rapidly. Its budget shows enhanced production in this region. This is balanced by the pressure transport term and the mean convective term due to wave motion. This length scale supports the notion of a vortex force, which is proportional to the Stokes drift in the Craik-Leibovich theory.

Except for the absence of a wave field in the 3DCL case, the flow field predicted by the Craik-Leibovich theory is similar to the 3Dwavy flow. In particular, the mean current in the two cases are quantitatively close in the two cases. The Langmuir circulations obtained are also qualitatively similar. However, the Craik-Leibovich theory predicts stronger mean Langmuir circulations and weaker turbulence, probably

because it neglects the interaction of turbulent eddies with time scales comparable to the wave period.

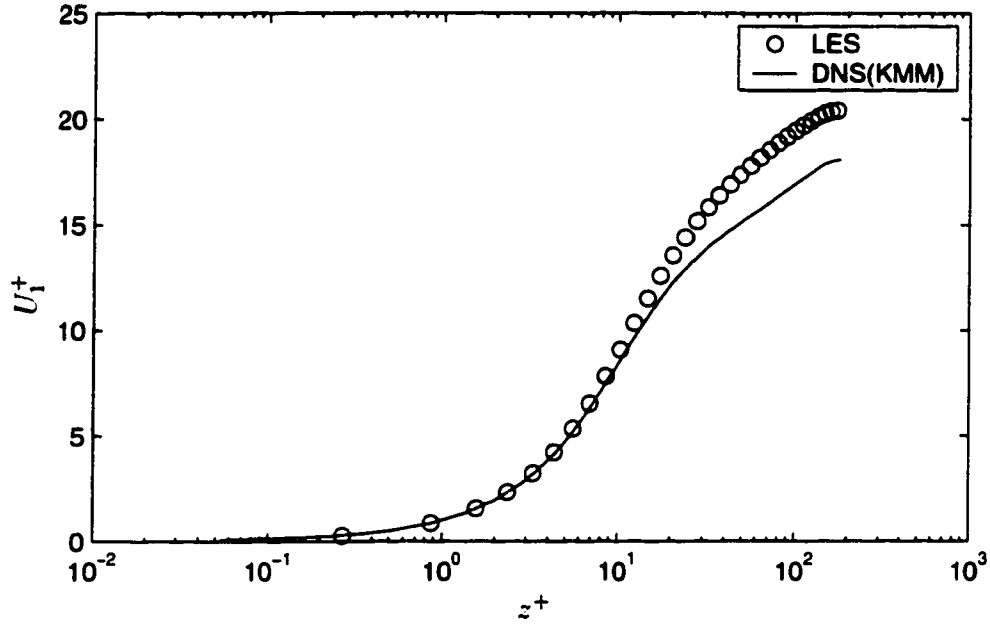

Figure 6.1: Comparison of mean velocity (normalized by u_*^d) from LES with DNS of Kim *et al.* (1987), $Re_* = 180$.

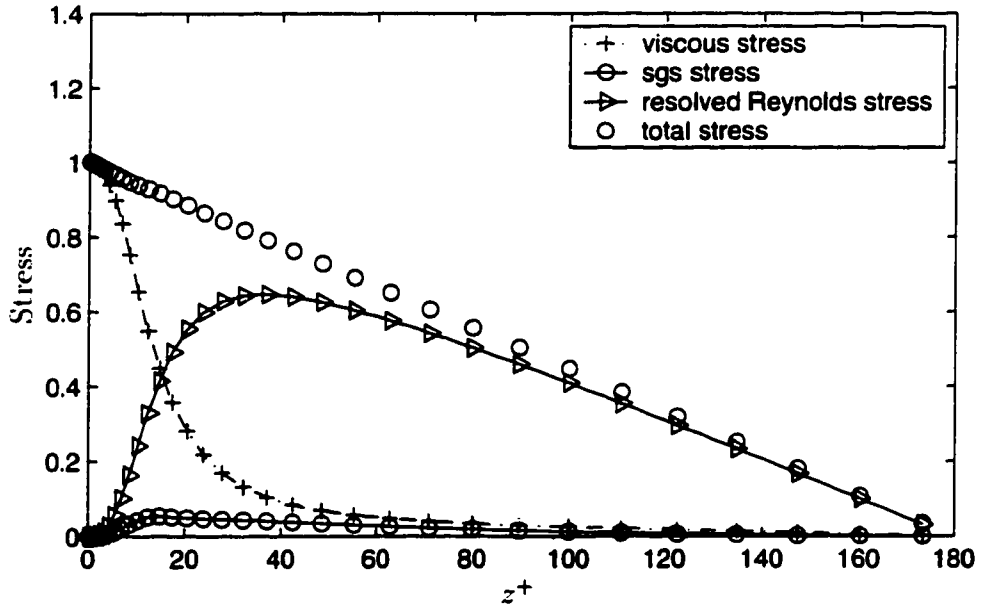

Figure 6.2: Stress components (normalized by u_*^{d2}) and the total stress of LES for $Re_* = 180$.

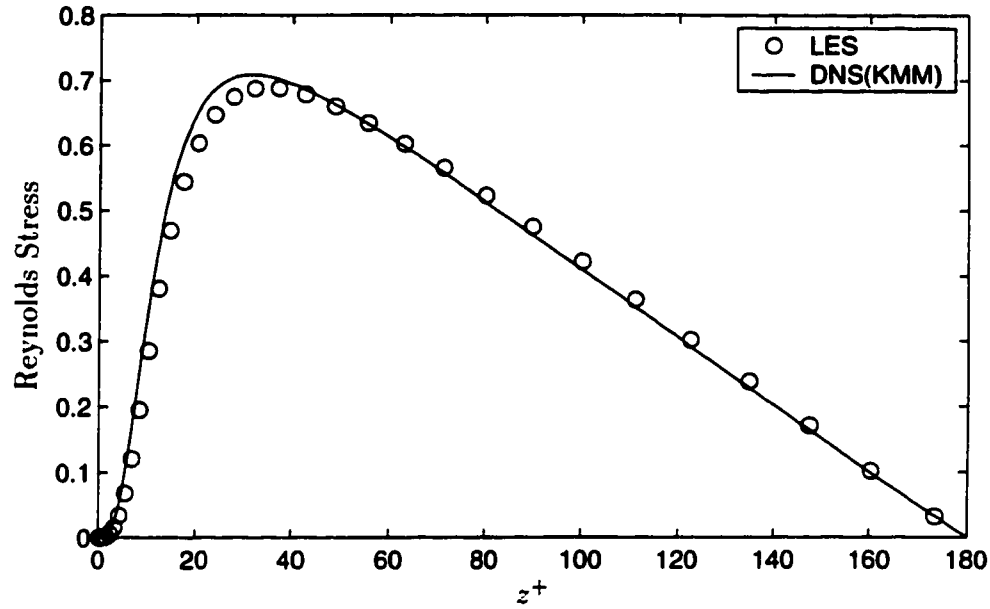

Figure 6.3: Comparison of Reynolds stress (normalized by u_*^{d2}) from LES ($- < u_1'' u_3'' > -q_{13}$) with DNS of Kim *et al.* (1987), $Re_* = 180$.

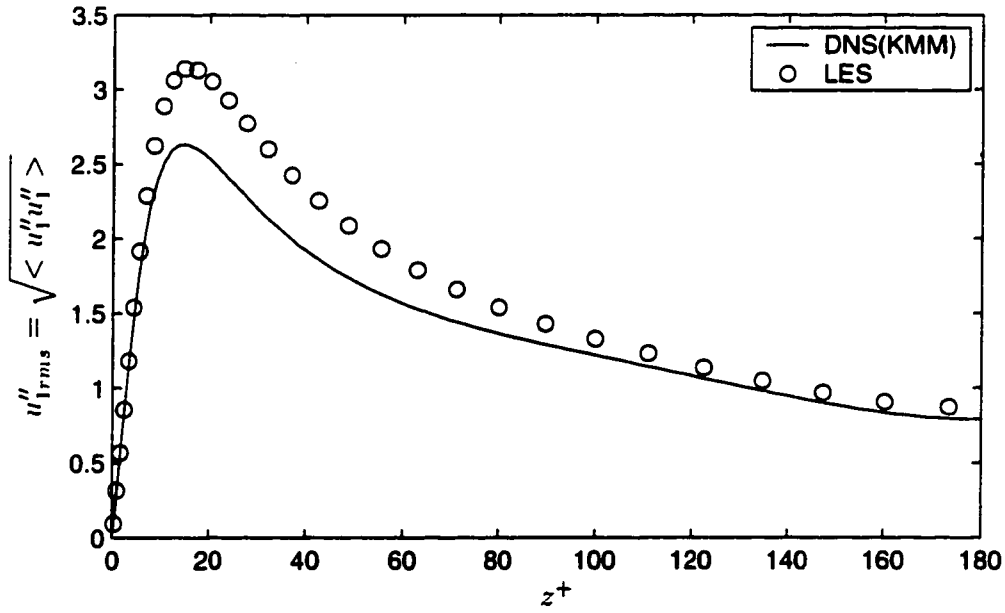

Figure 6.4: Comparison of u''_{1rms} (normalized by u_*^d) from LES with DNS of Kim *et al.* (1987), $Re_* = 180$.

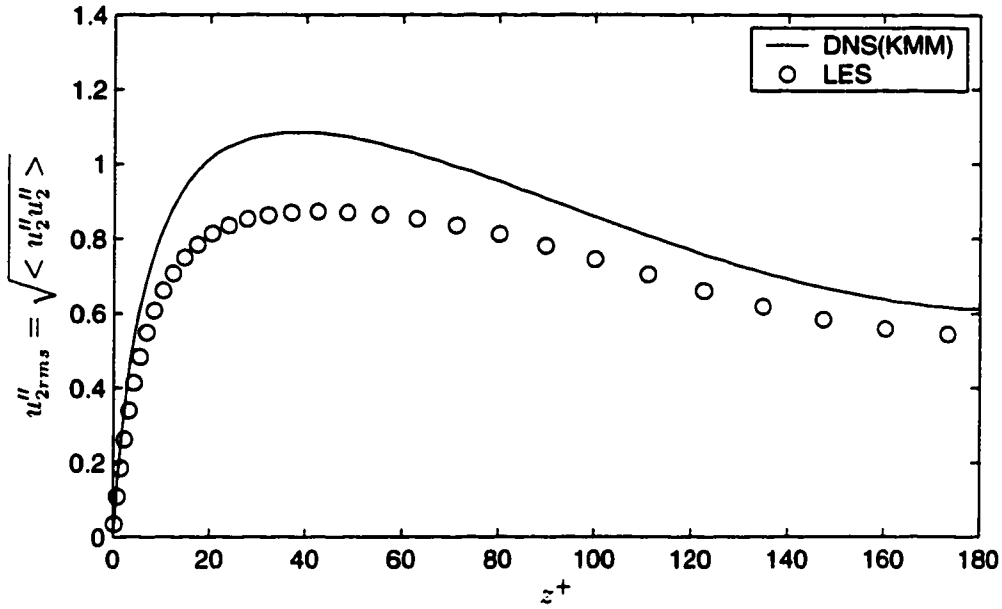

Figure 6.5: Comparison of u''_{2rms} (normalized by u^d_*) from LES with DNS of Kim *et al.* (1987), $Re_* = 180$.

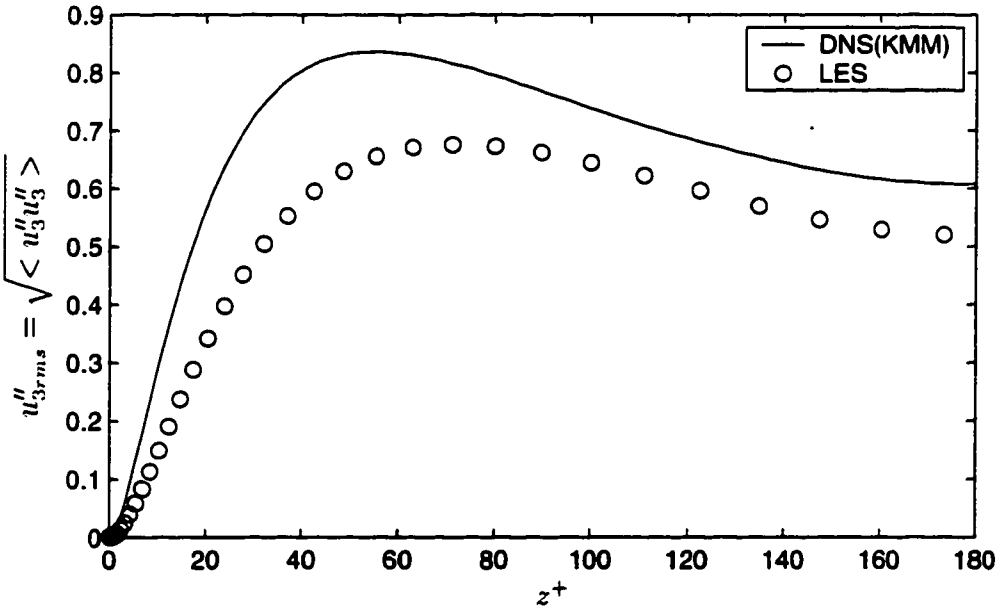

Figure 6.6: Comparison of u''_{3rms} (normalized by u^d_*) from LES with DNS of Kim *et al.* (1987), $Re_* = 180$.

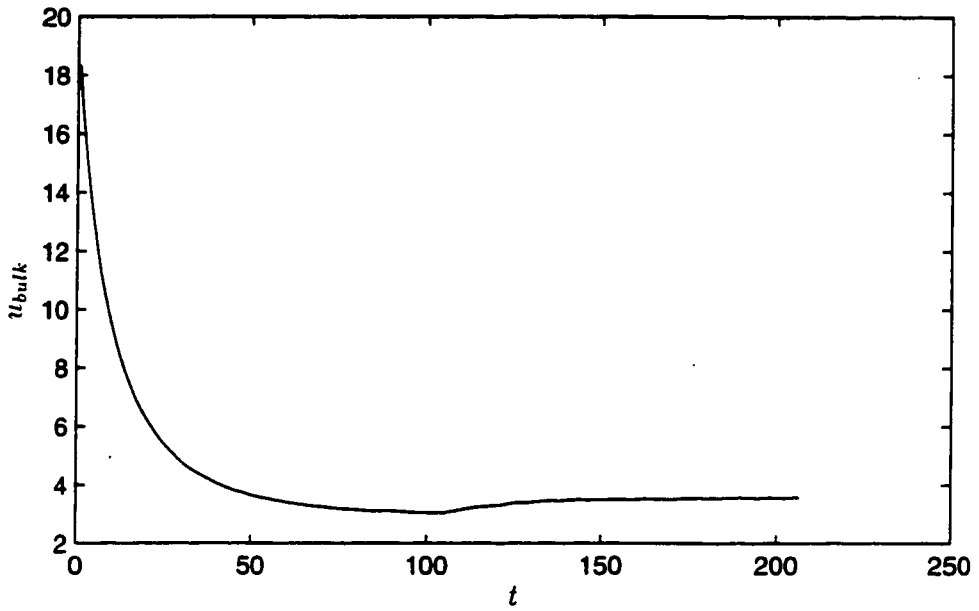

Figure 6.7: Time evolution of u_{bulk} (u_{bulk} normalized by u_∞^d, t by h/u_∞^d).

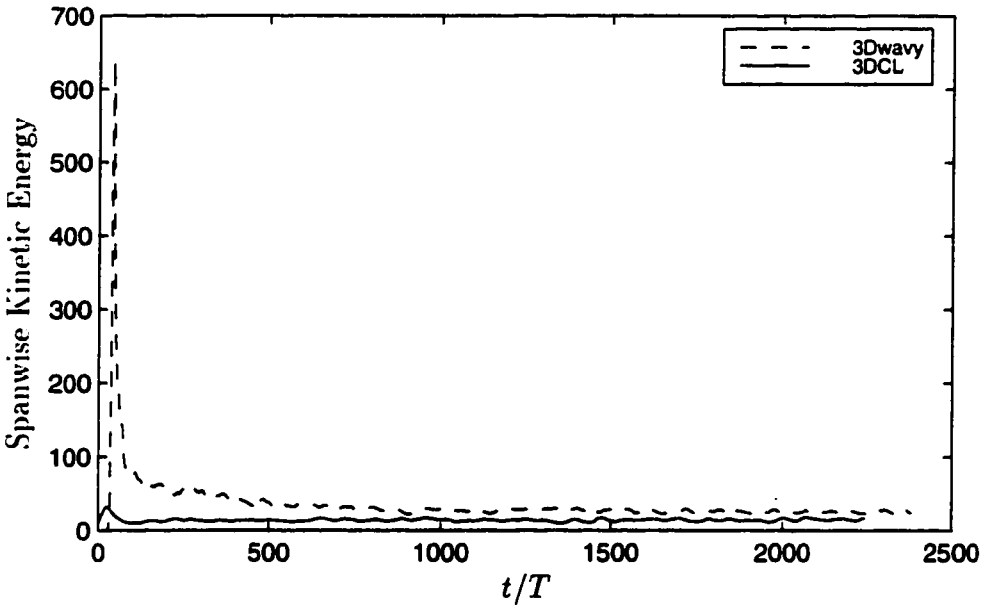

Figure 6.8: Time evolution of spanwise kinetic energy (normalized by S^2).

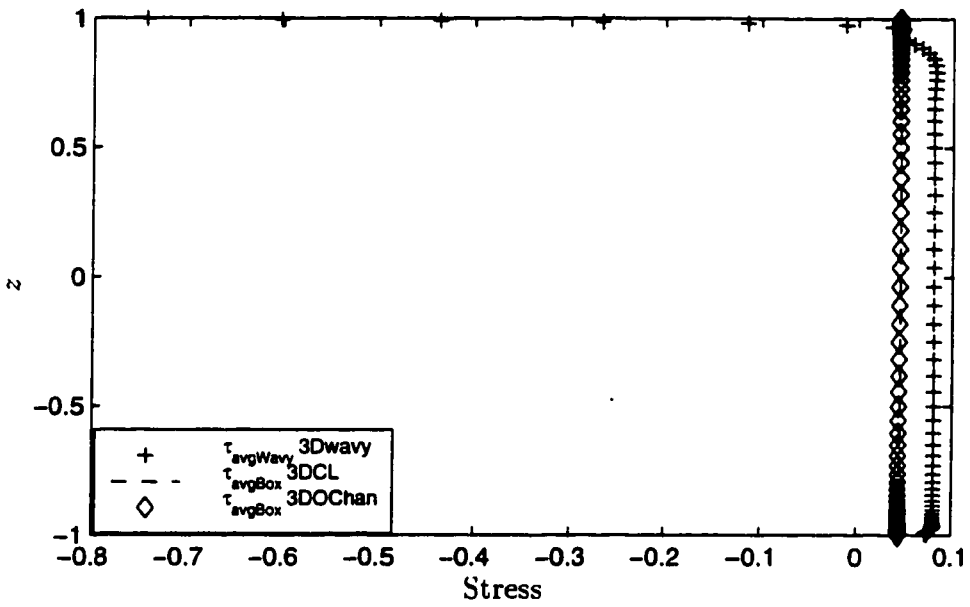

Figure 6.9: Top stress estimation for the turbulent box cases. (Stress is normalized by S^2, z is normalized by h)

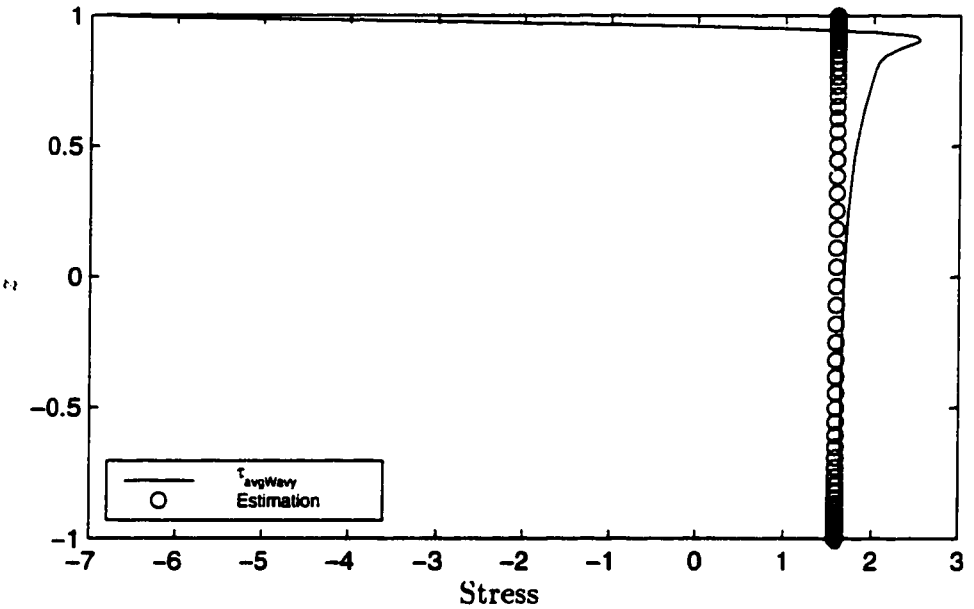

Figure 6.10: Top stress estimation for the laminar box case based on the Craik-Leibovich theory. (Stress is normalized by S^2, z is normalized by h)

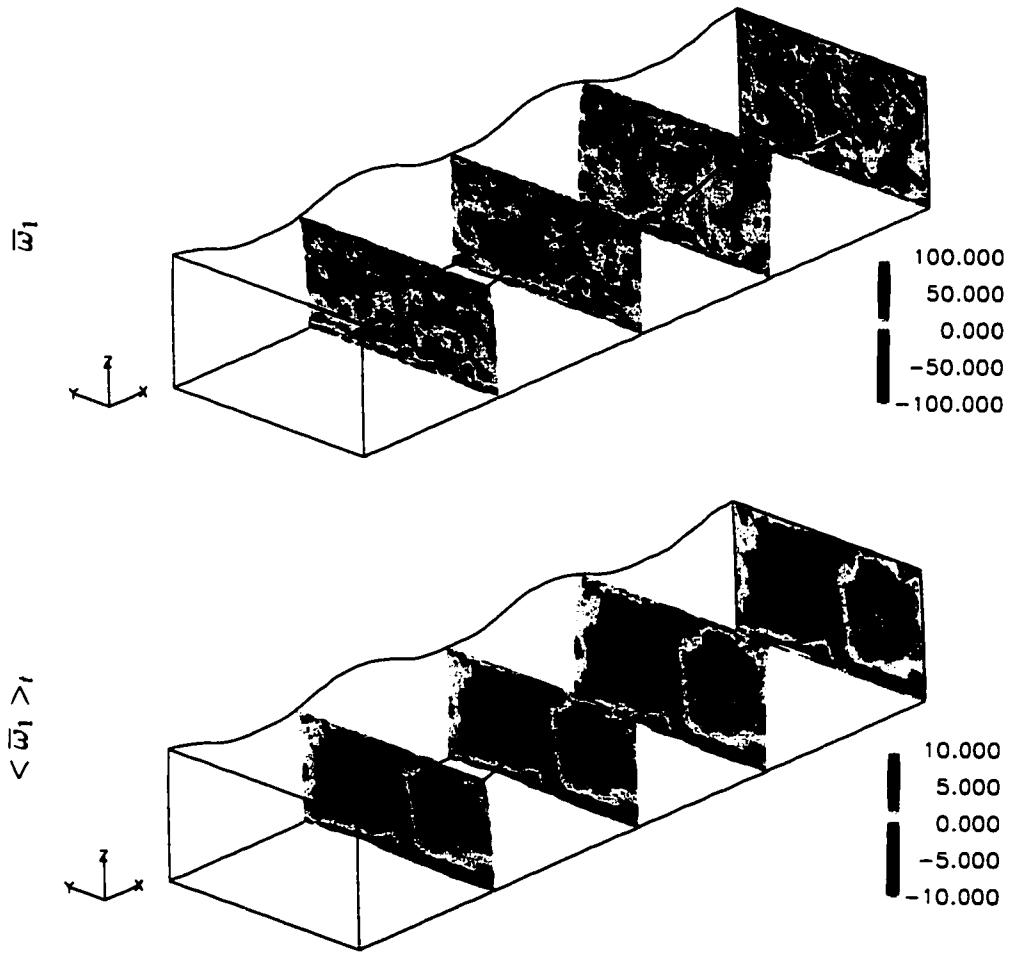

Figure 6.11: 3DwavyT1 case. Vorticity contours on spanwise-vertical planes. (normalized by u^d_{*wavy}/h)

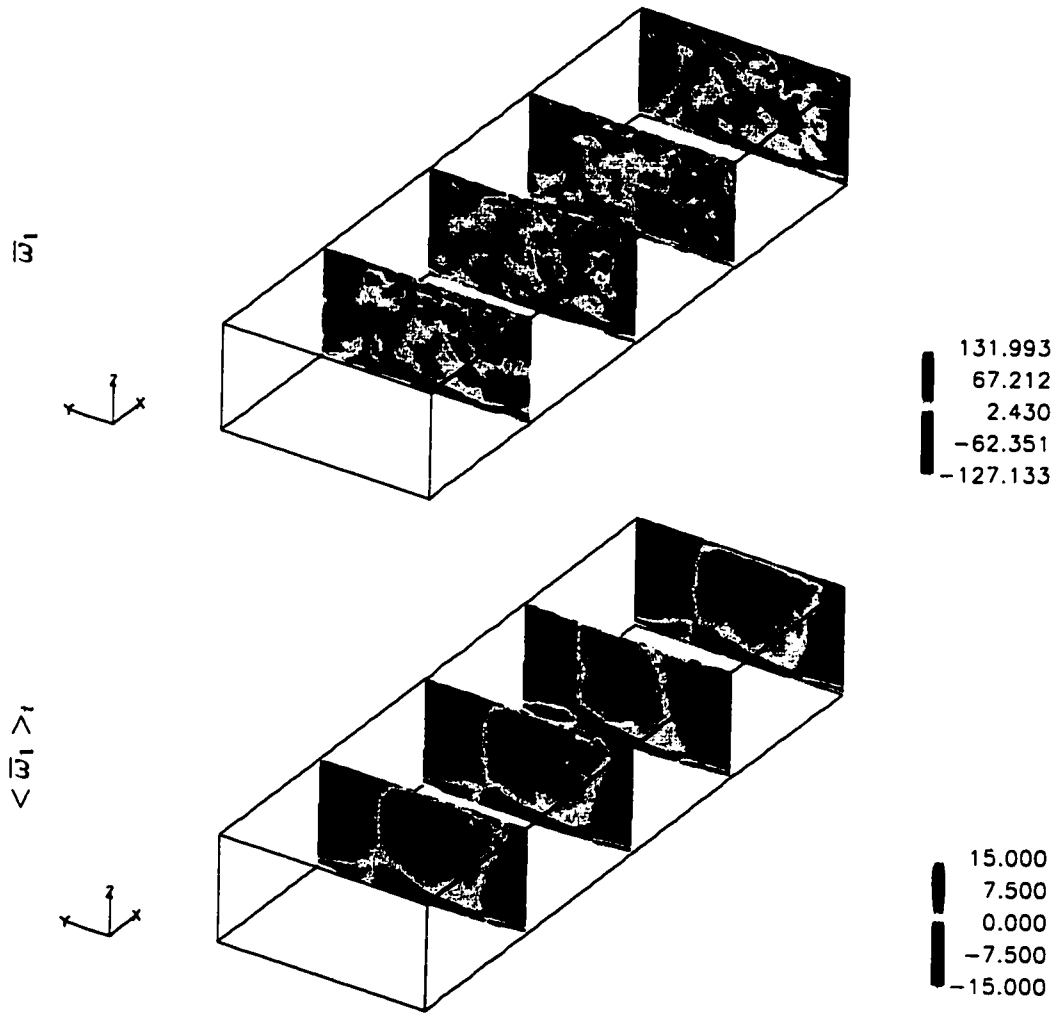

Figure 6.12: 3DCLT1E case. Vorticity contours on spanwise-vertical planes. (normalized by u^d_{*CL}/h)

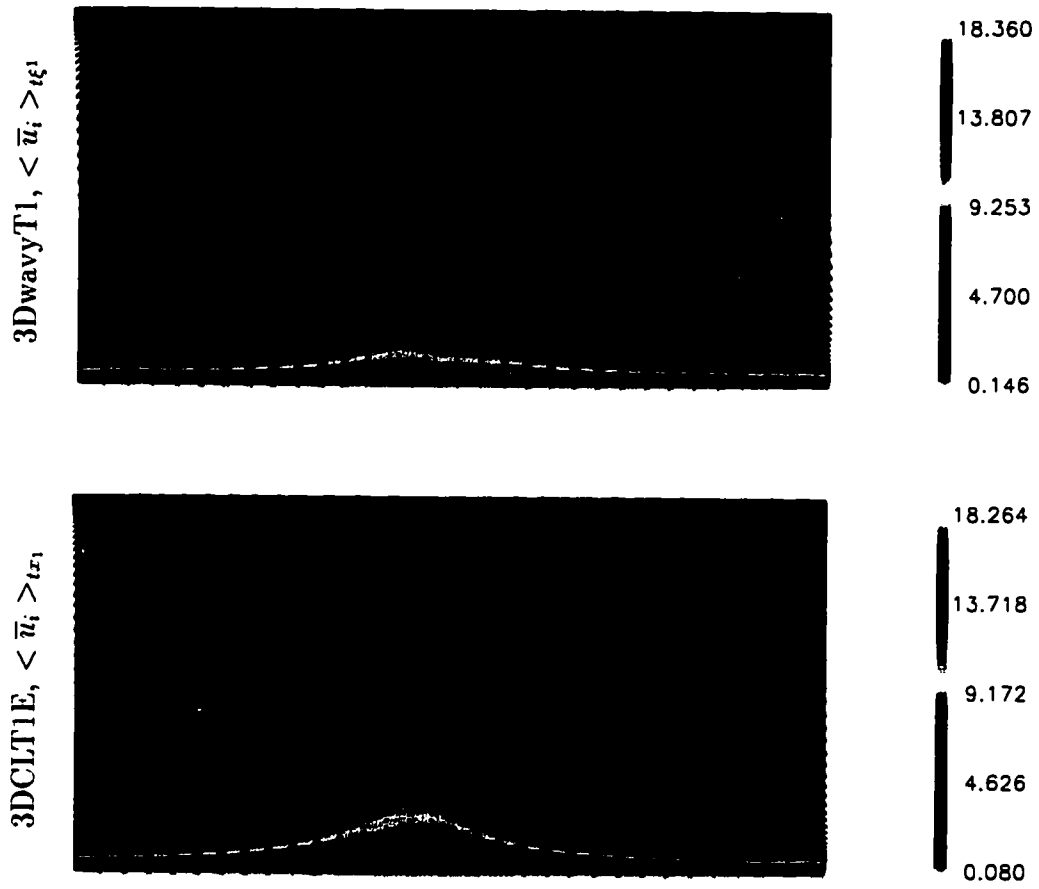

Figure 6.13: Comparison of the 3DwavyT1 and 3DCLT1E streamwise velocity contours and spanwise-vertical velocity vectors. They are shown on spanwise-vertical planes, with the mean current flow out of the paper. The plot of the 3DCLT1E case is phase-shifted in the spanwise direction. (3DwavyT1: normalized by u^d_{*wavy}, 3DCLT1E: normalized by u^d_{*CL}.)

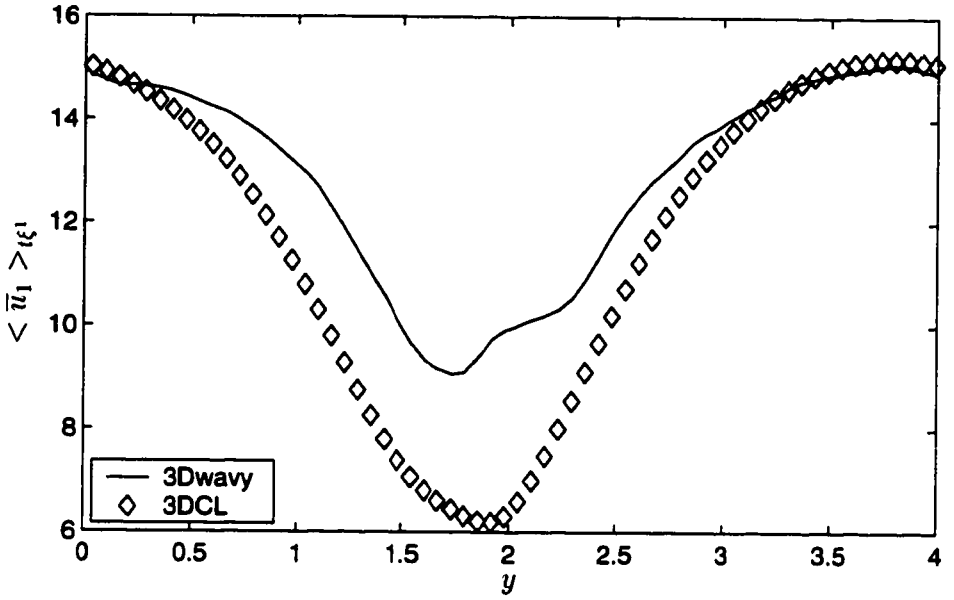

Figure 6.14: Comparison of 3DwavyT1 and 3DCLT1E streamwise velocity profiles as functions of the spanwise coordinate, where maximum downwind jet occurs. The profile of the 3DCLT1E case is phase-shifted in the spanwise direction. (Velocity normalization: 3DwavyT1 by u^d_{*wavy}, 3DCLT1E by u^d_{*CL}; y is normalized by h)

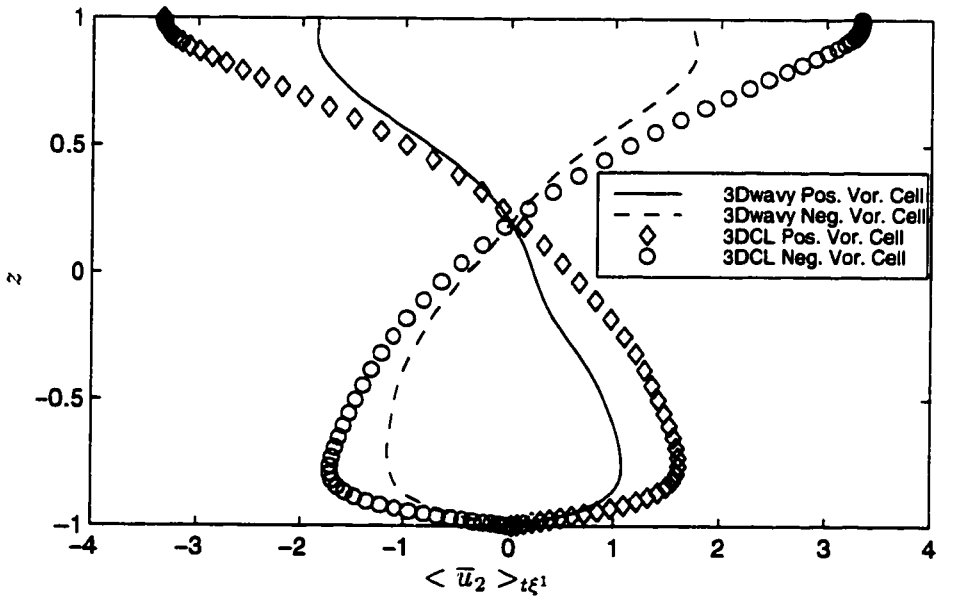

Figure 6.15: Comparison of 3DwavyT1 and 3DCLT1E spanwise velocities along the vertical centerlines of the Langmuir cells. (Velocity normalization: 3DwavyT1 by u^d_{*wavy}, 3DCLT1E by u^d_{*CL}; z is normalized by h)

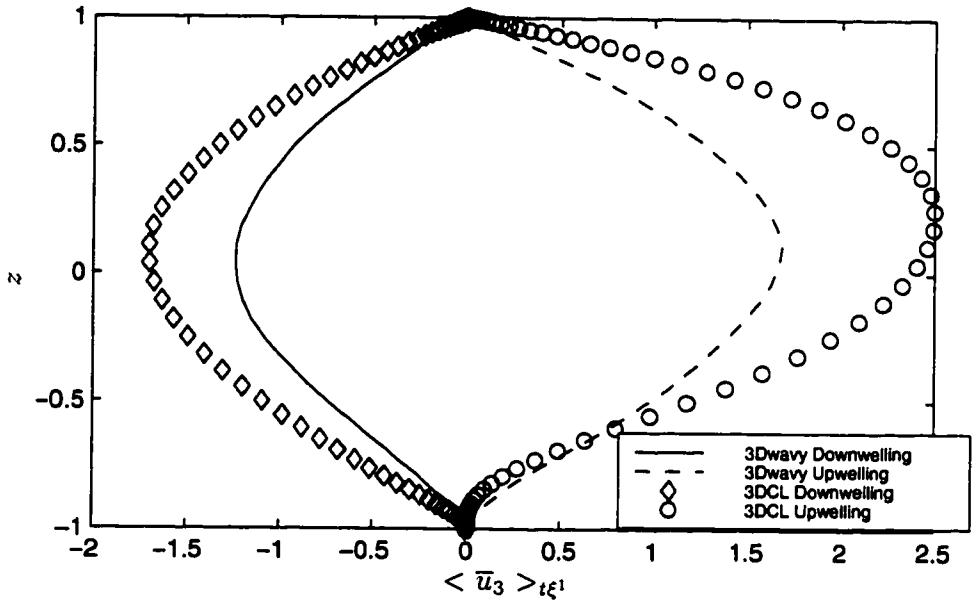

Figure 6.16: Comparison of 3DwavyT1 and 3DCLT1E vertical velocities at the upwelling and downwelling zones. (Velocity normalization: 3DwavyT1 by u^d_{*wavy}, 3DCLT1E by u^d_{*CL}; z is normalized by h)

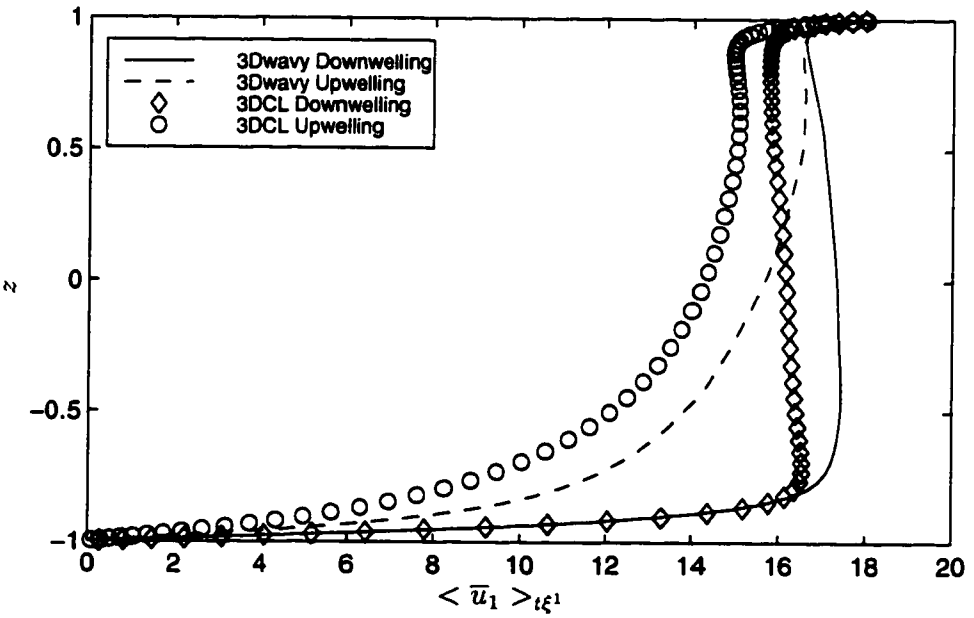

Figure 6.17: Comparison of 3DwavyT1 and 3DCLT1E streamwise velocities at the upwelling and downwelling zones. (Velocity normalization: 3DwavyT1 by u^d_{*wavy}, 3DCLT1E by u^d_{*CL}; z is normalized by h)

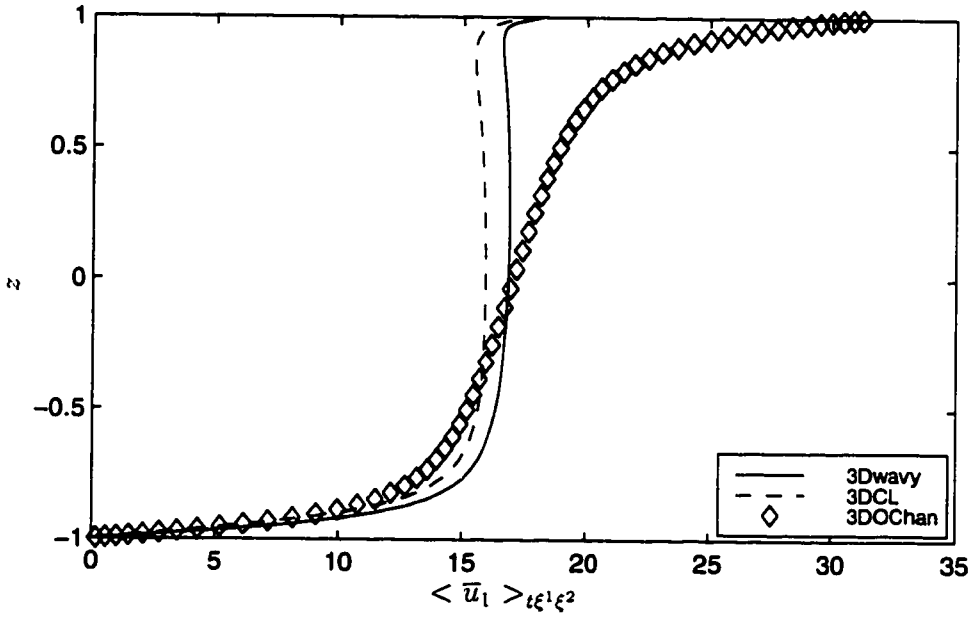

Figure 6.18: Comparison of 3DwavyT1, 3DCLT1E and 3DOchanT1E cases. Mean streamwise current profile. (Velocity normalizations: 3DwavyT1 by u^d_{*wavy}, 3DCLT1E by u^d_{*CL}, 3DOchan by u^d_{*OChan}; z is normalized by h)

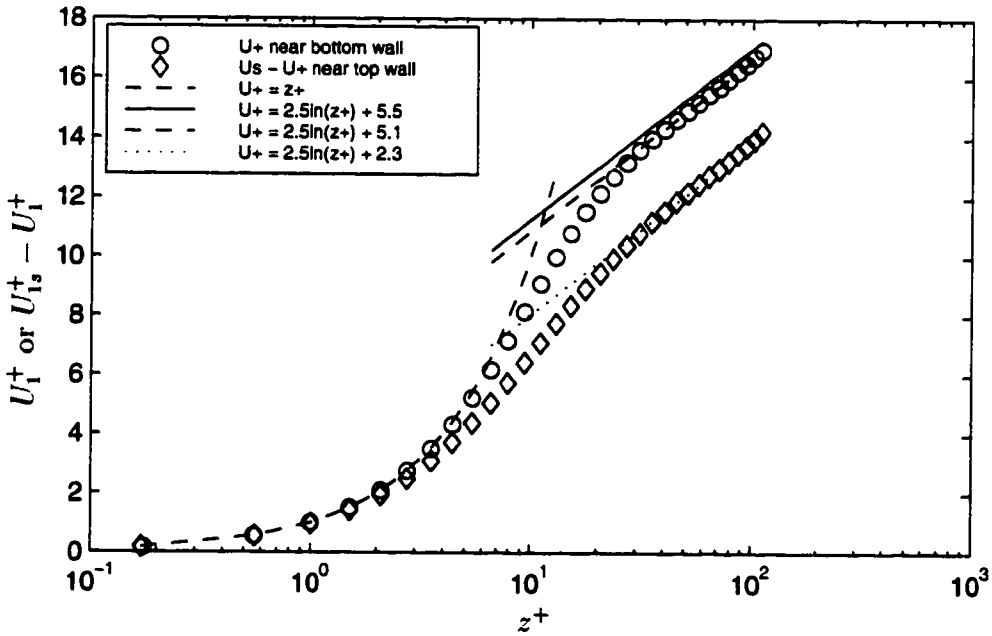

Figure 6.19: 3DOChanT1E. Mean streamwise velocity profiles in wall units. ($U_1^+ =< \overline{u}_1^d >_{tx_1x_2} / u^d_{*OChan}$, $z+$ is the distance from the wall scaled by ν/u^d_{*OChan}, U_{1s}^+ is the value of U_1^+ at the top surface)

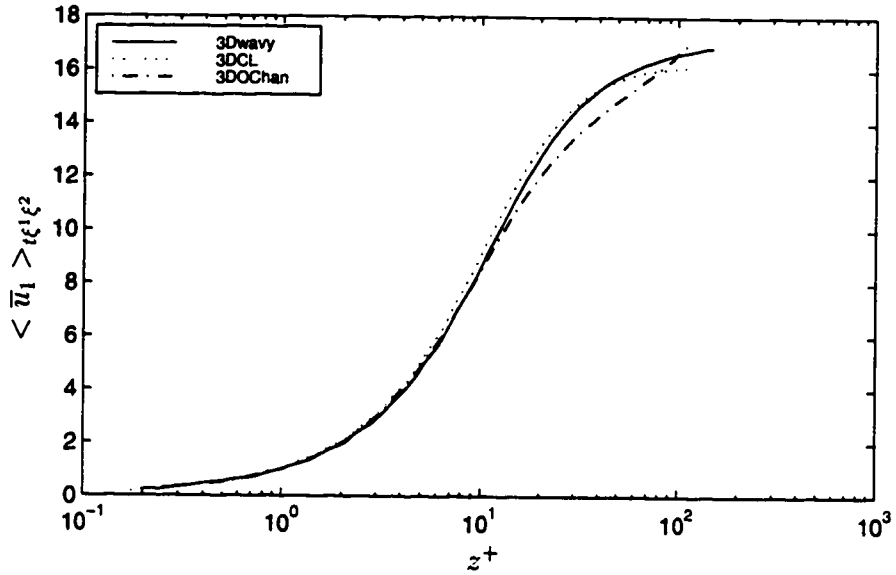

Figure 6.20: Comparison of the mean velocity profiles near the bottom wall for cases 3DwavyT1, 3DCLT1E, and 3DOChanT1E. (Velocity normalizations: 3DwavyT1 by u^d_{*wavy}, 3DCLT1E by u^d_{*CL}, 3DOchan by u^d_{*OChan}; the plus units of z are based on the shear velocity of each case)

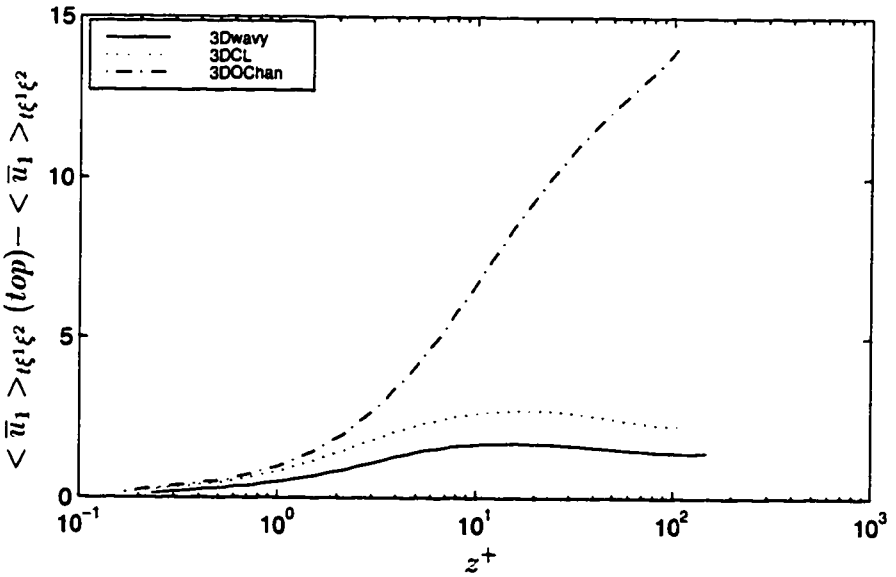

Figure 6.21: Comparison of the mean velocity deficit profiles near the top wall for cases 3DwavyT1, 3DCLT1E, and 3DOChanT1E. (Velocity normalizations: 3DwavyT1 by u^d_{*wavy}, 3DCLT1E by u^d_{*CL}, 3DOchan by u^d_{*OChan}; the plus units of z is based on the shear velocity of each case)

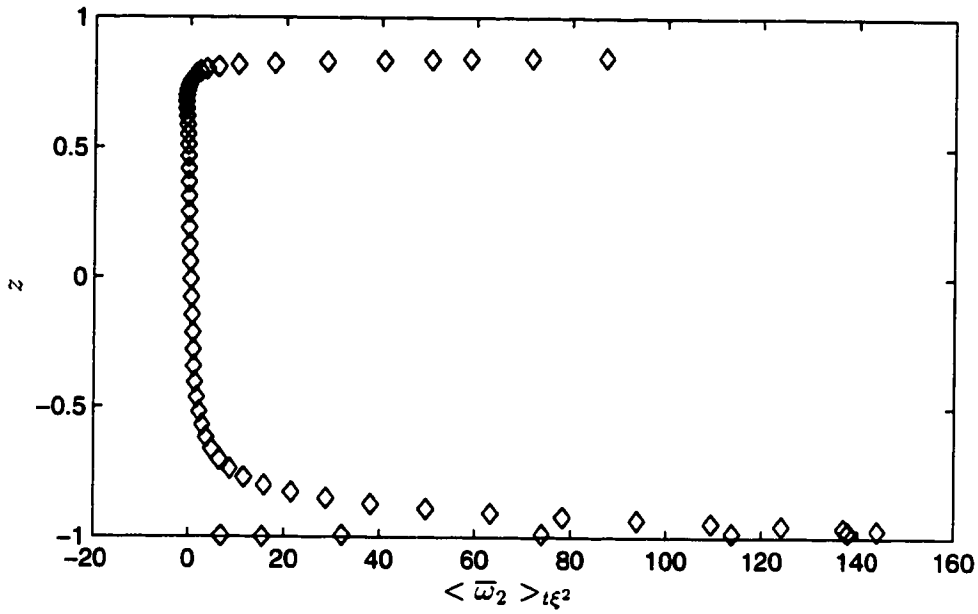

Figure 6.22: 3DwavyT1 case. Spanwise vorticity $< \overline{\omega}_2 >_{t\xi^2}$ (normalized by $u^d_{*wavy}/h.$) as a function of depth (normalized by h) under the trough of the surface wave.

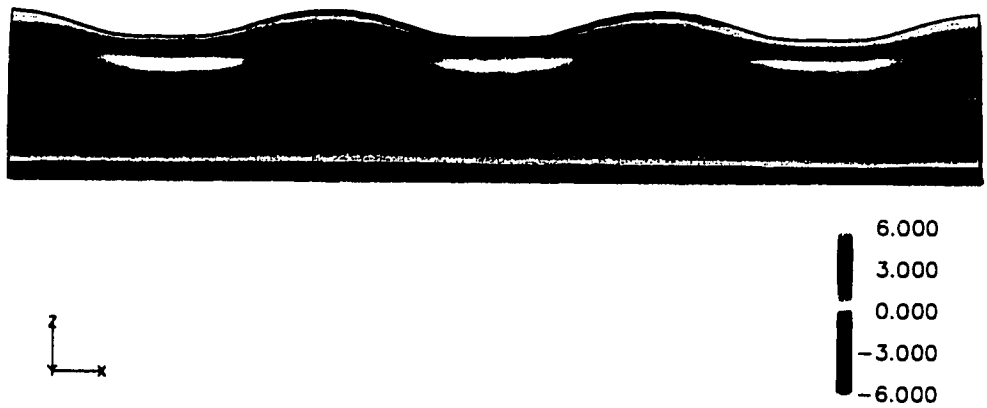

Figure 6.23: 3DwavyT1 case. Contours of $< \overline{\omega}_1 >_t$ (normalized by u^d_{*wavy}/h) in the streamwise-vertical plane at the center of the Langmuir circulation with positive streamwise vorticity.

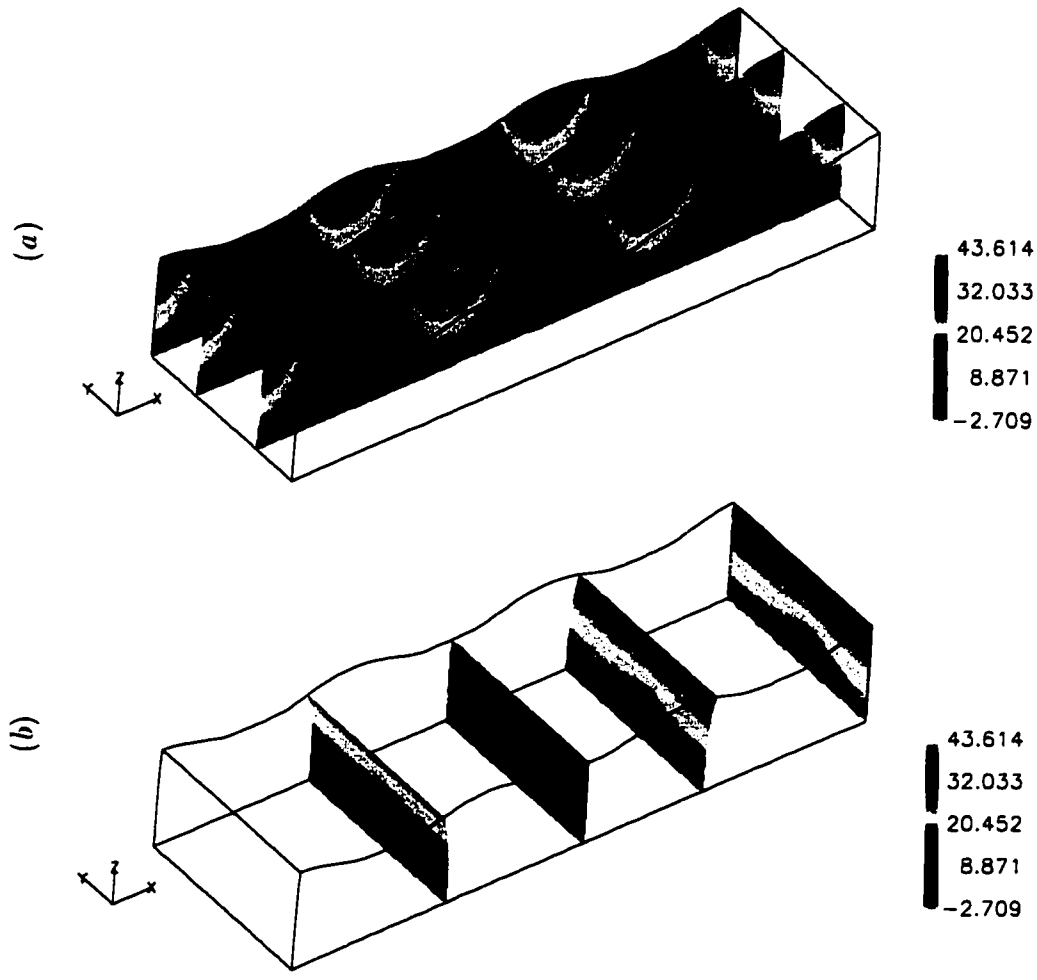

Figure 6.24: 3DwavyT1 case. $< \overline{u}_1 >_t$ contours (normalized by u^d_{*wavy}).

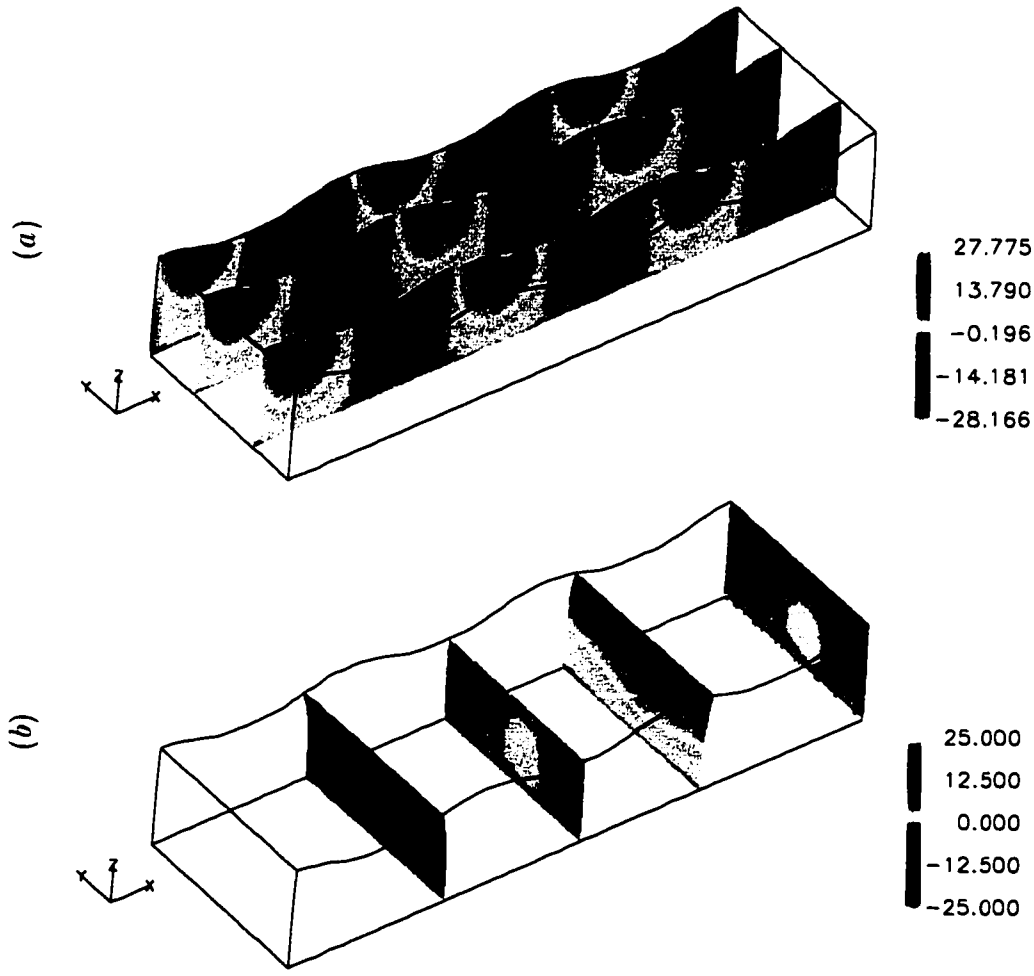

Figure 6.25: 3DwavyT1 case. $< \overline{u}_3 >_t$ contours (normalized by u^d_{*wavy}).

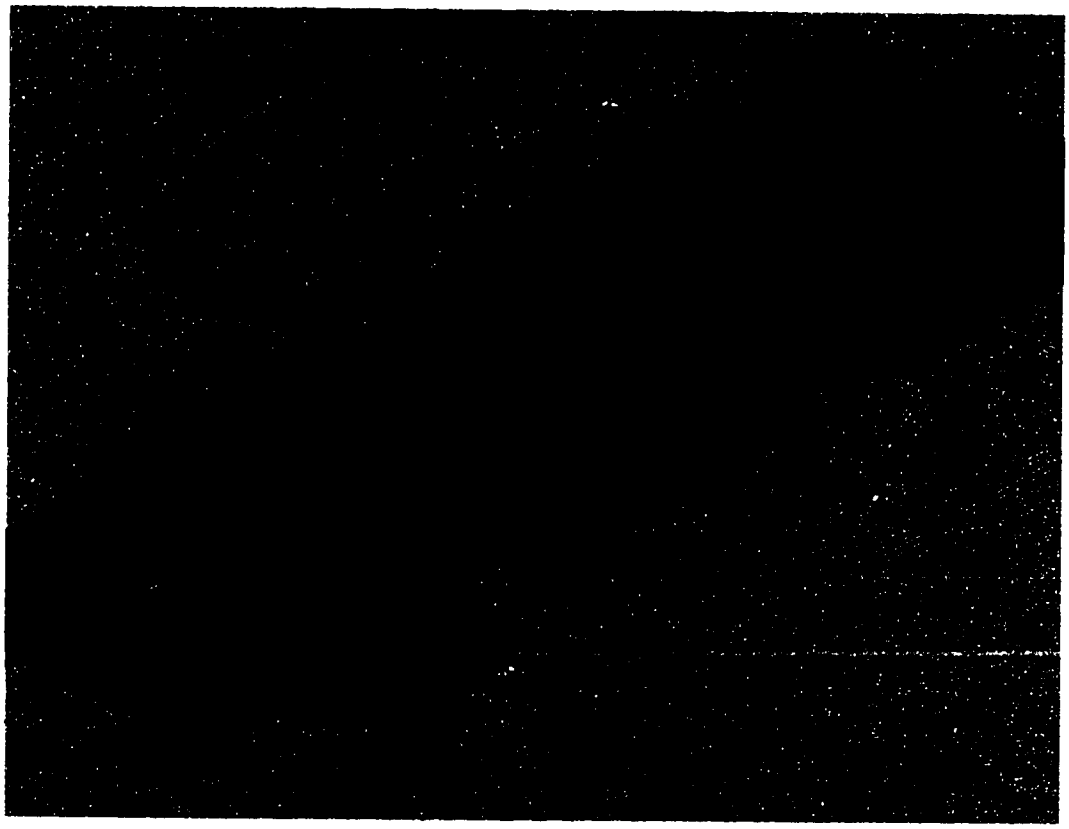

Figure 6.26: 3DwavyT1 case. Instantaneous iso-surfaces of $\overline{\omega}_1$ near the top surface at $0.7 < \eta_3 < 1.0$ (in the curvilinear system). The surface values are 6.5 (red) and -6.5 (blue) (normalized by u^d_{*wavy}/h).

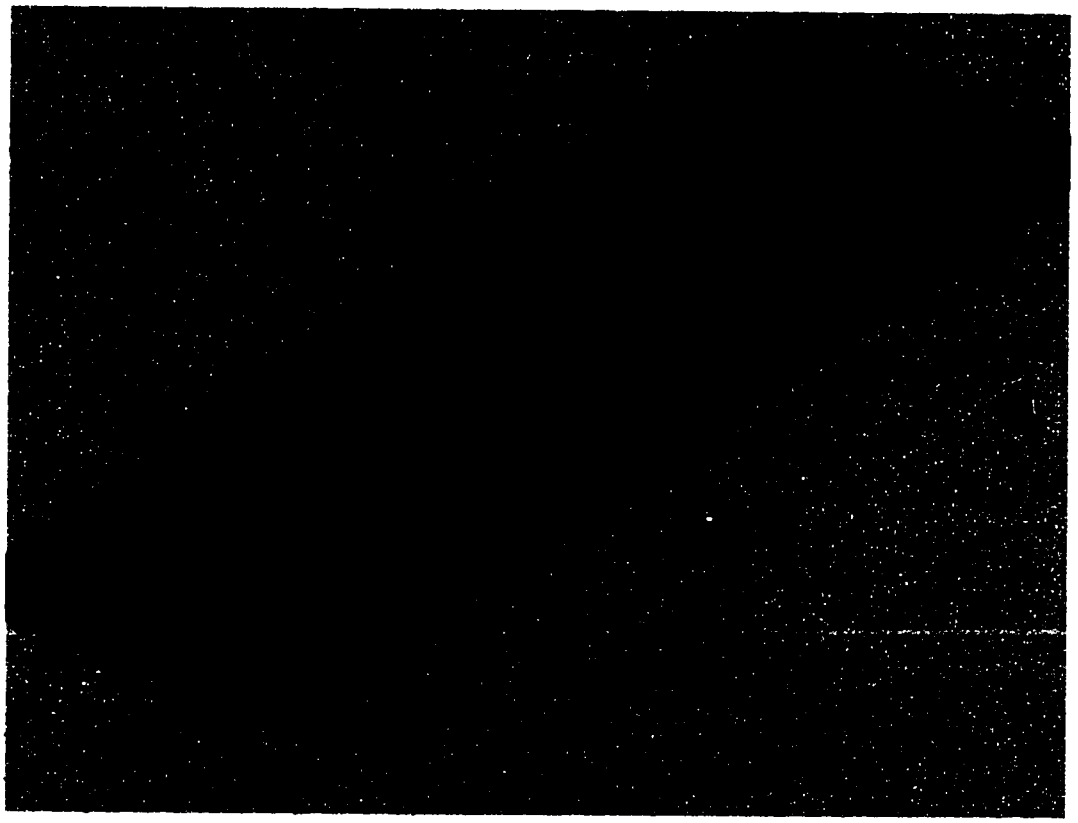

Figure 6.27: 3DCLT1E case. Instantaneous iso-surface of $\overline{\omega}_1$ near the top surface at $0.7 < x_3 < 1.0$. The surface values are 6.5 (red) and -6.5 (blue) (normalized by u^d_{*CL}/h).

Figure 6.28: 3DOChanT1E case. Instantanuous iso-surface of $\overline{\omega}_1$ near the top surface at $0.7 < x_3 < 1.0$. The surface values are 6.5 (red) and -6.5 (blue) (normalized by $u^d_{=OChan}/h$).

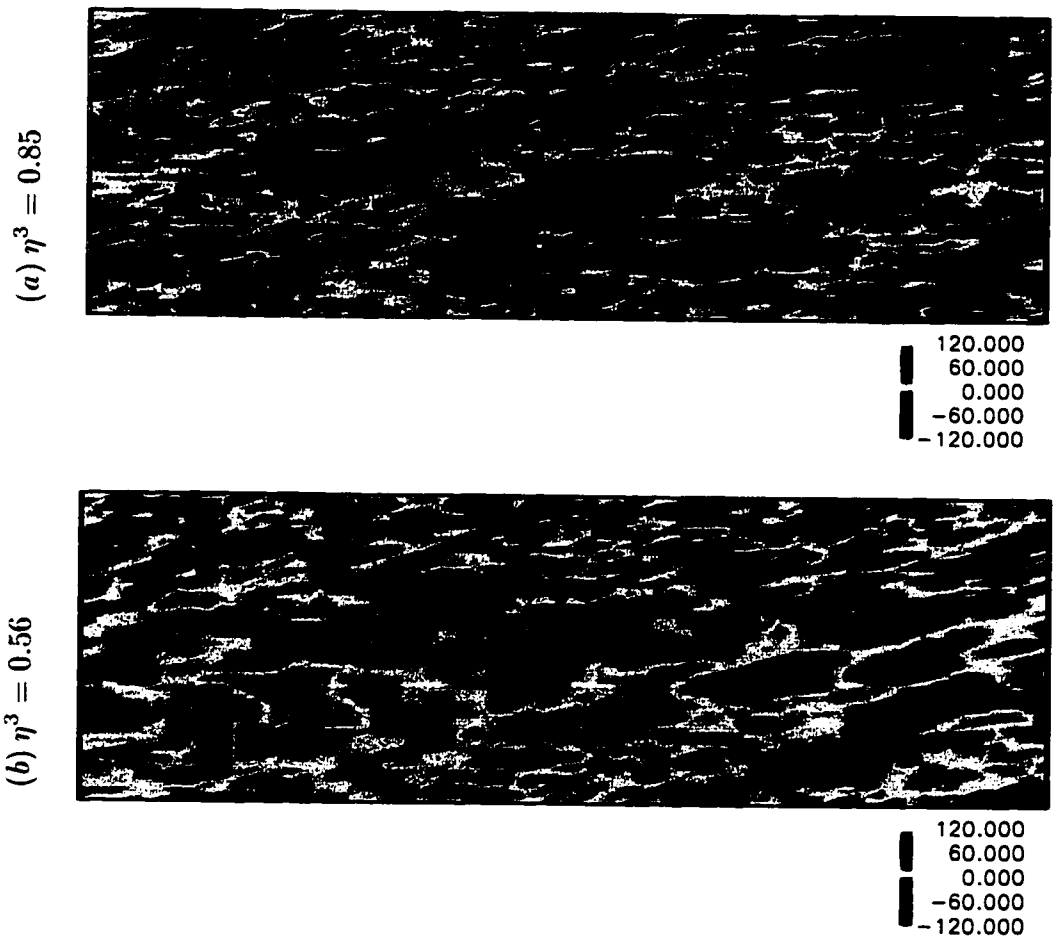

Figure 6.29: 3DwavyT1 case. Instantaneous contours of $\overline{\omega}_1$ (normalized by u^d_{*wavy}/h) at different depths. (part 1 of 2)

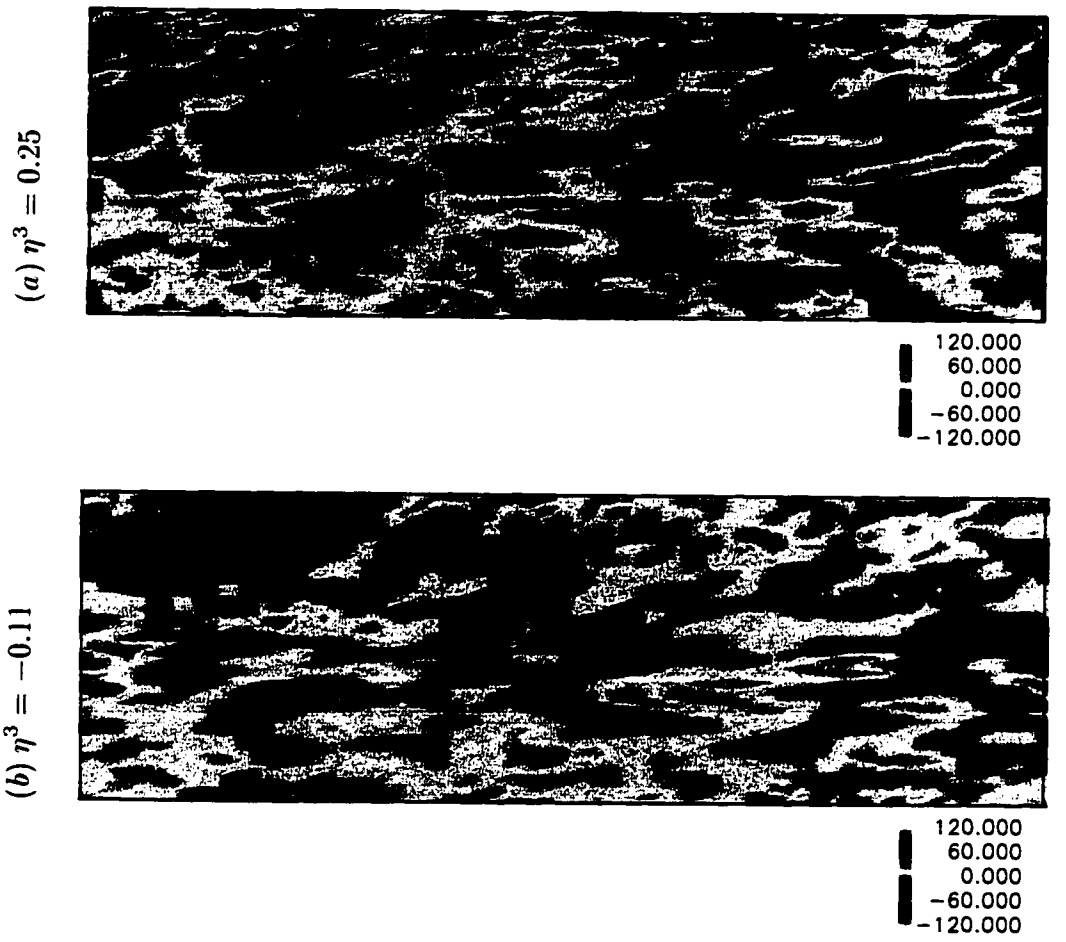

Figure 6.30: 3DwavyT1 case. Instantaneous contours of $\overline{\omega}_1$ (normalized by u^d_{*wavy}/h) at different depths. (part 2 of 2)

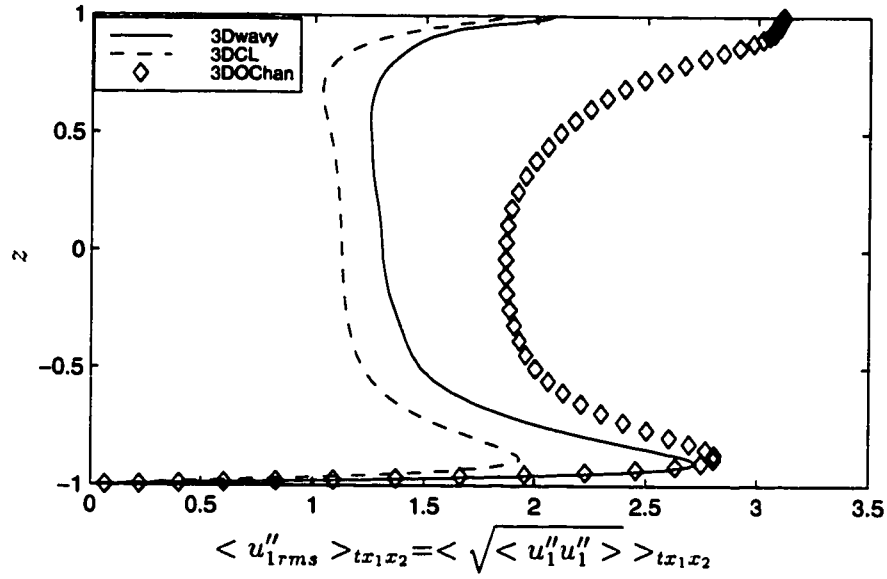

Figure 6.31: Comparison of 3DwavyT1, 3DCLT1E, and 3DOChanT1E cases. Profiles of $< u''_{1rms} >_{tx_1x_2}$. For the 3Dwavy case, the average is along the curvilinear coordinates. (Velocity normalizations: 3DwavyT1 by u^d_{*wavy}, 3DCLT1E by u^d_{*CL}, 3DOchan by u^d_{*OChan}; z is normalized by h)

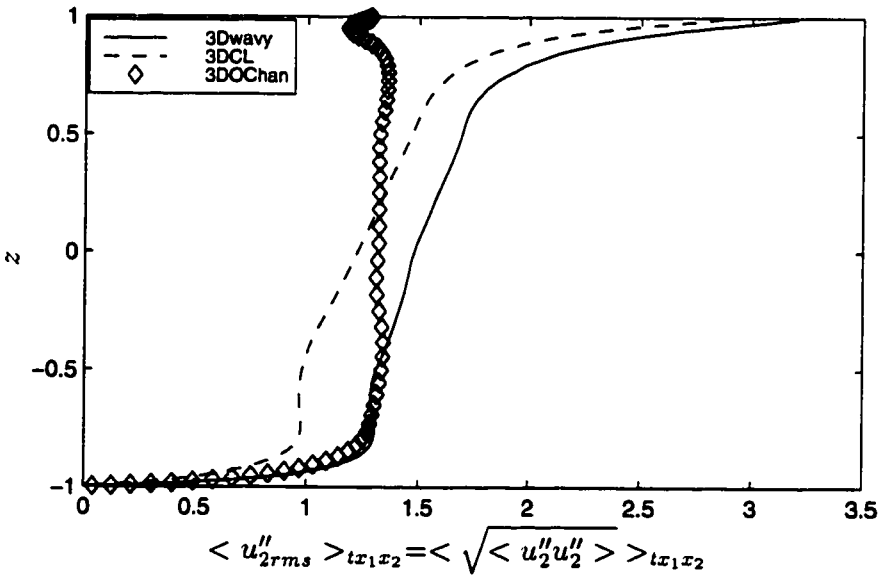

Figure 6.32: Comparison of 3DwavyT1, 3DCLT1E, and 3DOChanT1E cases. Profiles of $< u''_{2rms} >_{tx_1x_2}$. For the 3Dwavy case, the average is along the curvilinear coordinates. (Velocity normalizations: 3DwavyT1 by u^d_{*wavy}, 3DCLT1E by u^d_{*CL}, 3DOchan by u^d_{*OChan}; z is normalized by h)

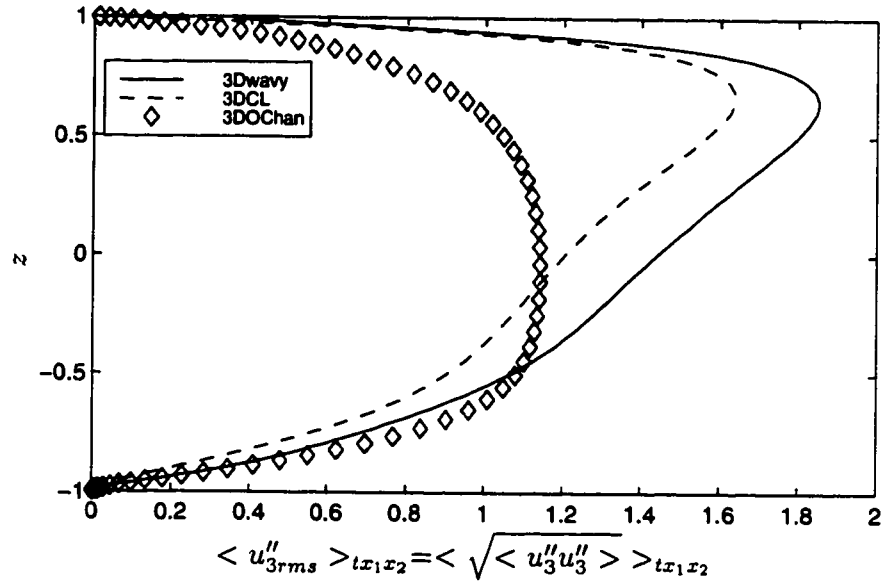

Figure 6.33: Comparison of 3DwavyT1, 3DCLT1E, and 3DOChanT1E cases. Profiles of $< u''_{3rms} >_{tx_1x_2}$. For the 3Dwavy case, the average is along the curvilinear coordinates. (Velocity normalizations: 3DwavyT1 by u^d_{*wavy}, 3DCLT1E by u^d_{*CL}, 3DOchan by u^d_{*OChan}; z is normalized by h)

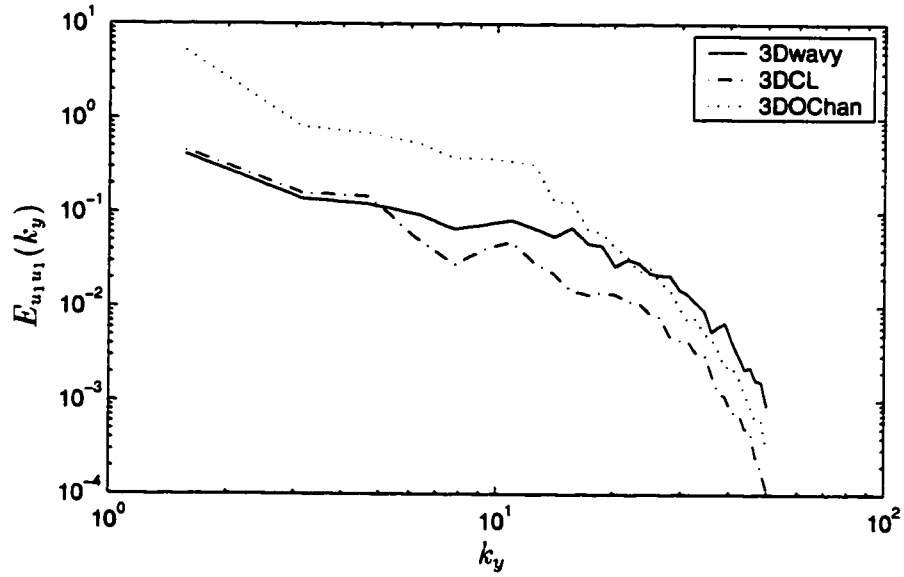

Figure 6.34: Comparison of 3DwavyT1, 3DCLT1E, and 3DOChanT1E cases. One dimensional energy spectra of streamwise velocity. The vertical location is $\eta^3 = 0.85 \simeq 1 - 1/4\kappa_x$. (normalizations: 3DwavyT1 by $u^{d2}_{*wavy}h^2$, 3DCLT1E by $u^{d2}_{*CL}h^2$, 3DOchan by $u^{d2}_{*OChan}h^2$; k_y is normalized by $1/h$)

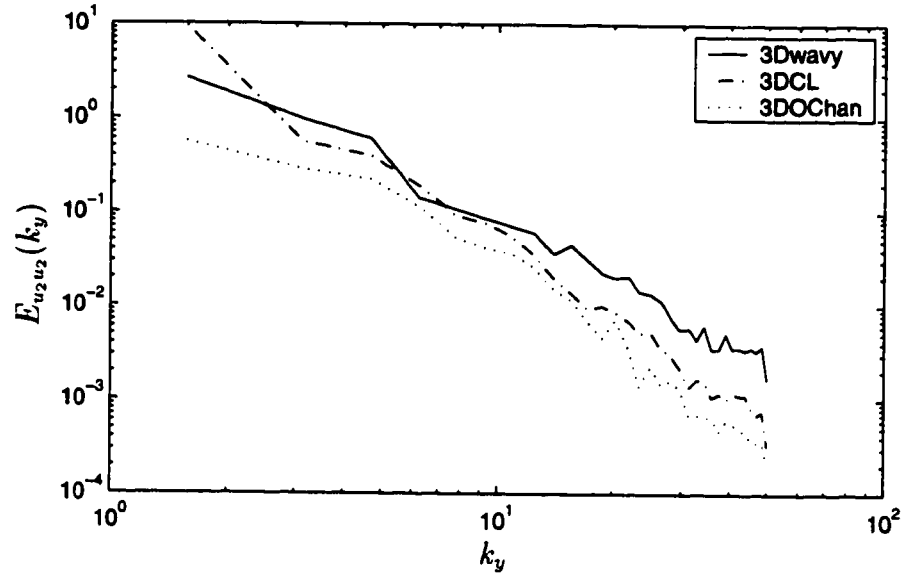

Figure 6.35: Comparison of 3DwavyT1, 3DCLT1E, and 3DOChanT1E cases. One dimensional energy spectra of spanwise velocity. The vertical location is $\eta^3 = 0.85 \simeq 1 - 1/4\kappa_x$. (normalizations: 3DwavyT1 by $u^{d2}_{*wavy}h^2$, 3DCLT1E by $u^{d2}_{*CL}h^2$, 3DOchan by $u^{d2}_{*OChan}h^2$; k_y is normalized by $1/h$)

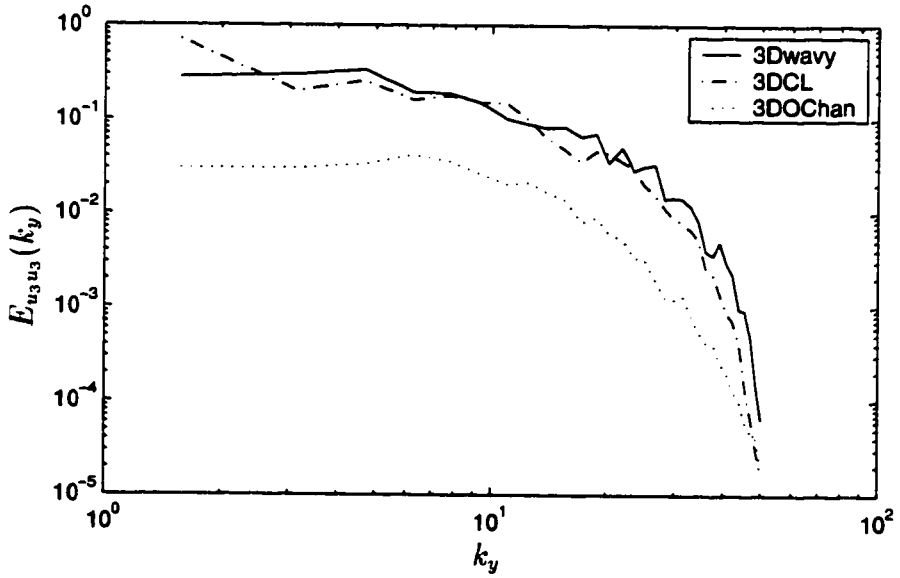

Figure 6.36: Comparison of 3DwavyT1, 3DCLT1E, and 3DOChanT1E cases. One dimensional energy spectra of vertical velocity. The vertical location is $\eta^3 = 0.85 \simeq 1 - 1/4\kappa_x$. (normalizations: 3DwavyT1 by $u^{d2}_{*wavy}h^2$, 3DCLT1E by $u^{d2}_{*CL}h^2$, 3DOchan by $u^{d2}_{*OChan}h^2$; k_y is normalized by $1/h$)

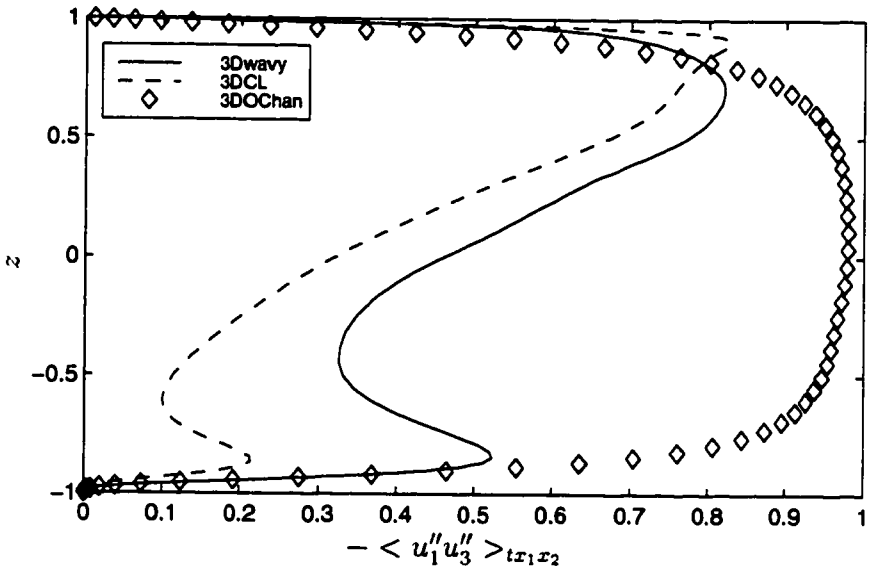

Figure 6.37: Comparison of 3DwavyT1, 3DCLT1E, and 3DOChanT1E cases. Reynolds stress $- < u_1'' u_3'' >_{tx_1x_2}$ profiles. For the 3Dwavy case, the average is along the curvilinear coordinates. (stress normalizations: 3DwavyT1 by u^{d2}_{*wavy}, 3DCLT1E by u^{d2}_{*CL}, 3DOchan by u^{d2}_{*OChan}; z is normalized by h)

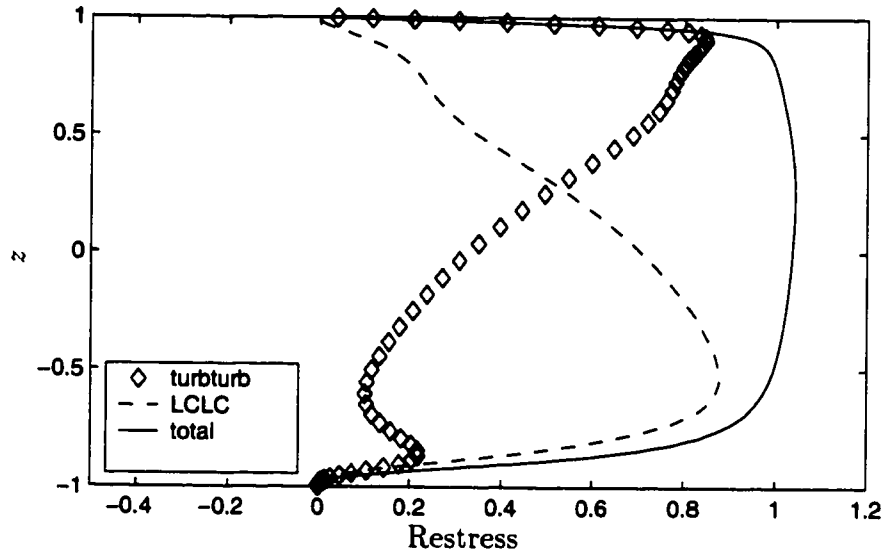

Figure 6.38: 3DCLT1E case. Decomposition of the total Reynolds stress $- < u_1 u_3 >_{tx_1x_2}$. (stress normalized by u^{d2}_{*CL}; z is normalized by h)

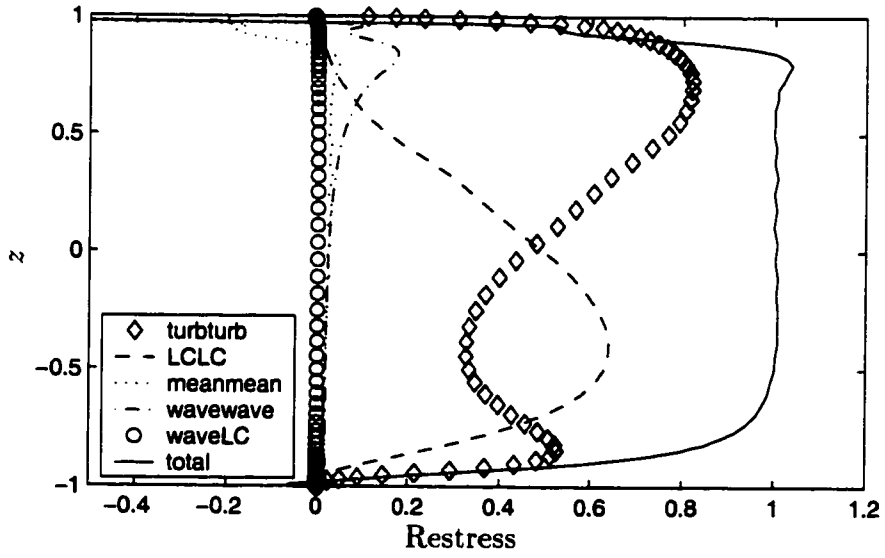

Figure 6.39: 3DwavyT1 case. Decomposition of the total Reynolds stress $- < u_1 u_3 >_{t\xi^1\xi^2}$. (stress normalized by u^{d2}_{*wavy}; z is normalized by h)

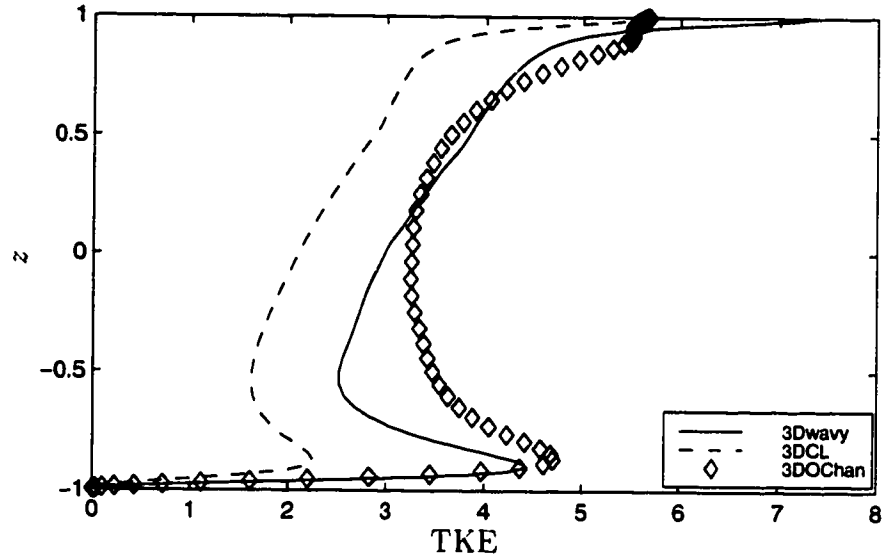

Figure 6.40: Comparison of 3DwavyT1, 3DCLT1E, and 3DOChanT1E cases. Turbulent kinetic energy $0.5 < u_i'' u_i'' >_{tx_1x_2}$ profiles. For 3Dwavy case, the average is along the curvilinear coordinates. (TKE normalizations: 3DwavyT1 by u^{d2}_{*wavy}, 3DCLT1E by u^{d2}_{*CL}, 3DOchan by u^{d2}_{*OChan}; z is normalized by h)

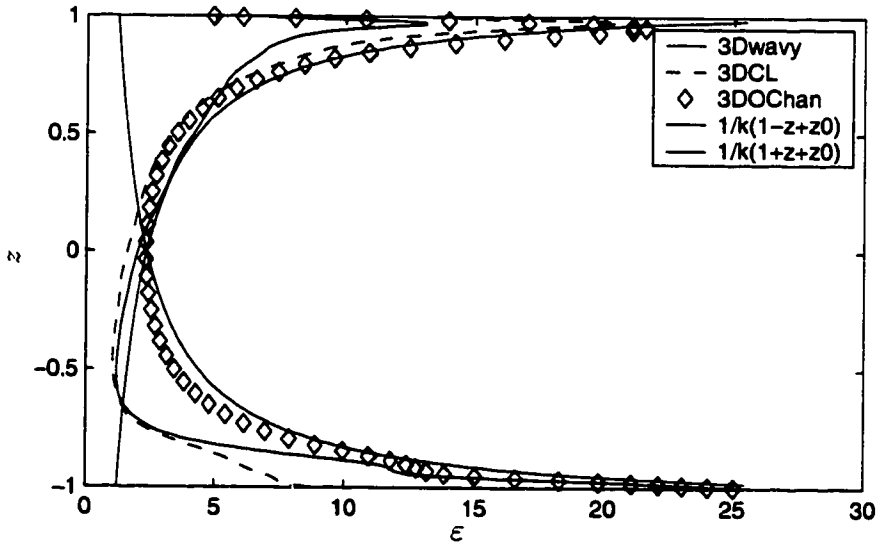

Figure 6.41: Comparison of 3DwavyT1, 3DCLT1E, and 3DOChanT1E cases. Profiles of viscous dissipation rate of turbulent kinetic energy. For 3Dwavy case, the average is along the curvilinear coordinates. (dissipation normalizations: 3DwavyT1 by u^{d3}_{*wavy}/h, 3DCLT1E by u^{d3}_{*CL}/h, 3DOchan by u^{d3}_{*OChan}/h; z is normalized by h)

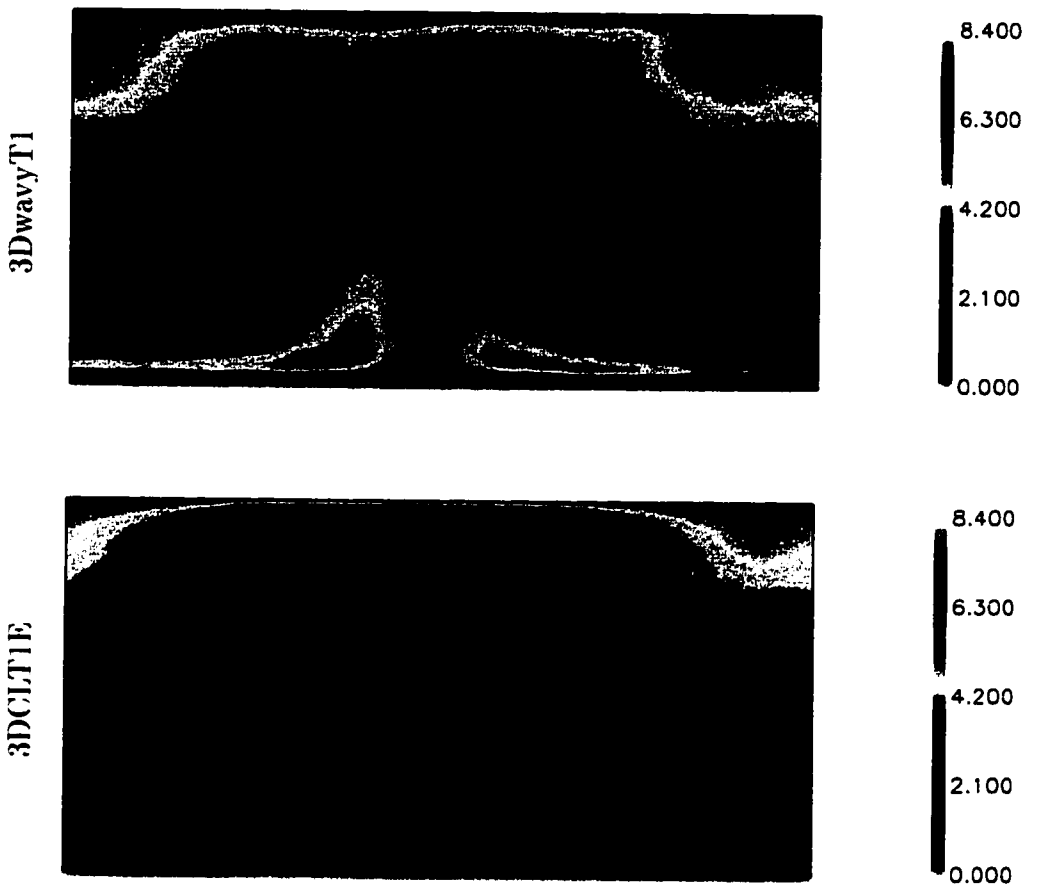

Figure 6.42: Comparison of 3DwavyT1 and 3DCLT1E cases. Turbulent kinetic energy contours. The planes are spanwise-vertical, with the mean current flow out of the paper. The contours of the 3DCLT1E case are phase-shifted in the spanwise direction. (3DwavyT1: normalized by u^{d2}_{*wavy}, 3DCLT1E: normalized by u^{d2}_{*CL})

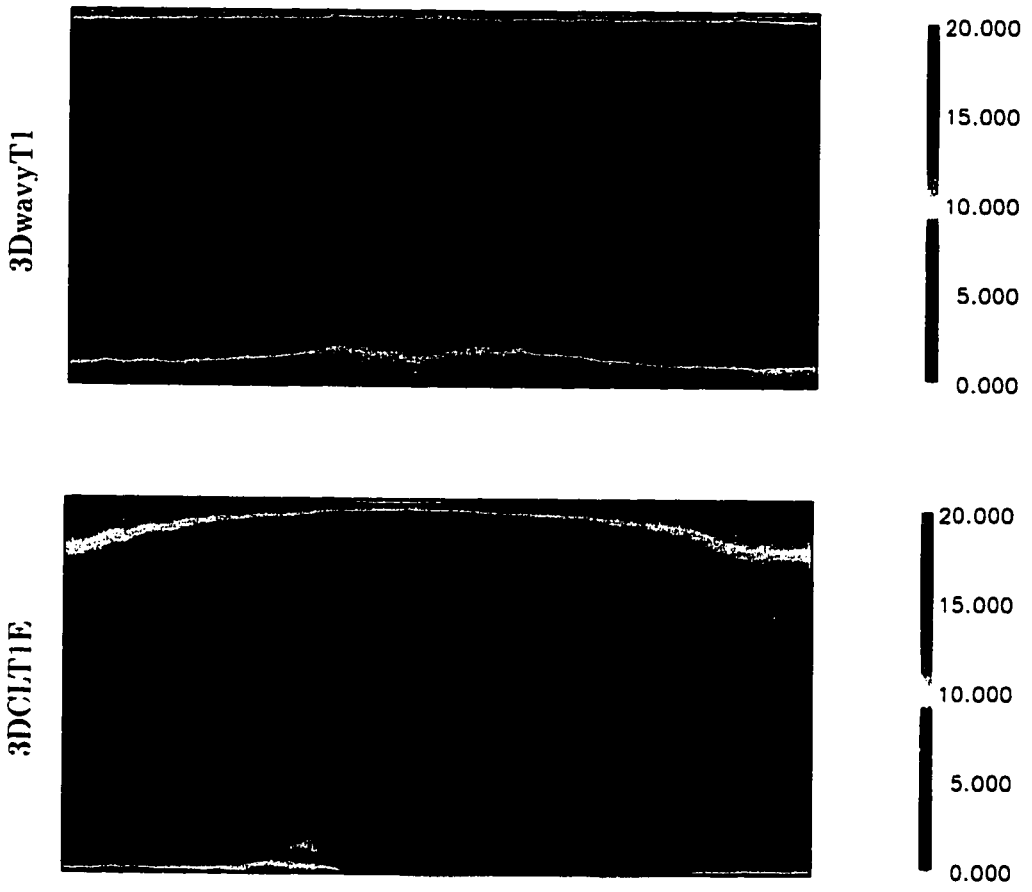

Figure 6.43: Comparison of 3DwavyT1 and 3DCLT1E cases. Viscous dissipation rate of turbulent kinetic energy. The planes are spanwise-vertical, with the mean current flow out of the paper. The contours of the 3DCLT1E case are phase-shifted in the spanwise direction. (3DwavyT1: normalized by u^{d3}_{*wavy}/h, 3DCLT1E: normalized by u^{d3}_{*CL}/h)

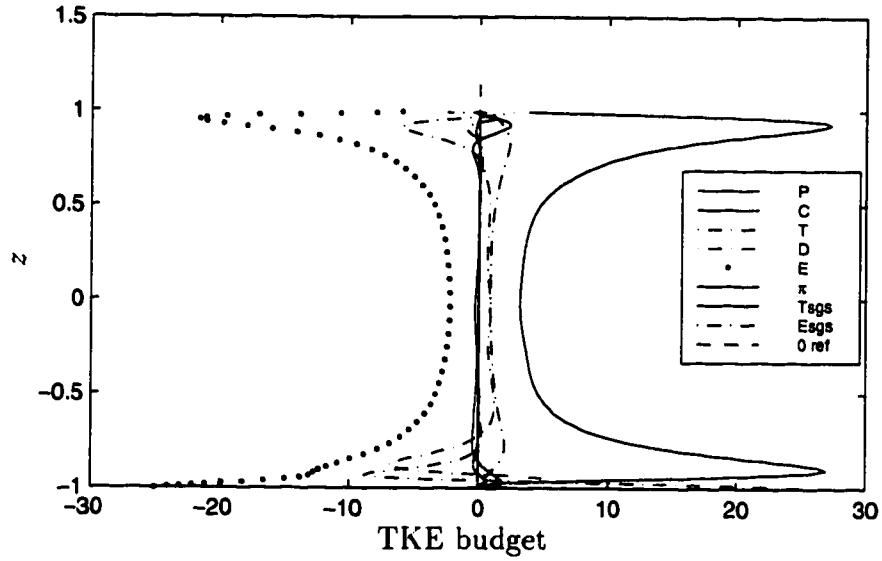

Figure 6.44: 3DOChanT1E case. Turbulent kinetic energy budget. (budget normalized by u^{d3}_{*OChan}/h; z is normalized by h)

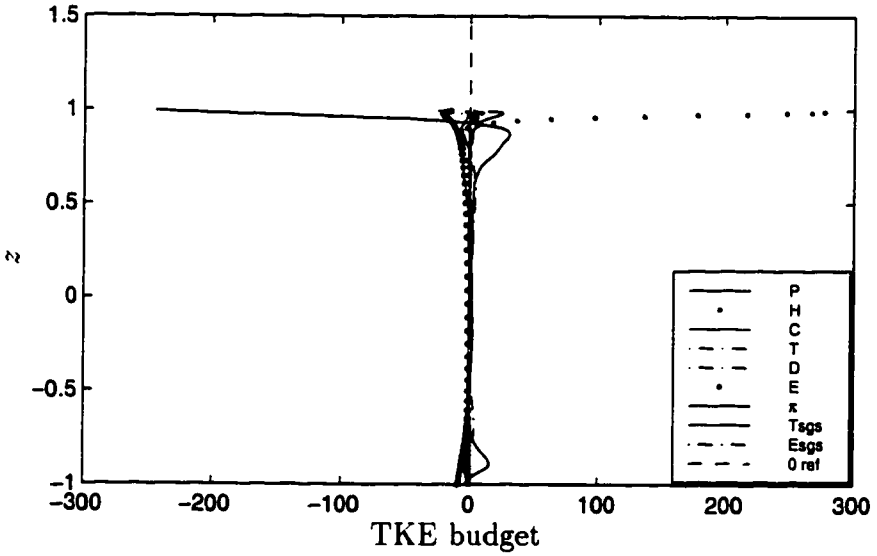

Figure 6.45: 3DCLT1E case. Turbulent kinetic energy budget. (budget normalized by u^{d3}_{*CL}/h; z is normalized by h)

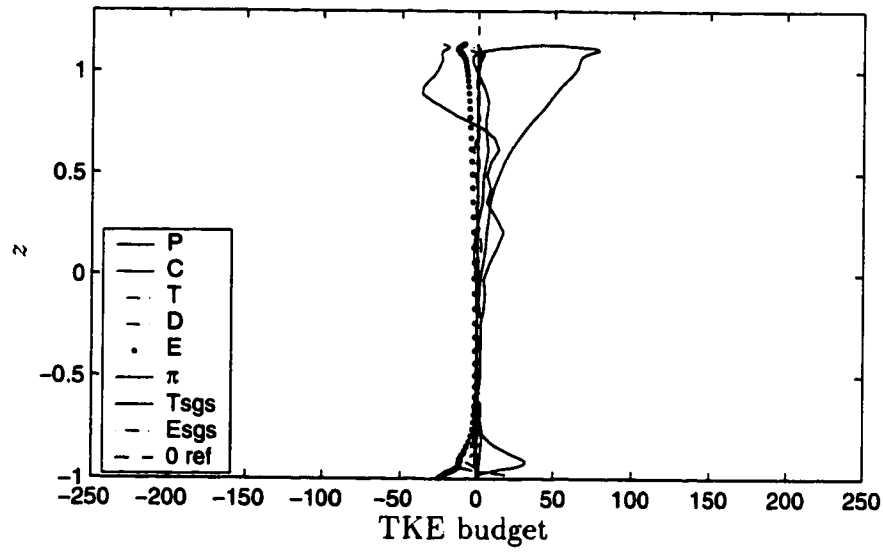

Figure 6.46: 3DwavyT1 case. Turbulent kinetic energy budget near wave crest. (budget normalized by u_{*wavy}^{d3}/h; z is normalized by h)

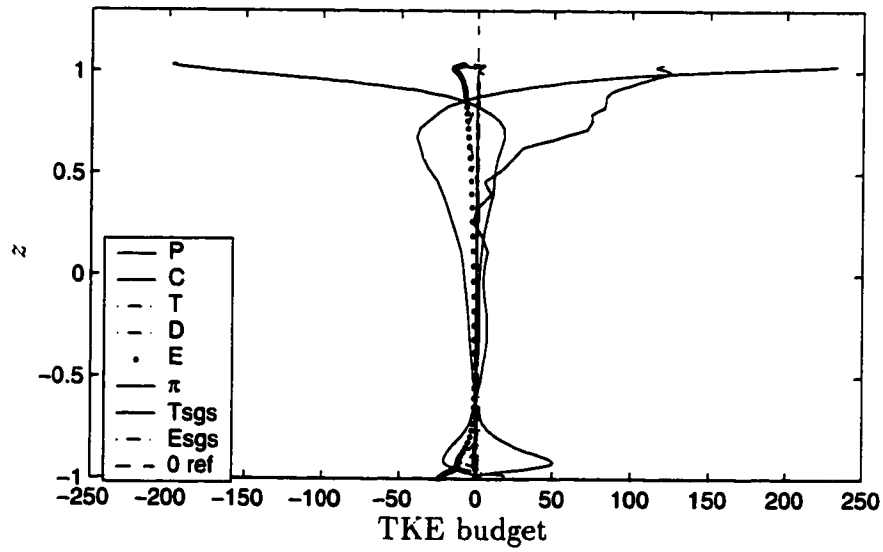

Figure 6.47: 3DwavyT1 case. Turbulent kinetic energy budget at the forward slope of the surface wave. (budget normalized by u_{*wavy}^{d3}/h; z is normalized by h)

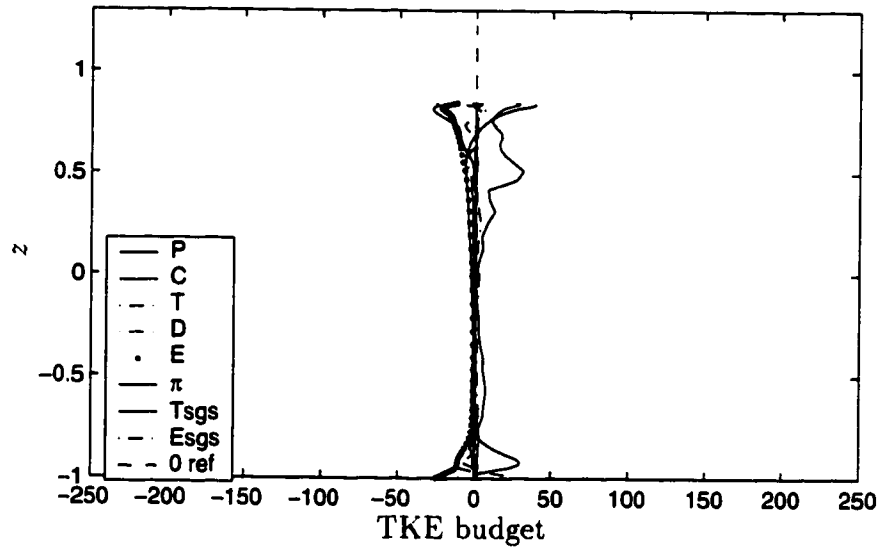

Figure 6.48: 3DwavyT1 case. Turbulent kinetic energy budget near wave trough. (budget normalized by u^{d3}_{*wavy}/h; z is normalized by h)

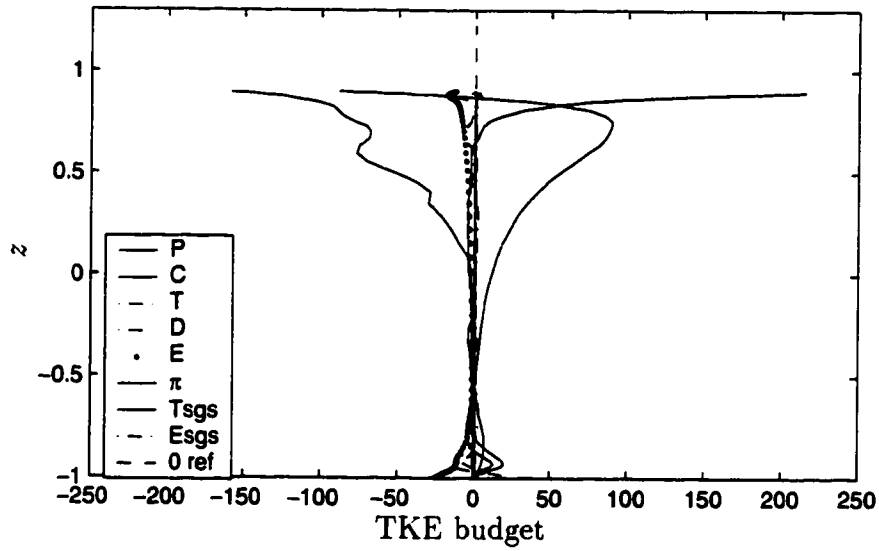

Figure 6.49: 3DwavyT1 case. Turbulent kinetic energy budget at the backward slope of the surface wave. (budget normalized by u^{d3}_{*wavy}/h; z is normalized by h)

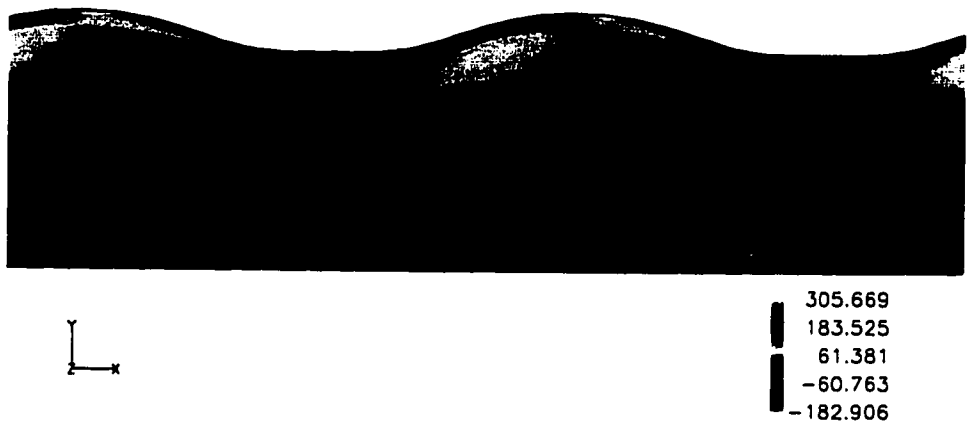

Figure 6.50: 3DwavyT1 case. Spanwise averaged turbulent kinetic energy production rate ($< P >_{t\xi^2}$) contours. (normalized by u^{d3}_{*wavy}/h)

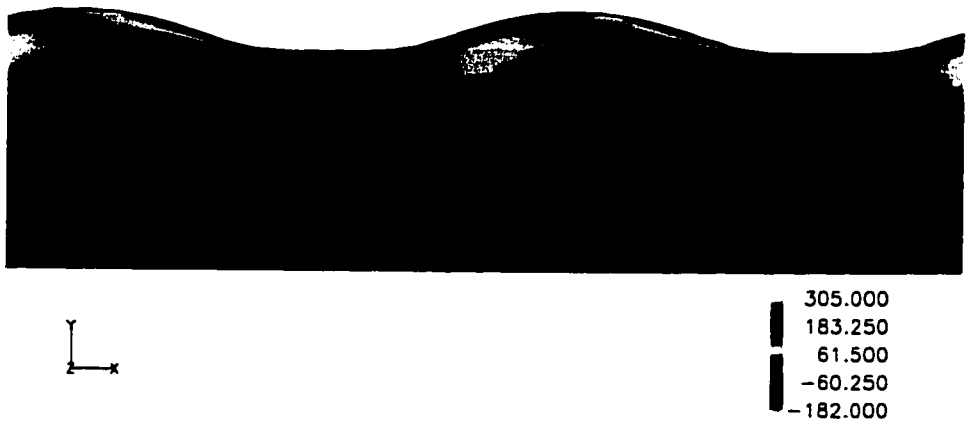

Figure 6.51: 3DwavyT1 case. Contours of $-[< u_1''u_1'' >_{t\xi^2} \frac{\partial <\overline{u}_1>_{t\xi^2}}{\partial x_1} + < u_3''u_3'' >_{t\xi^2} \frac{\partial <\overline{u}_3>_{t\xi^2}}{\partial x_3} + < u_1''u_3'' >_{t\xi^2} (\frac{\partial <\overline{u}_1>_{t\xi^2}}{\partial x_3} + \frac{\partial <\overline{u}_3>_{t\xi^2}}{\partial x_1})]$. (normalized by u^{d3}_{*wavy}/h)

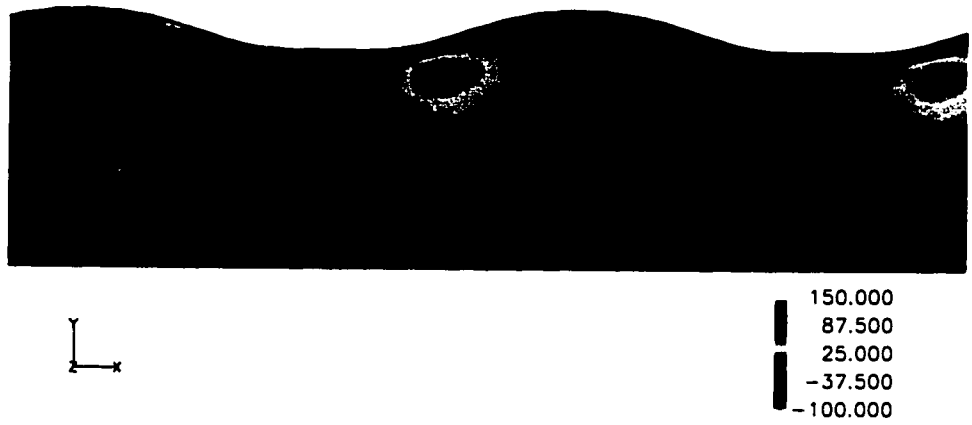

Figure 6.52: 3DwavyT1 case. Contours of $-(< u_1'' u_1'' >_{t\xi^2} \frac{\partial < \overline{u}_1 >_{t\xi^2}}{\partial x_1} + < u_3'' u_3'' >_{t\xi^2} \frac{\partial < \overline{u}_3 >_{t\xi^2}}{\partial x_3})$. (normalized by u^{d3}_{*wavy}/h)

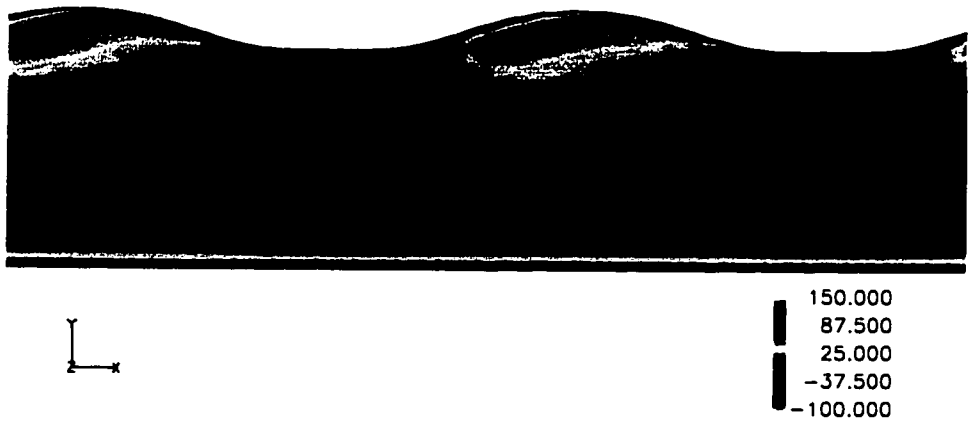

Figure 6.53: 3DwavyT1 case. Contours of $- < u_1'' u_3'' >_{t\xi^2} (\frac{\partial < \overline{u}_1 >_{t\xi^2}}{\partial x_3} + \frac{\partial < \overline{u}_3 >_{t\xi^2}}{\partial x_1})$. (normalized by u^{d3}_{*wavy}/h)

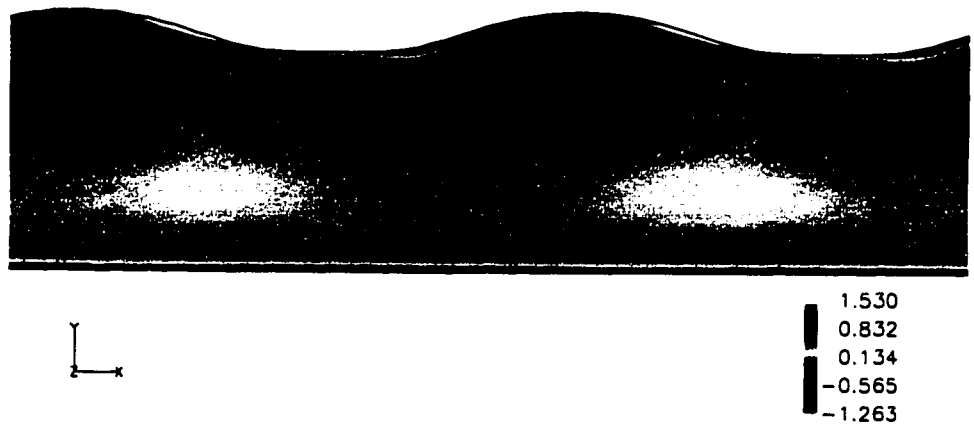

Figure 6.54: 3DwavyT1 case. Spanwise averaged Reynolds stress ($- < u_1'' u_3'' >_{t\xi^2}$) contours. (normalized by $u^{d3}_{\infty wavy}/h$)

Figure 6.55: 3DwavyT1 case. Spanwise averaged mean convection rate (C). (normalized by u^{d3}_{*wavy}/h)

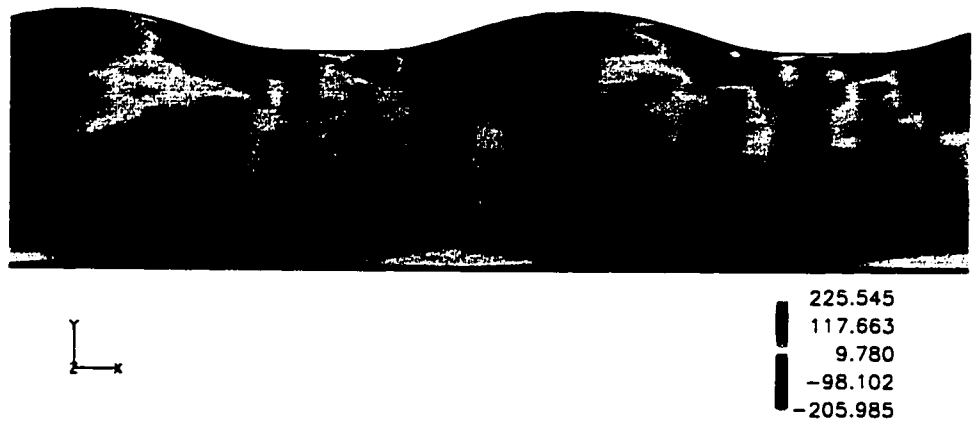

Figure 6.56: 3DwavyT1 case. Contours of $-(< \overline{u}_1 >_{t\xi^2} \frac{\partial 1/2 < u_i'' u_i'' >_{t\xi^2}}{\partial x_1} + < \overline{u}_3 >_{t\xi^2} \frac{\partial 1/2 < u_i'' u_i'' >_{t\xi^2}}{\partial x_3})$. (normalized by u^{d3}_{*wavy}/h)

Figure 6.57: 3DwavyT1 case. Contours of $- < \overline{u}_1 >_{t\xi^2} \frac{\partial 1/2 < u_i'' u_i'' >_{t\xi^2}}{\partial x_1}$. (normalized by u^{d3}_{*wavy}/h)

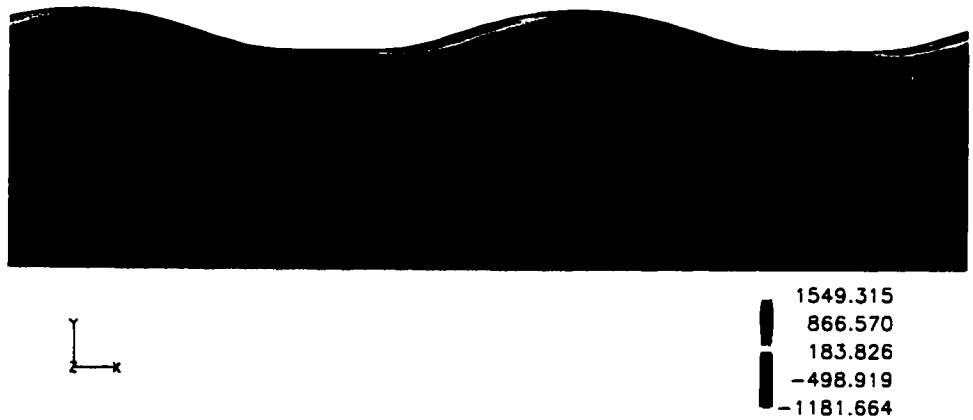

Figure 6.58: 3DwavyT1 case. Contours of $- < \overline{u}_3 >_{t\xi^2} \frac{\partial 1/2 < u_i'' u_i'' >_{t\xi^2}}{\partial x_3}$. (normalized by u^{d3}_{*wavy}/h)

Chapter 7

Conclusions and Recommendations for Future Work

7.1 Conclusions

Langmuir circulations in a wavy domain have been simulated for the first time by directly solving the Navier-Stokes equations in a curvilinear coordinate system. The computations were carried out for both laminar and turbulent flows in an open channel with a second order Stokes wave propagating at the surface. A constant tangential stress imposed at the top drives a mean current that interacts with the surface wave to generate Langmuir circulations. With heat transfer, stratification, and Coriolis force excluded, the simulations serve as a first step to understanding the mechanism and dynamics of Langmuir circulations and to predicting their effects on mixing.

In our model, the kinematic and dynamic boundary conditions are applied on the wavy surface. As a first approximation, we assume that the shape of the surface wave remains unchanged. An orthogonal transformation is used to map the wavy physical domain into a rectangular computational domain. The fixed shape of the wave and the orthogonality of the transformation greatly reduced the computational cost. The numerical method is a modified version of the fractional step method of Zang *et al.* (1994) for solving the Navier-Stokes equations in a generalized curvilinear coordinate system. In the turbulent cases, dynamic subgrid scale model of Germano *et al.* (1991) is used. The computer code is written in a modularized fashion and is fully vectorized. It is also optimized by using a improved multigrid method for the pressure Poisson equation on a vertically stretched grid. The correctness of the computer code is verified by the results for the benchmark cases.

The Langmuir circulations produced by the simulations agree with the experimental observations. The initial perturbations grow exponentially in time. Higher modes

with short wavelengths develop first. They later combine and there are large counter rotating Langmuir cells in the final equilibrium state. As observed in the field, the Langmuir cells are asymmetric, separated by an upwelling zone and a downwelling zone, the downwind velocity being greater at the convergence zone than at the divergence zone (current anomaly), and the maximum downwelling velocity being located just above the mid-depth of the channel. They coexist with the wave field and are modulated by the surface wave. The predicted pitch, defined as the ratio of the maximum downwind jet velocity to the maximum downwelling velocity, and the relation between the maximum downwelling velocity and the wind speed agrees well with field observations.

In turbulent flow, the Langmuir circulations are embedded in a much stronger, chaotic instantaneous field; nonetheless, they can be identified by time averaging. The turbulence is stronger near the top, giving rise to a weaker current anomaly in this region than near the bottom wall. Relative to the non-wavy stress-driven open channel flow, the mean flow is greatly modified. Close to the bottom wall, the logarithmic region is destroyed by the penetration of Langmuir cells. Near the top surface. Langmuir cells destroy most of the logarithmic profile found in turbulent Couette flow, leading to a more uniform mean current.

By studying instantaneous snapshots of the longitudinal vorticity field, a rich structure is observed that contains shorter, randomly distributed, streamwise oriented streaks and more irregular small scale motions. This is supported by the multiple scales observed in the field (Weller and Price 1988, Thorpe 1992).

Compared with turbulent Couette flow, the streamwise turbulent fluctuations are weaker but the spanwise and vertical perturbations are stronger in the prsence of waves. Unlike open channel flow turbulence, in which streamwise momentum is transported vertically mainly by turbulent motions, in Langmuir turbulence, the mixing due to the turbulence and the mean Langmuir circulations are of approximately equal importance. The momemtum transport by the Langmuir circulations is the dominant contribution in the lower half of the channel. This confirms the importance of the role of Langmuir circulations in mixing. The turbulent kinetic energy budget shows that in the top surface layer, the production rate is enhanced in Langmuir turbulence.

The pressure transport term is also significant in this region; this is not the case for turbulent Couette flow.

The numerical results for the wavy flow were also used to study the Craik-Leibovich (CL) theory in a rectangular domain. A two dimensional free surface flow under a second order Stokes wave was examined first. From the analytical solutions for the inviscid flow and numerical solutions for the viscous flow, we found two components intrinsic to the wave field that drive the Langmuir circulations: the Stokes drift caused by the irrotational wave motion, and the Eulerian mean flow induced by the top wavy boundary layer.

Comparison of the wavy flow with the simulations results based on CL theory suggests that, in addition to the Stokes drift included in the CL theory, the Eulerian mean flow induced by the surface wavy boundary layer is important. Including its effects in the simulation based on the CL theory is essential to predicting the correct quantitative properties of Langmuir circulations, especially the pitch. For laminar flows, when the wave-induced stress is included, excellent agreement is achieved between the computed streamwise-averaged wavy flow and that predicted by the CL theory. It should also be noticed that the relative importance of the Eulerian mean flow induced stress versus the wind stress is sensitive to the eddy viscosity near the surface, which needs to be futher investigated experimentally. The simulation based on the Craik-Leibovich theory also shows that the cell merging process largely resembles the inverse energy cascade in two dimensional turbulence.

In Langmuir turbulence, although the Langmuir circulation structure obtained from CL theory is similar to what is found in turbulent wavy flow, significant quantitative differences are observed. The Langmuir circulations in the wavy field is only about 2/3 as strong as those predicted by CL theory. However, the flow in the wavy domain has greater turbulent intensities. A possible reason is that CL theory fails to account for the wave-current interaction between the turbulent eddies with time scale comparable to the wave period.

7.2 Recommendations for Future Work

All the calculations in this work only consider the momentum transport. Therefore, an immediate extension of our model should be the incorporation of thermal convection and stratification effects caused by diurnal surface heating and salinity nonuniformity, respectively. Additional differential equations must be included to account for scalar transport, and a buoyancy term needs to be added to the momentum equations. In addition, the turbulence model needs to be extended to close the scalar transport equation.

Surface heating effects can be studied by simulating a wavy flow with a constant surface heat flux. Additional nondimensional parameters introduced by including heating are the Prandtl number and the ratio between the vortex forcing and the convective forcing due to the surface heat flux. Our model can also be extended by imposing stabilizing stratification in the initial flow field. The deterioration of the stratification by the Langmuir circulation can shed new light on the process of mixed layer deepening and the themocline erosion, as suggested by Langmuir (1938) and Smith *et al.* (1987).

The length scales of Langmuir cells in ocean are up to hundreds of meters. Under these circumstances, the Coriolis force becomes important. Ekman layer spiral patterns have been reported by Assaf *et al.* (1971), Thorpe (1992), and Farmer and Li (1995). In order to account for these motions, Coriolis force must be included in the model.

It has been suggested that in addition to wind stress, wave breaking can generate enough shear near the top of a free surface wave to produce Langmuir circulations (Skyllingstad and Denbo 1995). To verify this conjecture, the wave breaking effects need to be included in our model. As suggested by Monismith and Magnaudet (1998), these effects can be modeled through a semi-random energy and vorticity input at the top surface.

One limitation of this work is that the flow is bounded at the bottom by a solid wall, whereas in most field observation it is by a thermocline. To accommodate for this condition, techniques used by Skyllingstad and Denbo (1995) and McWilliams

et al. (1997) can be adapted. The bottom boundary is set well below the thermocline, which is a strongly stratified layer beneath the mixed layer. An internal wave radiation boundary condition (Klemp and Duran 1983) should be applied at the bottom boundary to absorb momentum flux. This simulation should enable us to better understand mixing in the upper ocean.

The cost of our computation is significant. Since the development of Langmuir circulations is slow compared with the wave motion, the code needs to run thousands of wave periods to reach an equilibrium state. Although good performance has been achieved on the Cray J90, a typical case consumes as much as 30 days on a single processor. The rapid development of parallel supercomputers provides an exciting way to improve the code efficiency. Thus, parallelization of this serial code is one of the major steps to be taken before sophisticated simulations can be carried out. Converting the computer algorithm using the standard MPI library is a good place to start, since the portability of the MPI library will enable the code to run on multiple platforms.

In our simulation, we assumed that the surface wave shape does not change. In future work, this restriction can be relaxed by using a more realistic wave surface at the top, with its shape defined by an extra unknown variable that is derived from a evolution equation. The numerical method of Hodges (1997) for unsteady turbulent free-surface flows can be adapted. However, the increase in cost will be substantial. Since the surface wave shape changes with time, we could no longer be able to take advantage of the orthogonal transformation for the second order Stokes wave used here. Instead, a non-orthogonal curvilinear system must be used. The off-diagonal metric terms will be nonzero, leading to more complicated transformed equations and larger storage requirements. The surface wave should be advanced at each time step and a new computational grid should be generated. Therefore, more CPU time is needed per time step. Furthermore, the grid advancement algorithm imposes more restrictions on the size of the time step. Therefore, the computer code efficiency needs to be improved considerably before this task is undertaken.

Bibliography

Andrews, D. G., and M. E. McIntyre. 1978. An Exact Theory of Nonlinear Waves on a Lagrangian-mean Flow. *Journal of Fluid Mechanics* 89:609–646.

Aris, R. 1989. *Vectors, Tensors, and the Basic Equations of Fluid Mechanics.* New York: Dover.

Assaf, G., R. Gerard, and A. L. Gordon. 1971. Some Mechanisms of Oceanic Mixing Revealed in Aerial Photographs. *Journal of Geophysical Research* 76:6550–6572.

Barlow, R., and J. Johnston. 1988. Structure of a Turbulent Boundary Layer on a Concave Surface. *Journal of Fluid Mechanics* 191:137–176.

Cabot, W. 1991. Large Eddy Simulation of Passive and Buoyant Scalars with Dynamic Subgrid-Scale Models. Annual reseach briefs, Center for Turbulence Research, Stanford University/NASA-Ames, Stanford, California.

Cheung, T. K. 1985. *A Study of the Turbulent Layer in the Water at an Air-Water Interface.* PhD thesis, Department of Civil Engineering, Stanford University, Stanford California, January.

Comte-Bellot, G. 1963. *Contribution a l'étude de la turbulence de conduite.* PhD thesis, University of Grenoble.

Cox, S. M., S. Leibovich, I. M. Moroz, and A. Tandon. 1992a. Hopf Bifurcations in Langmuir Circulations. *Physica D* (59):226–254.

Cox, S. M., S. Leibovich, I. M. Moroz, and A. Tandon. 1992b. Nonlinear Dynamics in Langmuir Circulations with O(2) Symmetry. *Journal of Fluid Mechanics* 241:669–704.

Craig, P. D. 1996. Velocity Profiles and Surface Roughness Under Breaking Waves. *Journal of Geophysical Research* 101:1265–1278.

Craig, P. D., and M. L. Banner. 1994. Modeling Wave-enhanced Turbulence in the Ocean Surface Layer. *Journal of Physics Oceanography* 24:2546–2559.

Craik, A. 1977. The Generation of Langmuir Circulations by an Instability Mechanism. *Journal of Fluid Mechanics* 81:209–223.

Craik, A. D. D. 1970. a Wave-interaction Model for the Generation of Windrows. *Journal of Fluid Mechanics* 41:801–821.

Craik, A. D. D. 1982. The Drift Velocity of Water Waves. *Journal of Fluid Mechanics* 116:187–205.

Craik, A. D. D. 1985. *Wave Interactions and Fluid Flows.* Cambridge, England: Cambridge Unversity Press.

Craik, A. D. D., and S. Leibovich. 1976. A Rational Model for Langmuir Circulations. *Journal of Fluid Mechanics* 73:401–426.

Crawford, G., and D. Farmer. 1987. On the Spatial Distributions of Ocean Bubbles. *Journal of Geophysical Research* 92:8231–8243.

Csanady, G. T. 1965. Windrow Studies. Report PR26, Great Lakes Institution, University of Toronto.

Deardorff, J. W. 1970. A Numerical Study of Three-dimensional Turbulent Channel Flow at Large Reynolds Numbers. *Journal of Fluid Mechanics* 41:453–480.

Evans, G., and F. Taylor. 1980. Phytoplankton Accumulation in Langmuir cells. *Limn. Ocean.* 92:840–845.

Faller, A. 1978. Experiments with Controlled Langmuir Circulations. *Science* 201:618–620.

Faller, A., and Caponi. 1978. Laboratory Studies of Wind Driven Langmuir Circulations. *Journal of Geophysical Research* 83:3517–3633.

Faller, A., and Cartwright. 1983. Laboratory Studies of Langmuir Circulations. *Journal of Physics Oceanography* 13:329–340.

Faller, A. J. 1964. The Angle of Windrows in the Ocean. *Tellus* 16:363–370.

Faller, A. J. 1969. The Generation of Langmuir Circulations by the Eddy Pressure of Surface waves. *Limn. Ocean.* 14:504–513.

Faller, A. J. 1971. Oceanic Turbulence and the Langmuir Circulations. *Ann. Rev. Ecol. Syst.* 2:201–236.

Faller, A. J., and S. J. Auer. 1988. The Roles of Langmuir Circulations in the Dispersion of Surface Tracers. *Journal of Physics Oceanography* 18:1108–1123.

Faller, A. J., and C. Perini. 1984. The Roles of Langmuir Circulations in Gas Transfer across Natural Water Surfaces. In W. Brutsaert and G. H. Jirka (Eds.), *Gas Transfer at Water Surface*, 191–198. D. Reidel Publishing Co.

Farmer, D. M., and M. Li. 1995. Patterns of Bubble Clouds Organized by Langmuir Circulations. *Journal of Physics Oceanography* 26:1426–1440.

Ferziger, J. H. 1998. Direct and Large Eddy Simulation of Turbulence. In *CRM Proceedings and Lecture Notes*, Vol. 16, 53–97, Centre de Recherches Mathematiques.

Ferziger, J. H., and M. Perić. 1997. *Computational Methods for Fluid Dynamics.* Springer. Second edition.

Filatov, N. N., S. V. Rjanzhin, and L. V. Zaycev. 1981. Investigation of Turbulence and Langmuir Circulation in Lake Ladoga. *J. Great Lakes Res.* 7:1–6.

Gammelsrod, T. 1975. Instability of Couette flow in a Rotating Fluid and Origin of Langmuir Circulations. *Journal of Geophysical Research* 80:5069–5075.

Garg, R. 1996. *Physics and Modeling of Stratified Turbulent Channel Flow.* PhD thesis, Stanford University, Stanford, CA.

Garg, R. P., S. G. Monismith, and J. H. Ferziger. 1992. Evaluation of the Craik-Leibovich Theory for a Wavy Turbulent Open-channel Flow. Unpublished, Stanford University, Department of Mechanical Engineering, Stanford University.

Garrett, C. J. R. 1976. Generation of Langmuir Circulations by Surface Waves: a Feedback Mechanism. *Journal of Marine Research* 34:117–130.

Germano, M., U. Piomelli, P. Moin, and W. H. Cabot. 1991. A Dynamic Subgrid-scale Eddy Viscosity Model. *Physics of Fluids A* 3:1760–1765.

Ghosal, S., and P. Moin. 1993. The Basic Equations for the Large Eddy Simulation of Turbulent Flows in Complex Geometry. *Journal of Fluid Mechanics* 282:1–27.

Gnanadesikan, A. 1996. Mixing Driven by Vertically Variable Forcing: an Application to the Case of Langmuir Circulation. *Journal of Fluid Mechanics* 322:81–107.

Goldstein, S. 1952. *Modern Development in Fluid Dynamics.* London: Oxford University Press.

Gordon, A. L. 1970. Vertical Momentum Flux Accomplished By Langmuir Circulation. *Journal of Geophysical Research* 75:4177–79.

Hamner, and Schneider. 1986. Regularly Spaced Rows of Medusae in the Bering Sea: Role of Langmuir Circulation. *Limn. Ocean.* 31:171–177.

Handler, R. A., T. F. Swean, R. I. Leighton, and J. D. Swearingen. 1993. Length Scale and the Energy Balance for Turbulence Near a Free Surface. *AIAA Journal* 31(11):1998–2007.

Harris, G. P., and J. N. A. Lott. 1973. Observations of Langmuir Circulations in Lake Ontario. *Limn. Ocean.* 18:584–589.

Hodges, B. R. 1997. *Numerical Simulation of Nonlinear Free-Surface Waves on a Turbulent Open-Channel Flow.* PhD thesis, Department of Civil Engineering, Stanford University, Stanford California, August.

Holm, D. D. 1996. The Ideal Craik-Leibovich Equations. *Physica D* 98:415–441.

Ichiye, T., J. McGrath, and M. Howard. 1985. Some Dynamic Features of Langmuir Circulations. In Y. Toba and H. Mitsuyasu (Eds.), *The Ocean Surface*, 479–486. D. Reidel Publishing Co.

Jenter, H. L., and O. S. Madsen. 1989. Bottom Stress in Wind-driven Depth-averaged Coastal Flows. *Journal of Physics Oceanography* 19:962–974.

Jones, I. 1985. Turbulence Below Wind Waves. In *The Ocean Surface-Wave Breaking, Turbulent Mixing and Radio Probing*, 437–442. Reidel.

Katz, B., R. Gerard, and M. Costin. 1965. Responses of Dye Tracers to Sea Surface Conditions. *Journal of Geophysical Research* 70:5505 - 5513.

Kenny, B. C. 1977. *An Experimental Investigation of the Fluctuating Currents Responsible for the Generation of Windrows.* PhD thesis, University of Waterloo.

Kim, J., and P. Moin. 1985. Application of a Fractional-Step Method to Incompressible Navier-Stokes Equations. *Journal of Computational Physics* 59:308–323.

Kim, J., P. Moin, and R. D. Moser. 1987. Turbulence Statistics in Fully Developed Channel Flow at Low Reynolds Number. *Journal of Fluid Mechanics* 177:133–166.

Klemp, J., and D. Duran. 1983. An Upper Boundary Condition Permitting Internal Gravity Wave Radiation in Numerical Mesoscale Models. *Mon. Weather Rev.* 11:430–444.

Kraus, E. B. 1967. Organized Convection in the Ocean Surface Later Resulting from Slicks and Wave Radiation Stress. *Physics of Fluids* 10S:294–297.

Lam, K., and S. Banerjee. 1992. On the Condition of Streak Formation in a Bounded Turbulent Flow. *Physics of Fluids A* 4:306 - 320.

Langmuir, I. 1938. Surface Motion of Water Induced by Wind. *Science* 87:119–123.

Leibovich, S. 1977a. Convective Instability of Stably Stratified Water in the Ocean. *Journal of Fluid Mechanics* 82:561–581.

Leibovich, S. 1977b. On the Evolution of the System of Wind Drift Currents and Langmuir Circulations in Ocean. Part 1: Theory and the Averaged Current. *Journal of Fluid Mechanics* 79:715–743.

Leibovich, S. 1980. On Wave-current Interaction Theories of Langmuir Circulations. *Journal of Fluid Mechanics* 99:715–724.

Leibovich, S. 1983. The Form and Dynamics of Langmuir Circulations. *Ann. Rev. Fluid Mech.* 15:391–427.

Leibovich, S., and S. K. Lele. 1982. Themocline Erosion and Surface Temperature Variability due to Langmuir Circulations. FDA Report 82-07, Cornell University, Ithaca, New York.

Leibovich, S., S. K. Lele, and I. M. Moroz. 1989. Nonlinear Dynamics in Langmuir Circulations and in Thermosolutal Convection. *Journal of Fluid Mechanics* 198:471–511.

Leibovich, S., and S. Paolucci. 1980a. Energy Stability of the Eulerian-mean Motion in the Upper Ocean to Three-dimensional Perturbations. *Physics of Fluids A* 23:1286–1290.

Leibovich, S., and S. Paolucci. 1980b. The Langmuir Circulation Instability as a Mixing Mechanism in the Upper Ocean. *Journal of Physics Oceanography* 10:186–207.

Leibovich, S., and S. Paolucci. 1981. The Instability of the Ocean to Langmuir Circulations. *Journal of Fluid Mechanics* 102:141–167.

Leibovich, S., and K. Radhakrishnan. 1977. On the Evolution of the System of Wind Drift Currents and Langmuir Circulations in the Ocean. Part 2: Structure of the Langmuir Vortices. *Journal of Fluid Mechanics* 80:481–507.

Leibovich, S., and A. Tandon. 1993. Three Dimensional Langmuir Circulation Instability in a Stratified Layer. *Journal of Geophysical Research* 98:16501–16507.

Leibovich, S., and D. Ulrich. 1972. A Note on the Growth of Small Scale Langmuir Circulations. *Journal of Geophysical Research* 77:1683–1688.

Lele, S. K. 1985. *Some Problems in Hydrodynamic Stability Arising in Geophysical Fluid Dynamics.* PhD thesis, Cornell University.

Leonard, B. P. 1979. A Stable and Accurate Convective Modelling Procedure Based on Quadratic Upstream Interpolation. *Journal of Computational Physics* 98:90–100.

LeVeque, R. L., and J. Oliger. 1981. Numerical Analysis Project. Manuscript na-81-16, Stanford University, Department of Computer Science, Stanford University.

Li, M., and C. Garrett. 1993. Cell Merging and Jet/Downwelling Ratio in Langmuir Circulation. *Journal of Marine Research* 51:737–769.

Li, M., and C. Garrett. 1995. Is Langmuir Circulation Driven by Surface Waves or Surface Cooling. *Journal of Physics Oceanography* 25:64–76.

Li. M., and C. Garrett. 1997. Mixed Layer Deepening Due to Langmuir Circulation. *Journal of Physics Oceanography* 27:121–132.

Lilly, D. K. 1992. A Proposed Modification of the Germano Subgrid Scale Closure Method. *Physics of Fluids A* 4:633–635.

Longuet-Higgins, M. S. 1953. Mass Transport in Water Waves. *Phil. Trans. Roy. Soc.* A.245:535–58.

Lund, T. S., S. Ghosal, and P. Moin. 1993. Numerical Experiments with Highly-variable Eddy Viscosity Models. ASME Fluid Engineering Conference, Washington, D. C., June.

McDonald, B. K. 1994. Modeling Laminar Flow Beneath a Prescribed Small Amplitude Wavy Surface. Engineering dissertation, Stanford University, Department of Civil Engineering, Stanford University.

McWilliams, J. C., P. R. Sullivan, and C. Moeng. 1997. Langmuir Turbulence in the Ocean. *Journal of Fluid Mechanics* 334:1–30.

Mei, C. C. 1983. *The Applied Dynamics of Ocean Surface Waves.* Wiley-Interscience.

Melander, M. V., N. J. Zabusky, and J. C. McWillams. 1988. Symmetric Vortex Merger in Two Dimensions: Causes and Conditions. *Journal of Fluid Mechanics* 195:303–340.

Melville, W. K., R. Shear, and F. Veron. 1998. Laboratory Measurements of the Generation and Evolution of Langmuir Circulations. *Journal of Fluid Mechanics* 364:31–58.

Mizuno. 1985. The Interaction of Crossed Waves and Wind-induced Currents in a Laboratory Tank. In Y. Toba and H. Mitsuyasu (Eds.), *The Ocean Surface*, 465–470. D. Reidel Publishing Co.

Mobley, C. D. 1977. *A Numerical Model of Wind and Wave-Generated Langmuir Circulations.* PhD thesis, University of Maryland, College Park, Maryland.

Moin, P., K. Squire, W. Cabot, and S. Lee. 1991. A Dynamic Subgrid-scale Model for Compressible Turbulence and Scalar Transport. *Physics of Fluids A* 3:2746–2757.

Monismith, S. G., and J. J. M. Magnaudet. 1998. On Wavy Mean Flows, Langmuir Cells, Strain, and Turbulence. In *Physical Processes in Lakes and Oceans*, Vol. 54 of *Coastal and Estuarine Studies*, 101–110.

Myer, G. E. 1971. *Structure and Mechanics of Langmuir Circulations on Small Inland Lake.* PhD thesis, State University of New York, Albany.

Nepf, H. M., E. A. Cowen, S. J. Kimmel, and S. G. Monismith. 1995. Longitudinal Vortices Beneath Breaking Waves. *Journal of Geophysical Research* 100:16211–16221.

Nepf, H. M., and S. G. Monismith. 1991. Experimental Study of Wave-induced Longitudinal Vortices. *Journal of Hydraulical Engineering* 117:1639–1649.

Nepf, H. M. 1992. *The Production and Mixing Effects of Langmuir Circulations.* PhD thesis, Department of Civil Engineering, Stanford University, Stanford California, August.

Perng, C. Y. 1990. *Adaptive-Multigrid Computations for Incompressible Flows, Including Geometry, Temperature, and Salinity Effects.* PhD thesis, Department of Mechanical Engineering, Stanford University, Stanford California.

Phillips, O. M. 1977. *The Dynamics ofthe Upper Ocean.* Cambridge, England: Cambridge University Press.

Pidgeon, E. 1999. *An Experimental Investigation of Breaking Wave Induced Turbulence.* PhD thesis, Department of Civil Engineering, Stanford University, Stanford California, June.

Piomelli, U. 1992. High Reynolds Number Calculations Using a Dynamic Subgrid Scale Model. In *Bull. Amer. Phys. Soc.*, Vol. 37, 1714–1715.

Piomelli, U., W. Cabot, P. Moin, and S. Lee. 1991. Subgrid-scale Backscatter in Turbulent and Transitional Flows. *Physics of Fluids A* 3:1766–1771.

Piomelli, U., J. H. Ferziger, and P. Moin. 1987. Models for Large Eddy Simulations of Turbulent Channel Flows Including Transpiration. Report TF-32, Department of Mechanical Engineering, Stanford University, Stanford, California.

Pollard, R. T. 1977a. Observations and Models of the Structure of the Upper Ocean. In E. Krauss (Ed.), *Modeling and Predictions of the Upper Layers of the Ocean*, 102–117. Oxford Pergamon Press.

Pollard, R. T. 1977b. Observations and Theories of Langmuir Circulations and Their role in Near Surface Mixing. In M. Angel (Ed.), *A Voyage of Discovery: George Deacon 70th Anniversary Volume*, 235–251. Oxford Pergamon Press.

Price, J. F., R. A. Weller, and R. Pinkel. 1986. Diurnal Cycling: Observations and Models of the Upper Ocean Response to Diurnal Heating, Cooling and Wind Mixing. *Journal of Geophysical Research* 91:8411–8427.

Scott, J., G. E. Myer, R. Stewrt, and E. G. Walther. 1969. On the Mechanism of Langmuir Circulations and Their Role in Epilimnion Mixing. *Limn. Ocean.* 14:493–503.

Scriven, L. E. 1960. Dynamics of A Fluid Interface, Equation of Motion For Newtonian Surface Fluids. *Chemical Engineering Science* 12:98–108.

Shyy, W., and T. C. Vu. 1991. On the Adoption of Velocity Variable and Grid System for Fluid Flow Computation in Curvilinear Coordinates. *Journal of Computational Physics* 92:82–105.

Skyllingstad, E. D., and D. W. Denbo. 1995. An Ocean Large-eddy Simulation of Langmuir Circulations and Convection in the Surface Mixed Layer. *Journal of Geophysical Research* 100:8501–8522.

Smagorinsky, J. 1963. General Circulation Experiments with the Primitive Equations, I. The Basic Experiment. *Monthly Weather Review* 91:99–164.

Smith, J. 1992. Observed Growth of Langmuir Circulation. *Journal of Geophysical Research* 97:5651–5664.

Smith, J., R. Pinkel, and R. Weller. 1987. Velocity Structure in the Mixed Layer During MILDEX. *Deep-Sea Research* 17:425–439.

Smith, J. A. 1998. Evolution of Langmuir Circulation During a Storm. *Journal of Geophysical Research* 103:12649–12668.

Smith, S. D. 1988. Coefficients for Sea Surface Wind Stress, Heat Flux, and Wind Profiles as a Function of Wind Speed and Temperature. *Journal of Geophysical Research* 93:15467–15472.

Stewart, R., and R. K. Schmitt. 1968. Wave Interaction and Langmuir Circulations. In *Proc. 11th Conf. Great Lakes Res.*, 31–32, Center of Great Lakes Studies, University of Wisconsin.

Stokes, G. G. 1847. On the Theory of Oscillatory Waves. In *Mathematical and Physical Papers*, Vol. I, 75–129, London. Cambridge University Press.

Sutcliffe, W. H., E. R. Baylor, and D. W. Menzel. 1963. Sea Surface Chemistry and Langmuir Circulations. *Deep-Sea Research* 10:233–243.

Tandon, A., and S. Leibovich. 1995a. Secondary Instability in Langmuir Circulations. *Journal of Physics Oceanography* 25:1206–1217.

Tandon, A., and S. Leibovich. 1995b. Simulation of Three-dimensional Langmuir Circulation in Water of Constant Density. *Journal of Geophysical Research* 100:22613–22623.

Thais, L., and J. Magnauduet. 1996. Turbulent Structure Beneath Surface Gravity Waves Sheared by the Wind. *Journal of Fluid Mechanics* 328:313–344.

Thompson, J. F., Z. U. A. Warsi, and C. W. Mastin. 1985. *Numerical Grid Generation, Foundation and Applications.* Elsevier.

Thorpe, S. 1982. On the Clouds of Bubbles Formed by Breaking Wind Waves in Deep Water, and Their Role in Epilimnion Mixing. *Phil. Trans. Roy. Soc.* A 304:155–210.

Thorpe, S. 1984. The Effect of Langmuir Circulations on the Distribution of Submerged Bubbles Caused by Breaking Waves. *Journal of Fluid Mechanics* 142:151–170.

Thorpe, S., and A. Hall. 1980. The Mixing Layer of Loch Ness. *Journal of Fluid Mechanics* 101:687–703.

Thorpe, S., and A. Hall. 1982. Observation of the Thermal Structure of Langmuir Circulations. *Journal of Fluid Mechanics* 114:237–250.

Thorpe, S. A. 1992. The Breakup of Langmuir Circulation and the Instability of an Array of Vortices. *Journal of Physics Oceanography* 22:350–360.

Thorpe, S. A. 1995. On the Meandering and Dispersion of a Plume of Floating Paticles Caused by Langmuir Circulation and a Mean Current. *Journal of Physics Oceanography* 25:685–690.

Turner, J. S. 1973. *Buoyancy Effects in Fluids.* Cambridge, England: Cambridge Univ. Press.

Welander, P. 1963. On the Generation of Wind Streaks on the Sea Surface by Action of Surface Film. *Tellus* 15:67–71.

Weller, R., J. P. Dean, J. Marra, J. Price, E. A. Francis, and D. C. Boardman. 1985. Three-dimensional Flow in the Upper Ocean. *Science* 227:1552–1556.

Weller, R., and J. Price. 1988. Langmuir Circulation Within the Oceanic Mixed Layer. *Deep-Sea Research* 35:711–747.

Whitham, G. B. 1974. *Linear and Nonlinear Waves.* New York: Wiley.

Woodcock, A. H., and J. Wyman. 1946. Convective Motion in Air Over the Sea. *Ann. NY Acad. Sci.* 48:749–776.

Zang, Y., R. L. Street, and J. R. Koseff. 1994. A Non-staggered Grid, Fractional Step Method for Time-dependent Incompressible Navier-Stokes Equations in Curvilinear Coordinates. *Journal of Computational Physics* 114:18–33.

Zang, Y. 1993. *On the Development of Tools for the Simulation of Geophysical Flows.* PhD thesis, Department of Mechanical Engineering, Stanford University, Stanford California, March.

Zedel, L., and D. M. Farmer. 1992. Organized Structures in Surbsurface Bubble Clouds: Langmuir Circulation in the Open Ocean. *Journal of Geophysical Research* 96:8889–8900.